Experimental and Model-based Analysis of the Steady-state and Dynamic Operating Behaviour of the Direct Methanol Fuel Cell (DMFC)

Experimentelle und modellbasierte Analyse
des stationären und dynamischen Betriebsverhaltens
der Direkt-Methanolbrennstoffzelle (DMFC)

Der Fakultät für Verfahrens- und Systemtechnik der
Otto-von-Guericke-Universität Magdeburg
zur Erlangung des akademischen Grades

Doktoringenieur
(Dr.-Ing.)

am 4.Mai 2004 vorgelegte Dissertation

von Dipl.-Ing. Thorsten Schultz

Preface

This dissertation thesis presents the major results of my research performed between 1999 and 2004 at the Max Planck Institute (MPI) for Dynamics of Complex Technical Systems in Magdeburg (Germany). I had the privilege to be one of the first researchers of this new institute, and the first assistant to my scientific mentor Prof. Dr.-Ing. Kai Sundmacher, to whom I owe my whole scientific career so far (without him calling me to Magdeburg I would not be a scientist at all). Helping to build up something totally new has been a unique and very exciting experience, even though especially in the first years it often meant spending more time on organisational rather than on scientific matters, like e.g. planning whole laboratories and assisting other new colleagues while the infrastucture was still in its buildup.

I wish to thank all those who accompanied and supported my work, starting with my parents who financed my university studies and always encouraged me in my scientific proceeding. Also to my wife Sandra I owe so much that it is impossible to put in words.

I thank all colleagues at the MPI and the Otto-von-Guericke University of Magdeburg for their cooperation, uncountable discussions and for being good friends. I did and still do enjoy working together with you. Special thanks go to Dipl.-Ing. Peter Heidebrecht and Dipl.-Ing. Richard Hanke for their assistance in reading and correcting the first version manuscript and for various hints in the fields of thermodynamics and modeling.

Many thanks I owe to the staff of the mechanical and electrical workshops of the MPI and the Institute for Process Engineering as well as to Dipl.-Ing. Torsten Schröder for their enthusiastic cooperation in development and production of various types of fuel cells. Now we have a full fuel cell toolbox enabling us to produce all variations of PEM fuel cells, whether operated on methanol or hydrogen (or.... who knows what else ?) as fuel. This should be a good basis for the whole experimental fuel cell activities in our research group (which has grown up to nine scientists since my beginning in 1999).

I thank Prof. Keith Scott from the University of Newcastle-upon-Tyne (UK) and Prof. Andreas Seidel-Morgenstern from the Otto-von-Guericke University Magdeburg for accepting to be co-referees of this thesis, and Prof. Scott also for his advice on practical aspects of DMFC production.

Concluding, I am looking forward to the continuation of the actual research work in the field of fuel cells and to the developing new topics at hand.

Magdeburg, May 2004

Vorwort (Preface in German Language)

Die vorliegende Dissertationsschrift entstand während meiner Assistententätigkeit, welche ich seit 1999 am Max-Planck-Institut (MPI) für Dynamik komplexer technischer Systeme in Magdeburg ausübe. Ich hatte das Privileg einer der ersten Wissenschaftler dieses neugegründeten Institutes zu sein, und erster Assistent meines wissenschaftlichen Mentors Herrn Prof. Dr.-Ing. Kai Sundmacher, dem ich meine gesamte bisherige wissenschaftliche Laufbahn verdanke (ohne seinen Ruf nach Magdeburg wäre ich heute mit Sicherheit kein Wissenschaftler). Mithelfen zu dürfen etwas ganz Neues aufzubauen war eine einmalige und sehr aufregende Erfahrung, auch wenn es, gerade in den ersten Jahren, oft bedeutete mehr Zeit mit organisatorischen denn mit wissenschaftlichen Dingen zuzubringen, wie z.B. ganze Labore auszustatten und Kollegen zu unterstützen als die Infrastruktur noch im Aufbau war.

Ich danke all jenen die mich und meine Arbeit unterstützt haben, allen voran meinen Eltern die mein Studium finanzierten und die mich immer aufs Neue ermutigten. Meiner Frau Sandra verdanke ich so unausprechlich viel, daß ich für immer in ihrer Schuld stehe.

Mein Dank gilt auch allen Kollegen am MPI und der Otto-von-Guericke-Universität Magdeburg für ihre Kooperation, unzählige Diskussionen, und für ihre Freundschaft. Ich genoß und genieße die Zusammenarbeit mit Euch. Besonderer Dank gebürt Herrn Dipl.-Ing. Peter Heidebrecht und Herrn Dipl.-Ing. Richard Hanke für die Korrekturlesung dieser Arbeit und für zahllose wichtige Hinweise in Bezug auf Thermodynamik und Modellierung.

Ich danke allen Mitarbeitern der mechanischen und elektrischen Werkstatt des MPI und des Instituts für Verfahrenstechnik der Otto-von-Guericke-Universität sowie Herrn Dipl.-Ing. Torsten Schröder für ihr enthusiastisches Engagament bei der Entwicklung und Herstellung von zahllosen Brennstoffzellenvarianten. Wir verfügen nunmehr über einen kompletten Brennstoffzellenbaukasten, mit dem es uns möglich ist die verschiedensten PEM Brennstoffzellentypen einheitlich herzustellen, egal ob sie als Brennstoff Methanol oder Wasserstoff (oder...mal sehen was noch) verwenden. Wir verfügen hiermit über eine gute Basis für weitere experimentelle Tätigkeiten in unserer seit 1999 auf neun Wissenschaftler angewachsenen Brennstoffzellen-Forschungsgruppe.

Besonderer Dank gilt auch Herrn Prof. Keith Scott von der Universität Newcastle-upon-Tyne (UK) und Herrn Prof. Andreas Seidel-Morgenstern von der Otto-von-Guericke Universität Magdeburg für ihre Bereitschaft als Zweitgutachter für diese Arbeit zu fungieren.

Magdeburg, im Mai 2004

Table of Contents

List of Symbols

Symbol	SI-Unit	Meaning
a	-	activity
$a^*_{H_2O}$	-	water vapour activity (assumed ideal gas, activity coefficient 1)
A	m^2	area
A^S	m^2	fuel cell cross-sectional area
A_i	-	parameter in various empirical correlations
B		transport matrix
B_0	m^2	permeability coefficient
B_i	-	parameter in various empirical correlations
c	mol m^{-3}	molar concentration in fluid phase
$\tilde{c}$	mol m^{-3}	molar pseudo-concentration w.r.t. total volume (in porous structures only)
C	F m^{-2}	capacity w.r.t. real (inner) surface area
$\hat{C}$	F m^{-2}	capacity w.r.t. cell cross-sectional area
C_i	-	parameter in various empirical correlations
C_p	J kg^{-1} K^{-1}	mass-based heat capacity at constant pressure
$\overline{C}_p$	J mol^{-1} K^{-1}	molar heat capacity at constant pressure
$\Delta_R \overline{C}_p$	J mol^{-1} K^{-1}	molar heat capacity change of reaction at constant pressure
d	m	thickness, diameter
D	m^2 s^{-1}	diffusion coefficient
$\mathbb{D}$	m^2 s^{-1}	Maxwell-Stefan binary diffusion coefficient
D_i	-	parameter in various empirical correlations
e	J m^{-2} s^{-1}	enthalpy flux density
E^A	J mol^{-1}	activation energy
E_i	-	parameter in various empirical correlations
f	-	fugacity (gas phase activity)
$f_{Schlögl}$	A s^2 kg^{-1}	lumped parameter (SCHLÖGL model, chapter 6.9.3.2)
f_{MS}	A s^2 kg^{-1}	lumped parameter (Maxwell-Stefan model, chapter 6.9.3.2)
F	A s mol^{-1}	Faraday's constant, F = 96485 A s mol^{-1}
$\Delta_F G$	J mol^{-1}	Gibbs energy of formation (from the elements)

$\Delta_R G$	J mol^{-1}	Gibbs energy of reaction
h	J mol^{-1}	specific enthalpy
$\Delta_F H$	J mol^{-1}	enthalpy of formation (from the elements)
$\Delta_R H$	J mol^{-1}	reaction enthalpy
i	A m^{-2}	current density
j	mol m^{-2} s^{-1}	individual molar flux density (only non-convective fluxes)
J		flux vector (in potential-flux-vector-concept)
k	mol m^{-3} s^{-1}	rate constant, kinetic constant
k_p	m^2	hydraulic permeability (SCHLÖGL model, chapter 6.9.3.2)
k_ϕ	m^2	electrokinetic permeability (SCHLÖGL model, chapter 6.9.3.2)
l	m	length
L	m	circumference
L_i	s m^{-2}	friction terms in chapter 6.9.3.2
m	kg m^{-2} s^{-1}	mass flux density
M	kg	mass
$\overline{M}$	kg mol^{-1}	molar mass
n	mol m^{-2} s^{-1}	overall molar flux density
ncv	-	number of control volumes (in spatial discretisation)
N	mol	number of moles
$\hat{N}$	mol m^{-2}	mole density (loading, used only in polymer material)
N_{cells}	-	number of single cells in a fuel cell stack (chapter 3.2.2)
$N_{M,cu}$	-	number of chain units between two polymer cross-links
Nu	-	Nusselt number
p	Pa	pressure
p_{cell}	W m^{-2}	cell power density
p_{sat}	Pa	saturation pressure
P	cm^3 g$^{0.25}$ s$^{-0.5}$	parachor (chapter 9.1.8)
P_{cell}	W	cell power
Pr	-	Prandtl number
q	J m^{-2} s^{-1}	heat flux density (due to thermal conduction)
Q	C = A s	charge
$\hat{Q}$	C m^{-2}	charge density w.r.t. cross-sectional area

$\widetilde{Q}$	C m^{-3}	volumetric charge density w.r.t. total volume
r	mol m^{-3} s^{-1}	reaction rate
R	J mol^{-1} K^{-1}	ideal gas constant, R = 8.314 J mol^{-1} K^{-1}
Re	-	Reynolds number
$\Delta_F S$	J mol^{-1} K^{-1}	entropy of formation (from the elements)
$\Delta_R S$	J mol^{-1} K^{-1}	reaction entropy
t	s	time
T	K	temperature
U	V	voltage
v	m s^{-1}	velocity
v		sensor value (only appendix chapter 8)
V	m^3	volume
$\overline{V}$	m^3 mol^{-1}	molar volume
$(\sum \overline{V}^*)$	cm^3 mol^{-1}	atomic diffusion volumes (appendix chapter 9.1.8)
$\Delta_R V$	m^3 mol^{-1}	molar volume of reaction
w	-	mass fraction
x	-	mole fraction in liquid phase
X		potential vector (in potential-flux-vector-concept)
y	-	mole fraction in gas phase
Y	-	loading [kg/kg]
z	-	cell coordinate perpendicular to cell plane
z^*	-	number of transferred electrons/single charges

Greek symbols

α	W m^{-2} K^{-1}	heat transfer coefficient
α_a, α_c	-	charge transfer coefficients (anodic, cathodic)
α_{Vignes}	-	thermodynamic factor (Vignes method, appendix chapter 9.1.8)
α'	-	viscous selectivity factor (chapter 6.3), set to unity in this work
β_{H^+/H_2O}	s m^{-2}	lumped parameter, chapter 6.9.3.2
γ	-	activity coefficient
κ	-	ratio of specific heat capacities, chapter 9.1.9
Γ	C m^{-3} s^{-1}	volumetric charge production (by electrochemical reactions)
ε	-	volume fraction (pore volume fraction = porosity)
ε^*	-	exponent in HAYDUK-MINHAS correlation
η	V	overpotential
η^{vis}	Pa s	dynamic viscosity
η_{th}	-	thermodynamic efficiency
θ	-	relative surface coverage
ϑ	°C	temperature
λ	W m^{-1} K^{-1}	thermal conductivity coefficient
Λ	-	relative water content in membrane
μ	J mol^{-1}	chemical potential
μ^{vis}	m^2 s^{-1}	kinematic viscosity
ν	-	stoichiometric coefficient
ρ	kg m^{-3}	mass density
τ	-	tortuosity factor
ϕ	V	electrical potential
χ	-	non-ideality coefficient in Flory-Huggins activity model

Indices

Upper Indices:

atmosphere	in standard atmosphere (sea level, standard conditions)
A, B, ..., Z	notation of on-line sensors (chapter 4.4 and appendix chapter 8)
A	anode compartment (supply channel structure)
AC	anode catalyst layer
ACP	polymer phase within (AC)
AD	anode diffusion layer
AF	anode feed
cross	crossover
C	cathode compartment (supply channel structure)
CC	cathode catalyst layer
CCP	polymer phase within (CC)
CD	cathode diffusion layer
CF	cathode feed
dew	dew point
eff	effective
M	membrane (PEM)
ref	at reference conditions (see chapter 2.2)
sat	saturated, saturation
T	transposed (vector/matrix)
vis	viscosity
θ	at standard conditions: $T^{\theta} = 298\ \mathrm{K},\ p^{\theta} = 10^5\ \mathrm{Pa}$

Lower Indices:

a	anode
air	air
BET	BET surface
c	cathode
carbon	carbon material
cat	catalyst
cat. layer	catalyst layer
cell	cell

cross	crossover
cu	polymer chain unit
CH_3OH	methanol
CO_2	carbon dioxide
delay	delay
dry	dry
eff	effective
eq	equilibrium
F	feed
gas	gas
(g)	in gas state
graphite	graphite material
h	hydraulic
H^+	proton
H_2O	water
i	counting index
j	counting index
Joule	Joule heating
k	counting index
liquid	liquid
(l)	in liquid state
max	maximum
min	minimum
M	solid matrix in porous materials
N_2	nitrogen
O_2	oxygen
p	at constant pressure
pipe	of pipe
pores	in pore(s)
P	polymer
PTFE	PTFE (polytetrafluorethylene, TEFLON™)
PTFE-treated Toray	TORAY™ carbon paper, treated with PTFE, see chapter 3.3.2
rel	relative

res	residence
rev	reversible
R-SO$_3^-$	sulfonate ion bound to polymer backbone
sat	saturated
sound	sound
storage	storage
sustain	sustain
S	solid
Schlögl	according to SCHLÖGL equation, see chapter 6.9.3.2
th	thermodynamic
thermoneutral	thermoneutral
tot	total
untreated Toray	TORAY™ carbon paper, as supplied by manufacturer
UNIFAC	UNIFAC activity model
wet	wet

Abbreviations

A	anode compartment (supply channel structure)
AC	anode catalyst layer
ACP	polymer phase within (AC)
AD	anode diffusion layer
bara	bar absolute (absolute pressure in bar)
C	cathode compartment (supply channel structure)
CC	cathode catalyst layer
CCP	polymer phase within (CC)
CD	cathode diffusion layer
DMFC	direct methanol fuel cell
M	membrane (PEM)
MCFC	molten carbonate fuel cell (fuel: hydrogen, methane etc.)
MEA	membrane electrode assembly (DMFC core component)
ODE	ordinary differential equations
PDE	partial differential equations
PEM	polymer electrolyte membrane

PEMFC	polymer electrolyte membrane fuel cell
PTFE	polytetrafluoeethylene, TEFLON™
scbm	standard cubic metre (m^3 gas at T=25°C, p=1bar)
SOFC	solid oxide fuel cell (fuel: hydrogen, methane etc.)

Abstract

Direct Methanol Fuel Cells (DMFC) are analysed experimentally and theoretically with respect to their steady-state and dynamic operating behaviour. The current status (2003) of the DMFC is presented with special focus on basic principle, functional materials of which the DMFC consists and modeling and simulation approaches. An own laboratory scale DMFC design is presented, as well as a fully automated miniplant used for its operation under various steady-state and dynamic operating conditions. The miniplant allows the determination of methanol and water crossover fluxes from anode to cathode. The DMFCs are fed with liquid methanol water solutions and air. Influences of methanol feed concentration, temperature, pressure and electric cell current are analysed using a rigorous one dimensional process model of the DMFC. In this model the generalised Maxwell-Stefan equations are used for describing mass transport in porous structures. A special focus lies on the realistic description of the polymer electrolyte membrane (PEM), where in the model even swelling and phase equilibria at the interfaces are accounted for. The results show that methanol and water crossover through the membrane are governed by diffusion rather than electro-osmosis, and that the model yields good approximations to experimental results.

Kurzzusammenfassung (German Abstract)

Das stationäre und dynamische Betriebsverhalten der Direkt-Methanolbrennstoffzelle wird experimentell und theoretisch untersucht. Ein Überblick über den aktuellen Forschungsstand (2003) mit Schwerpunkten Funktionsweise, Funktionsmaterialien sowie Modellierung und Simulation wird gegeben. Das selbstentwickelte DMFC-Design wird präsentiert, ebenso die für die Untersuchungen verwendete vollautomatische Miniplant. Die Miniplant erfaßt neben anderen Prozeßgrößen die zellinternen Stoffströme (sog. Crossover) von der Anode zur Kathode. Die DMFCs werden mit flüssigen Methanol-Wasser-Mischungen und Luft betrieben. Die Einflüsse von Methanolkonzentration, Temperatur, Druck und elektrischem Zellstrom werden analysiert. Hierzu wird ein rigoroses eindimensionales Prozeßmodell vorgestellt. Es verwendet die verallgemeinerten Maxwell-Stefan-Gleichungen für Stofftransportvorgänge in porösen Strukturen. Einen Schwerpunkt der Modellierung bildet die realistische Beschreibung der Polymerelektrolyt-Membran unter Berücksichtigung von Quellungsvorgängen und äußeren Phasengleichgewichten. Die Simulationsergebnisse zeigen gute Übereinstimmung mit den experimentellen Werten. Insbesondere zeigt sich, daß die Wasser- und Methanol-Crossover-Ströme durch die Zellmembran überwiegend durch diffusive und nicht durch elektroosmotische Effekte bestimmt werden.

1 Introduction to the Direct Methanol Fuel Cell (DMFC)

In the last twenty years, the interest in fuel cells of all types has increased dramatically. Not only the prospect of high efficiencies and the abscence of gaseous pollutants like sulfur dioxide and the various nitrogen oxides, but also the striking simplicity of a fuel cell and the abscence of moving parts led to the conclusion that a real alternative for internal combustion engines was at hand. Research activities in industry and universities have reached enourmous extents, and fuel cell related sessions have become a regular part of many international conferences and fairs. The possible applications of fuel cells reach from stationary power production in Megawatt dimensions down to portable systems to supply mobile consumer electronics with below one Watt. Inbetween these two extremes lies the application as vehicle power source, with nearly all major car manufacturers having their own research program now.

Recently, after many years of research and development on fuel cells, the initial euphoria has somewhat vanished, as many problems are yet unsolved. Especially for mobile applications, most material components in fuel cell systems are still too expensive, the systems are more complex than initially anticipated, sometimes difficult to control and still the discussion is far from an end which will be the best fuel for them (see e.g. [1][2]). While hydrogen is the best fuel in terms of operating the fuel cell itself, its production, storage and distribution is complicated. Alternatively liquid hydrocarbons are discussed, like conventional gasoline, methanol or ethanol. These are easy to store and to distribute, but their conversion in a fuel cell system is difficult. Either one produces hydrogen from them in a fuel processor (reformer) to feed a standard Polymer Electrolyte Fuel Cell (PEMFC), or one uses a fuel cell which can convert a liquid fuel directly, like the Direct Methanol Fuel Cell (DMFC) [3][4][5][6]. The

Figure 1-1 *Fuel cell system for Laptop developed by Casio Corp. (Japan). System consists of hydrogen fuel cell (PEMFC) and integrated micro reformer fed with methanol-water solutions.*

complexity of a system combining a hydrogen production unit and a hydrogen-consuming fuel cell have led many people to the conclusion that the DMFC is the more favourable option for certain mobile and portable applications, although recently advancements in producing micro-scale reforming reactors for portable applications have been reported (e.g. by Casio Corporation, Japan, see Figure 1-1).

The advantage of hydrocarbon fuels (which are liquid under ambient conditions) over hydrogen with respect to storage can be demonstrated impressively when considering the volume and mass required for an appropriate tank system to store a specific energy, e.g. the equivalent of 50 dm^3 of conventional petrol (approx. 1500 MJ), as presented in Table 1-1. Additionally the simple handling of liquid hydrocarbons compared to that of pressurised or liquified hydrogen is a major advantage.

Table 1-1 *Comparison of different fuels with respect to the necessary storage system for the equivalent of 50 dm^3 of standard petrol (=1500 MJ).Original data from [7][8][9].*

Fuel	***Temperature within tank [K]***	***Pressure within tank [bar]***	***Fuel volume [dm^3]***	***Mass of tank system [kg]***	***Volume of tank system [dm^3]***
Petrol	300	1	50	42	61
Diesel fuel	300	1	44	42	54
Ethanol	300	1	71	71	84
Methanol	300	1	95	95	116
Natural gas	300	200	208	160	260
Hydrogen gas (GH_2), standard gas bottle	300	207	-	148	920
Hydrogen gas (GH_2), high-pressure tank	300	690	-	190	510
Hydrogen in MgNi-Hydride	567	6.1	-	837	275
Hydrogen in FeTi-Hydride	310-535	34.5	-	863	235
Liquid hydrogen (LH_2)	20	2	177	75	312

1.1 Principle and Main Features of the DMFC

The basic principle of the DMFC is illustrated in Figure 1-2. Like any other type of low temperature fuel cell, the DMFC consists of seven layers. The middle layer is an ion-conductive membrane, which acts as electronic isolator and barrier for all non-ionic species. In the case of the DMFC it is a proton conducting polymer film usually referred to as polymer electrolyte membrane (PEM). The typical commercially available materials are between 20 and 200 µm thick. On either side of this PEM, a thin porous layer is applied, which contains the electrocatalysts on whose surfaces the electrochemical reactions take place. These catalyst layers are the fuel cells electrodes (anode and cathode). They are usually around 10 to 20 µm thick, depending on the preperation method. Next to the catalyst layers are porous layers responsible for electron and reactant transport. These so-called diffusion layers are made from carbon fibre papers or woven carbon cloth with thicknesses around 200-500 µm, having a good electron conductivity and high porosity. In most commercial products also a porous layer made from carbon black and some polymeric binders (like e.g. Teflon^{TM}) is prepared on

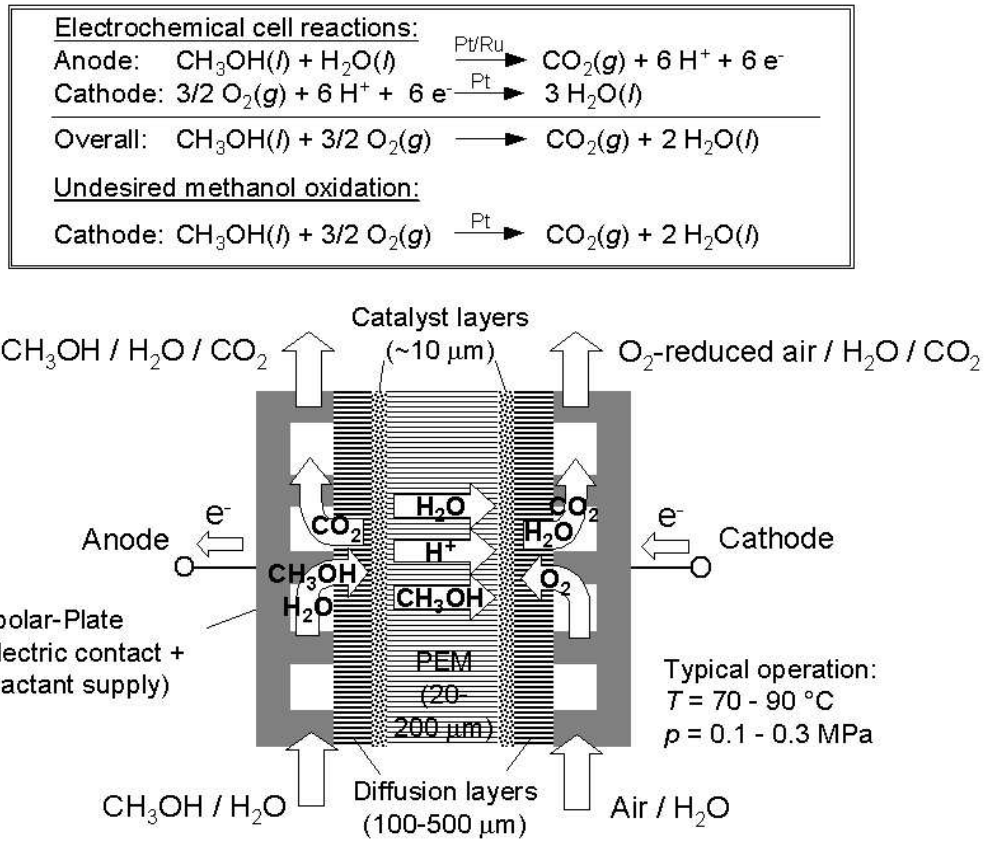

Figure 1-2 *Structure and principle of the Direct Methanol Fuel Cell (DMFC) [11].*

top of the carbon paper/carbon cloth. It has quite the same structure as the catalyst layers and shall improve especially the electronic contact to the catalyst layers. The last layer on either side are usually called anode and cathode compartment, respectively. Typically they are channel structures adjacent to the diffusion layers, machined into electron conductive plates (made from graphite, stainless steel or other highly corrosion resistive materials). Through the channels, the reactants are distributed across the diffusion layers.

To the DMFC anode compartment, methanol and water are fed, either in liquid or vapour phase. The reactants diffuse through the anode diffusion layer towards the anode catalyst layer. There they are converted to carbon dioxide, protons and electrons. The carbon dioxide is transported towards the anode compartment, as the PEM is nearly impermeable to gases. The protons are transported through the PEM to the cathode side. The electrons are transported over the anode diffusion layer, anode cell plate, external circuit (where they can be used to perform work), cathode cell plate and cathode diffusion layer to the cathode catalyst layer. There, the protons and electrons reduce oxygen (from air) to form water. The oxygen is transported through the cathode diffusion layer, in opposite direction to the water produced at the cathode, which leaves the cathode catalyst layer towards the cathode compartment.

Calculating the thermodynamic open circuit cell voltage (i.e. without current load), the Nernst equation predicts values around 1.2 V, depending on temperature, activities of all species, pressure and operation mode (i.e. liquid or vapourized methanol-water mixtures fed to the anode, detailed thermodynamic calculations of the open circuit cell voltage under standard conditions are presented in chapter 2.1). For the liquid operated mode, these theoretical values are given in Figure 1-3, in dependence on the methanol feed concentration. Also plotted in this figure are typical experimental data [68]. They are significantly lower than the theoretical values, which shows the necessity (but also the potential) to improve the performance by identifying and examining the major problems of the DMFC.

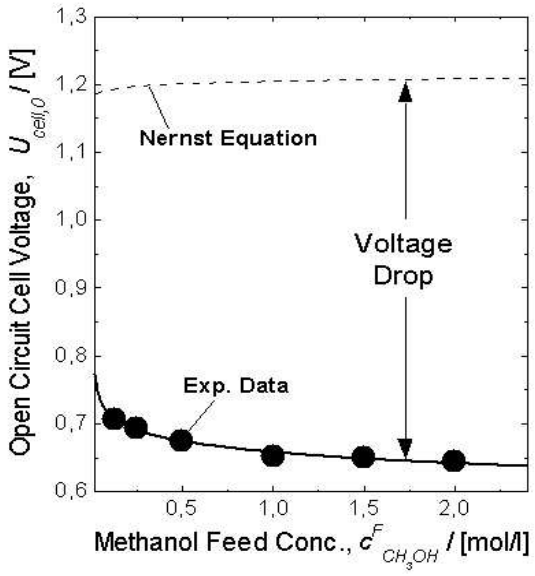

Figure 1-3 *Thermodynamic and experimental cell voltages of the DMFC, adopted from [68]*

The classical experiment to evaluate the performance of a fuel cell is to measure the stationary current-voltage characteristics (U-i curve). Typical data from a DMFC (own experiments) are plotted in Figure 1-4. One can see S-shaped curves which are typical for fuel cells. The curves reflect the different limiting mechanisms occuring during the operation of a fuel cell. At zero current (open circuit condition), the cell voltage lies around 0.65 V, which is only half the value expected from thermodynamics (as already mentioned above, Figure 1-3). At low current densities (left, between first and second data point, respectively), the cell voltage is mainly influenced by reaction kinetic limitations. At high current densities (right, last 3 data points) mass transport limitations dominate the process. At a certain current density (limiting current density, here roughly 150 and 250 mA/cm^2 respectively), the cell voltage drops to zero. The middle section of the curves is a transition region where the cell voltage shows quasi-ohmic (i.e. linear) behaviour. The right hand side plot in Figure 1-4 shows the same data plotted as cell power density over current density. It is also typical for any type of fuel cell, that the maximum cell power is achieved at roughly two thirds of the limiting current

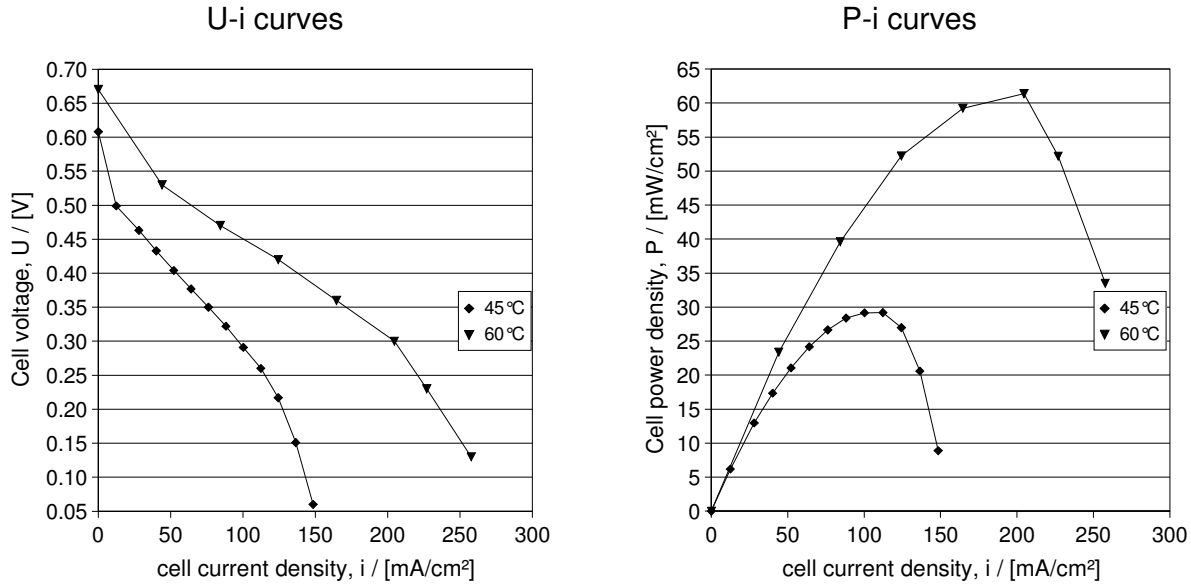

Figure 1-4 *Typical experimental current-voltage (U-i) and cell power (P-i) curves:*
Cell temperature T=45/60°C, system pressures p_a=p_c=1.7 bara
Flow rates V_a=0.5 dm^3/min, V_c=0.5 scbm/h
Methanol concentration c=1 mol/dm^3, cathode feed dry air
Cell specifications: Anode: 5 mg/cm^2 PtRu black atomic ratio 1:1
Cathode: 5 mg/cm^2 Pt black
PEM: NAFION™ N105

density. For the DMFC that means a cell voltage of around 0.3 V. Obviously, it is most attractive to operate such a fuel cell in the intermediate power region between one and two thirds of the limiting current density.

The current voltage characteristics given in Figure 1-4 show a maximum power density of 0.06 W cm^{-2}, but recently values around 0.1 to 0.25 W cm^{-2} have been reported for the DMFC, e.g. by the ZSW in Ulm (Germany), though such results are usually achieved for much higher operating temperatures (around 100°C) and feed air pressures (up to 4 bara). Compared to the hydrogen-fed PEMFC (actually maximum values around 1.0 to 1.5 W cm^{-2} at above 100°C and system pressures above 2 bara), this is still a significantly lower performance.

In the following sections, the actual state of development concerning the DMFC will be presented shortly, with a special focus on the various problems and recent activities in the respective fields. A much more detailed treatment of most of these topics is available in a comprehensive review paper by ARICO et al. (2001) [13]. A broad overview over the full range of fuel cell development can be found in a very extensive review paper by CARRETTE et al. (2001) [14].

1.2 Anodic Methanol Oxidation

While the anodic oxidation of hydrogen on noble metal catalysts is a well-understood fast reaction with only low reaction overpotentials. The anodic oxidation of methanol is much more complicated. Overall, six electrons are transferred, consequently many (surface-bound) reaction intermediates can be expected.

First studies of the reaction mechanism were made in the late 1970's and early 1980's during the first evaluations for direct methanol fuel cells (e.g. MCNICHOL at Shell Laboratories [15]). It turned out that platinum catalysts as used for hydrogen oxidation show only poor performance, whereas the use of binary or ternary noble metal catalysts (always with platinum as one component) leads to significant improvements. Intensive studies of reaction mechanisms on platinum and platinum/ruthenium catalysts were performed e.g. by KENNEDY and HAMNETT in Oxford in the early 1990's [17]. The conclusion of all these works is that some very stable reaction intermediates exist that need at least one other catalytic functionality to react further as that provided by platinum alone. Many possible reaction mechanisms have been proposed (see e.g. Figure 1-5, reaction mechanism adopted from [15], rate expressions formulated by SUNDMACHER et al. [16]), nonetheless the reaction mechanism is still not fully understood. The most common opinion is that platinum-bound carbon monoxide (Pt-CO) or

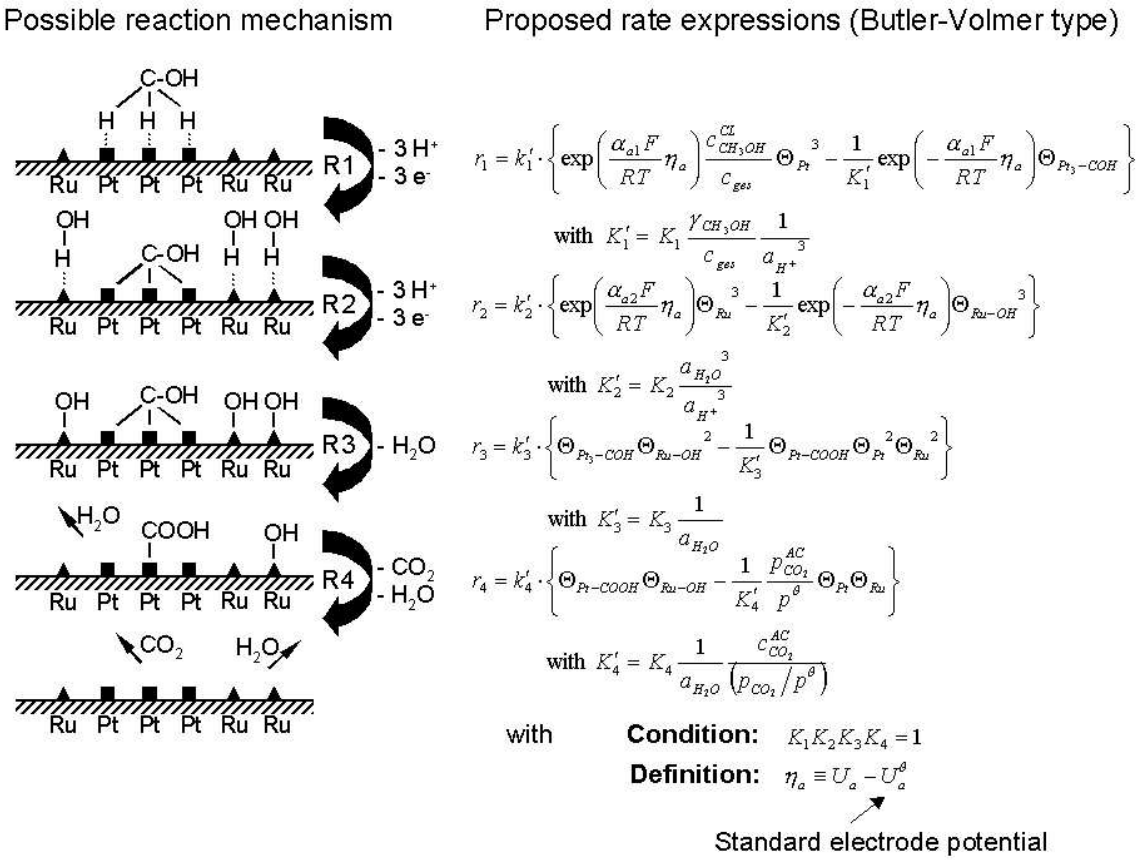

Figure 1-5 *Possible reaction mechanism of the anodic methanol oxidation on platinum ruthenium catalysts (mechanism adopted from [15], rate expressions first published in [16])*

carbon hydroxide (Pt-COH) is the long-living intermediate. In any case, one needs surface-bound OH-groups for the conversion of the intermediate(s) to carbon dioxide. OH-groups are preferably formed on ruthenium, tin and other metals [17][18][19][20] at fairly low electrode potentials (~ 0.3 V vs. NHE), whereas on platinum one needs much higher potentials (~ 0.9 V vs. NHE). Important research on the electrochemical methanol oxidation was done by the group of VIELSTICH (University of Bonn, Germany), with a main focus on the reaction mechanism on platinum and its numerous modifications, and the influence of the cristalline surface structure (i.e. where on the surface does the reaction preferably take place and what does that imply for catalyst design) [21].

Another group working on this field is that of GÖTZ and WENDT et al. [19] (Technical University of Darmstadt, Germany), their focus being ternary catalysts consisting of platinum and ruthenium with a third metal (tungsten, molybdenum, tin) as promotor.

There are also many groups working on CO-tolerant catalysts for hydrogen-consuming fuel cell anodes for use in combinations of a hydrocarbon reformer and PEMFC. As adsorbed CO is supposed to play a significant role in the DMFC as well (see previous paragraph), these results should also be considered. Here the groups of ARICO and ANTONUCCI (CNR-TAE, Messina, Italy, e.g. [22]), BÖNNEMANN (Max-Planck-Institute for Carbon Research, Mülheim, Germany) and VOGEL et al. (Fritz-Haber-Institute of the MPG, Berlin, Germany) [18] and CIUREANU and WANG [23] (H Power Inc., Quebec, Canada) shall be mentioned. ARICO and ANTONUCCI et al. are working on CO-tolerant platinum-ruthenium catalysts with tungsten as promotor and on the influence of the catalyst support. Their current work deals with the question whether a support is necessary at all. BÖNNEMANN and VOGEL are focusing on CO-tolerant platinum-tin-alloy catalysts and a novel sol-gel-based preparation method. CIUREANU and WANG have made intensive studies on the behaviour of platinum-ruthenium catalysts for the oxidation of hydrogen in the presence of CO. Their approach is measuring impedance spectra and modeling equivalent circuits. The same has been extensively done by MÜLLER and URBAN (DaimlerChrysler AG, Ulm, Germany) for the DMFC [24] showing the potentials of this method for the characterisation of kinetics and mass transport phenomena.

The general agreement between the results of the groups working on hydrogen/CO mixtures and the groups working on methanol supports the theory of surface-bound CO being the long-living intermediate, which is responsible for the slow overall reaction kinetics and the need for improved catalysts.

Another important factor for the anode catalyst performance (at least for the famous platinum-ruthenium catalysts) is the nature of the support, the catalyst particle size and the atomic ratio between platinum and ruthenium. ARICO et al. [25] and the group of GOTTESFELD (Los Alamos, USA, [26]) found that thinner support layers and even unsupported catalysts produced the best performance. The GOTTESFELD group also found out, that, as expected, smaller particles and higher surface areas are beneficial for the process [26]. In contrast to these parameters, the atomic ratio between platinum and ruthenium seems to have a lower influence [26]. For standard operating temperatures above 70°C typically optimal performance has been found with atomic ratios of platinum to ruthenium in the region of 1:1, wheras at lower temperatures a higher relative platinum content seems to be beneficial.

Recently, a totally different approach for catalyst design is emerging, based on a bionic point of view. The transformation of hydrocarbons to carbon dioxide under abstraction of electrons and protons not only takes place in fuel cells, but can also be found in each biological cell, as part of the breathing process. Here cell enzymes (either immobilised or within living cells)

without any noble metals content are the catalysts. Even higher hydrocarbons as e.g. glucose can be converted to carbon dioxide and (in the first step) electrochemical energy in the form of charge transporting molecules, which carry the released protons and electrons. First research projects on so-called bio fuel cells are under way and current densities of a few mA/cm^2 have been reached under ambient temperature and pressure using e.g. glucose as fuel [27][28][29]. The potential of such bio-analogue catalysts has not yet been evaluated properly for the use in technical applications, as the current densities are still much too low for most applications. Nonetheless for further research in the field of the DMFC and other low-temperature fuel cells, these developments should be more closely examined. Another closely connected aspect is the formation of proton conductive membranes in biological cells, which will be shortly mentioned in the next section.

Finally, besides the search for more active anode catalysts, another approach is thinkable to improve the performance of a DMFC which is based on adding another active component to the methanol water solution. This idea has been widely accepted in the field of hydrogen-fed PEMFCs, where a so-called air-bleed (or the use of hydrogen peroxide instead of pure water in the humidifier [30]) adds small quantities of oxygen to the hydrogen-rich (but CO-containing) anode feed gas. This oxygen helps to remove adsorbed CO from the anode platinum catalyst, thus increasing the number of active catalyst sites. As in the DMFC similar poisoning effects on platinum sites play an important role, the same idea might be applicable. The problem here is that in a liquid-fed DMFC it is difficult to supply oxygen gas to the anode catalyst. As water-soluble alternative, hydrogen peroxide has been discussed very recently. First (yet unpublished) experiments of some research groups have shown promising effects.

Not only is the electrochemical methanol oxidation itself a complex phenomenon which limits performance, the necessary structure of the catalyst layers (and this applies to the cathode catalyst layer in the same manner) is also very complicated. The educts (e.g. methanol and water or oxygen) are supplied through the diffusion layer. The products (e.g. carbon dioxide) leave on the same way, as the PEM is nearly impermeable for gases. The produced or consumed protons are transported via the ionic conducting polymer phase connecting the catalyst layer to the PEM, the electrons are transported through the metallic catalyst particles to the electron conductive (carbon) matrix, which forms the diffusion layer. This complex structure is depicted schematically in Figure 1-6. Only catalyst particles, which are in contact with both the electron conducting phase (i.e. the diffusion layer matrix) and the ionic conducting phase (i.e. the PEM) are active. It is not yet clear, whether also a certain amount of

free catalyst surface (i.e. direct contact with the fluid phase/free pore space) is necessary for an active particle. Particles which are totally coverd by ionomer might at least be less active due to the additional transport resistance for educts and products. In today' s typical catalyst layers, most of the catalyst is not fulfilling all of these requirements and is therefore inactive. The term used in this respect is “catalyst utilisation”. As it is still not clear, which basic necessities have to be fulfilled for an actice catalyst site, very different definitions for this utilisation exist, which vary broadly. Therefore, no numbers are given here.

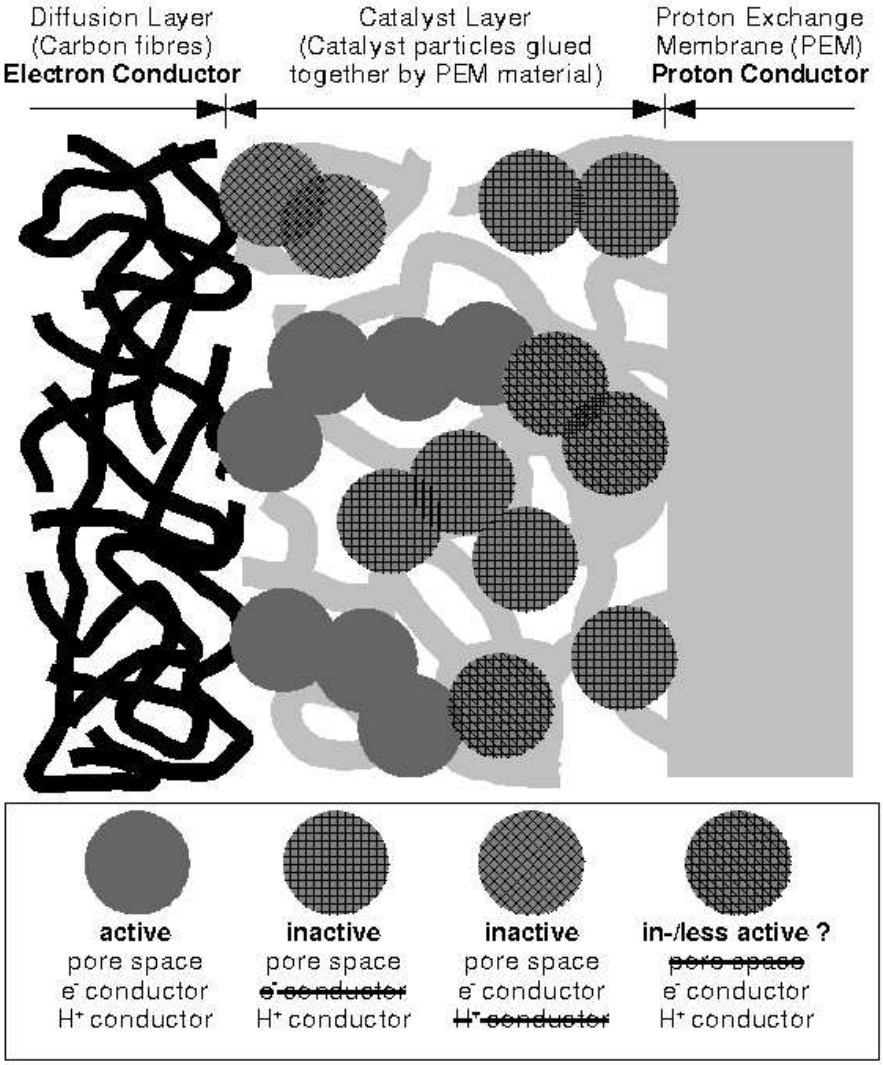

Figure 1-6 *Schematic of catalyst layer, state of catalyst particles shown (active particle simultaneously needs connection to open pore space, electron and proton conductor)*

1.3 Polymer Electrolyte Membrane (PEM)

Heart of the DMFC is the PEM. Ideally it has to combine a good proton conductivity with being an isolator for electron transport and being impermeable for all other molecules. Additionally it has to have a very high chemical and thermal stability. Operation at up to 120°C has been realised with commercial products like NAFION™ (by DuPont), GoreSelect/PRIMEA™ (by Gore), Flemion™ (by Asahi Glass) and other quite similar fluorinated polymers carrying sulfonic acid groups. But even higher temperatures are desired when DMFC' sare operated in the vapour phase. Some results with newly designed special high temperature membranes (e.g. based on acid-doped polybenzimidazole, PBI, available from PEMEAS, formerly a division of Celanese) indicate that above 150 - 200°C the kinetics of the methanol oxidation is not a limiting factor any more [31][32][33].

As a matter of fact, until very recently, there is still only one commercially available product on the free market fulfilling at least some of these requirements: NAFION™ by DuPont (Figure 1-7). It is a polymer with a fully fluorinated backbone carrying sulfonic acid groups (-SO_3H) for proton conductivity. Thicknesses between 50 and 200 µm are available, but there are also new developments featuring a mechanical reinforcement to allow for thicknesses down to 20 µm (e.g. PRIMEA™ by Gore). New materials are under evaluation with

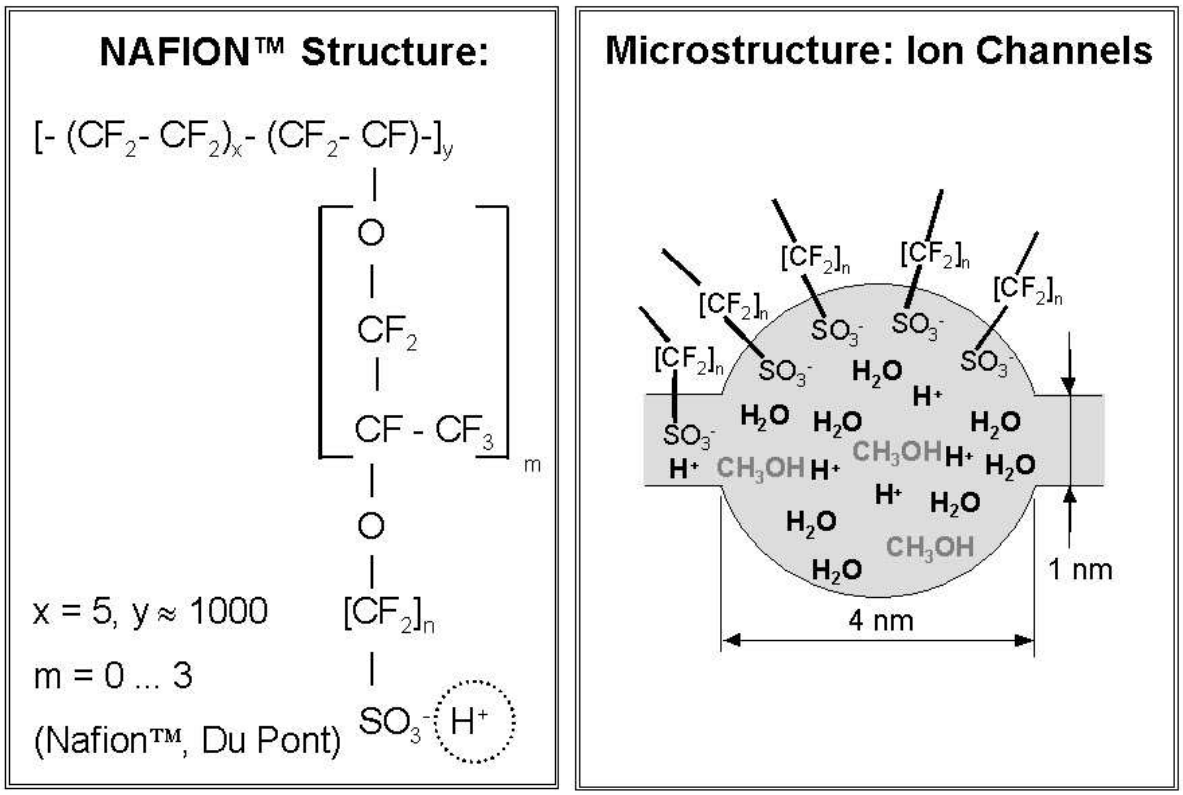

Figure 1-7 *Polymer structure (left) and microscopic structure of wet NAFION™ (right)*

promising results, at least for use in hydrogen fuel cells (e.g. developed by the Paul-Scherrer-Institute, e.g. [34]), but most of these materials are not yet available on the free market. This is either due to the early stage of development of some of these materials or due to the fact that most membrane developers are already bound to industrial partners, mainly car manufacturers, and are therefore not selling their products to independent manufacturers or research groups. Successful industrial developments have been reported e.g. by Giner Inc., 3M, Gore, OMG, Fumatech and many others, but mostly without any published results useful for critical assessment and comparison. Freely available since 2003 are membranes by fumatech, and complete MEAs from PEMEAS, 3M, Gore and DuPont,

Unfortunately, protons within NAFION™ (and the same is true for all other similar products) only become mobile when there is water within the material to solvate them and the counterion (in NAFION™ SO_3^-), which is fixed to the polymer backbone. The material is strongly hygroscopic and soaks up large amounts of water (up to 25 weight-%, which makes for a 10% thickness increase due to swelling). On a microscopic scale, NAFION™ is no homogeneous material (Figure 1-7, right): There are water-filled channels with walls formed from the sulfonic acid groups, and totally aliphatic regions where only the polymeric backbones are present. The water-filled channels have diameters between one and roughly 4 nanometers, which is only a few molecule diameters of a water molecule. As these channels cross the whole material, water is easily transported through it, even a slight pressure difference is sufficient. As the proton transport resistance increases rapidly with decreasing water content within the material, a high water content has to be maintained during fuel cell operation.

In hydrogen-fed fuel cells, this places the demand to humidify the hydrogen to prevent the anode side of the membrane from drying out, as the water within the membrane is transported towards the cathode side by the protons (electro-osmosis, electro-osmotic drag). Also using thinner membranes (like e.g. the already mentioned PRIMEA™ by Gore) helps to reduce the problem of the water management.

But the problem gains another quality for the DMFC, as methanol is easily transported through NAFION™ by means of (a) active transport together with the protons and their solvation shell water (electroosmotic drag) as well as (b) diffusion through the water-filled pores and (c) diffusion through the aliphatic (polymer backbone) regions in the NAFION™ itself. This phenomenon is usually called “methanol crossover”. Its severe implications on cell performance will be discussed in the next section (cathode reactions).

For comparison of different membrane materials, very often a methanol permeation equivalent is calculated, which is the Faradaic current density of the methanol crossover flux through the membrane according to Faraday's law:

$$i_{crossover} = z\,F\,n_{CH_3OH} \qquad (1\text{-}1)$$

where z=6 is the number of transferred electrons for full oxidation of one methanol molecule, F=96485 C mol^{-1} is Faraday's constant and n_{CH_3OH} is the molar methanol permeation flux density [mol s^{-1} cm^{-2}] with respect to the cross-sectional area of the cell.

For NAFION™ 117, the methanol permeation equivalent reaches values from 100 up to several 100 mA/cm^2, while the total cell current densities are typically between 100 and 500 mA/cm^2. This emphasises the dramatic losses due to the methanol crossover phenomenon. More detailed information about this can be found in e.g. [35][36][37][38].

A further disadvantage of NAFION™ is its high price (500-1000 US$/m^2), which contributes severly to the overall costs of PEM fuel cell types. For cost reduction, generally membrane materials are under development that are chemically and thermally stable even without fluor contents, but instead featuring a highly aromatic backbone (e.g. [39], Figure 1-8). The acidic function is supplied by sulfonic acid groups, as in NAFION™. Some of these materials showed lower methanol permeation than NAFION™. Extensive studies in this direction have been published by the group of ROZIERE, where polybenzimidazole (PBI), polyetherketone (PEK) and polyetheretherketone (PEEK) are the polymer backbones, respectively, which are functionalised in several different ways [40].

Another approach was proposed by KREUER [41] [42](Max-Planck-Institute for Solid State Research, Stuttgart, Germany). The intercalated water within NAFION™ (or other proton exchange material) should be replaced by another proton donor/acceptor like imidazole. Protons are mobile in these systems without being solvated, so no other molecules should be transported together with the protons. Also the pores in such PEM materials would be filled up with the substitute leading to an overall reduced water (and methanol) permeability. The main drawback is the insufficient thermal stability of imidazole, which can be overcome by using benzimidazole instead. A quite similar approach was used by the group of NARAYANAN (California Inst. of Technology and Jet Propulsion Laboratory, Pasadena, USA). They investigated composite membranes consisting of an organic supporting matrix of polyvinylidene fluoride (PVDF) which contained an inorganic phase of $CsHSO_4$ as proton conductor [43]. The major problem about all these presented modified membranes is the supposedly limited long-term stability, as the proton conducting species may bleed out during

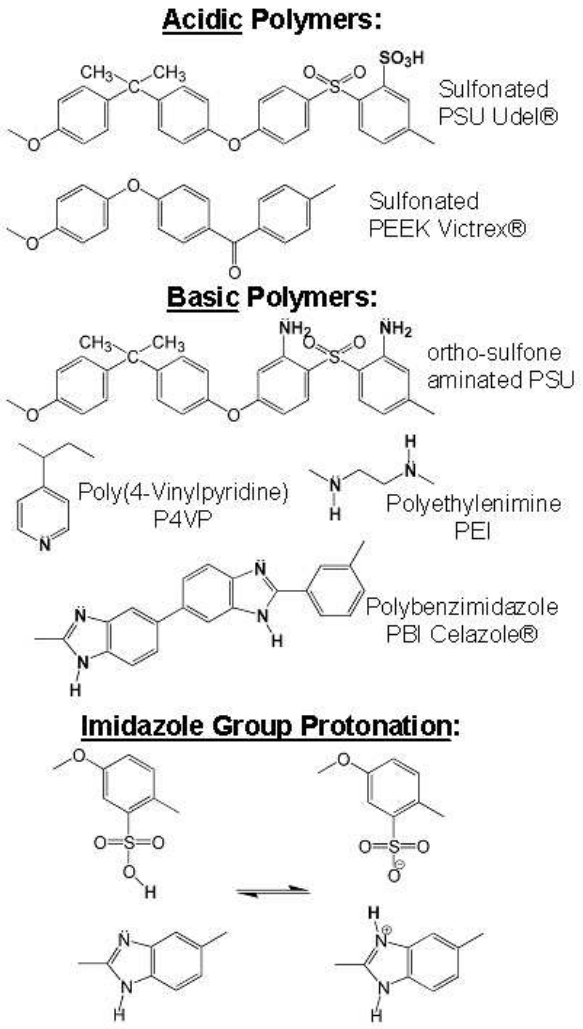

Figure 1-8 *Examples of alternative PEM materials: Acidic polymers (top), basic polymers (middle) as blend components and mechanism of the imidazole group protonation (bottom), adopted from [44][45]*

operation of the fuel cell. Presently, tests are carried out to evaluate this possible problem.

The groups of KERRES et al. and WALKER et al. (University of Stuttgart, Germany) [44][45] have recently combined the already described approaches by using blends of two polymers, one with an acidic function (sulfonic acid groups), one with a basic function (amine, imine or imidazole groups), both featuring an aromatic backbone (Figure 1-8). These polymer blends have only a small water uptake (swelling) combined with a proton conductivity comparable to NAFION™. Also the methanol permeation is lower, for some types only a tenth of the value for NAFION™. Tests on long-term stability are under way and showed encouraging results.

A quite similar approach is that first proposed by the group of SAVINELL et al. at the Case Western Reserve University in Cleveland (USA). They propose to use highly aromatic polymers with basic functions, like e.g. polybenzimidazoles, poly(pyridines), polyimidazoles etc., which form complexes with stable acids like sulfuric acid (H_2SO_4) and phosphoric acid (H_3PO_4) [31][32][33]. Conductivities better than that of NAFION™ under typical fuel cell operation conditions have been found. Also, long term thermal and chemical stability at up to 250°C have been shown. The methanol permeability is significantly lower than with NAFION™ (methanol permeation equivalent of only 5-11 mA/cm^2). First efforts are made by several companies to commercialise these materials.

Another option to reduce methanol permeation is to modify NAFION™ (or other materials) by coating, i.e. producing an asymmetric composite membrane. A coating can be achieved by

either applying a thin (polymer) film onto the membrane surface or by sputtering the surface e.g. with plasma or radiation to modify the NAFION™ structure [45][46]. Both measures have the aim to close the outer water-filled pores, so that no water (and methanol) can enter or leave the membrane. Still the intercalated water (now trapped within the material) provides for the proton mobility. KERRES et al. [44], WALKER et al. [45] and FINSTERWALDER and HAMBITZER [46] found significantly lower methanol permeation rates for these types of materials than for unmodified NAFION™. First use of these modified membranes in the DMFC is under way in several research groups. But still these materials do not solve the problem of the high production costs as they, momentarily, still rely on NAFION™.

Very recently [47], an idea has been taken up which has already been investigated in the early 1990s [48][49]. It aims at reducing selectively the methanol permeability by adding proton conductive zeolites (e.g. Mordenite) to the polymer, whose pores are too small for methanol. Consequently protons can still pass this composite system unhindered using the direct (straight) way, while methanol is forced to permeate around the zeolite particles which means a much longer way and narrow pathways. The principle is illustrated in Figure 1-9. Such materials show proton conductivities which are only slightly smaller than that of NAFION™ and are quite similar to that of other possible fuel cell membrane materials (e.g. Polybenzimidazole, PBI), while the methanol permeability is 20 times lower than that of NAFION™ [47]. The applied polymer material is PVA (polyvinylalcohol), which is a rather cheap commodity polymer compared to NAFION™ . Also the applied zeolites are commercial bulk materials, therefore such composite materials can be assumed to be comparably cheap. Long-term testing under fuel cell relevant conditions as well as data on thermal stability (range of working temperature) have not yet been reported. First products are available from fumatech GmbH.

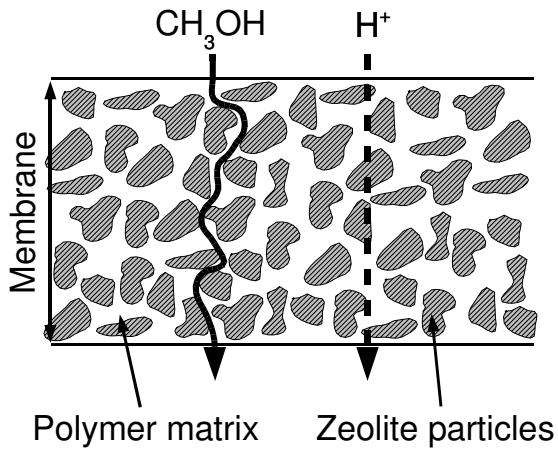

Figure 1-9 *Polymer-zeolite composite membrane: Highly selective zeolite particles embedded within a proton conductive polymer membrane. Protons can pass zeolite whereas methanol can not. (Figure adopted from [47])*

As mentioned in the previous section, another possible approach for a better membrane material is the bionic one. It aims at understanding the structure of biological proton conducting membranes

to apply comparable structures to technical membranes. But in this field, research has only just started, technical products coming out of this will not be available soon. Anyhow, it surely is an interesting and emerging field for polymer scientists.

A much more extensive treatment of the topic of membrane development for PEM fuel cells has been published by KERRES [50], giving a broad overview over the main transport phenomena, the different available materials and the current developments in material design.

1.4 Cathode Reactions

At the cathode, the reduction of oxygen to water usually takes place on platinum catalysts (pure or supported on carbon black). This electrochemical reaction has been broadly examined in the last twenty years accompanying the development of hydrogen-consuming low-temperature fuel cells (PEMFC) (see e.g. [51][52]), electrolysers and membrane reactors for hydrogen peroxide production. The reaction is much slower than the anodic hydrogen oxidation, therefore it plays a major role in optimizing the performance of these cells and reactors. In the DMFC, though, the anodic methanol oxidation is even slower, so the cathodic oxygen reduction can not be assumed to be the rate determining step under most operating conditions.

In the DMFC, also a second reaction takes place at the cathode platinum catalyst: The direct oxidation of methanol permeating through the PEM. All experimental results so far show, that although all reaction intermediates of the methanol oxidation (such as formaldehyde and formic acid) can be found on the cathode catalyst, none of them appears to be in the cathode exhaust gas of a DMFC. As the oxygen stoichiometry is usually very high (oxygen number >> 3), a full oxidation of methanol to carbon dioxide can be assumed to take place. Therefore, at least no poisonous or corrosive reactants leave the DMFC cathode.

The oxidation of crossover methanol as an undesired side reaction leads to a mixed potential formation at the cathode, which results in a severely reduced electrode potential, and therefore also a severely reduced overall cell voltage. Figure 1-3 (page 4) shows the open circuit cell voltage of a DMFC with standard NAFION™ PEM compared to the thermodynamic cell voltage according to the Nernst equation. The dramatic voltage difference between thermodynamic and experimental data is to a large extent due to the oxidation of crossover methanol. Therefore, to achieve better performance a significant reduction in the methanol permeation through the PEM is necessary. This can either be achieved by PEM materials less permeable for methanol (see previous section), by optimized (possibly dynamic) methanol

feeding strategies (see following sections), by simply using low methanol feed concentrations (at the moment values around 1 mol/dm^3 for liquid operation show best performance [26]) or by realising high methanol conversion at the anode (i.e. high fuel utilisation [26]).
On the other hand, using cathode catalysts that are unable to oxidise methanol under the given conditions is unattractive as methanol is poisonous and would in that case be emitted by a DMFC system as a contaminant of the cathode exhaust air. In this case, a consecutive exhaust air cleaning mechanism would be necessary (e.g. based on absorption on activated carbon or other materials, or on a catalytic oxidation zone outside the active cell compartments).

1.5 Water Management in the DMFC

Another important aspect of the DMFC is a possible water flooding of the cathode pore and channel structure due to the water transport through the membrane and the water production at the cathode. The formation of water within the cathode catalyst and its transport through the cathode diffusion layer adds another mass transport resistance for oxygen on its flow towards the reaction zone, and therefore reduces the limiting cell current with respect to the cathodic reactions. This is even worse when condensation occurs. It is not yet fully understood, under which conditions liquid water can be found within the (hydrophobic) pore system of typical diffusion layer materials (usually PTFE impregnated carbon paper or carbon cloth). Due to the high contact angle of water on such materials (>> 90°) and the small mean pore size (usually below 150 µm) condensation is quite unlikely except for low operating temperatures. But outside the diffusion layer, condensation is very likely to occur, and has been reported by many experimental research groups, including our own experiences.
Basically, this aspect plays a similar role like for the PEMFC, and can therefore be addressed likewise (see e.g. [53]). But especially for the liquid-fed DMFC, extremely high water fluxes through the PEM membrane can be observed, which makes cathode flooding much more important than it is for other PEM fuel cell types. The application of improved PEM materials which are less permeable for water (see previous sections) will therefore lead to a significantly improved operation of PEMFCs and DMFCs also in this respect. While such materials are not easily available, one has the only options to operate a DMFC with very high air flow rates (which means providing a sufficient water vapour transport capacity to keep the water partial pressure well below saturation), or accept the high additional mass transport resistance.

1.6 Carbon Dioxide Production

Another problem of the DMFC results from the fact that at the anode a product of limited solubility (carbon dioxide) is generated. In the most common DMFC operation mode, the anode is fed with liquid water-methanol mixtures, which have a fairly low capacity for dissolved carbon dioxide. Therefore, it is widely accepted that even at low current densities carbon dioxide bubbles are forming within and at the outer surface of the porous electrode structure (see flow visualisations conducted by SCOTT et al., e.g. [54][55], and Figure 1-10). These bubbles can block the way for fresh methanol to the catalyst, which leads to an increased transport limitation, i.e. lower cell performance. Hints for describing/modeling this phenomenon can be found for example in [56].

Therefore, in liquid operated DMFCs one has to remove these bubbles from the cell or prevent them from being formed at all by applying high pressures and high liquid flow rates to the methanol water cycle. In any case, one has to remove the carbon dioxide from the methanol water mixture leaving the cell, before it is recycled (see schematic of a liquid operated DMFC-system in Figure 1-11, page 19).

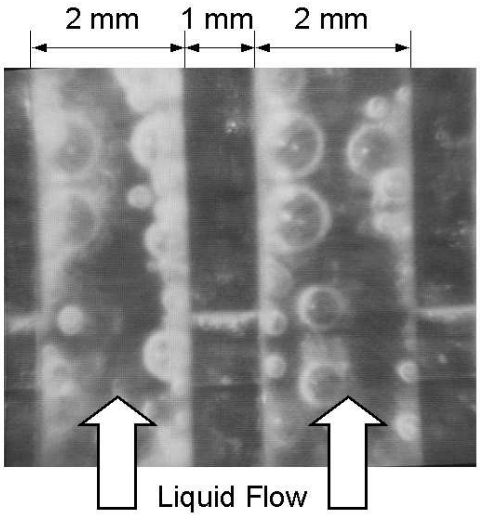

Figure 1-10 *View into two anode compartment channels of a DMFC showing carbon dioxide bubbles released from the diffusion layer into the methanol-water solution. Experiments carried out by SCOTT et al., University of Newcastle (UK) [54][55]*

In liquid-fed cells, this purpose is usually achieved by using a classical stripping column, with a countercurrent strip gas stream. This means one looses a part or the total system pressure at this stage, which consequently means extra power demand to build it up again before the mixture is fed back to the cell. Especially at high working temperatures, the pressure release also leads to the evaporation of large quantities of methanol and water within the stripping column, which makes it necessary to apply a condenser on top of it in order to collect the methanol. In conclusion, stripping off the carbon dioxide by these means leads to a reduced overall system efficiency. Another way of stripping off the carbon dioxide from liquid methanol water mixtures, which has not been reported before, is the use of a carbon dioxide selective

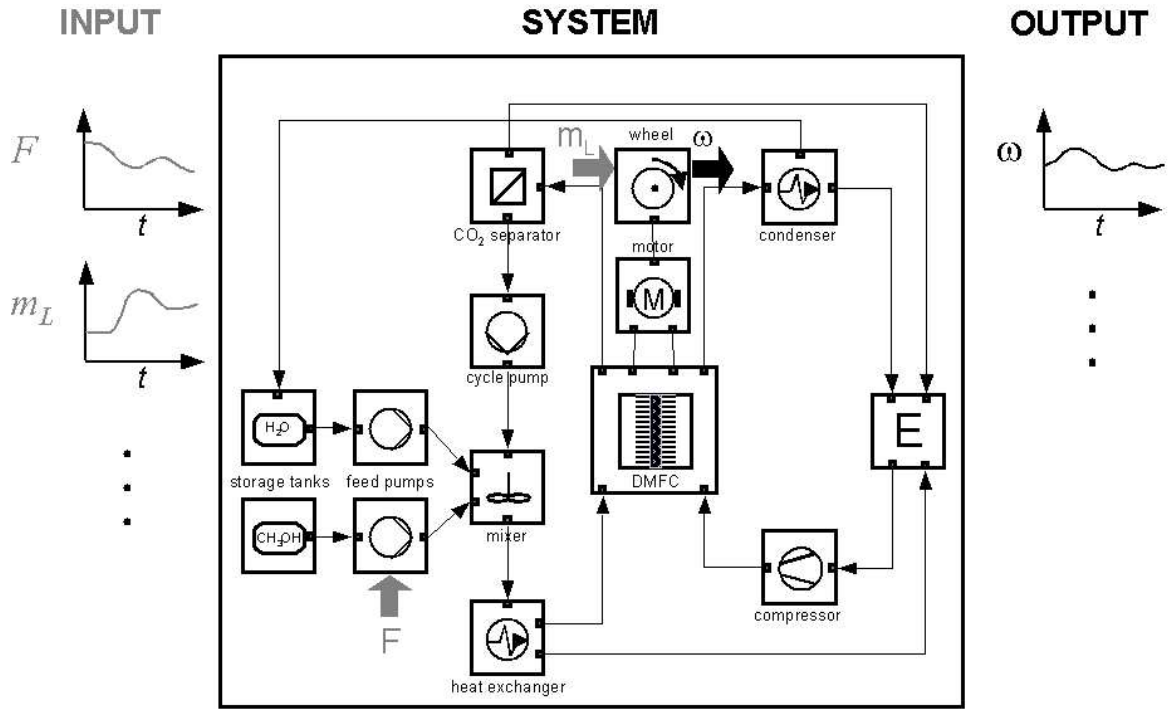

Figure 1-11 *Possible layout of a DMFC automobile drive train featuring an anode liquid cycle with methanol and water dosing, integrated carbon dioxide removal unit, air supply by a compressor and internal water recovery by condensing part of the cathode exhaust water vapour.*
The module "E" represents the environment.

pervaporation membrane, e.g. arranged as hollow fibres. The liquid mixture is streaming through thin porous hollow fibres, which are coated with a gas-selective membrane. On the outside of the fibres, a stripping gas (e.g. air) at low pressure is flowing by. The higher pressure within the liquid is the driving force to transport the carbon dioxide through the membrane into the strip gas. In this arrangement the system pressure in the liquid stays nearly constant (no need to build it up again) and also energy losses due to heat transfer are much lower than for the stripping column arrangement. The task remaining is to improve the selectivity of the pervaporation membrane towards carbon dioxide, because also water and methanol can pass through the membrane to a certain extent. An alternative for using an external membrane contactor for carbon dioxide removal might be to integrate the selective membrane into the anode compartment of the fuel cell itself, opposite the diffusion layer.

In contrast, for the case of vapour operation, the anode is fed with a mixture of water and methanol vapour. Here only a gaseous phase exists, so the carbon dioxide release does not lead to a significant reduction in the methanol supply to the anode, except for at high current densities, depending on the operating conditions, when the carbon dioxide mass flux away

from the catalst layer begins to dominate the convective part of the mass flux through the diffusion layer. But despite the advantages concerning the cell operation itself, the carbon dioxide has to be removed from the cells exhaust stream, as also for this operation mode a recycle loop is necessary (only differential conversion as well) unless one blows out the anode compartment regularly to remove the carbon dioxide and supply fresh reactants, which means possibly high losses in valuable reactants. Now, the easiest way to separate the carbon dioxide from this gas stream is to condense the vapour components (water and methanol) in a stripping condenser. But this, consequently, means that the condensed components fed back to the cycle have to be evaporated again before being fed back to the cell once more. Unless large energy losses are tolerable, quite sophisticated coupled heat exchangers are necessary to fulfill this task efficiently, concerning the whole fuel cell system. This, in turn, leads to difficulties especially during dynamic operation, where most possible applications are for the DMFC (automobiles, mobile power sources). Therefore, vapour operation seems to be less attractive especially for DMFC systems with low power output, although many groups in the field of the DMFC are known to be also working on this topic (e.g. Research-Center Jülich, Germany, and some car manufacturers).

1.7 Modeling and Simulation of DMFC Systems

It is widely accepted that the formulation of mathematical models is essential for a thorough understanding of a technical system. One has to distinguish between steady-state and dynamic models. While steady-state models are mostly used for the identification of potential improvements in terms of overall reaction kinetics (catalysts), mass transport limitations etc. under fixed operating conditions, dynamic models are used to simulate the transient behaviour of a system under changing operation conditions to identify possible problems like e.g. response times, oscillation and overshooting phenomena etc.. As many fuel cell systems are developed for more or less dynamic operation (e.g. in cars, small power stations, portable power supplies), there is a need for information about the dynamic behaviour of such systems. For fuel cells in general, a lot of mathematical models have been formulated: 0-dimensional input-output models as well as 1-dimensional (like e.g. [57]), or even complex 2- (e.g. [58]) and 3-dimensional (e.g. [59]). Most of these models, though, are only describing the steady-state behaviour of the fuel cell, especially for the evaluation of optimization potentials in terms of improving material properties and cell design (e.g. catalysts, reactant supply, mass transfer limitations etc.). Moreover, many of these models are characterised by using lots of

empirical relations rather than physically and electrochemically based ones.

For most types of fuel cells, also dynamic models have been formulated, e.g. for the Molten Carbonate Fuel Cell (MCFC) (e.g. [60][61][62]), the Solide Oxide Fuel Cell (SOFC) (e.g. [63]) and the PEMFC (e.g. [64][65]).

For the DMFC, only few models were formulated so far and most of them are steady-state. Significant efforts have been made by the group of SCOTT et al. (University of Newcastle-upon-Tyne, UK) [66][67] together with SUNDMACHER (Max Planck Institute for Dynamics of Complex Technical Systems Magdeburg and University Magdeburg, Germany) [68] and a group at the DLR Stuttgart and the University of Stuttgart (Germany) [69]. Also active in this field is a group at the Research Center Jülich, Germany [70][71] and one at the University of California in Berkeley headed by NEWMAN [72][73][74]. All their models are 1-dimensional or (1+1)-dimensional physico-chemical models mainly used to predict current-voltage characteristics and simulate concentration and potential profiles.

To the authors knowledge, no dynamic models of the DMFC have been published so far, except for own publications [16][75], but very recently an increased interest in this field can be observed. The modeling strategy, which will be extensively presented in the modeling chapter, follows the idea of a modular composition of the model on hierarchical length scales from pre-defined modules. The final aim is to develop a modular database ("virtual fuel cell lab"), from which different fuel cell modules can be chosen and connected together to get a specific model of a single cell, cell stack or even a whole fuel cell system, which is appropriate for the current task in terms of complexity and detail level. Figure 1-12 shows a possible decomposition of a DMFC single cell (compare to physical structure of the DMFC depicted in Figure 1-2 on page 1). The decomposition is carried out according to the network theory for chemical processes developed by GILLES [76] and MANGOLD et al. [77].

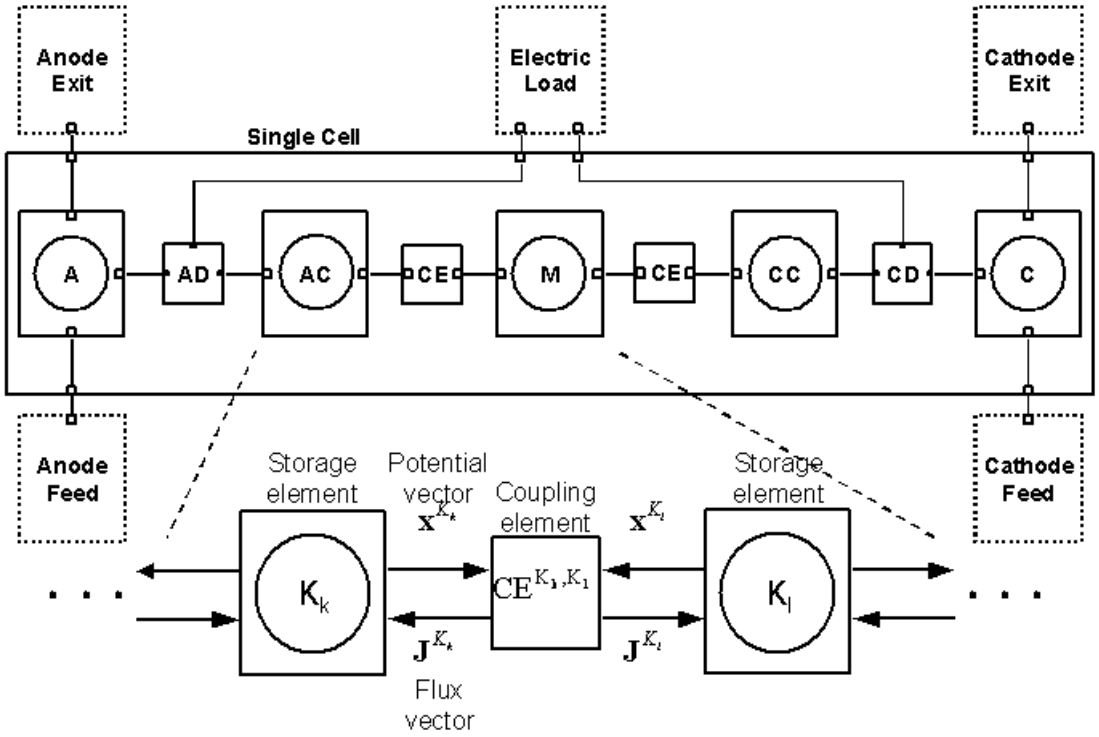

Figure 1-12 *Possible decomposition of a DMFC into structural modules (A=anode compartment, AD=anode diffusion layer, AC=anode catalyst layer, M=membrane, CC=cathode catalyst layer, CD=cathode diffusion layer, C=cathode compartment)*

1.8 Operation and Control of DMFC Systems

For the practical application of fuel cells, not only the behaviour of the cell (or stack) is important, but the behaviour of the whole fuel cell system including all necessary peripherals has to meet specific requirements, depending on the application (see Figure 1-11). Therefore, not only the fuel cell has to be simulated for evaluation and optimization purposes, but the whole system. All system components have to be implemented in the mathematical models, as well as control elements (PID controllers etc.). The simulation of a whole fuel cell system can be done e.g. using software tools like MatLab/SIMULINK or ProMoT/DIVA [78].

Especially for vehicle applications, a DMFC-system has to cope with highly dynamic load conditions, i.e. real driving cycles. Such driving cycles have been standardized already for comparing cars with standard internal combustion engines, battery powered electric cars etc.. The most important standard is the ECE-15 European driving cycle (Figure 1-13, left), which defines a speed profile over time. To use this for simulation of an electric car (whether using a

fuel cell or a battery as electric power source), this profile has to be converted to an electric load demand profile, which depends on the car' sparameters (electric motor characteristics, vehicle mass, friction etc.). Such a profile is also given in Figure 1-13 (right) for a middle-class passenger car with 50 kW maximum power available at the wheel [79]. Such profiles are used for mathematical and experimental simulations of fuel cell systems e.g. by the groups of EMONTS et al. (Research Center Jülich, Germany) [80] and GUZZELLA and AMSTUTZ (ETH Zürich, Switzerland) [81].

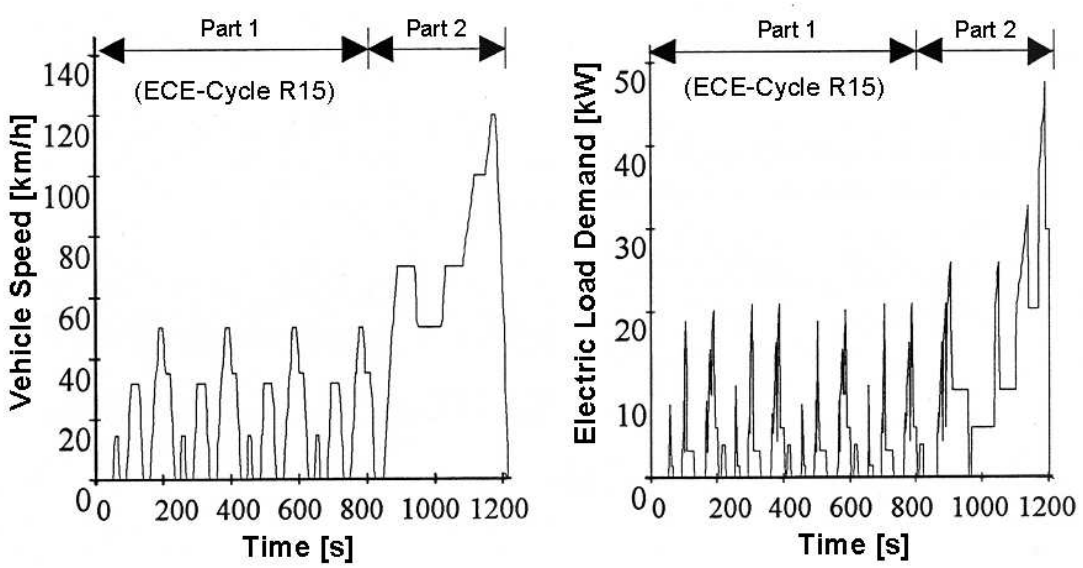

Figure 1-13 *Standard driving cycle ECE-R15 (left) and resulting load demand cycle for an electric car with 50 kW motor, adopted from [81]*

1.9 Conclusions and Scope of This Work

As outlined above, material problems remain a major issue in DMFC research and development, but in these fields (especially membrane and catalyst design) already notable efforts are made by various groups and companies. What is still less recognized is the need for reliable mathematical models of fuel cells, but also for models of complete fuel cell systems. Such models can help in design as well as in control of practical systems.

So far the main focus in terms of modeling is on steady-state models which is very valuable for the design of fuel cell stacks. But for the design of complete systems, also system control has to be accounted for, and this means the system behaviour under (realistic) dynamic operating conditions has to be predicted correctly by adequate models. Also, as the practical design procedure usually has several stages starting at core components such as the PEM, then

sequentially putting them together and adding auxiliary components, it makes sense to reflect this scheme in the model structure as well. Therefore, it is desirable to establish a library of model elements consisting of (preferably physical) sub-models for the fuel cell core components which can be linked together to easily generate a fuel cell system model of adequate complexity [82].

With respect to the DMFC the first steps towards such a model library are the formulation of rigorous physical dynamic models of the core components of single cells. This is the main scope of this work. To be able to formulate such models, the physical and chemical phenomena inside the DMFC have to be understood. For this purpose steady-state and dynamic experiments are carried out. Especially the methanol and water crossover fluxes through the membrane are analysed as they have major influence on the cell performance and behaviour. The emphasis in this work is placed on a realistic physical description of mass and energy transport phenomena. The complex adsorption and multi-step charge transfer mechanisms (electrode reactions) are not yet accounted for, as here a better understanding has yet to be achieved by separate experimental [83] and model-based studies [84]. With respect to mass transport the polymer electrolyte membrane plays a key role. Formulating models for it is complicated due to its complex structure and strong dependence of nearly all transport parameters on the water (and methanol) content (swelling behaviour).

All core layers (diffusion layers, catalyst layers, membrane) of the DMFC are porous structures with the (fluid) active components moving inside solid matrices (which is true for all other types of fuel cells as well). Therefore, the generalised Maxwell-Stefan equations are used as conceptual basis for mass transport modeling. These equations account for all fluid-solid and fluid-fluid interactions and all various driving forces for mass transport with a minimum set of parameters. Also non-idealities can be easily incorporated in this model concept by using activities instead of concentrations.

In the following chapters first the thermodynamics of the DMFC is analysed focusing on the influence of the major process parameters on the reversible open circuit cell voltage (Chapter 2). It is followd by a description of the experimental setup and the cell design (Chapter 3). The obtained experimental results (steady-state and dynamic) are presented in Chapters 4 and 5. Finally, the DMFC model is formulated and simulation results are presented (Chapter 6). In the appendix the derivation of all necessary model parameters is given in detail, as well as some other important information with respect to the modeling.

2 Thermodynamics of the DMFC

2.1 Basic Considerations

In the liquid fed DMFC, stoichiometrically the following electrochemical reactions take place (see also Figure 1-2), not accounting for the complex multi-step nature of the overall electrode reactions and intermediate adsorption steps:

Anode:	$CH_3OH(l) + H_2O(l)$	$\longrightarrow CO_2(g) + 6\ H^+(aq) + 6\ e^-$	(2-1)
Cathode:	$3/2\ O_2(g) + 6\ H^+(aq) + 6\ e^-$	$\longrightarrow 3\ H_2O(g)$	(2-2)
Sum:	$CH_3OH(l) + 3/2\ O_2(g) + H_2O(l)$	$\longrightarrow CO_2(g) + 3\ H_2O(g)$	(2-3)
Overall:	$CH_3OH\ +\ 3/2\ O_2$	$\longrightarrow CO_2 + 2\ H_2O$	(2-4)

Undesired side reactions like e.g. oxidation of methanol at the cathode (crossover phenomenon, see chapter 1) are also not accounted for here. One can see that water is an educt at the anode, as well as a product at the cathode. It is assumed here that carbon dioxide is produced as gas (bubbles, see chapter 1.6). Also it is assumed that the water produced at the cathode is in the vapour phase (no condensation within the active layers of the cathode).

The reaction enthalpy $\Delta_R H$ of the overall reaction is converted into electrical energy and heat. If a total conversion into electrical energy would be possible, an open circuit cell voltage of

$$U_{thermoneutral} = -\frac{\Delta_R H}{zF} \tag{2-5}$$

could be reached. It is called the thermoneutral cell voltage. z denotes the number of transferred electrons per molecule methanol (z=6) and F is Faraday's constant (F=96485 C mol^{-1}). But it can be shown that the maximum open circuit cell voltage is lower than the thermoneutral cell voltage. It is called the reversible cell voltage and is calculated from the Gibbs energy of the reaction $\Delta_R G$:

$$U_{rev} = -\frac{\Delta_R G}{zF} = -\frac{\Delta_R H - T\,\Delta_R S}{zF} \tag{2-6}$$

For the comparison of energy conversion processes, the thermodynamic efficiency η_{th} can be used. It is defined as the ratio of the theoretical maximum technical (i.e. electrical) work, $\Delta_R G$, and the reaction enthalpy, $\Delta_R H$:

$$\eta_{th} = \frac{\Delta_R G}{\Delta_R H} = \frac{U_{rev}}{U_{thermoneutral}} \tag{2-7}$$

At standard conditions, the DMFC (liquid operation) reaches a thermodynamic efficiency of roughly 97%, whereas the hydrogen consuming PEMFC only reaches 83% [12]. Standard combustion processes are limited to a maximum thermodynamic efficiency of around 65% (Carnot efficiency of a conventional thermodynamic cycle at typical operating temperatures).

2.2 Reversible Cell Voltage

The thermodynamic (reversible) cell voltage of the DMFC can be calculated using eq. (2-6). The Gibbs energy of the reversible reaction can be formulated as a function of temperature and all species concentrations (formulated as activities, a_j, for species in liquid phase, and as fugacities, f_j, divided by the standard pressure, p^θ, for species in gas phase). The exponents of the concentration terms are the stoichiometric coefficients of eq.(2-3):

$$\Delta_R G(T, a^A, f^C) = \Delta_R G^\theta(T) + RT \cdot \ln\left(\frac{\left(\frac{f^A_{CO_2}}{p^\theta}\right)(a^A_{H^+})^6}{a^A_{CH_3OH}\, a^A_{H_2O}} \cdot \frac{\left(\frac{f^C_{H_2O}}{p^\theta}\right)^3}{(a^C_{H^+})^6 \left(\frac{f^C_{O_2}}{p^\theta}\right)^{1.5}} \right) \tag{2-8}$$

The upper indices (*A, C*) denote the anode and cathode side, respectively. In eq.(2-8) the Gibbs energy of reaction consists of two additive terms: The first is the standard Gibbs energy, $\Delta_R G^\theta$, which is independent of the species concentrations, but a function of temperature. The second term describes the influence of the species concentrations. The activities are defined as

$$a_j = \gamma_j x_j \tag{2-9}$$

with the activity coefficients γ_j and the mole fractions x_j. The fugacities are defined as

$$f_j = \varphi_j p_j = \varphi_j y_j p \tag{2-10}$$

with the fugacity coefficients φ_j, partial pressures p_j [Pa], gas mole fractions y_j and total pressure p [Pa].

Assuming the polymer electrolyte membrane is an ideal electrolyte, it is only permeable for

protons. In this case the activities of the protons on either side of the fuel cell are equal $\left(a^{A}_{H^+} = a^{C}_{H^+}\right)$, simplifying eq.(2-8) to

$$\Delta_R G(T, a^A, f^C) = \Delta_R G^\theta(T) + RT \cdot \ln \frac{\left(\frac{f^A_{CO_2}}{p^\theta}\right)\left(\frac{f^C_{H_2O}}{p^\theta}\right)^3}{a^A_{CH_3OH}\, a^A_{H_2O} \left(\frac{f^C_{O_2}}{p^\theta}\right)^{1.5}} \quad . \tag{2-11}$$

In a first step, the standard Gibbs energy of reaction is calculated. In the second step the concentration dependent second term of this equation is dealt with.

The standard Gibbs energy of reaction can be split up into the standard reaction enthalpy and the standard reaction entropy:

$$\Delta_R G^\theta(T) = \Delta_R H^\theta(T) - T \cdot \Delta_R S^\theta(T) \quad . \tag{2-12}$$

The standard reaction enthalpy and the standard reaction entropy can both be expressed as functions of the temperature by use of the heat capacity change of reaction $\Delta_R \overline{C}_p$:

$$\Delta_R H^\theta(T) = \Delta_R H^\theta(T^\theta) + \int_{T^\theta}^{T} \Delta_R \overline{C}_p(T^*)\, dT^* \tag{2-13}$$

$$\Delta_R S^\theta(T) = \Delta_R S^\theta(T^\theta) + \int_{T^\theta}^{T} \frac{\Delta_R \overline{C}_p(T^*)}{T^*}\, dT^* \tag{2-14}$$

The reference values can be calculated from the enthalpies and entropies of formation of all species at the reference temperature, $\Delta_F H^\theta_j$ and $\Delta_F S^\theta_j$ respectively, and the stoichiometric coefficients:

$$\Delta_R H^\theta(T^\theta) = \sum_j \nu_j \cdot \Delta_F H^\theta_j(T^\theta) \quad , \tag{2-15}$$

$$\Delta_R S^\theta(T^\theta) = \sum_j \nu_j \cdot \Delta_F S^\theta_j(T^\theta) \quad . \tag{2-16}$$

In the same way, also the change in the heat capacity can be expressed:

$$\Delta_R \overline{C}_p(T) = \sum_j \nu_j \overline{C}_{p,j}(T) \quad . \tag{2-17}$$

For $\Delta_F H^\theta_j$ and $\Delta_F S^\theta_j$ data are available in the literature. For the heat capacities correlations exist, formulated as polynomials in terms of the temperature T:

$$\overline{C}_{p,j}(T) = A_j + B_j T + C_j T^2 + D_j T^3 + E_j \frac{1}{T^2} \quad . \tag{2-18}$$

In Table 2-1 all necessary data for the investigated reaction system are given.

Table 2-1 *Enthalpies and entropies of formation, and coefficients for calculation of heat capacities, data taken from NIST webbook [85], T^{θ}=273K (Similar correlations and parameters can also be found e.g. in [86a])*

	CH_3OH (l)	***H_2O (l)***	***H_2O (g)***	***O_2 (g)***	***CO_2 (g)***
ν_j	-1	-1	+3	-1.5	+1
$\Delta_F H_j^{\theta}(T^{\theta})$ [kJ/mol]	-238.4	-285.8	-241.8	0	-393.15
$\Delta_F S_j^{\theta}(T^{\theta})$ [J/(mol K)]	127	69.95	188.84	205.15	213.79
A_j [J/(mol K)]	81	-203.6	30.09	29.66	25
B_j [J/(mol K^2)]	0	1.52	$6.833\cdot10^{-3}$	$6.137\cdot10^{-3}$	$55.187\cdot10^{-3}$
C_j [J/(mol K^3)]	0	$-3.196\cdot10^{-3}$	$6.793\cdot10^{-6}$	$-1.187\cdot10^{-6}$	$-33.691\cdot10^{-6}$
D_j [J/(mol K^4)]	0	$2.474\cdot10^{-6}$	$-2.534\cdot10^{-9}$	$0.096\cdot10^{-9}$	$7.948\cdot10^{-9}$
E_j [(J K)/mol]	0	$3.855\cdot10^{6}$	$0.082\cdot10^{6}$	$-0.22\cdot10^{6}$	$-0.137\cdot10^{6}$

With these data, the standard reaction enthalpy and entropy at standard temperature result as

$$\Delta_R H^{\theta}(T^{\theta}) = -594.35\,\frac{\text{kJ}}{\text{mol}}, \qquad \Delta_R S^{\theta}(T^{\theta}) = 275.6\,\frac{\text{J}}{\text{mol K}} \quad .$$

Using the polynomial expressions for the heat capacities, eq.(2-18), one obtains the heat capacity change of reaction:

$$\Delta_R \overline{C}_p(T) = A + BT + CT^2 + DT^3 + ET^{-2} \tag{2-19}$$

with

$$A = \sum_j \nu_j A_j = 193.38\,\frac{\text{J}}{\text{mol K}}, \qquad B = \sum_j \nu_j B_j = -1.46\,\frac{\text{J}}{\text{mol K}^2},$$

$$C = \sum_j \nu_j C_j = 3.18\cdot10^{-3}\,\frac{\text{J}}{\text{mol K}^3}, \quad D = \sum_j \nu_j D_j = -2.47\cdot10^{-6}\,\frac{\text{J}}{\text{mol K}^4},$$

$$E = \sum_j \nu_j E_j = -3.42\cdot10^{6}\,\frac{\text{J K}}{\text{mol}}.$$

The integrals in eq.(2-13) and eq.(2-14) can easily be derived from the polynomial expression, eq.(2-18), as

$$\int_{T^\theta}^{T} \Delta_R \overline{C}_p(T^*)\,dT^* = A\,(T - T^\theta) + \frac{B}{2}(T^2 - (T^\theta)^2) + \frac{C}{3}(T^3 - (T^\theta)^3) + \frac{D}{4}(T^4 - (T^\theta)^4) - E\,(T^{-1} - (T^\theta)^{-1}) \qquad (2\text{-}20)$$

and

$$\int_{T^\theta}^{T} \frac{\Delta_R \overline{C}_p(T^*)}{T^*}\,dT^* = A\,\ln\frac{T}{T^\theta} + B\,(T - T^\theta) + \frac{C}{2}(T^2 - (T^\theta)^2) + \frac{D}{3}(T^3 - (T^\theta)^3) - \frac{E}{2}(T^{-2} - (T^\theta)^{-2}) \quad . \qquad (2\text{-}21)$$

Now all data are available except for the activity and fugacity coefficients needed to calculate activities and fugacities in eq.(2-11) from the molar fractions of the components. In the anode liquid mixtures the activity coefficients of methanol and water are calculated using the UNIFAC method [87] with parameters taken from [86b]. The results are presented in Figure 2-1. One can see that for typical DMFC operation (i.e. methanol concentrations below a few moles per dm³) the water activity is negligibly different from one while that of methanol has values between 2 and 2.3. The temperature dependence of the activity coefficients is very small in the typical DMFC operation range between 0°C and 100°C.

It is further assumed that carbon dioxide exists only in the gas phase, and that no methanol and water evaporate into the gas bubbles. Under these assumptions, the fugacity coefficient of

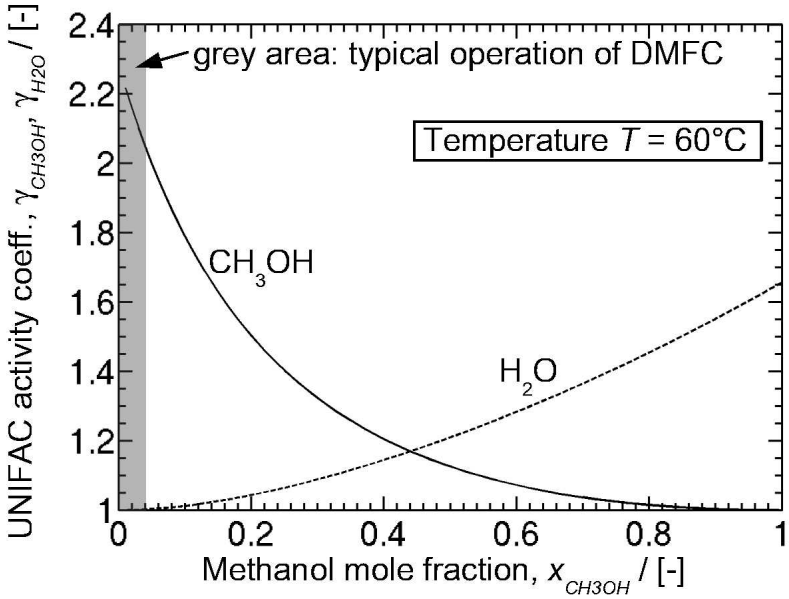

Figure 2-1 *UNIFAC activity coefficients for methanol and water (method according to* [87], *parameters taken from* [86b].

carbon dioxide is equal to one, as well as the molar fraction. Therefore, the carbon dioxide fugacity equals the anode pressure. On the cathode side ideal gas behaviour is assumed, accordingly also here all fugacity coefficients are one. This simplifies eq.(2-11) to

$$\Delta_R G(T, x^A, y^C, p_a, p_c) = \Delta_R G^\theta(T) + RT \ln\left(\frac{(y^C_{H_2O})^3}{\gamma_{CH_3OH} \cdot x^A_{CH_3OH} \cdot \gamma_{H_2O} \cdot x^A_{H_2O} \cdot (y^C_{O_2})^{1.5}} \left(\frac{p_a}{p^\theta}\right) \left(\frac{p_c}{p^\theta}\right)^{1.5} \right) \quad . \quad (2\text{-}22)$$

Divided by (-zF) the reversible open circuit cell voltage for the DMFC is obtained (eq.(2-6)):

$$U_{rev}(T, x^A, y^C, p_a, p_c) = \frac{\Delta_R G^\theta(T)}{zF} - \frac{RT}{zF} \ln\left(\frac{(y^C_{H_2O})^3}{\gamma_{CH_3OH} \cdot x^A_{CH_3OH} \cdot \gamma_{H_2O} \cdot x^A_{H_2O} \cdot (y^C_{O_2})^{1.5}} \left(\frac{p_a}{p^\theta}\right) \left(\frac{p_c}{p^\theta}\right)^{1.5} \right) \quad . \quad (2\text{-}23)$$

In the following eq.(2-23) is used to analyse the influence of the main operating parameters of a DMFC. These parameters are (in brackets: Typical ranges and reference values used for later analysis; Reference values indicated by an upper index "*ref*"):

- the uniform cell temperature T (10..120°C = 283..393K, reference T^{ref} = 60°C = 333 K),
- the anode and cathode pressures p_a and p_c (1..5 bara = 1..5·10^5 Pa, reference $p^{ref}_a = p^{ref}_c$ = 1.7 bara),
- the methanol concentration at the anode (0.1..5.0 mol/dm^3, reference $c^{A,ref}_{CH_3OH} = 1$ mol/dm^3),
- the relative humidity Q_{rel} of the cathode gas/air (0..100% = 0.00..1.00, reference Q^{ref}_{rel}=0.5)
- and the oxygen content in the dry cathode gas/air (0..100 vol% = 0.00...1.00, reference value $y^{C,ref}_{O_2,dry} = 0.21$).

The relative humidity and the oxygen content in the dry cathode gas can be used to calculate the oxygen and water mole fractions on the cathode in eq.(2-22):

$$y^C_{H_2O} = \frac{Q_{rel}\, p_{sat,H_2O}(T)}{p_c} \quad , \quad (2\text{-}24)$$

$$y^C_{O_2} = y^C_{O_2,dry}(1 - y^C_{H_2O}) \quad , \quad (2\text{-}25)$$

with the temperature dependent water saturation pressure given in the form of the Antoine equation [85]

$$\frac{p_{sat,H_2O}(T)}{[\text{bara}]} = 10^{A - \frac{B}{\frac{T}{[\text{K}]} + C}} \quad (2\text{-}26)$$

The parameters of eq.(2-26) are [85]:

A = 5.20389, B = 1733.926, C = -39.485 (for T = 304..333 K);

A = 5.0768, B = 1659.793, C = -45.854 (for T = 334..363 K).

The water and methanol mole fractions on the anode can be calculated from the anode methanol concentration

$$x^{A}_{CH_3OH} = \frac{c^{A}_{CH_3OH}}{c^{A}_{tot}}, \qquad x^{A}_{H_2O} = 1 - x^{A}_{CH_3OH} \qquad \text{(2-27), (2-28)}$$

with the total concentration approximated by that of pure water (as the typical methanol concentrations are below 2 mol/dm^3):

$$c^{A}_{tot} = 55.555 \frac{\text{mol}}{\text{dm}^3} \quad .$$

With all this information the influence of the main operating parameters on the reversible open circuit cell voltage can be predicted within the typical ranges defined in the above list using eq.(2-23). The results are plotted in Figure 2-2. In each of the three plots, two of the six operating parameters are varied, while the other four are on the reference values given in the above list.

In Figure 2-2a the dependence of the reversible open circuit cell voltage on the methanol and oxygen feed concentrations is shown. Not surprisingly, for higher educt concentrations higher cell voltages result. In the given range of concentrations, cell voltages between 1.18 V and 1.21 V are obtained. Remarkably, spanning the whole range between air as cathode feed with an oxygen content of 21 vol% (in dry air) and pure oxygen, only 20 to 25 mV higher cell voltages are obtained.

Figure 2-2b shows the influence of the anode and cathode pressures. Higher cathode pressures lead to higher cell voltages due to the higher partial pressure of the educt oxygen, whereas higher anode pressures lead to a decrease of the cell voltage due to the higher partial pressure of the product carbon dioxide. Again the cell voltage varies only between 1.18 V and 1.21 V.

Finally, Figure 2-2c shows the influence of the cell temperature and the relative humidity at the cathode. Higher temperatures lead to a decreased cell voltage. From lowest (10°C) to highest (120°C) temperature, it goes down about 20 to 40 mV, depending on the other parameters. As water vapour is the product on the cathode side, a higher relative humidity (i.e. higher water vapour pressure = higher water mole fraction) also leads to a decrease in the cell voltage. The maximum span of this decrease is 60 mV for the highest temperatures. The relatively strong dependence on the cell temperature (compared to the other process variables) results mainly from the fact that with rising temperatures the same relative humidity means

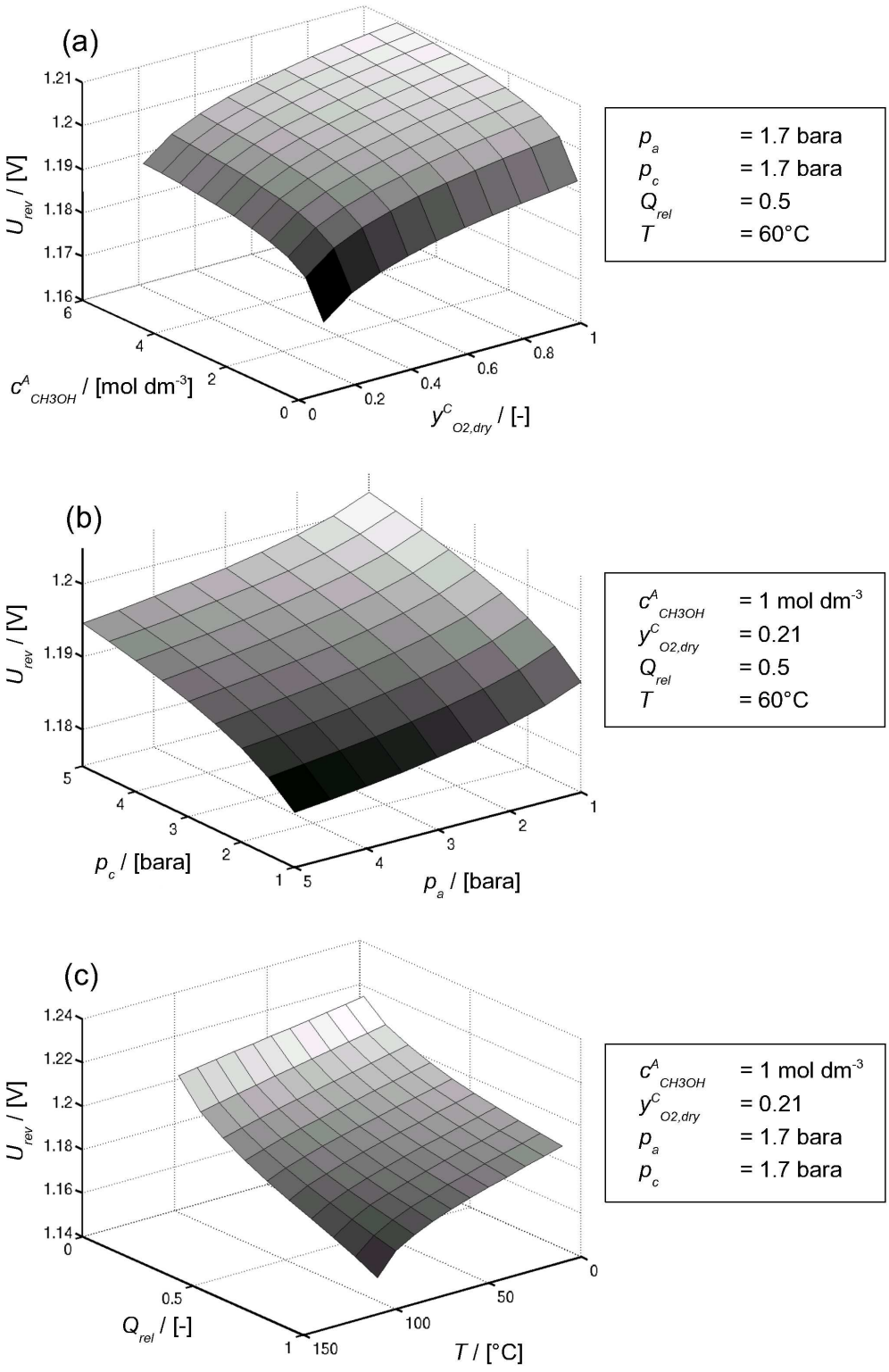

Figure 2-2 *Reversible open circuit cell voltage U_{rev} of DMFC as function of*
(a) methanol and oxygen feed concentrations c^A_{CH3OH}, $y^C_{O2,dry}$
(b) anode and cathode pressures p_a, p_c
(c) cell temperature T and rel. humidity Q_{rel} in cathode gas

much higher water mole fractions, as the water saturation pressure increases exponentially with the temperature (see eq.(2-26)). This effect reduces the oxygen mole fraction which then leads to a lower cell voltage.

2.3 Concluding Remarks

The derived reversible cell voltage will be used later in the modeling and simulation for the calculation of the real cell voltage under operating conditions. Therefore, it is necessary to be able to calculate it as a function of these operating conditions. But as could be shown, its dependence on the major operating conditions is not very large (values between 1.16 and 1.22 V for the maximum range of operating conditions). Therefore, for first simulations it is sufficient to use a fixed mean value of 1.21 V.

3 Experimental Setup

For experimental investigations of liquid-feed DMFCs, two different test facilities have been designed: A very simple laboratory-scale facility for first evaluations under restricted operating conditions, and a highly sophisticated miniplant for the maximum coverage of operating conditions. Furthermore, the necessary equipment and facilities for the preparation of membrane electrode assemblies (abbreviation: MEA) have been installed. The last important part of the experimental setup are the different cells and cell stacks, which have been designed and constructed.

3.1 Laboratory-scale Test Facility

For first evaluations and simple experiments with small-scale single cells and small stacks, a laboratory-scale test facility was designed. A schematic is given in Figure 3-1.

The test facility enables the operation of DMFCs with anodic methanol water feed as well as PEMFC with anodic hydrogen feed. As cathode feed, dry air is available (dew point varying,

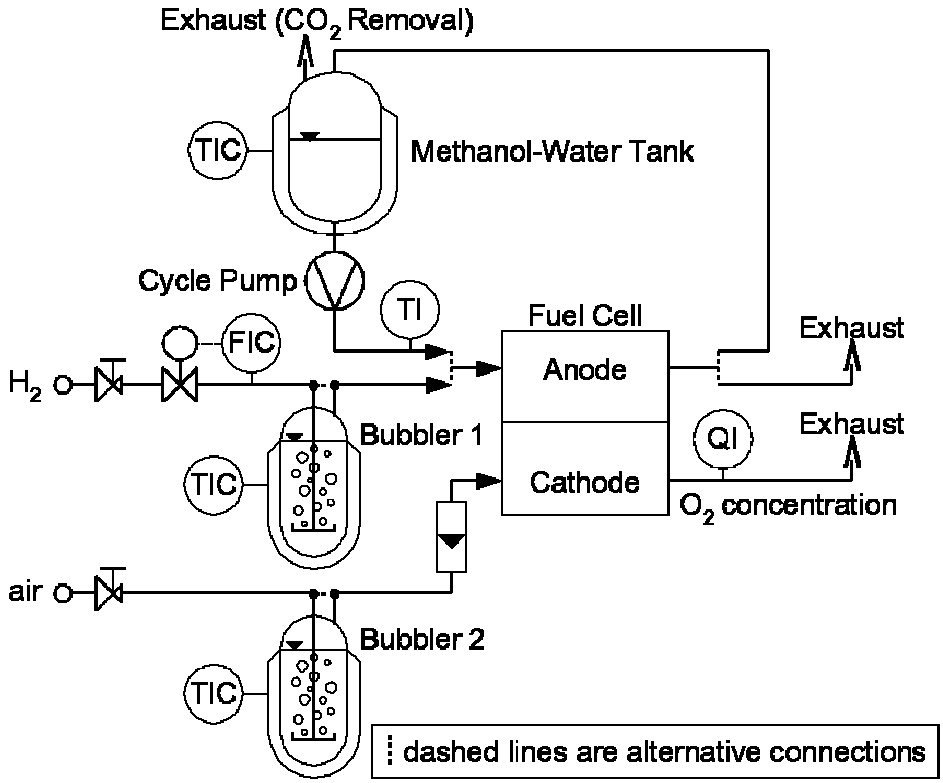

Figure 3-1 *Laboratory-scale test facility for operation of PEM fuel cells with hydrogen or liquid methanol-water solutions as anode feed, and air (or oxygen) as cathode feed. Both gases can be humidified using thermostated washing bottles (bubblers).*

but below -3°C), as well as pure oxygen. Both gaseous feeds (hydrogen and air) can be sent through thermostated washing bottles for humidification (bubbler 1 and 2). As anode feed for DMFC operation, a liquid cycle is available which consists of a thermostated holdup vessel of 2.5 dm^3 volume, a cycle pump and a thermometer which measures the temperature of the liquid feed at the cell entry. The holdup vessel also has the purpose to strip off the carbon dioxide produced in the DMFC. Hydrogen for PEMFC operation is supplied through an electronic mass flow controller (Bronkhorst), the mass flow of the dry air is measured in a rotameter (Krohne DK800R, max. air flow 250 Ndm^3/h) and can be adjusted manually with a needle valve.

As the holdup vessel and the washing bottles are made of glass, it is not possible to apply pressures higher than ambient on the liquid cycles. Therefore, no pressure indicator exists.

As electronic load, a Zahner IM6e Electrochemical Workstation is used, in combination with a Zahner EL101 High Power Electronic Load. With this equipment, potentiostatic and galvanostatic experiments can be carried out with maximum cell voltages of 4 V and maximum currents of 25 A. Therefore, cell stacks with a maximum of 4 cells (hydrogen.fed PEMFC) or 6 cells (DMFC) and a maximum power output of 100 W can be examined. With the same equipment, also cyclovoltammograms and impedance spectra can be recorded.

The test facility is mainly used for conditioning of newly assembled DMFCs. For that purpose, the cells are operated on hydrogen/air for at least 24 hours at a cell potential of 0.2 V, until a stable performance (stable cell current) is achieved. For this purpose, as alternative to the Zahner potentiostat, also a simple electronic load is available (Type 3229.1 by Statron, modification of standard type 3229.0 with connection for external voltage source to reach cell voltages below 1 V, max. current 50 A, max. power 400 W).

3.2 DMFC Miniplant

For full-scale testing of DMFCs, a miniplant was designed, which is fully automated (process control system PC-S7/WinCC by Siemens) to enable automatic testing procedures and 24-hour-operation (Figure 3-2: flowsheet; Figure 3-3: main operator panel screenshot; Figure 3-4: photo of complete miniplant).

The key features are:

- supply of dry air or oxygen on the cathode side without humidification,
- liquid cycle for methanol-water solution on the anode side,
- second, identical alternative liquid cycle to enable a sustained pulsed periodic operation of the anode side of the cell in terms of a regular change between methanol-water mixtures and pure water, as well as for step exeriments where the cell feed is changed from methanol-water solution to pure water only once,
- liquid holdup tanks in each liquid cycle for equilibration of pressure changes and also for carbon dioxide removal under certain circumstances,
- permanent carbon dioxide removal from the liquid cycle realised in an hollow fibre membrane module supplied by GKSS Forschungszentrum GmbH (Geesthacht, Germany),
- temperature range of all media lines of -20°C up to 150°C (253..423 K), except for the membrane module (max. temperature 60°C), therefore operation is also possible circumventing it, stripping off carbon dioxide in the liquid holdup tank (see above),
- liquid cycle, cathode gas feed and fuel cell thermostated by one integrated thermo oil cycle and an external thermostat (Haake DC40-K30),
- pressure range of all media lines of ambient up to 5 bars absolute ($1..5 \cdot 10^5$ Pa), which is necessary to keep the liquid methanol-water mixture below boiling point at temperatures above 57°C (boiling point of methanol-water aceotrope at ambient pressure),
- anode and cathode pressures are controlled independently,
- electronic load (Wenking High Power Potentiostat HP60-50) as electric power sink for fuel cells of below 1 Watt up to 1000 Watt at a maximum of 50 Amperes, constant-current (galvanostatic) and constant-potential (potentiostatic) operation possible, with the possibility to run also user-defined load scenarios (analogue inputs),
- full material balancing of the entire miniplant by on-line detection of mass flow rates and concentrations of all important substances (oxygen, methanol, water, carbon dioxide) as well as the electric cell current, and
- automated user-defined test programs with the possibility to change any plant parameter at a pre-defined time using the BatchFlexible software add-on for the process control system (Siemens PC-S7/WinCC), enables e.g. load scenarios like standard car driving cycles, automated collection of current voltage characteristics etc.

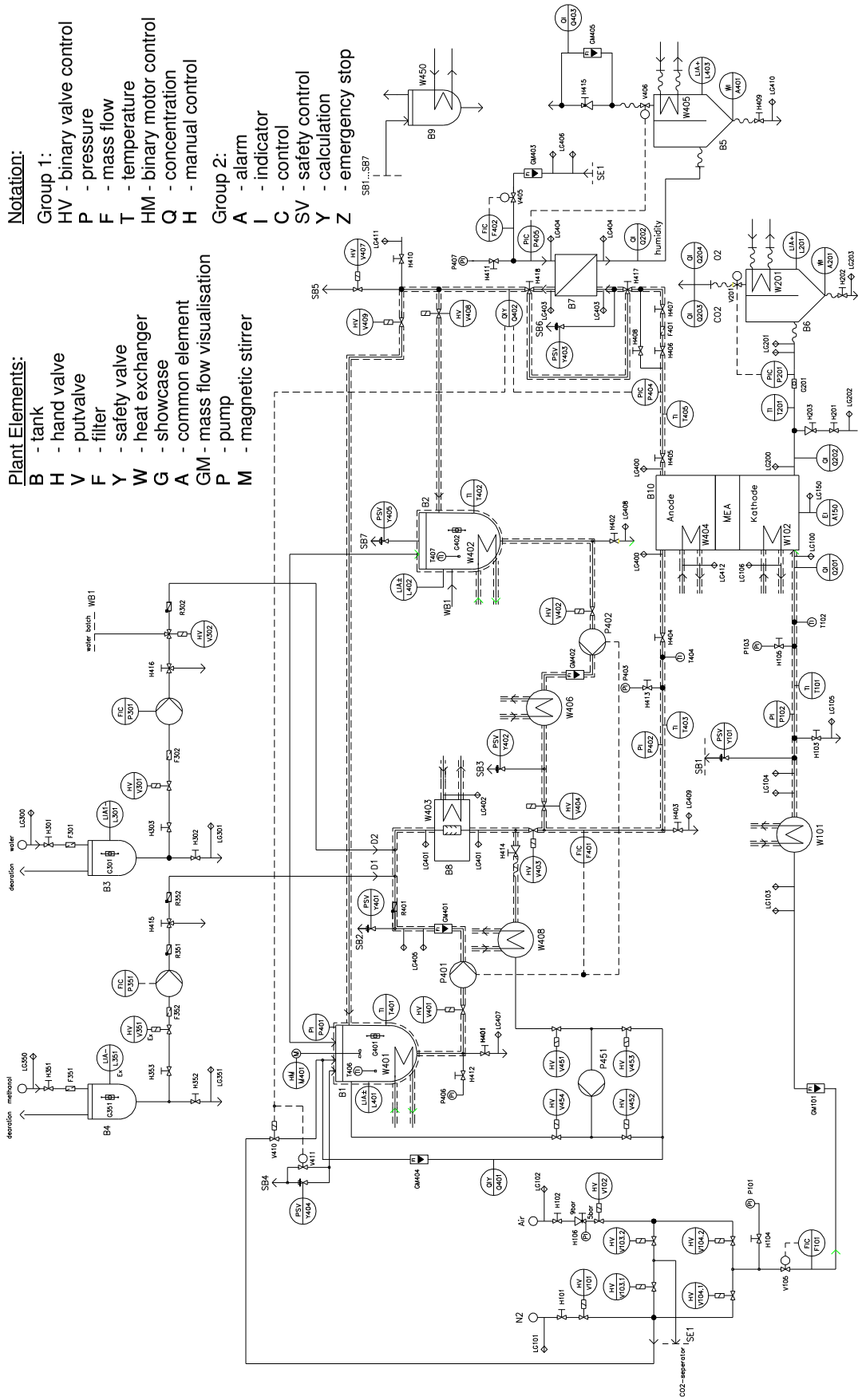

Figure 3-2 *Flow scheme of the designed DMFC miniplant*

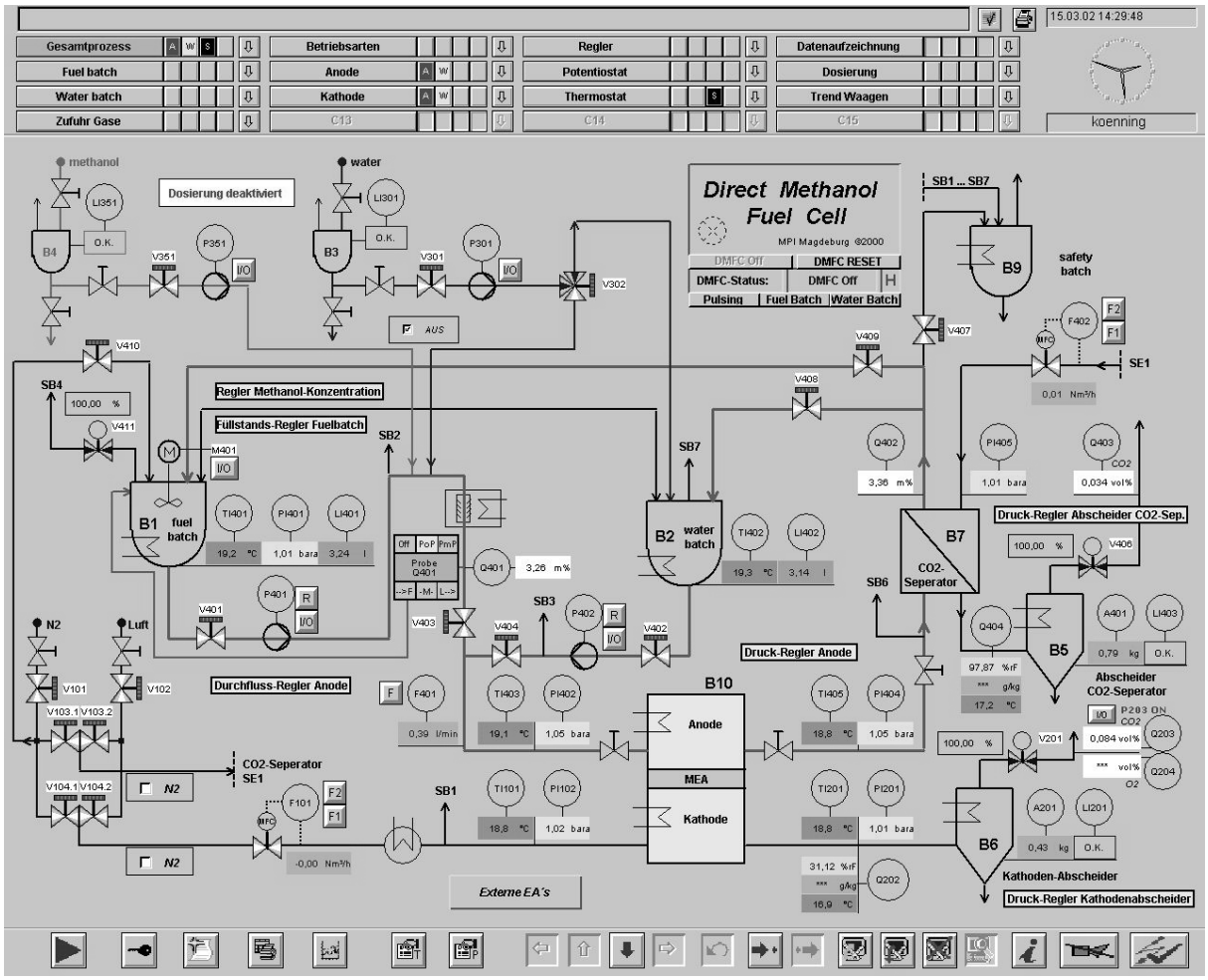

Figure 3-3 *Screenshot of process control systems main operator panel*

3.2.1 Basic Features

The DMFC miniplant consists of the following subsystems:

1. Anodic methanol-water cycle (flow rate 0.3 .. 5.0 dm^3/min; max. pressure 5 bara=$5 \cdot 10^5$ Pa)
2. Alternative anodic pure water cycle with similar specifications
3. Cathodic air supply (flow rate 0.4 .. 5.0 scbm/h; max. pressure 5 bara=$5 \cdot 10^5$ Pa)
4. Stripping air supply for the carbon dioxide removal membrane module (flow rate 0.4 .. 5.0 scbm/h; max. pressure 5 bara=$5 \cdot 10^5$ Pa)
5. Methanol and water dosing (flow rates 0.2 .. 18.0 cm^3/min)
6. Thermostat cycle
7. Cooling water cycle
8. Plant hardware security scheme featuring several mechanic blow-out valves all leading into a blow-out tank of 5 dm^3

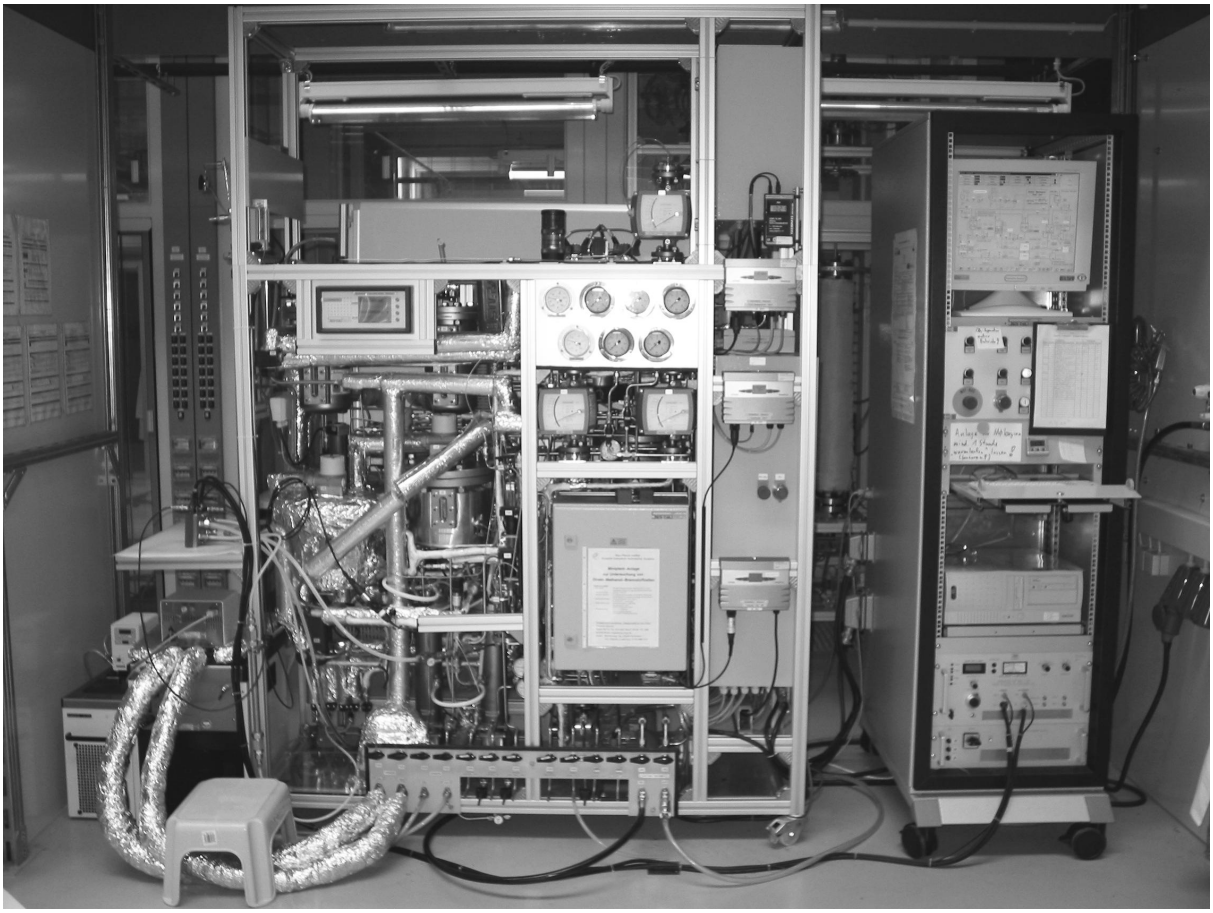

Figure 3-4 *Photo of complete DMFC miniplant*

All elements of the plant which are in contact with any media are made from stainless steel (type: SS316) or plastic materials with high thermal and chemical resistance (PTFE, PFA, PVDF). All hand valves are Swagelok ball valves, all automated valves were supplied by Bürkert.

Both anodic liquid cycles feature an equilibration tank with a liquid holdup of 1.6 to 3.5 dm^3. Their main purpose is to equilibrate pressure changes due to methanol and water losses in the system, which occur within the fuel cell and the carbon dioxide separator module. The tank on the methanol-water cycle (fuel batch) can also be used for carbon dioxide removal when the carbon dioxide separator (membrane module) is circumvented. Both tanks are connected to the thermostat cycle for pre-heating the liquids. Both tanks tops are connected to ensure the same pressure on both cycles. A nitrogen blanket is used to build up the desired system pressure.

Both liquid cycles are equipped with Scherzinger gear pumps, heat exchangers prior to the fuel cell (with integrated static mixer on the methanol-water cycle), on-line sensors for flow rate, temperature, pressure and methanol concentration (for sensor details see next section) and several hand valves for sample collection during operation.

The cathode side of the fuel cell as well as the stripping gas section of the carbon dixide separator are supplied with air from a supply system (8 bars abs., "technically oil free"=less than 0.003 mg oil/scbm, dew point below -3°C, ambient temperature). The flow rates are controlled by Bürkert MassFlow Controllers (Mass6020). Both air lines end up in condensor vessels with pressure regulation valves. The condensors feature a coil through which cooling water is pumped. By this, condensable contents of the fuel cell and membrane module exhaust gases are collected as liquids. The gas streams leaving the condensors therefore have a relative humidity well below 100% (dew point around 10°C), which is compulsory for the pressure regulation valves as well as for some of the on-line gas sensors (see next section). Both condensors are footed on damped weighing cells to measure the overall condensate mass. Level indicators will give a warning signal to the process control system if more than 0.5 dm^3 of condensate is collected. It is possible to empty the condensors during plant operation.

To control the methanol concentration in the methanol-water cycle and to compensate for methanol and water losses, pure methanol and water can be pumped into the methanol-water cycle by using micro gear ring dosing pumps (mzr-2905 by HNP Mikrosysteme, Germany). The flow rates can be controlled in the range from 0.2 up to 18 cm^3/min.

The thermostat cycle connects all heat exchangers in the plant. It is operated in combination with an external thermostat (Haake DC40-K30) which is filled with thermo oil. By adjusting the temperature within the thermostat, the desired media temperatures within the plant can be achieved, although not independent from each other. The most important temperature, though, is the fuel cell temperature, which is mainly determined by the anode liquid cycle temperature, due to the high heat capacity of methanol-water solutions compared to the cathodic air stream.

Finally, a cooling water cycle supplies the condensors, one sample line heat exchanger and the blow-out vessel (safety batch) with water of 5..15°C. A simple bath thermostate with maximum cooling power of 700 W is used for circulating and cooling the water.

3.2.2 On-Line Sensors

In Figure 3-2 and Figure 3-3 all sensors are shown. The basic idea was to get as many information on-line as possible, which excludes gas or liquid chromatographs as concentration sensors. In the following, a short description of the applied sensors is given, with a focus on special requirements and limitations. More details especially concerning sensor tolerances are given in section 2.2.4 (Material Balance).

Temperatures are measured using standard Pt100 sensors. Most important temperatures are those of the media entering (T403, T101) and leaving the fuel cell (T405, T201) (methanol-water solution and air feeds). Also the temperatures within both liquid holdup tanks are measured (T401, T402).

Pressures are measured using sensors supplied by WIKA. Sensors are at the same locations as the temperature sensors (P402, P404, P102, P201, P401), plus one which measures the inlet stripping air pressure of the membrane module (P405).

Gas flow rates (for cathode feed gas and membrane module stripping gas) are controlled by Bürkert MassFlow Controllers calibrated for air (F101, F402). The anode feed flow rate is measured using a Corioles-type mass flow meter by Danfoss calibrated for pure water (F401).

All important temperatures, pressures and flow rates are also measured by nonelectronic thermometers, pressure gauges and rotameters for reasons of redundancy.

For adjustment of the electrical parameters of the fuel cell, a high power potentiostat is used (type WENKING HP-60 50). It can be operated in galvanostatic mode (constant current) as well as potentiostatic mode (constant cell voltage). Always cell voltage and cell current are recorded simultaneously.

The most important concentration value which has to be known is that of methanol in the anode liquid cycle. It has to be known at the fuel cell entry (Q401), as this is one of the major parameters influencing the fuel cell performance. Desirable is also to have a similar sensor at the fuel cell exit to be able to determine the methanol consumption of the cell. For the task to measure methanol concentrations in water at temperatures between -20 and +150°C and pressures between 1 and 5 bars abs., conventional sensors like electrochemical ones are not applicable. Therefore, it was decided to use an indirect method for the determination of the methanol concentration, using the influence of different methanol concentrations on the speed of sound in the mixture. For this purpose, an ultrasound sensor is used (LiquiSonic30 by SensoTech GmbH, Germany). It was calibrated for methanol concentrations of up to 5 wt-%. Problems about this method are a high temperature dependence of the speed of sound and a high sensitivity towards gas bubbles. It was found, that in the temperature range from 50 to

90°C no significant dependence of the speed of sound on the methanol concentration can be detected in the respective concentration range. Therefore, it is not possible to operate the sensor directly in the anodic liquid cycle, as the mentioned temperature range is of special interest for the DMFC and cannot be ignored in the experiments. For this reason it was decided to apply a bypass on the liquid cycle, which takes a small part of the anode feed, cools it down to below 50°C and feeds it to the sensor, whereafter the stream is sent back to the holdup tank, circumventing the fuel cell. To ensure a constant flow rate, a dosing pump is used (mzr-7205 by HNP Mikrosysteme, Germany), which is a bigger version of those used for methanol and water dosing. This method leads to reliable concentration data, with the disadvantage of a time delay between taking the sample and having the concentration value. Depending on the mode of operation, this delay time lies around 30 seconds. Therefore, this sensor is only applicable for controlling a steady state methanol concentration or slow changes. Fast changes cannot be detected.

A second ultrasound sensor of the same type (Q402) is used to detect the methanol concentration of the mixture leaving the membrane module. Due to the sensors sensitivity for gas bublles, it is not possible to place it directly at the fuel cell exit, as here carbon dioxide bubbles are present at typical operating conditions, especially for high fuel cell currents and cell temperatures. This second sensor is measuring directly in the anode cycle (not via a thermostated bypass), as even the first bypass takes up a significant amount of the total anode feed flow. As the mixture in the bypass is cooled down, this leads to a high heat loss which decreases the maximum possible fuel cell temperature. A second sensor bypass would therefore place the need for a bigger thermostat to compensate for the even higher heat losses. At the current stage the disadvantages with respect to the temperature range limitation of the second sensor have to be accepted. In any case, this sensor is not vital for a complete mass balance of the plant, as will be shown later.

In the gas phase (cathode air feed and stripping air for the membrane module), water, carbon dioxide, oxygen and methanol concentrations are of special interest. Water can be detected by capacitive humidity sensors (Q202, Q404, type HygroClip IE by rotronic, Switzerland) that measure relative humidity. Together with the actual temperature and pressure at the sensor, the water vapour concentration can be calculated. For carbon dioxide, IR sensors are available (Q203, Q403, type OEM-NDIR EGC-5% by Pewatron, Switzerland), which work on the basis of the specific absorption of infrared light by the gas molecules. Oxygen is only detected in the cathode exhaust gas (Q204), as in the membrane module no conversion of oxygen takes place. For oxygen, no IR sensors are available, only options are so-called λ-

sensors, well known in burning processes, and paramagnetic sensors. The first suffer from their cross sensitivity with respect to oxidisable compounds, like e.g. methanol. These sensors are operated at high temperatures (above 300°C) at which such compounds would burn together with the oxygen, leading to a mismeasurement of the oxygen concentration. Moreover, this type of sensor usually exhibits a relatively high drift. Therefore, a paramagnetic sensor was chosen (PAROX 1000 H by MBE AG, Switzerland), which has a negligible cross sensitivity to all gas components to be expected. A membrane gas pump by KNF Flodos (Germany) ensures constant gas flow through the oxygen sensor.

The carbon dioxide sensors as well as the oxygen sensor have to be protected from condensation within their sensor heads. Therefore, they are placed behind the condensor vessels of both gas lines, whereas the humidity sensors are placed directly behind the fuel cell and the membrane module, respectively. As all three gas sensors (for CO_2 and O_2) measure at atmospheric pressure (exhaust end open), an extra pressure sensor measures the atmospheric pressure and the concentration values of the three sensors are corrected within the process control system. On the operator panels, only the corrected values are displayed.

A simple and specific sensor for methanol in the gas phase is not available. The only possibility is the use of a sensor for burnable compounds as often used for detection of explosive atmospheres (TOC sensors). But first of all, significant methanol concentrations in the cathode exhaust gas were never reported before, and second, if there were also other compounds originating from partially oxidised methanol, the sensor would not be able to distinguish between them. Therefore, at the cathode exhaust gas line, a connection for a gas chromatograph was fitted, for a possible later use. To the time being, the assumption is made that methanol permeating from the fuel cell anode to the cathode is fully oxidised to carbon dioxide. The results obtained from the material balancing (see section2.2.4) confirm this assumption.

3.2.3 Carbon Dioxide Separator (Membrane Module)

The carbon dioxiode separator module has been produced by the GKSS Research Center (Geesthacht, Germany). It consists of a hollow fibre module with inlet and outlet fittings for the liquid flow and the stripping gas. The module features 650 hollow fibres with an outer diameter of 1.01 mm and an inner diameter of 0.72 mm (membrane area 0.53 m^2). The liquid methanol-water solution passes through the fibres, while the stripping air is on the outside. The membrane is asymmetric, consisting of a porous support for mechanical strength and a dense silicone coating of 20 µm thickness, which is the active separation membrane.

It was found that per hour between 300 g (at 30°C) and 700 g (at 60°C) methanol-water mixture are stripped from the liquid cycle in the membrane module, with the ratio methanol:water being roughly 1:1. The humidity sensor at the stripping air outlet of the membrane module shows 100% relative humidity under all applicable process conditions, the stripping air always leaves the module saturated with water. Very often even liquid water was found at the stripping air outlet of the membrane module.

The conclusion is that the membrane module is not applicable for its desired purpose. Either the permeabilites for water and methanol are too high, or the module has a too big membrane surface. Further tests have to be carried out to answer these questions. Meanwhile the membrane module is circumvented and the carbon dioxide is stripped off in the liquid holdup vessel via the gas blanket.

3.2.4 Balance of Plant

As already described, a number of on-line sensors provides information about all key components entering and leaving the fuel cell. These key components are water, methanol, oxygen and carbon dioxide. With the help of this sensor arrangement it is possible to calculate the whole mass balance of the fuel cell, revealing information about mass fluxes within the cell, which can not be measured directly. Figure 3-5 shows the whole sensor arrangement.

On the gas (cathode) side, dried air is supplied from an in-house system at 8 bara. The air flow rate is controlled by the mass flow controller F101. The water content is measured by a humidity sensor (Q101). At the cathode exhaust, again humidity is measured by a similar sensor (Q202), as well as oxygen and carbon dioxide content (sensors Q204 and Q203).

On the liquid (anode) side, the methanol concentration is measured prior to the cell inlet (sensor Q401) and behind the carbon dioxide separator module (sensor Q402). The mass flow is measured in a Corioles type massflow meter (F401).

The stripping air for the carbon dioxide separator is taken from the same supply as the cathode inlet air, its composition is therefore the same. Like for the cathode air supply, a mass flow controller (F402) controls the flow rate. At the outlet, an humidity sensor is installed (Q404), as well as one for carbon dioxide (Q403).

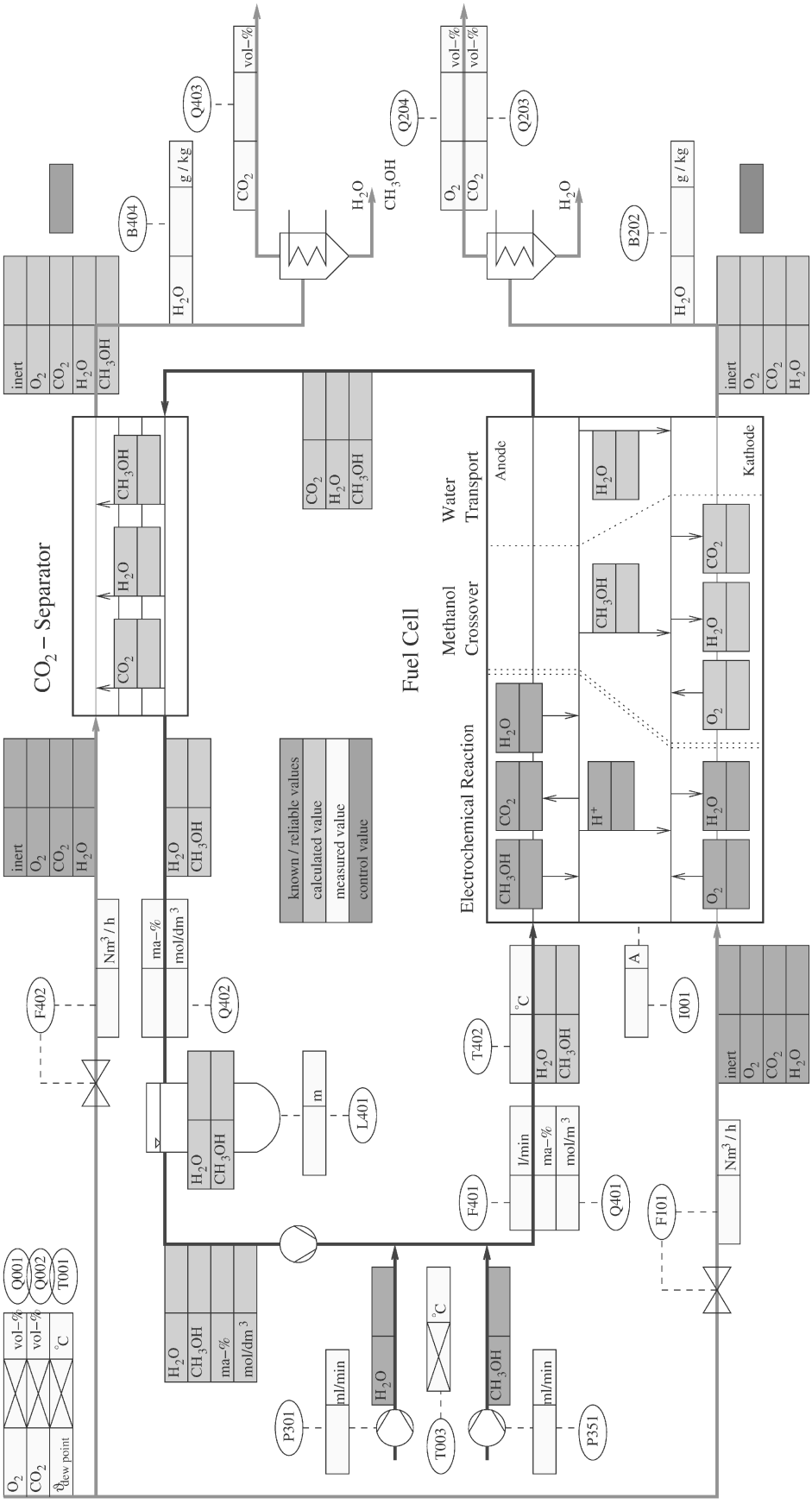

Figure 3-5 *Simplified miniplant flow scheme with all relevant sensors for material balance*

For all calculations with respect to air, the composition of dry atmospheric air is used as base values:

Oxygen (O_2):	20.95 Vol-%	=> $y_{O2} = 0.2095$
Carbon dioxide (CO_2):	350 ppm	=> $y_{CO2} = 0.00035$
Nitrogen (N_2) including all other inert gases:	79.015 Vol-%	=> $y_{N2} = 0.79015$

In the following material balances are formulated for subsystems of the miniplant, as shown in Figure 3-6. Molar fluxes entering or leaving balance sections are marked by a corresponding superscript index of italic capital letters (*A*..*Z*). In the following figures normal characters represent measured quantities (sensor information).

The balance equations will be derived in the following, and rearranged to calculate the unknown molar fluxes. In a defined sequence, all fluxes can be calculated subsequently, using some simple and reasonable assumptions, which will be introduced in the respective context. For all gases ideal behaviour is assumed.

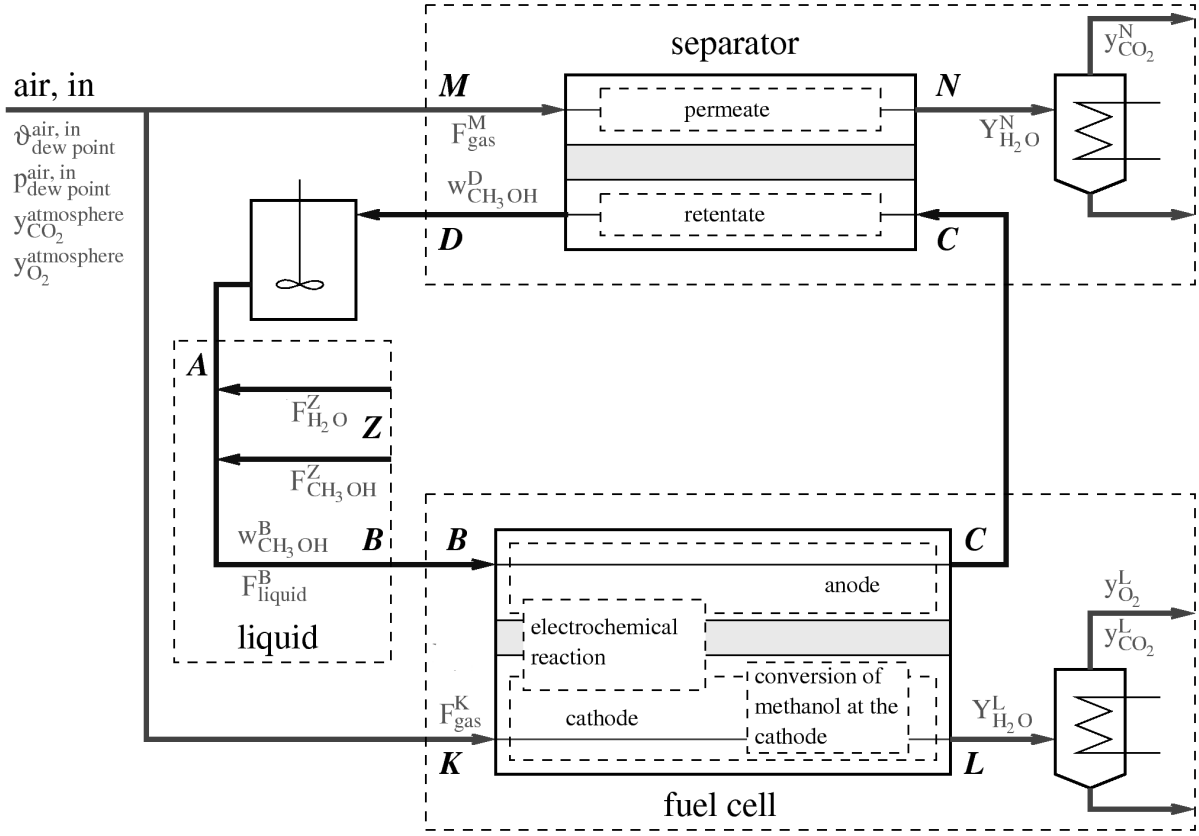

Figure 3-6 *Overview over all balanced subsystems of the DMFC miniplant*
(Normal characters: Measured quantities; Italic characters: Indexes of fluxes)

Starting point is the air supply for both cathode air and stripping air. The water mole fraction y_{H2O} can be calculated from the measured water partial pressure p_{H2O} and the known pressure at the sensor Q101, p_{Q101}=5 bara:

$$y_{H_2O} = \frac{p_{H_2O}}{p_{Q101}} \tag{3-1}$$

The other gas components can now be calculated from:

$$y_j = y_{j,\,dry\,air}(1 - y_{H_2O}), \qquad j = O_2, CO_2 \tag{3-2}$$

$$y_{N_2} = 1 - y_{O_2} - y_{CO_2} - y_{H_2O} \tag{3-3}$$

With the total volumetric flow rate F^K and the molar volume of an ideal gas $\overline{V}$, the molar fluxes entering the fuel cell cathode can be derived:

$$n_j^K = \frac{F^K}{\overline{V}} y_j, \qquad j = N_2, O_2, CO_2, H_2O \tag{3-4}$$

As nitrogen is an inert component in the fuel cell cathode, the nitrogen flux at the cathode outlet is the same as at the inlet:

$$n_{N_2}^L = n_{N_2}^K \tag{3-5}$$

With the measured values of the cathode outlet concentrations of oxygen and carbon dioxide (y^L_{O2}, y^L_{CO2}), their molar fluxes n_j^L result as

$$n_j^L = y_j^L \frac{n_{N_2}^L}{1 - y_{O_2}^L - y_{CO_2}^L}, \qquad j = O_2, CO_2 \quad . \tag{3-6}$$

The molar water flux $n_{H_2O}^L$ can be calculated from the measured water loading Y^L_{H2O}:

$$n_{H_2O}^L = \frac{Y_{H_2O}^L}{\overline{M}_{H_2O}} \left(n_{N_2}^L \overline{M}_{N_2} + n_{O_2}^L \overline{M}_{O_2} + n_{CO_2}^L \overline{M}_{CO_2} \right) \quad . \tag{3-7}$$

Another available measured value is the electrical cell current I_{cell}. Assuming the anodic methanol oxidation having 100% conversion without any by-products, the molar flux of protons through the fuel cell membrane $n_{H^+}^Q$ can be calculated according to Faraday's law

$$n_{H^+}^Q = \frac{I_{cell} N_{cells}}{F} \tag{3-8}$$

with the number of cells in the fuel cell stack N_{cells} and Faraday's constant F (see Figure 3-7). In the presented experiments, always only single cells (N_{cells} = 1) were used. But for the implementation in the process control system of the miniplant it was decided to formulate it more general to be prepared for coming experiments with DMFC stacks consisting of more than one cell.

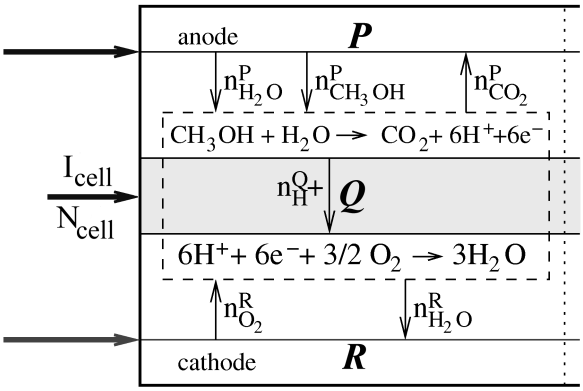

Figure 3-7 *Electrochemical cell reactions, educt and product fluxes*
(Sensor information: Cell current I_{cell}; Additional information: Number of cells N_{cell})

The same is true for the oxygen consumed at the cathode for this desired cell reaction, $n^R_{O2,}$ and the resulting water flux produced, n^R_{H2O}:

$$n^R_{O_2} = \frac{I_{cell} N_{cells}}{4F} \tag{3-9}$$

$$n^R_{H_2O} = \frac{I_{cell} N_{cells}}{2F} \tag{3-10}$$

Oxygen is consumed at the cathode by the desired electrochemical reaction, n^R_{O2}, but also by the oxidation of crossover methanol (Figure 3-7, Figure 3-8). Because the first is known, represented by n^R_{O2}, as the cathode inlet oxygen flux, n^K_{O2}, and outlet oxygen flux, n^L_{O2}, the oxygen flux consumed to oxidise the crossover methanol can be calculated:

$$n^T_{O_2} = n^L_{O_2} + n^R_{O_2} - n^K_{O_2} \tag{3-11}$$

Assuming the direct methanol oxidation at the cathode having 100% conversion without any byproducts, the stoichiometry of this reaction directly yields the ratio of the oxygen flux consumed by this reaction, n^T_{O2}, to the methanol flux consumed by this reaction, n^S_{CH3OH} (which equals the methanol crossover flux through the membrane):

$$n^S_{CH_3OH} = \frac{2}{3} n^T_{O_2} \tag{3-12}$$

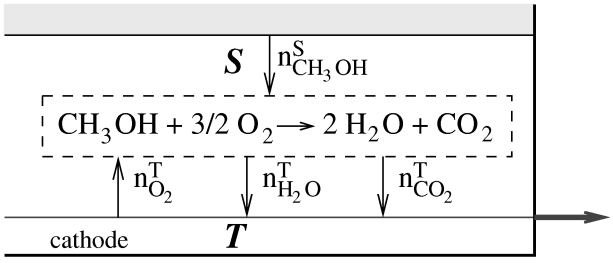

Figure 3-8 *Oxidation of crossover methanol, educt and product fluxes*

In the same manner, the productions of carbon dioxide and water from this reaction result as:

$$n^T_{CO_2} = \frac{2}{3} n^T_{O_2} \quad , \quad n^T_{H_2O} = \frac{4}{3} n^T_{O_2} \qquad (3\text{-}13)\ (3\text{-}14)$$

Now all water fluxes to and from the cathode are known except for the crossover flux through the membrane, which therefore results from the water balance at the cathode (Figure 3-9) as

$$n^S_{H_2O} = n^L_{H_2O} - (n^K_{H_2O} + n^R_{H_2O} + n^S_{H_2O} + n^T_{H_2O}) \quad . \qquad (3\text{-}15)$$

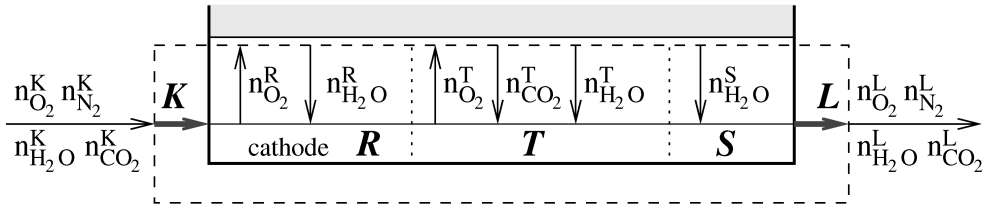

Figure 3-9 *Cathode mass balance, all fluxes*

The above sequence of equations offers direct access to the two crucial crossover fluxes through the DMFC membrane. As a number of different sensor information are used in this sequence, it is necessary to estimate the reliability of the two final molar fluxes by accounting for the error tolerances of all sensor informations. This procedure can be found in chapter 8 (appendix A). The resulting error tolerances of the crossover fluxes of water and methanol are usually below 20% (see Table 3-1), which is a rather good result accounting for the number of used sensor informations and the sequential calculation procedure.

With the help of the methanol and water crossover fluxes, the material balance around the fuel cell anode can be formulated. At the anode liquid cycle, the molar fluxes of water and methanol being pumped into the cycle (Figure 3-10) are given by the volume flow rates of the dosing pumps F_i^Z and the liquid densities calculated from the temperatures of the liquid storage tanks T^Z:

$$n_i^Z = \frac{\rho_i(T^Z)}{\overline{M}_i} F_i^Z \quad , \qquad i = H_2O, CH_3OH \quad . \qquad (3\text{-}16)$$

Here $\overline{M}_i$ is the molar mass [kg mol^{-1}] and $\rho_i(T^Z)$ is the density [kg m^{-3}].

The water and methanol fluxes entering the fuel cell can be determined from the measured methanol mass fraction w^B_{CH3OH} and the temperature at the anode inlet T^B:

$$n^B_{H_2O} = \frac{F^B}{\overline{M}_{H_2O}} \frac{1}{\frac{1}{\rho_{H_2O}(T^B)} + \frac{w^B_{CH_3OH}}{1 - w^B_{CH_3OH}} \frac{1}{\rho_{CH_3OH}(T^B)}} \qquad (3\text{-}17)$$

$$n^B_{CH_3OH} = \left(F^B - \frac{n^B_{H_2O} \overline{M}_{H_2O}}{\rho_{H_2O}(T^B)} \right) \frac{\rho_{CH_3OH}(T^B)}{\overline{M}_{CH_3OH}} \qquad (3\text{-}18)$$

Table 3-1 *Tolerances of calculated molar fluxes at the cathode (for typical operating conditions)*

Molar flux	Typical value [mmol/s]	Error tolerance
Cathode Inlet:		
n^K_{N2}	4.890	± 6.50%
n^K_{O2}	1.297	± 6.50%
n^K_{CO2}	0.002	± 6.50%
n^K_{H2O}	0.006	± 6.50%
Cathode Outlet:		
n^L_{N2}	4.892	± 6.50%
n^L_{O2}	1.238	± 6.53%
n^L_{CO2}	0.062	± 12.03%
n^L_{H2O}	0.353	± 6.67%
Crossover Fluxes through Membrane:		
n^S_{CH3OH}	0.031	± 19.04%
n^S_{H2O}	0.261	± 8.14%
Crossover Methanol Oxidation:		
n^T_{O2}	0.046	± 19.04%
n^T_{CO2}	0.031	± 19.04%
n^T_{H2O}	0.062	± 19.04%

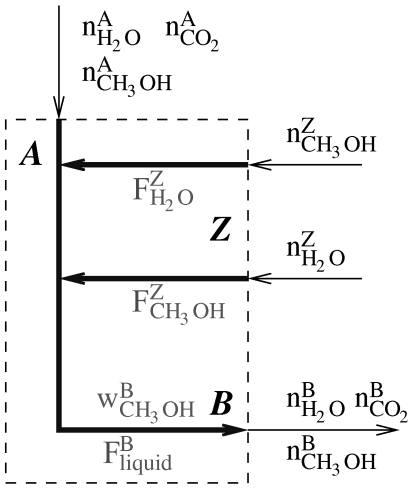

Figure 3-10 *Fluxes at anode inlet (Sensor information: methanol dosing pump flow rate F^Z_{H2O}, water dosing pump flow rate F^Z_{CH3OH}, methanol mass fraction in anode liquid cycle w^B_{CH3OH} and anode liquid cycle flow rate F^B_{liquid})*

Using the crossover fluxes through the membrane, eq.(3-12) and eq.(3-15), the molar fluxes at the anode outlet are finally (see Figure 3-11):

$$n_j^C = n_j^B - (n_j^P + n_j^S), \qquad j = CO_2, CH_3OH, H_2O \tag{3-19}$$

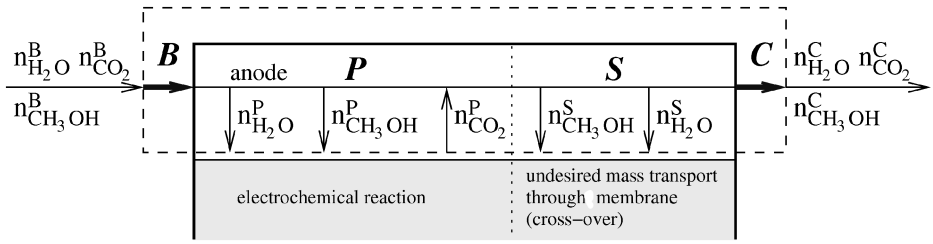

Figure 3-11 *Anode mass balance, all fluxes*

It is assumed that practically no carbon dioxide is present in the liquid cycle at the outlet of the holdup vessel (see Figure 3-5, point *A*), as well as that the fuel cell membrane is impermeable for gases. This means that the respective fluxes (n_{CO2}^B, n_{CO2}^S) are zero. The carbon dioxide flux at the anode outlet is therefore equal to the production at the anode:

$$n_{CO_2}^C = n_{CO_2}^P \quad . \tag{3-20}$$

To this point, of the four balance equations at the cathode only three have been used (N_2, O_2, H_2O). The fourth balance equation (CO_2) can then be used to calculate a control value for the carbon dioxide flux at the cathode outlet:

$$n_{CO_2}^{L^*} = n_{CO_2}^K + n_{CO_2}^T \tag{3-21}$$

Ideally, n_{CO2}^L and $n_{CO2}^{L^*}$ should be the same. The control value is displayed together with the base value by the process control system.

Last in the sequential balancing procedure is the carbon dioxide separator (Figure 3-12):

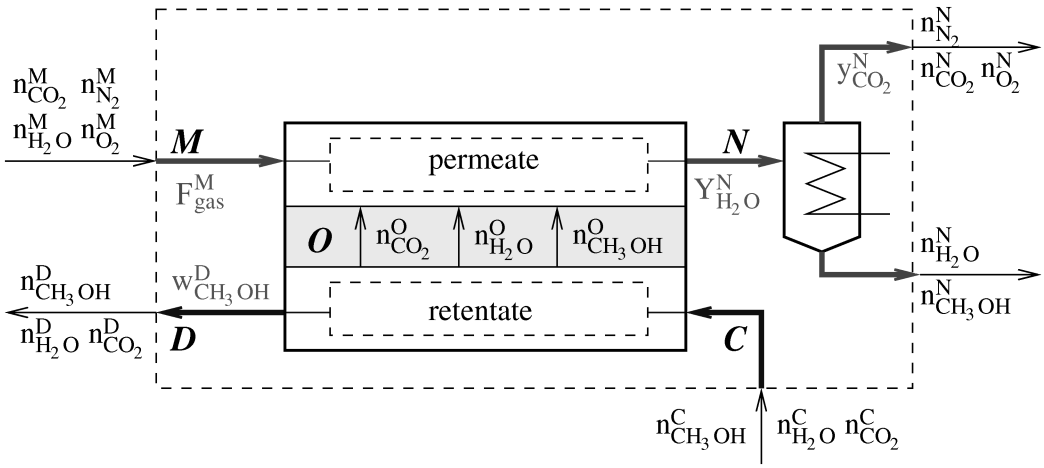

Figure 3-12 *Carbon dioxide separator with all mass fluxes (Sensor information: Stripping air flow rate F^M_{gas}, outlet air relative humidity Y^N_{H2O}, outlet air carbon dioxide content y^N_{CO2} and methanol mass fraction at liquid outlet of separator w^D_{CH3OH})*

First, the molar fluxes at the gas inlet and outlet are calculated from the known composition of the air, the measured values of water and carbon dioxide concentrations at the outlet and the gas flow rate. The equations have the same structure as those already presented for the fuel cell cathode. The gas inlet fluxes of the separator are:

$$n_j^M = \frac{F^M}{\overline{V}}\, y_j, \qquad j = N_2, O_2, CO_2, H_2O \tag{3-22}$$

The nitrogen and oxygen fluxes are assumed to be the same at the outlet, as the permeability of the membrane is very low for these gases, compared to that for carbon dioxide and water:

$$n_j^N = n_j^M, \qquad j = N_2, O_2 \tag{3-23}$$

Using these and the measured value of the outlet carbon dioxide concentration y^N_{CO2}, the carbon dioxide flux at the gas outlet is:

$$n_{CO_2}^N = \frac{y_{CO_2}^N}{1 - y_{CO_2}^N}(n_{N_2}^N + n_{O_2}^N) \tag{3-24}$$

Alternatively, this value can be calculated from the carbon dioxide balance on the permeate and retentate side, as a control value:

$$n_{CO_2}^{N*} = n_{CO_2}^M + n_{CO_2}^O \tag{3-25}$$

The water and methanol fluxes can be calculated from the linear set of equations formed by the measured water loading at the gas outlet

$$Y_{H_2O}^N = \frac{n_{H_2O}^N \overline{M}_{H_2O}}{\sum_j n_j^N \overline{M}_j}, \qquad j = N_2, O_2, CO_2, CH_3OH \;, \tag{3-26}$$

the methanol mass fraction at the liquid outlet

$$w_{CH_3OH}^D = \frac{n_{CH_3OH}^D \overline{M}_{CH_3OH}}{n_{H_2O}^D \overline{M}_{H_2O} + n_{CH_3OH}^D \overline{M}_{CH_3OH}} \tag{3-27}$$

and the balance equations for water and methanol

$$0 = n_{CH_3OH}^C - (n_{CH_3OH}^D + n_{CH_3OH}^N) \tag{3-28}$$

$$0 = (n_{H_2O}^C + n_{H_2O}^M) - (n_{H_2O}^D + n_{H_2O}^N) \;. \tag{3-29}$$

From this set of equations, the water and methanol fluxes at the gas outlet of the carbon dioxide separator result:

$$n^N_{H_2O} = \frac{\sum_j n^N_j \overline{M}_j - \frac{w^D_{CH_3OH}}{1 - w^D_{CH_3OH}} (n^C_{H_2O} + n^M_{H_2O}) \overline{M}_{H_2O}}{\overline{M}_{H_2O} \left(\frac{1}{Y^N_{H_2O}} - \frac{w^D_{CH_3OH}}{1 - w^D_{CH_3OH}} \right)} \tag{3-30}$$

with j = N_2, O_2, CO_2, CH_3OH, and

$$n^N_{CH_3OH} = \frac{\frac{n^N_{H_2O} \overline{M}_{H_2O}}{Y^N_{H_2O}} - \sum_{j = N_2, O_2, CO_2} n^N_j \overline{M}_j}{\overline{M}_{CH_3OH}} \tag{3-31}$$

with j = N_2, O_2, CO_2.

The balances finally lead to values for the water and methanol fluxes at the liquid outlet of the carbon dioxide separator:

$$n^D_{CH_3OH} = n^C_{CH_3OH} - n^N_{CH_3OH} \tag{3-32}$$

$$n^D_{H_2O} = (n^C_{H_2O} + n^M_{H_2O}) - n^N_{H_2O} \quad . \tag{3-33}$$

Finally, it is possible to calculate the carbon dioxide flux and the undesired water and methanol fluxes from the retentate/liquid to the permeate/gas side of the separator from the liquid side balances:

$$n^O_j = n^C_j - n^D_j, \qquad j = CO_2, CH_3OH, H_2O \quad . \tag{3-34}$$

3.2.5 Corrosion Problems

All miniplant elements which are in contact with the anode liquid methanol-water solution are made from stainless steel of high quality (US standard SS316). Nonetheless it has been found out that after even a few days of operation, significant amounts of several metal ions have contaminated the liquid cycle. The following Table 3-2 shows metal ion contents in the anode cycle liquid determined using Total-Reflection X-ray Fluorescence (TXRF) with Gallium as internal standard. All four samples contain 1 mol/dm^3 methanol in water. All sample vials were made from polyethylene and thoroughly cleaned using diluted nitric acid (HNO_3) and MILLIPORE™ conductivity water. The samples were stabilised with 1% HNO_3 and stored at 6°C.

Table 3-2 *Metal ion content in anode methanol-water solution after 7 days of miniplant operation. Most important samples and significant changes are highlighted ('n.d.': not detectable).*

Element	***Metal content [µg/dm³]***			
	Sample #1 blind sample (MILLIPORE™ water and high grade methanol)	*Sample #2* blind sample (MILLIPORE™ water and techn. quality methanol)	*Sample #3* anode solution after 7 days	*Sample #4* mixture prepared from educt vessels
Cr	<1	<1	4.8 (0.09 µmol/dm³)	<1
Mn	<1.5	<1.5	10.3 (0.19 µmol/dm³)	4.8
Fe	7.1	38.2	71 (1.27 µmol/dm³)	9.7
Co	n.d.	n.d.	102 (1.73 µmol/dm³)	<2
Ni	1.61	<1	405 (6.90 µmol/dm³)	7.9
Cu	<1	<1	168 (2.65 µmol/dm³)	7.8
Zn	10.1	21.3	97 (1.48 µmol/dm³)	7.2

The first sample is a blind probe, where a mixture of fresh MILLIPORE™ conductivity water and fresh methanol (quality p.a. > 99.5%, Merck) has been prepared. Also the second sample is a blind probe, but prepared from much cheaper technical methanol (> 98%, Merck) as the more desirable fuel for practical applications (this methanol is not used in the experiments yet). The third sample was drawn from the anode cycle after 7 days of operation. The fourth sample was prepared from methanol and MILLIPORE™ conductivity water, which were stored in the miniplants educt vessels (methanol tank and water tank) for 7 days. The miniplant was drained, thoroughly rinsed with MILLIPORE™ conductivity water and filled with fresh media prior to the 7-day-run. The plant was operated at various experimental settings during that week, covering the whole typical temperature and pressure range (30-90° C, 1.5-3 bara) on the anode side.

One can clearly see that all typical ingredients of stainless steel (Cr, Mn, Fe, Co, Ni, Cu, Zn) show dramatic increases after only 7 days of operation. Obviously these elements have been leached out of the stainless steel by the MILLIPORE™ conductivity water. The total content of these elements is 14.31 µmol/dm³. With a total liquid volume of about 5 dm³ in the anode cycle, this leaves a total amount of 71.55 µmol metal ions accumulated over 7 days. The anode process mixture after 7 days of operation clearly does not fulfill the requirements for

fuel cell operation, as the fuel cell membrane (PEM) is a good ion exchanger which attracts any metal ion and releases its protons in exchange leading to an increased ohmic resistance of the membrane, and thus a decreased fuel cell performance, as observed in the experiments.

To resolve this apparent problem, an ion exchange module was manufactured. It is installed directly at the cell anode inlet to absorb as many metal ions from the anode inlet solution as possible, before it enters the cell. The module was made from a stainless steel tube of 17 mm inner diameter and a length of 250 mm. It is filled with 25 cm^3 of water soaked ion exchange resin (Amberlyst 15, ion exchange capacity >1.7 mmol/cm^3 dry material, dry sphere diameter 0.4-1.1 mm, supplied by Merck). This is equivalent to approximately 19 cm^3 of dry material (volume increase due to swelling in water: approx. 25%). The total ion exchange capacity of the module is therefore at least 30 mmol of single charged ions. As the average charge of the detected metal ions (Cr, Mn, Fe, Co, Ni, Cu, Zn) is roughly two, 15 mmol of them should be absorbed. This is about 200 times the amount found in the liquid cycle after 7 days of operation (see Tab.2-2). To ensure a maximum ion exchange effectivity, the module is refilled with freshly reprotonised resin after two weeks of miniplant operation. The ion-loaded resin is reprotonised by boiling in sulfuric acid at 80°C (1 mol/dm^3 H_2SO_4) for four hours, followed by a sequence of one hour treatment in boiling MILLIPORE™ conductivity water until the pH value of the water stays above 5. It is stored in a plastic container in MILLIPORE™ conductivity water until next use.

To check the performance of the ion exchange module, another 7 days run of the miniplant was carried out, starting with rinsing and refilling the whole liquid cycle. Again blind samples were prepared as before and samples were taken just after refilling and after different operating times. The results are presented in Table 3-3. Obviously, the ion exchange module fulfills its desired task to keep the ion content within the anode cycle solution as low as possible. But in any case it should be checked whether it is possible to exchange as many steel parts (piping, pumps, sensors) by e.g. PTFE material. This would, of course, mean a high investment. For new installations in the field of DMFC testing and operation this experience should be kept in mind.

Table 3-3 *Metal ion content in anode cycle methanol-water solution: Evaluation of ion exchange module. Most important samples and significant changes are highlighted*

Element	***Metal content [µg/dm³]***					
	Sample #1 anode cycle drained, rinsed, freshly filled	*Sample #2* after 1 h non-stop operation	Sample #3 after 3 h non-stop operation	*Sample #4* after 15 h non-stop operation	*Sample #5* after additional 12 h standstill	*Sample #6* after a total of 1 week with 35 h of operation
Cr	<6	<3	<3	3.8	<5	<2.7
Mn	<5	<2.5	<2.5	<2.5	<2.2	<3.1
Fe	16.6	19.3	13.2	12.5	14.1	9.9
Ni	<5	16.7	7.7	17.4	8.9	14.4
Cu	<1	3.4	4.6	6.9	3.2	1.9
Zn	6.5	21.8	20.7	36.2	35.4	37.4
K	89	<15	<13	21	<21	33
Ca	149	85	77	91	86	75

3.3 Fuel Cell Design

As to the time being there are no commercial DMFCs available, it was necessary to develop an in-house cell and stack design. The basic demands were:

- use of standard state-of-the-art materials, which are available on the market,
- high flexibility (i.e. easy change of flowfields, exchangable media connections, operation as single cell as well as multi-cell stack, easy scale-up),
- easy handling in terms of assembly and connection,
- and a design which can also be used as a basis for a series production.

The cell stack consists of the elements (Figure 3-13):

- Membrane electrode assemblies (MEA)
- Diffusion layers
- Gaskets
- Bipolar/monopolar plates with flowfields and media manifoldings
- Connector plates for electrical contacting
- End plates and bolts for bracing the stack together
- Auxiliary elements and media connectors

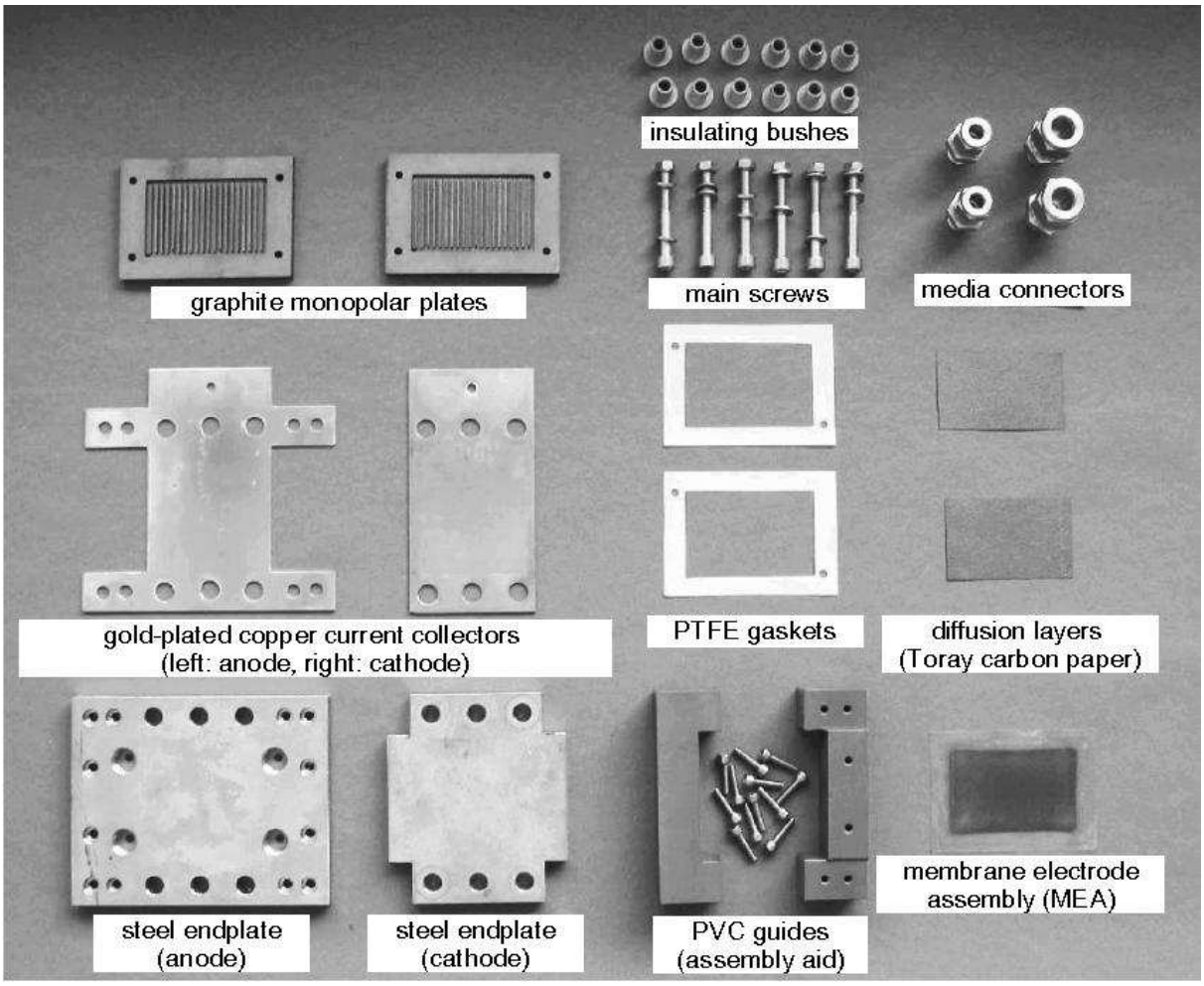

Figure 3-13 *All parts of the DMFC*

In the following sections, the developed cell design is presented in detail (fully assembled cell connected to the DMFC miniplant shown in Figure 3-14).

3.3.1 Membrane Electrode Assembly (MEA)

Two main production paths exist for the preparation of this core element of a polymer exchange membrane (PEM) fuel cell. In both cases, the final result is basically the same, it consists of five layers already described in the introduction (anode diffusion layer, anode catalyst layer, membrane, cathode catalyst layer, cathode diffusion layer).

One preparation methode is to apply the catalyst layers onto the respective diffusion layers and to hot-press these gas diffusion electrodes onto either side of the membrane. This method is widely used, as pre-fabricated gas diffusion electrodes are commercially available (e.g. from E-TEK, ElectroChem etc.). The disadvantages are the very high prices for these electrodes and the lack of information one gets from the suppliers with respect to physical properties (porosity, type and manufacturer of the catalyst, thicknesses of the layers of the

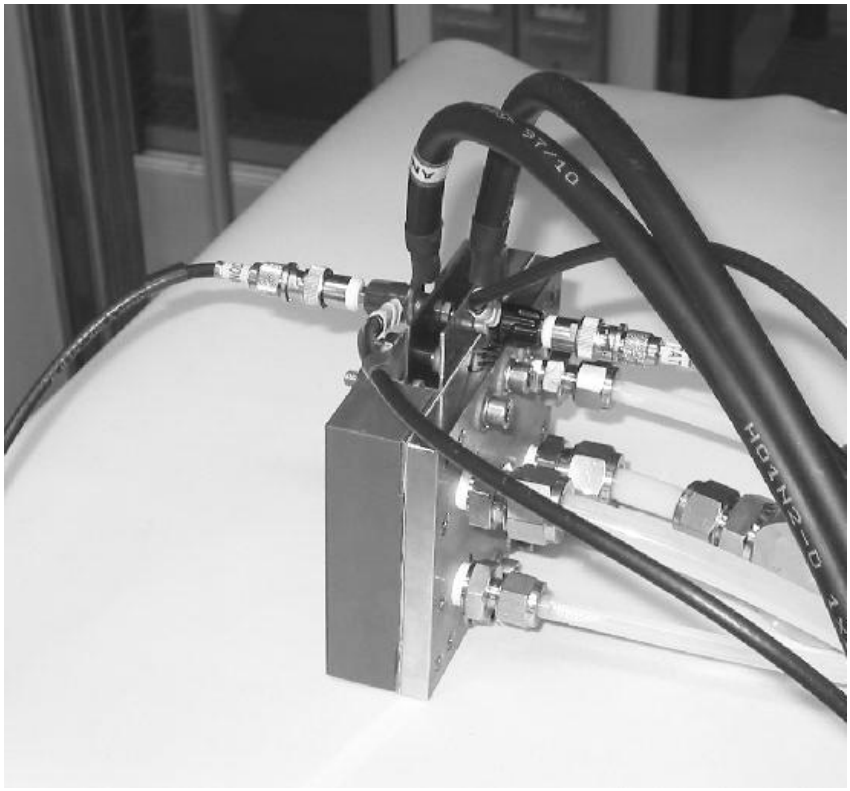

Figure 3-14 *DMFC connected to miniplant*

structure etc.). Especially the latter is very disadvantageous for the formulation of mathematical models of the physical processes within the fuel cell, as such modeling places the demand for reliable parameters of the structures in focus. Another disadvantage of the pre-fabricated electrodes is the fact, that they are also mainly produced by hand. Each electrode sheet looks different from the other, the thicknesses vary significantly etc.. Therefore, the reproducability of obtained results is in doubt.

For all these reasons it was decided to apply the second widely used method for MEA preparation: The preparation of the catalyst layer on the membrane surface (instead of on the diffusion layer surface). The method applied has been developed by the ZSW Ulm, based on the methods published by WILSON and GOTTESFELD [88]. In the following, the abbreviation MEA always refers to a membrane coated with catalyst layers, but without diffusion layers.

First, the membrane (usually NAFION™ by DuPont) is pre-treated. This pre-treatment consists of boiling the membrane consecutively in hydrogen peroxide solution (5 mass-% H_2O_2), MILLIPORE™ conductivity water, sulfuric acid (0.5 m H_2SO_4) and finally again MILLIPORE™ conductivity water (1 hour in each solution).

In the next step, the wet membrane is fixed in an aluminium frame to prevent it from shrinking. It is dried in an oven at 120°C. Due to the unavoidable shrinking process

accompanying the water loss, the membrane is forming an absolutely smooth hard film under high tension stress within the frame. In this state, the frame is placed on a heated table, where the membrane is placed on top of a teflon-coated heated plate with many small holes in, through which a light vacuum is applied. This ensures that the membrane is constantly heated to 120°C, while being fixed on a flat surface.

Now a catalyst ink prepared from catalyst powder (supplied by Alfa Aesar Johnson Matthey Germany), NAFION™ solution (supplied by C.G.Processing USA) and MILLIPORE™ conductivity water is applied to the open membrane surface using an airbrush pistol. By weighing of the whole frame, a defined overall catalyst loading can be reached. A main disadvantage of this method is the obvious problem that an even distribution of the catalyst over the total electrode surface can not be guaranteed. A lot of experimental experience and application of many thin layers is necessary to ensure good and reproducible results.

After application of both catalyst layers onto the membrane, the whole MEA is sintered in an oven at 135°C. This results in mechanically stable catalyst layers, which do not break even when the MEA is bent. Then, diffusion layers made from carbon paper (e.g. TORAY™ TGP-H060) or carbon cloth (e.g. Carbel™ from GORE) can be put on either side of the MEA, and the whole sandwich structure can be mounted between the monopolar plates of the fuel cell. If desired, the diffusion layer can also be hot-pressed onto the MEA to get a compact sandwich, but this was not done in the presented work.

Unsupported platinum black (Alfa Aesar Johnson Matthey HiSPEC™ 1000) and platinum-ruthenium black (Alfa Aesar Johnson Matthey HiSPEC™ 6000; Pt:Ru ratio as stated by the supplier: Pt 66 wt%, Ru 34 wt% meaning an atomic ratio of 1:1; according to XRD measurements Pt 45 atomic%, Ru 55 atomic% [89]) were used as catalysts.

For preparation of the catalyst inks, the NAFION™ solution (DuPont EW1100, 15 wt% NAFION™ dissolved in an unknown mixture of alcohols, other solvents and water) is cleared from hydrocarbons by vacuum distillation and further dilution with MILLIPORE™ conductivity water. The final ready-to-use solution contains 5-8 wt% NAFION™ in water.

The MEA is prepared based on a NAFION™ N105 membrane, with catalyst loadings of 5 mg metal per square centimeter on both anode and cathode side. The resulting MEA has a membrane thickness of 100-110 µm and the catalyst layers are each about 35 µm thick. This means the preparation method leads to a decrease of the membrane's thickness of about 20% (original thickness of NAFION™ N105: 125-130 µm).

The morphology of the resulting catalyst layers can be studied by SEM (scanning electron microscope) images taken from the surface of some produced MEAs (images taken by WEINBERG at the Fritz-Haber Institute of the Max Planck Society, Berlin, Germany), as shown in Figure 3-15.

The structure corresponds to that shown schematically in Figure 1-6. One can see that the catalyst particles are forming agglomerates, which are glued together by ionomer threads. The latter can not be seen on SEM images, but have been found by XPS scans over the surface (distinct due to the fluorine content in the used ionomer NAFION™, XPS results not presented here as they were not part of this work and need a detailed accompanying analysis and discussion). At the outer surface, the diffusion layer made from carbon paper is ensuring electrical connection, on the other side is the membrane, which transports the protons. As both, electronic and ionic conductivity are necessary to carry out the electrochemical reactions at the catalyst surface, only those catalyst particles are active, which are are in contact with both the diffusion layer material (via other catalyst particles or directly) and a continuous thread of ionomer connected to the membrane. Also it might not be desirable to have the catalyst surface covered totally by the ionomer, as it is not yet understood whether this might place a high mass transfer resistance for the educts and the products, and therefore lead to at

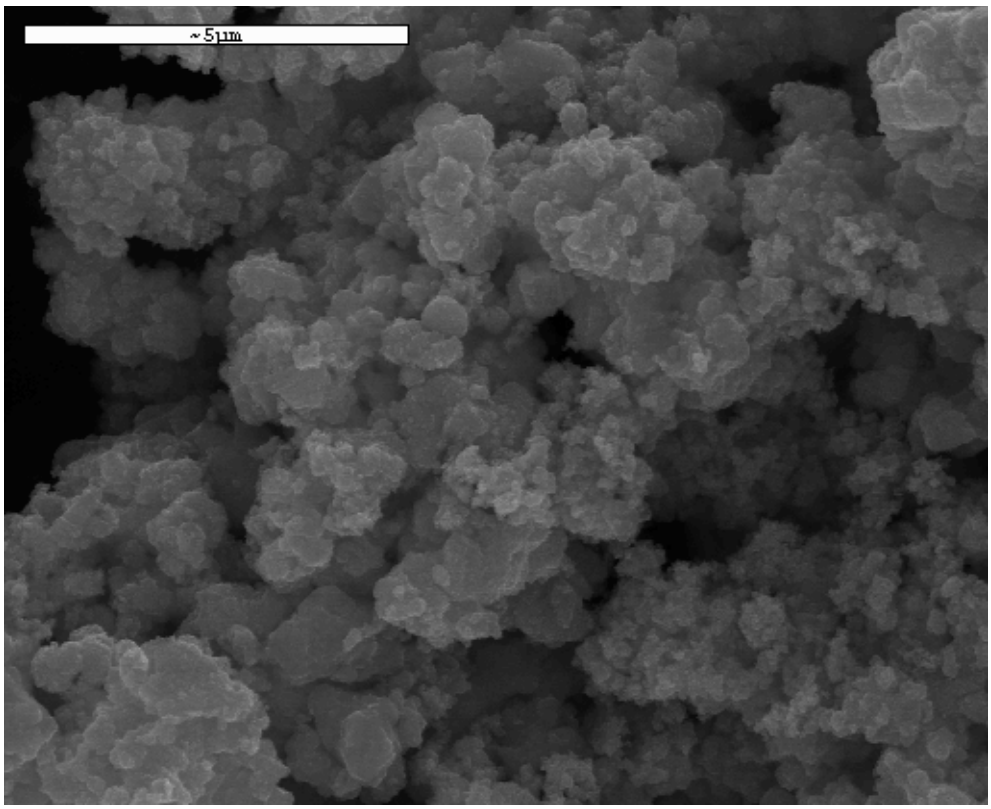

Figure 3-15 *SEM image from MEA surface (only metal particles visible)*

least a reduced activity of the respective particles. Ideally, therefore, an active catalyst particle has to have also a certain amount of free surface in contact with the fluid phase.

An important physical parameter of the catalyst layer is the porosity ε. It can be calculated from the catalyst loading, the ink composition and some physical properties of the used materials. The calculation is presented in the appendix (chapter 9.2.2). The obtained values are $\varepsilon = 0.81$ for the anode catalyst layer, and $\varepsilon = 0.86$ for the cathode catalyst layer. The porosities are obviously very high, which is of course desired to a certain degree to achieve as many accessible catalyst sites as possible for the fluid phases. Nonetheless also an appropriate amount of ionomer phase is necessary to ensure good protonic contact of the catalyst particles.

3.3.2 Diffusion Layers

As diffusion layers, TORAY™ carbon paper is used (type TGP-H-060). To achieve a higher hydrophobicity, the carbon paper is coated with PTFE, with a final PTFE content of 22-25 wt%. The treatment consists of immersing in diluted PTFE emulsion (10 wt% PTFE, original emulsion Dyneon TF5032 by DuPont with 60 wt% PTFE), drying at 80°C for 1 h, and sintering at 330°C for 30 min). The physical properties of untreated TORAY™ paper and the calculation of the porosity of the PTFE-treated material are given in the appendix (chapter 9.2.1). The value of the latter results in $\varepsilon_{Toray+PTFE} = 0.71$. The mean pore size of the untreated material is $d_{pore} \approx 40$ µm. As the porosity is only slightly decreased by the PTFE (untreated material: $\varepsilon_{Toray} = 0.78$), it is assumed that the mean pore diameter is not affected by the PTFE content. There are no experimental pore size distributions available in the literature for PTFE treated carbon paper.

Finally, it shall be mentioned that other authors report positive results when using untreated TORAY™ paper on the anode side [90].

3.3.3 Gaskets

In former experiments with DMFCs at other research facilities, often cell performance degradation took place due to contaminations originating from the applied gasket material, mostly from additives (see e.g. [91]). To avoid such problems it was decided to use solely gaskets made from PTFE foils, which do not contain any other additive (Supplier: Bohlender GmbH, Germany; Thicknesses: 0.12 mm and 0.25 mm). The thickness was chosen depending on the structures and thicknesses of the MEAs and diffusion layers. For the standard type MEA and TORAY™ paper TGP-H060, 0.12 mm gaskets were found to be the optimal choice.

3.3.4 Monopolar Plates

The monopolar plates are made from graphite plates (thickness 7 mm) supplied by Schunk Kohlenstofftechnik (Germany). The necessary flowbed structures for the reactant distribution over the MEA surface are millcut into the plates.

The basic structure of the flowbeds is very simple (Figure 3-16). It consists of parallel channels of 2 mm width and 2 mm depth, with 1 mm wide ribs between them. Perpendicular

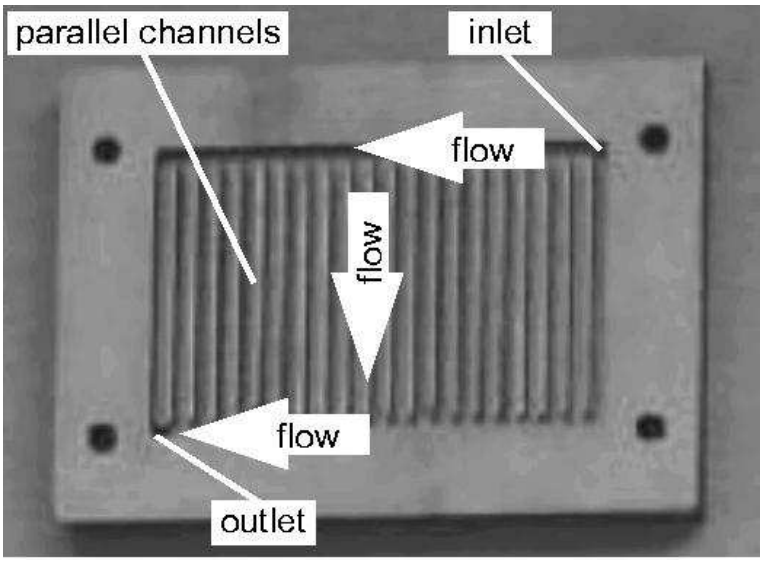

Figure 3-16 *Photo of monopolar plate showing inlet, outlet and flow direction in flowbed structure*

distributor (top) and collector channel (bottom) connect the parallel channels to the inlet and outlet, respectively. The respective medium (air or methanol-water solution) is supplied in one corner of the rectangular flowbed and leaves at the opposite corner (flow direction indicated in Figure 3-16).

The used standard flowbed has the outer dimension 65 x 40 mm, identical to the catalyst layer on the MEAs, which leads to an active area of A^S=26 cm^2. As the diffusion layer is compacted by the flowbed ribs (observable at disassembled cells), one can suspect that the catalyst beneath these compaction zones is only poorly supplied with the reactants. But even without such a compaction or assuming the compaction is only slightly decreasing the porosity of the diffusion layer in this region, one has to assume that the maximum achievable current density in the respective catalyst layer regions is lower than directly opposite to the flowbed channels, simply due to the longer and less direct path for the reactants as well as the reaction products. Simulation results by KULIKOVSKY et al. [58][70] indicate such an influence, which leads to a decrease of the active electrode area.

Assuming that the areas beneath the flowbed ribs are not supplied with reactants at all, the used flowbed design leads to a minimum active area A^S_{min} of

$$\begin{aligned} A^S_{min} &= A^S - (number\ of\ ribs \cdot width\ of\ ribs \cdot length\ of\ ribs) \\ &= 26\ cm^2 - 21 \cdot 0.1\ cm \cdot 3.6\ cm = 18.44\ cm^2 \end{aligned} \tag{3-35}$$

which is 71% of the catalyst impregnated area. As the effect of longer and maybe even blocked supply paths due to these effects is not fully understood so far and an assumption on the reduction of the overall cell performance would only be speculative, for all further discussions still the total active area is used. The same is true for the analysis of all experimental data (calculation of current densities etc.).

3.3.5 Connector Plates

For the electrical connection of the graphite end (=monopolar) plates, gold plated copper plates of 1.5 mm thickness are used. Also all further electrical connectors are gold plated. This shall ensure minimal ohmic resistances at the various connection points.

3.3.6 End Plates and Stack Assembly

Finally, for bracing the stack and applying the desired tension on the bipolar plates and gaskets, 10 mm thick stainless steel plates (material code 4571) are used. Both end plates are connected by a total of 6 bolts (diameter 6 mm, three on each long side of the cell stack), running through plastic bushes to prevent electrical contact between the end plates. As a standard, the stack is assembled applying a torque of 5 Nm on the nuts and bolts.

3.3.7 Auxiliary Elements and Media Connections

The media are supplied through one end plate via screwed-in HyLok connectors made from stainless steel (type SS 316). To avoid electrical contact between connector plates and the respective end plates, and to ensure an even pressure distribution over the bipolar plates, a PTFE foil (thickness 0.25 mm) is put between connector and end plates, respectively.

Finally, to simplify the stack assembly, two U-shaped PVC elements are fitted to the base end plate which form a duct for the bipolar plates, gaskets and MEAs. This ensures a correct relative position of the different stack components, except for the diffusion layers. During assembly, they are fixed to the graphite plate by wetting them (surface tension holds them in place).

3.4 Concluding Remarks

To be able to perform experimental investigations on DMFCs, a variety of installations was set up. A lab-scale production scheme for MEAs is available now using an airbrush technique for applying the catalyst layers onto pre-treated membranes of any type. For conditioning and testing of newly assembled DMFCs with hydrogen a simple lab-scale plant is used (Figure 3-1). For the final experiments under realistic DMFC operating conditions a fully automated miniplant was designed and set up, in which steady-state and dynamic experiments can be carried out. As a special feature the on-line balancing capabilities of this miniplant enable the analysis of mass transport within the DMFC, especially of the undesired crossover of methanol and water from anode to cathode.

Finally, a complete DMFC design was developed and improved offering the opportunity to be able to influence all design parameters independent of any external supplier. Based on this design concept even a full toolbox of components usable for hydrogen-fed PEMFCs (with internal air manifolding or open cathode) was developed.

4 Steady-state Experiments

As basis for model validation and parameter fitting, steady-state (stationary) experiments were carried out. The cells were first operated with hydrogen/air to determine the maximum performance in terms of power densities. These data can be used as first benchmarks in comparison with data from other research groups. Also each freshly assembled cell was conditioned by hydrogen/air operation prior to operation with methanol-water mixtures. As standard stationary experiment, current voltage curves were collected. In DMFC operation using the miniplant also the online balancing function was used to measure the methanol and water crossover fluxes through the DMFC' s polymer electrolyte membrane.

4.1 Cell Conditioning Procedure

Before a freshly assembled cell is operated with methanol-water mixtures, it is operated with hydrogen and air following a well-defined procedure. The cell is fed with both gases at ambient temperature and pressure. Both gases are humidified in washing bottles, which are also at ambient temperature. Hydrogen is fed at a flow rate of 100 cm^3/min, air is fed at a flow rate of 250 dm^3/h.

The cells are purged with the gases for 10 minutes, starting with a very thorough purging on the hydrogen side to blow out all air as fast as possible (in order to avoid self ignition of air/hydrogen mixtures at the anode catalyst). A nitrogen purge prior to the hydrogen feed was not performed for simplicity reasons and as the cells are small.

Then, the cells are connected to a simple electronic load (Statron 3229.1 with external voltage source to achieve cell voltages down to 100 mV). A current density of 200 mA/cm^2 is applied for 8 hours. If stable operation is reached, the current density is increased to 300 mA/cm^2 for 8 more hours. If also here stable operation is achieved, the current density is further increased to 400 mA/cm^2 for again 8 hours. Finally, it is increased to a maximum value at which a stable cell voltage of 100 mV is maintained. Usually the cells reach this point at current densities around 450 mA/cm^2.

This maximum current density is quite low compared to those achieved by PEM fuel cells produced by the main car manufacturers and research centres (max. current densities of 1000-2000 mA/cm^2 being reported). But taking into account the operating conditions (ambient pressures and temperatures, no sophisticated humidification/water management) and the simple cell design and MEA preparation procedure the performance is satisfactory.

4.2 Steady-state Current Voltage Curves with Hydrogen/Air Operation

As first tests of the new cell design and as benchmark for comparison with other cells, stationary current voltage curves were recorded with hydrogen and air as feed gases. Both gases were supplied at ambient temperature and pressure and humidified in washing bottles thermostated to 20°C. The cell entry temperatures and humidities are unknown, but the temperature of the cells always was close to ambient. Due to experiences of other groups with similar settings, it can be expected that the relative humidities were above 80% at 20°C. The curves were recorded using a Zahner IM6e potentiostat in combination with an electronic load EL-101. The curves were recorded automatically using the following settings:

- potentiostatic measurement, cell voltages 950 mV down to 100 mV (step 25 mV)
- steady-state sampling mode: measuring time minimum 20 s (max. 60 s), cell current recorded at absolute current tolerance $<10^{-4}$ A/s and relative current tolerance 10^{-4} 1/s

A series of recorded current-voltage and current-power density curves is given in Figure 4-1 and Figure 4-2:

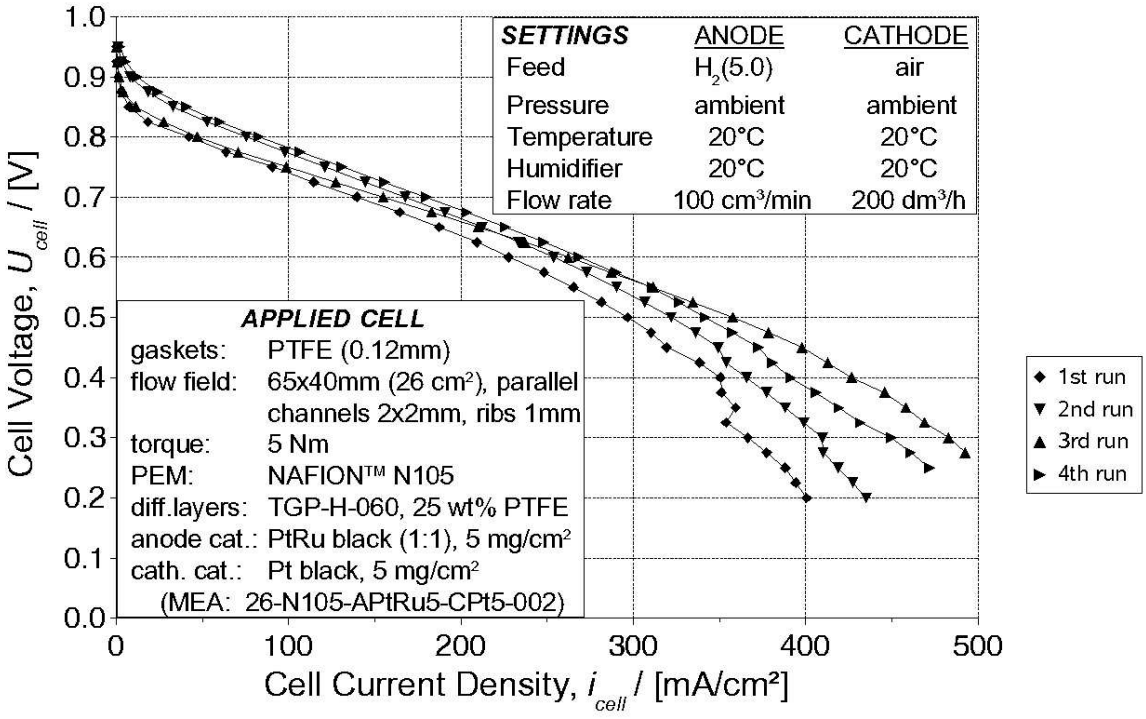

Figure 4-1 *Steady state current voltage curves; cell fed with hydrogen and air. The four runs were performed with intervals of less than one minute between two runs.*

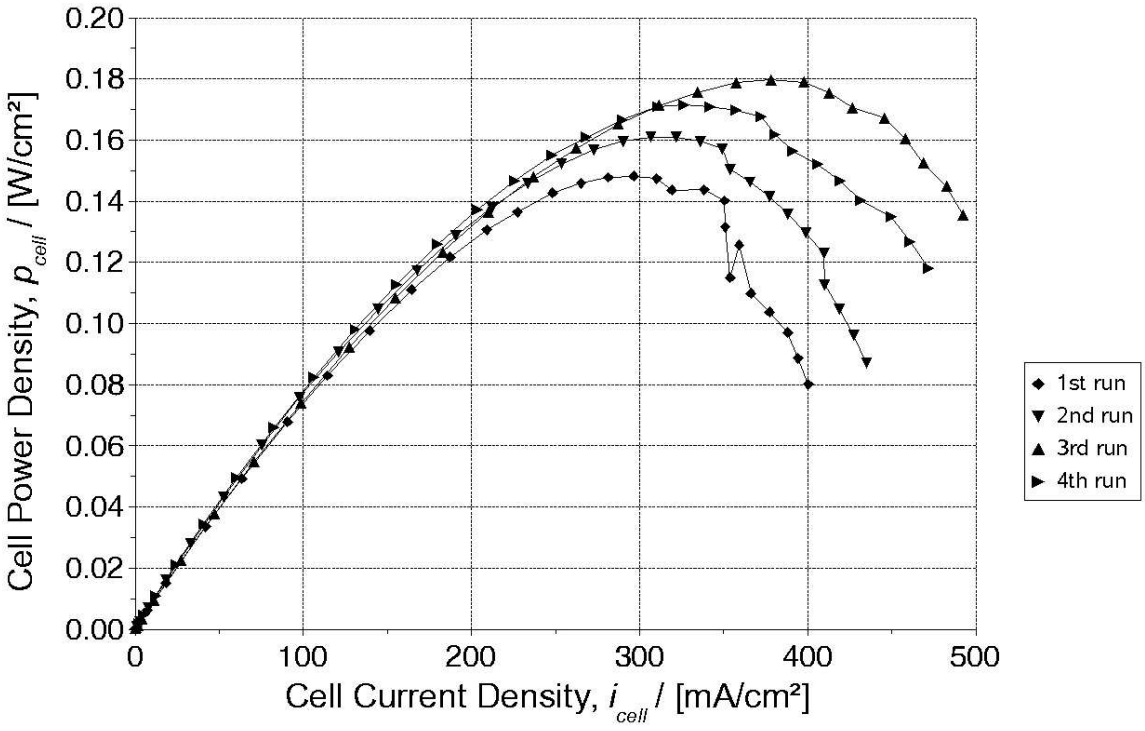

Figure 4-2 *Steady state current power density curves (operating conditions: see Figure 4-1). The four runs were performed with intervals of less than one minute between two runs.*

One can see, that while the same measurement is repeated several times, the maximum performance is first increasing, but beginning with the fourth run it goes down again slightly in the high current density region (above 250 mA/cm^2). In the low to medium current density region (up to 250 mA/cm^2), the performance goes up steadily, but also slightly. Almost, a stable performance was reached. The fluctuations in the high current density region seem to be due to cathode flooding (liquid water forming in the cathode), as water drops have been observed to leave the cathode outlet of the cell.

The presented results show that our cell design is reliable and provides for stable and reproducible results. Also the cell performance is satisfactory keeping in mind the operating conditions (ambient temperature and pressures, low feed gas humidification levels).

4.3 Steady-State Current Voltage Curves with Methanol/Air Operation

The next step after hydrogen/air operation is the stationary operation with methanol-water solution as anode feed. These experiments were carried out using the DMFC miniplant. The standard operating conditions were:

Anode: Methanol feed concentration c^{AF}_{CH3OH} = 1 mol/dm^3 = 3.2 wt%
Pressure p^A = 1.7 bara = 1.7·10^5 Pa
Flow rate F^{AF} = 0.5 dm^3/min
Temperature T^A varied (30 / 45 / 60 / 75 / 90°C)

Cathode: Dry air (dew point approx. -20°C)
Pressure p^C varied (1.3 / 1.7 / 2.2 bara)
Flow rate F^{CF} = 0.5 scbm/h (at 1.013·10^5 Pa and 20°C)
Temperature T^C ambient (20°C)

The cell was operated galvanostatically, in contrast to the potentiostatic operation for the previously described experiments with hydrogen. The reason for this change in the operation mode is that the potentiostat used for hydrogen testing can perform automated current-voltage curves, but only in potentiostatic mode, while the potentiostat in the DMFC miniplant is best operated in galvanostatic mode.

At each current applied, the cell was operated two minutes to reach a steady state. Then the cell voltage and the on-line calculated methanol and water crossover fluxes through the membrane (see next section) were observed for two more minutes and average values were recorded. Some typical current voltage and current power density curves are shown in Figure 4-3.

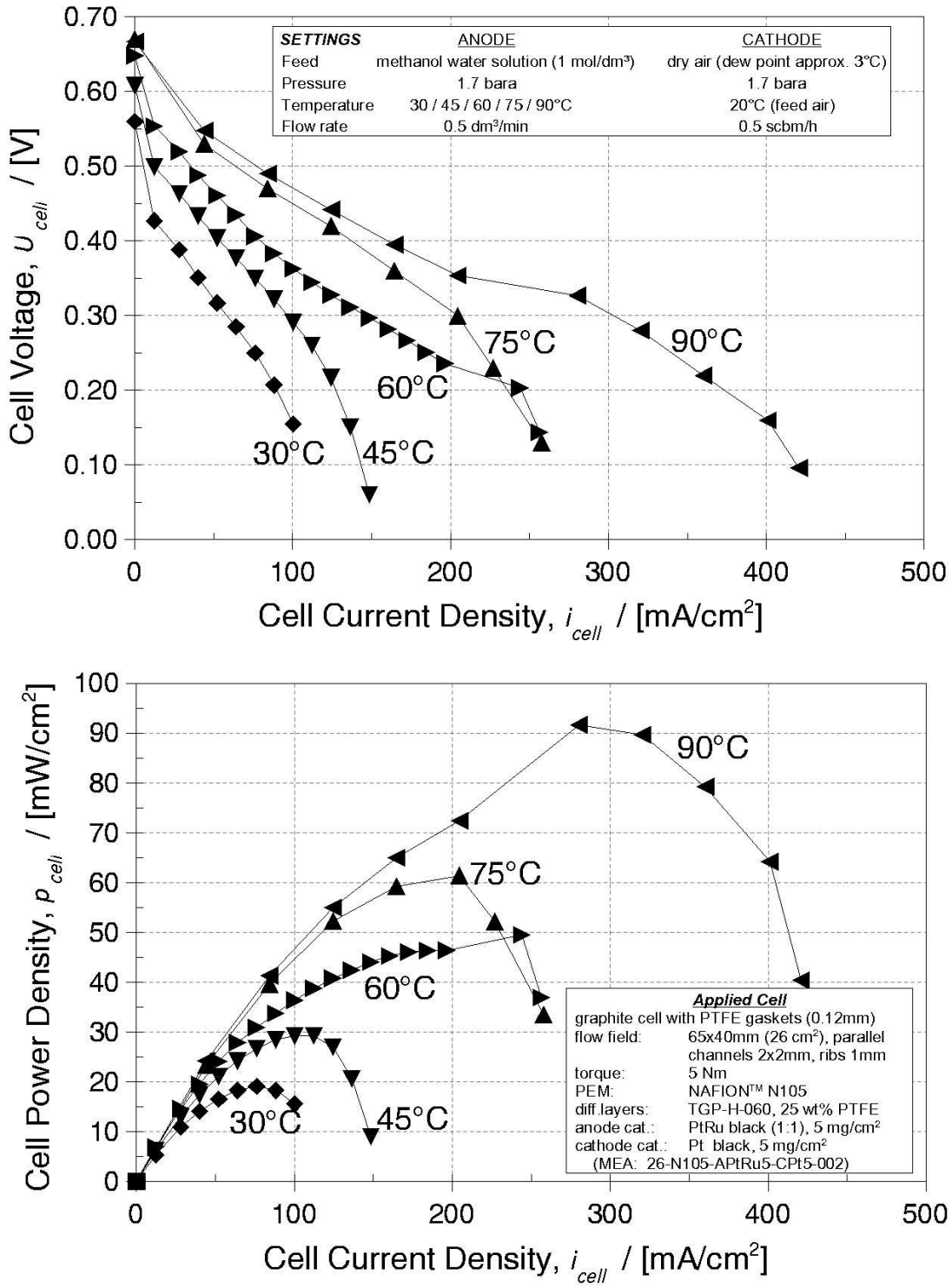

Figure 4-3 *Steady state current voltage and current power density curves for different cell temperatures (methanol operation). No pressure difference between anode and cathode.*

4.4 Steady-state Analysis of Membrane Crossover Fluxes

The main task of the set of experiments described in the previous section was to determine the influence of the cell operating temperature and of the pressure difference between anode and cathode compartments on the steady state cell behaviour, especially on the methanol and water membrane crossover fluxes. These results are presented in Figure 4-4 and Figure 4-5.

One can see, that the methanol crossover fluxes are going down slightly with higher cell current densities, whereas the water crossover fluxes show a slight increase. Noteably both fluxes show only a weak dependence on the current density, with a relatively high base value even under open circuit conditions (no cell current).

To get a better impression of the order of magnitude of the methanol crossover fluxes, the right y-axis shows the electrochemical equivalent current densities. They are calculated using Faraday' s law:

$$i_{crossover} = 6Fn_{CH3OH,\ crossover} \tag{4-1}$$

Base values of more than 900 mA/cm^2 are reached, which is twice as much as the maximum cell current density (450 mA/cm^2). Typically, the methanol crossover flux at maximum cell power density is roughly equivalent to the cell current density. This shows the tremendous influence of this undesired phenomenon, and the order of magnitude of the resulting loss of valuable fuel.

Also cell temperature and the pressure difference between anode and cathode compartment have a significant influence on the crossover fluxes. One can see that applying a higher pressure on the cathode side than on the anode side reduces the crossover fluxes of water and methanol significantly. Obviously, it does not make any sense to apply a cathode pressure which is even lower than the anode pressure, as this results in severely increased crossover fluxes. Applying even higher cathode overpressures, on the other hand, seems to be beneficial. E.g. the group of JÖRISSEN at the ZSW (Ulm, Germany) operates at up to 1.5 bars cathode overpressure [90]. The temperature dependence of the water crossover flux seems to be much stronger than for the methanol flux. But generally, as could be expected, higher temperatures lead to increased crossover fluxes.

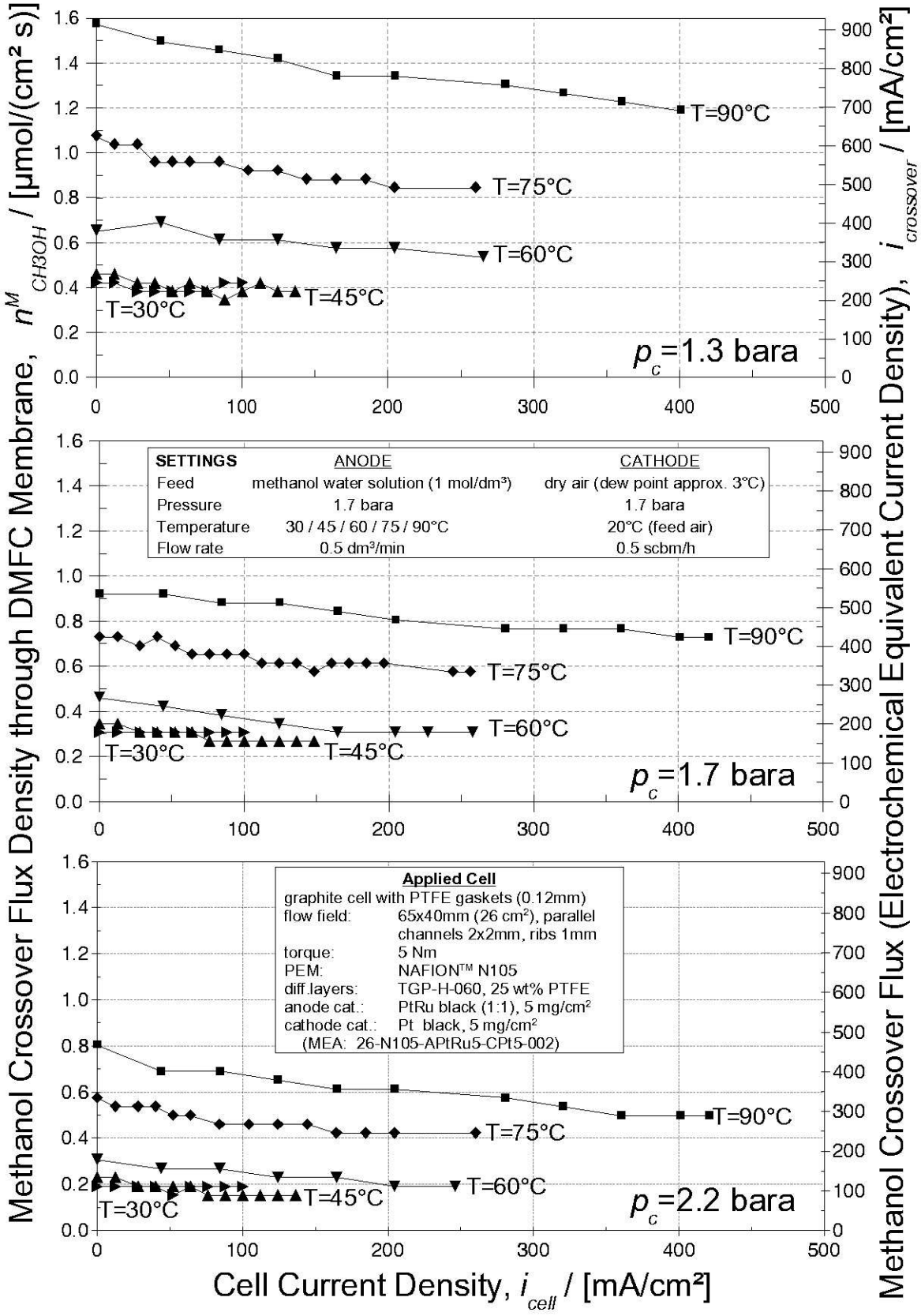

Figure 4-4 *Methanol crossover fluxes determined from miniplant on-line balances. Cell temperatures 30-90°C (see legend), fixed anode pressure (1.7 bara), cathode pressure varied (top = 1.3 bara, middle = 1.7 bar, bottom = 2.2 bara)*

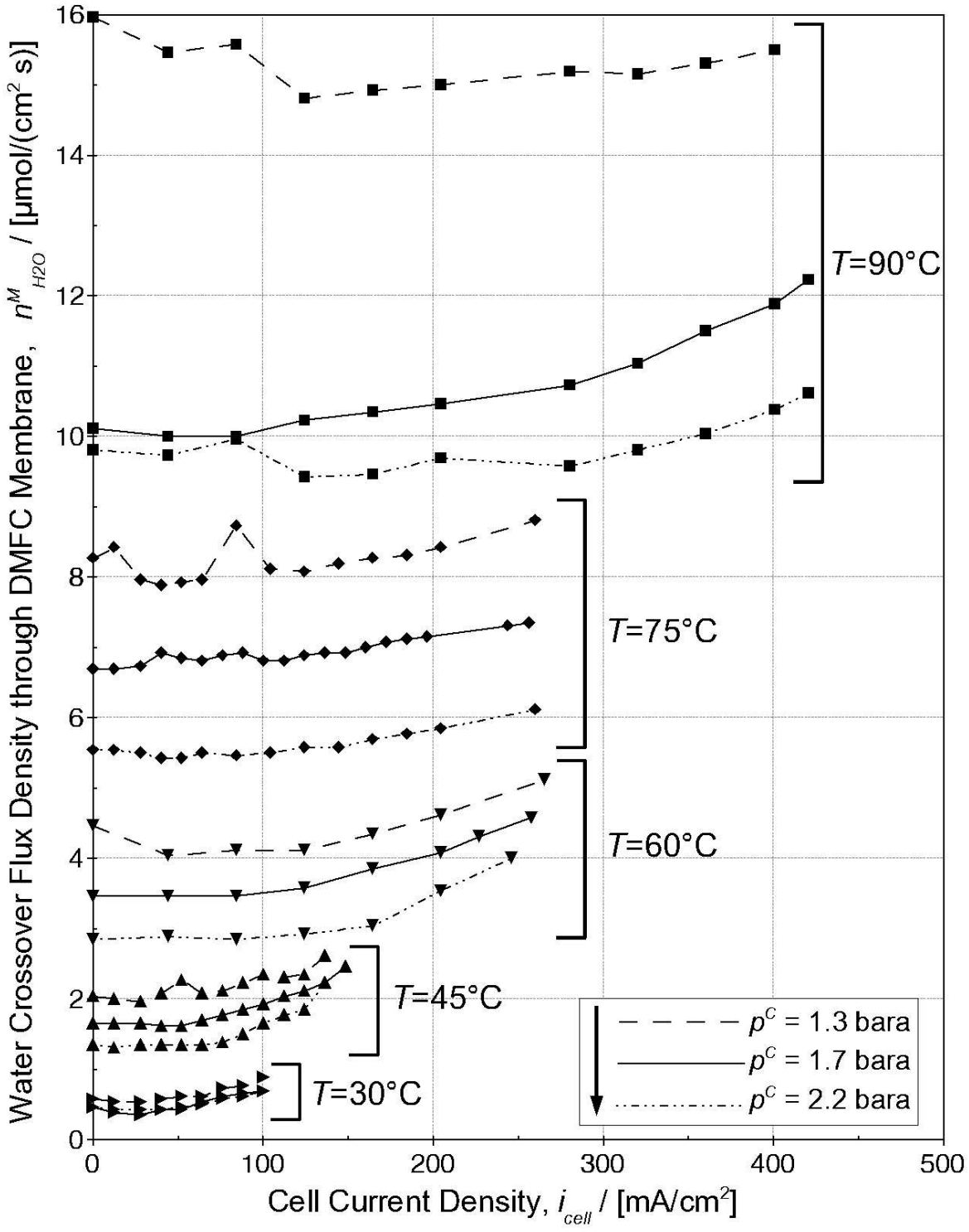

Figure 4-5 *Water crossover fluxes determined from miniplant on-line balances.*

Operating conditions: see Figure 4-4

Under open circuit conditions (OCV, i.e. no current flux) and without pressure difference between anode and cathode, especially the water flux density seems to follow an exponential law (see Figure 4-6, left). Assuming the crossover fluxes n_i would follow an Arrhenius-type temperature dependence

$$n_i = n_i^0 e^{-\frac{E_{A,i}}{RT}}, \qquad i = CH_3OH, H_2O \quad , \tag{4-2}$$

an Arrhenius plot of ln(n_i) over 1/T and a linear regression

$$\ln(n_i) = \ln(n_i^0) - \frac{E_{A,i}}{R}\frac{1}{T}, \qquad i = CH_3OH, H_2O \tag{4-3}$$

gives the activation energy $E_{A,i}$ of the two (Fick) diffusion coefficients. The respective data and linear regressions are given in Figure 4-6 (right).

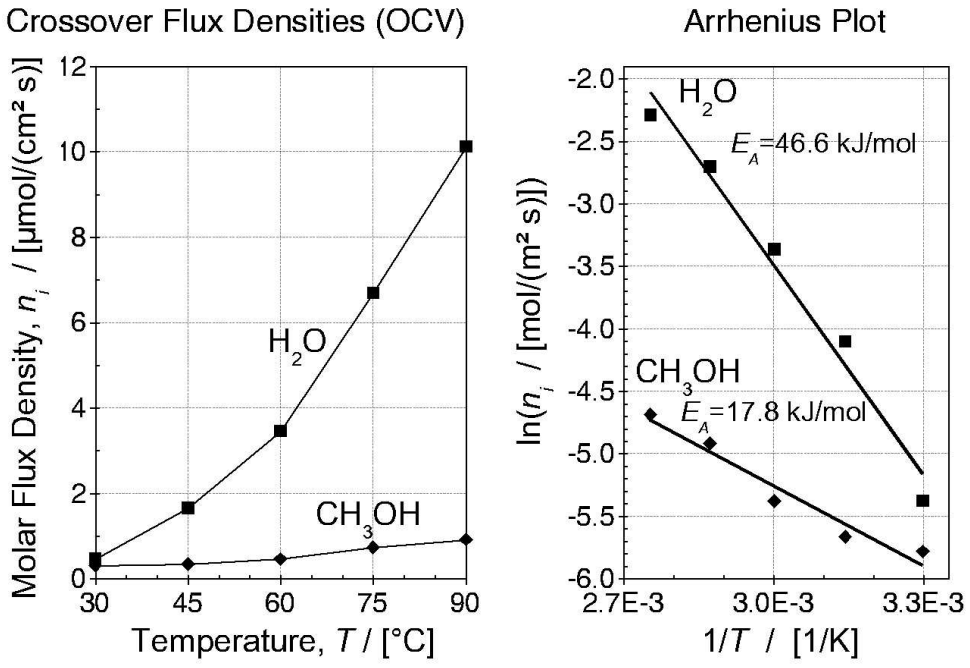

Figure 4-6 *Temperature dependence of water and methanol crossover flux densities at open circuit conditions (OCV) without pressure difference between anode and cathode. Linear plot (left), Arrhenius-type plot with linear regression (right).*

Now, extending the analysis of the open circuit crossover fluxes to their dependence on the pressure difference between anode and cathode compartment, the data plotted in Figure 4-7 are obtained. One can clearly see the benefits of a cathode overpressure. The data seem to reflect some kind of exponential decay with pressure difference.

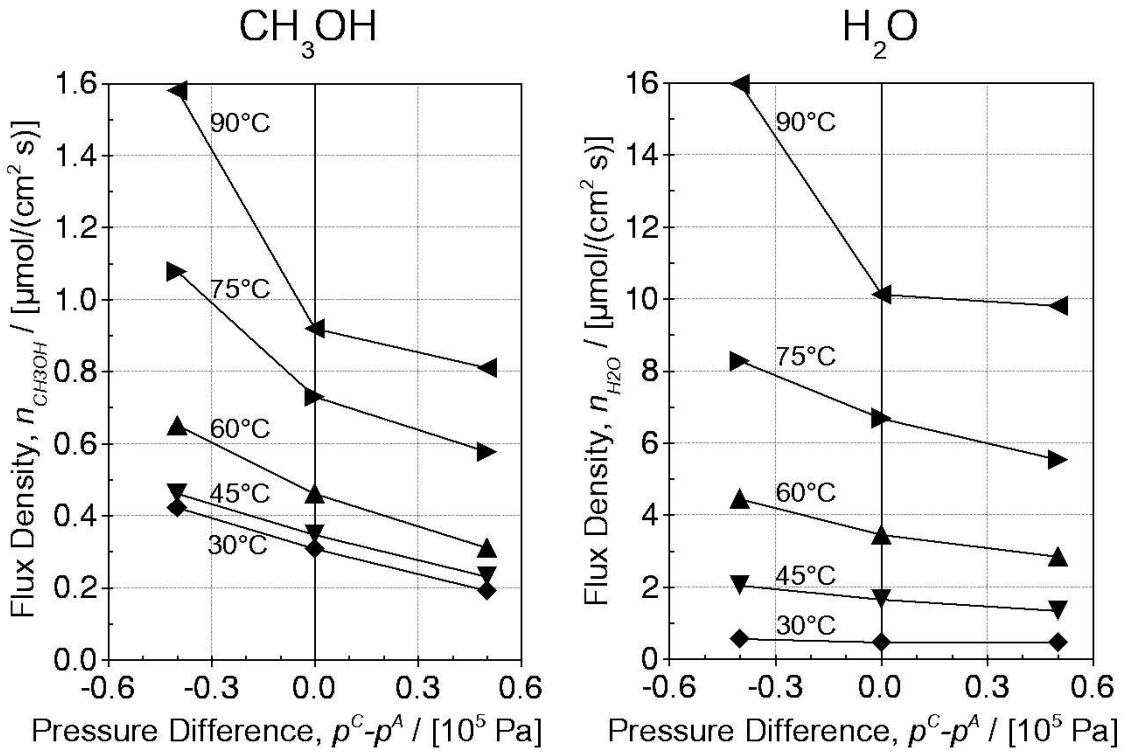

Figure 4-7 *Influence of pressure difference between anode and cathode compartment on crossover fluxes, open circuit conditions (OCV). Methanol (left), water (right).*

4.5 Concluding Remarks

DMFCs have been produced, conditioned and tested with hydrogen and methanol-water solution as fuels. Typical current voltage curves have been obtained which show a stable performance and reproducability. At methanol operation, current densities above 400 mA/cm² can be achieved, the related maximum power densities are closely below 0.1 W/cm².

Also the on-line balancing of the miniplant has produced valuable results. The water and methanol flux densities reach quite high values, especially at high cell temperatures. The temperature dependence of the flux densities follows an Arrhenius-type law. Even at open circuit conditions (no electrical current) significant values are reached, while the influence of the electrical current density was found to be relatively small. These results lead to the conclusion that in the liquid-operated DMFC diffusive mass transport is predominant in the crossover phenomenon, and not electro-osmotic flow.

5 Dynamic Experiments

Dynamic experiments are necessary for two reasons: On one hand the mathematical DMFC model to be presented in chapter 6 contains some parameters which only influence the dynamic behaviour of the model. Therefore they can only be fitted using results from dynamic experiments. On the other hand, practical DMFC systems need to be controlled in order to achieve optimal performance under various operating conditions. The typical input parameter of a DMFC system is the cell current, which is determined by the electric load the system is powering. The most obvious control parameter is the methanol feed concentration (see e.g. DMFC system presented in Figure 1-11, page 19). Therefore knowledge about the dynamic response of the DMFC to changes in the cell current and the methanol feed concentration is necessary for controller design and synthesis.

Typically, in such experiments only one operating parameter is changed. This change is a single step from one value to a significantly different value. Such experiments are often referred to as step or transient experiments. As the cell is operated galvanostatically in all experiments to be presented, always the cell voltage response is recorded and plotted.

5.1 Methanol Feed Concentration Step-Down

First experimental examinations

In 1998 SUNDMACHER together with the group of SCOTT performed steady-state experiments with liquid-fed DMFCs [16]. They operated DMFCs in galvanostatic mode until a steady state was reached. Then they rinsed the anode compartment of the cells with pure water while the electronic load remained switched on. What happened then was a very interesting, at that time unexpected cell voltage response to this dramatic change in operating conditions (Figure 5-1). Instead of an immediate decrease of the cell voltage due to fuel shortage, the cell voltage was sustained for some time, then increased, before it finally broke down. This sustaining and overshooting phenomenon was then observed under various operating conditions and led to many speculations about the underlying reasons. Only part of the sustaining time can be explained with dead volumes in the experimental setup (volumes inside pipes etc. between feed switch valve and DMFC anode feed inlet). Obviously some internal storages for educts, intermediate reaction products or charge are responsible for this behaviour. An appropriate dynamic model of a DMFC should account for such phenomena and show similar simulation results.

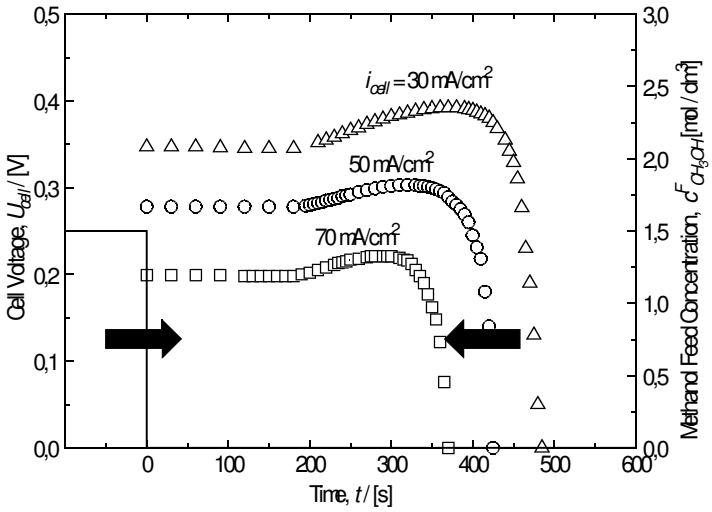

Figure 5-1 *Step-down of methanol feed concentration: Results from SUNDMACHER et al. [16]*

Experiments of this work

As the presented experimental data from SUNDMACHER et al. (Figure 5-1) were obtained using a DMFC with some materials different from those used in the experiments of this work, similar dynamic step-down experiments were performed under various operating conditions using our equipment. The most important operating conditions to be varied are the cell temperature, the methanol feed concentration before the step-down and the cell current density during the experiments. The latter was kept constant during the experiments (galvanostatic operation). The full set of operating conditions is:

Anode:	Methanol feed concentration = 1 / 1.5 mol/dm^3 = 3.2 /5.0 wt%
	Pressure = 1.7 bara = 1.7·10^5 Pa
	Flow rate = 0.5 dm^3/min
	Temperature = 60 / 75 / 90°C
Cathode:	Dry air (dew point approx. -2°C)
	Pressure = 1.7 bara = 1.7·10^5 Pa
	Flow rate = 0.5 scbm/h (at 1.013·10^5 Pa and 20°C)
	Temperature = 30°C

As the feed switch is not located directly at the fuel cell inlet, a certain dead time occurs depending on the anode feed flow rate. In the miniplant, the distance between the feed switch valves and the cell inlet is nearly six meters, with the pipes having an inner diameter of six millimeters.

This leads to a total dead volume of

$$V_{dead} = A_{pipe} L_{pipe} = \frac{\pi}{4} d_{pipe}^2 L_{pipe} = \frac{\pi}{4} (0.6\,cm)^2\, 600\,cm = 170\,cm^3 \quad . \qquad (5\text{-}1)$$

At the given flow rate of 500 cm³/min the dead time results as

$$t_{dead} = \frac{V_{dead}}{F^{AF}} = \frac{170\,\mathrm{cm}^3}{500\,\mathrm{cm}^3/\mathrm{min}} = 20\,\mathrm{s} \quad . \qquad (5\text{-}2)$$

The results are presented in Figure 5-2, Figure 5-4 and Figure 5-3. The dead time is marked by a vertical dashed line at 20 seconds after the feed switch. Presented are the influence of the current density, cell temperature and initial methanol feed concentration.

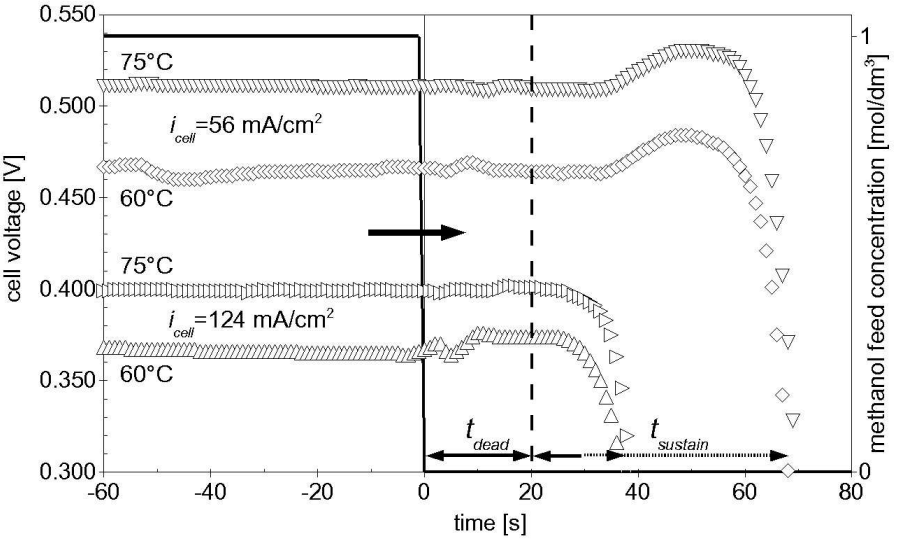

Figure 5-2 *Methanol feed concentration step-down experiments (galvanostatic operation) at different cell current densities and cell temperatures*

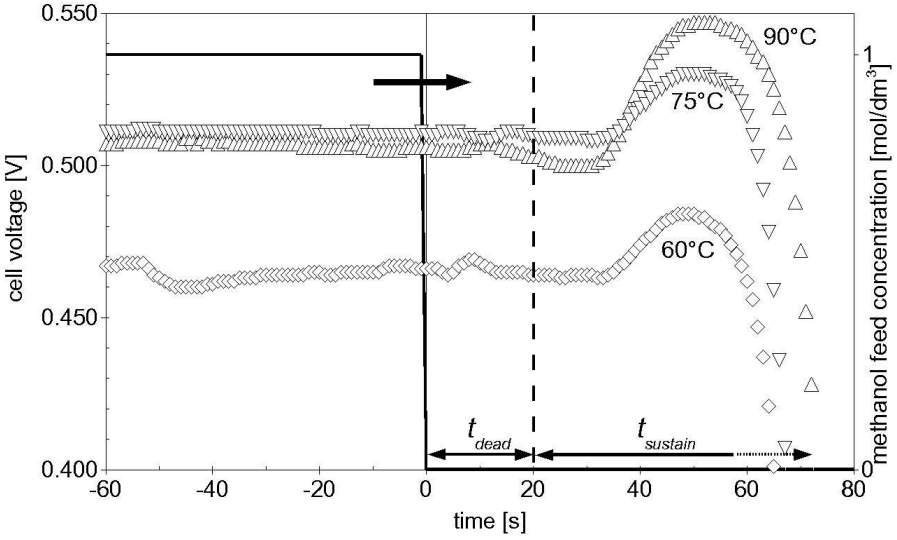

Figure 5-3 *Methanol feed concentration step-down experiments (galvanostatic operation) at different cell temperatures, cell current density i_{cell} = 56 mA/cm²*

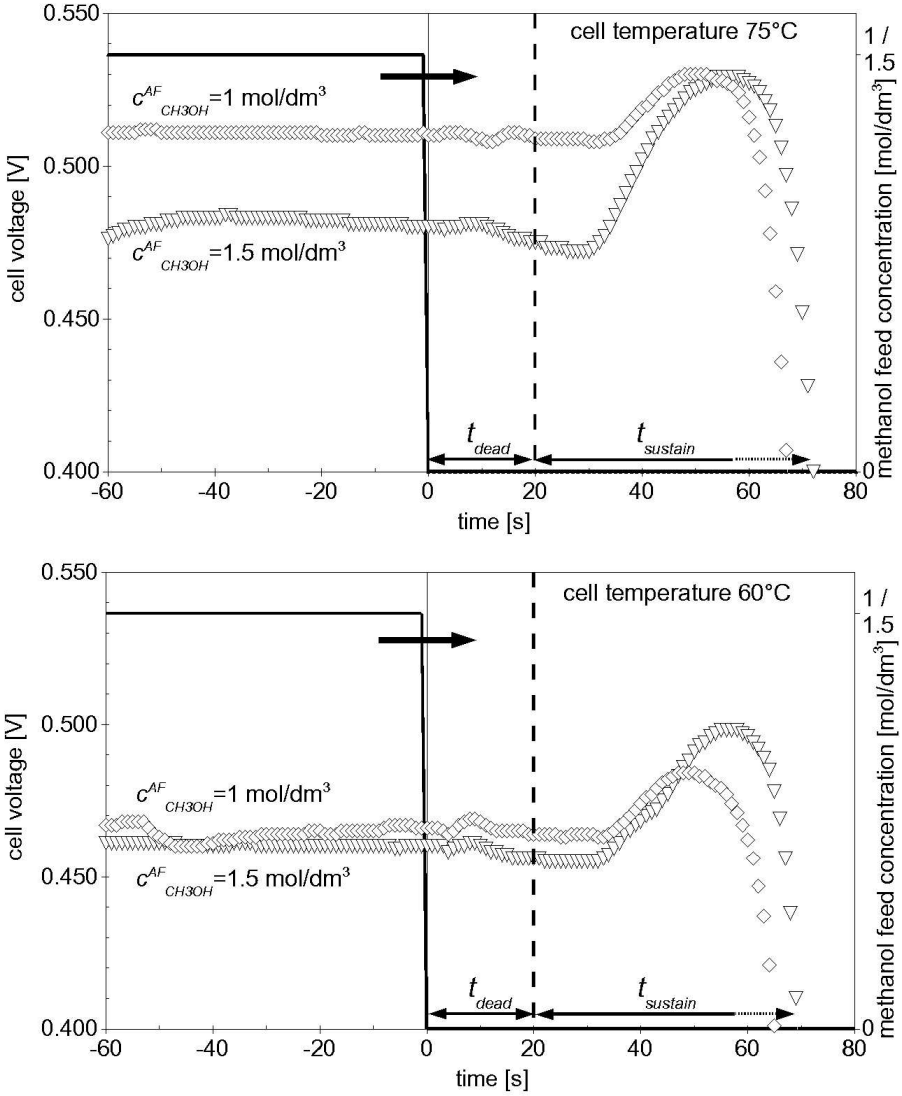

Figure 5-4 *Methanol feed concentration step-down experiments (galvanostatic operation) at different initial methanol feed concentrations and cell temperatures, cell current density* i_{cell} *= 56 mA/cm²*

In general, a behaviour similar to that reported by SUNDMACHER et al. [16] is observed. The response of the DMFC to the presented step changes of the methanol feed concentration can be characterised qualitatively as follows:

- Overshooting of the cell voltage only occurs for low current densities.
- The higher the initial methanol feed concentration, the higher the level of overshooting.
- The higher the cell temperature, the higher the level of overshooting.
- The sustaining time $t_{sustain}$ (i.e. the time between end of dead time t_{dead} and the time the cell voltage has broken down to zero) is only a function of the cell current density.

Discussion

The experimental observations support the assumption, that internal storages for methanol and/or other anode intermediate reaction products play a major role for this behaviour. The DMFC exhibits reservoirs of educts to draw from for a certain time, even when there is no more methanol supply:

- Unreacted methanol present in the pores of the anode catalyst and diffusion layer and within the membrane (PEM) material (crossover methanol),
- and reaction intermediates adsorbed on the anode catalyst (e.g. CO, see Figure 1-5, chapter 1.2).

In the following, based on the experimental results, these two possible explanations are checked for plausibility individually by means of some simple calculations assuming that only one or the other would be the reason for the observed behaviour, respectively.

From the sustaining time $t_{sustain}$, the size of the assumed internal storages can be calculated in terms of total charge per square area and methanol per square area. The total storage charge density $\hat{Q}_{storage}$ in [C m^{-2}] is thus given by:

$$\hat{Q}_{storage} = t_{sustain}\, i_{cell} \tag{5-3}$$

where i_{cell} is the cell current density in [A m^{-2}].

Assuming total oxidation of methanol to carbon dioxide, this value simply has to be divided by 6 times Faraday's constant to get a mean methanol density $\hat{N}_{CH_3OH,\,storage}$ in [mol m^{-2}] with respect to the cross-sectional cell area A^S in [m^2]:

$$\frac{N_{CH_3OH,\,storage}}{A^S} = \hat{N}_{CH_3OH,\,storage} = \frac{\hat{Q}_{storage}}{6F} \quad . \tag{5-4}$$

Explanation 1: Unreacted methanol

If only methanol within the pores of the anode diffusion layer, the anode catalyst layer and the PEM is responsible for the observed sustaining times, the mean equivalent concentration of methanol within this total pore volume in the moment of the switch from methanol water solution to pure water at the DMFC anode inlet can be calculated. The total pore volume can be estimated as

$$V^{AD+AC+M} = A^S\left(\varepsilon^{AD} d^{AD} + \varepsilon^{AC} d^{AC} + \varepsilon^{M} d^{M}\right) \tag{5-5}$$

$$= A^S\left(0.71 \cdot 170\,\mu\text{m} + 0.81 \cdot 35\,\mu\text{m} + 0.4 \cdot 110\,\mu\text{m}\right) = A^S \cdot 193.05 \cdot 10^{-6}\,\text{m}$$

(nearly full hydration of the membrane material is assumed: $\varepsilon^M = 0.4$). The porosities and other parameters of the used materials can be found in the appendix, chapter 9.

The equivalent concentration can then be calculated as:

$$c_{CH_3OH}^{AD+AC+M} = \frac{\hat{N}_{CH_3OH,\,storage}\, A^S}{V^{AD+AC+M}} = \frac{\hat{N}_{CH_3OH,\,storage}}{193.05 \cdot 10^{-6}\,\mathrm{m}} \quad . \tag{5-6}$$

The values resulting from these calculations are given in Table 5-1 (p.81). One can see that the resulting equivalent methanol concentrations within the pores are about one fifth of the methanol feed concentrations, so this type of storage is a possible explanation for the observed sustaining times.

Explanation 2: Reaction intermediates adsorbed to anode catalyst

The second mentioned explanation for the sustaining times is that on the surface of the anode catalyst long-living reaction intermediates like carbon monoxide (CO) exist (see chapter 1.2) which are fully oxidised when there is no more supply of fresh methanol. Assuming that only adsorbed CO would be present on the platinum sites and no other species were contributing to the storage function, an equivalent CO coverage of the available platium sites can be calculated. In the literature ([89]) for the applied anode catalyst (Johnson-Matthey HiSPEC 6000) a CO stripping charge density with respect to the BET surface of $\hat{Q}_{CO}$ =160 µC/cm$^2_{\mathrm{BET}}$ was measured after operation in a methanol fuel cell. The relative BET surface was found to be $A_{rel,BET}$ = 67 m$^2_{\mathrm{BET}}$/(g catalyst). Therefore, the total available CO stripping charge per square area in the here discussed case can be calculated from the catalyst loading $w_{a,cat}$ = 5 mg/cm² , the BET surface $A_{rel,BET}$ [(m$^2_{\mathrm{BET}}$) (g catalyst)$^{-1}$] and the stripping charge density:

$$\hat{Q}_{CO,\,total} = \hat{Q}_{CO}\, A_{rel,\,BET}\, w_{a,\,cat} \tag{5-7}$$

$$= 1.6\,\frac{\mathrm{C}}{\mathrm{m}^2_{\mathrm{BET}}} \cdot 67\,\frac{\mathrm{m}^2_{\mathrm{BET}}}{\mathrm{g\,cat}} \cdot 5\,\frac{10^{-3}\,\mathrm{g\,cat}}{\mathrm{cm}^2} = 0.536\,\frac{\mathrm{C}}{\mathrm{cm}^2} = 5360\,\frac{\mathrm{C}}{\mathrm{m}^2} \quad .$$

Now this value can be compared to the total storage charge density determined from the dynamic experiments by calculating their ratio (which could be interpreted as an equivalent CO coverage):

$$\theta_{CO,\,eq} = \frac{\hat{Q}_{storage}}{\hat{Q}_{CO,\,total}} \quad . \tag{5-8}$$

The values are also given in Table 5-1. As can be seen they are well above unity, so adsorbed CO can not be the only reason for the sustaining behaviour

Conclusions

The presented reasoning is only checking possible explanations for the observed experimental behaviour of the DMFC for plausibility. Obviously both storages, unreacted methanol as well as adsorbed intermediates like CO, are necessary to explain the experimental results. It has

also to be mentioned, that also other storages might play a role here, like e.g. water adsorbed on the ruthenium catalyst (as Ru-OH) and on platinum sites which are not accessible for methanol adsorption (e.g. due to morphology or cristalline state). As the active ruthenium area can be assumed to be in the same order of magnitude as the platinum area in the used catalyst (atomic ratio Pt:Ru = 1:1), an amount of charge similar to that due to CO adsorption could be stored in this form, depending on the overall reaction mechanism. Another storage which is present is the electrochemical double layer. But its charge and discharge happens much faster (within a few seconds or even milliseconds) than the observed slow dynamics in the range of some ten seconds.

Table 5-1 *Calculation of anode educt storage capacities from methanol feed concentration step-down experiments*

cell current density i_{cell}	56 mA/cm²	124 mA/cm²	56 mA/cm²
methanol feed concentration $c_{CH_3OH}^{AF}$	1 mol/dm³	1 mol/dm³	1.5 mol/dm³
sustaining time $t_{sustain}$	45 s	18 s	49 s
storage charge density $\hat{Q}_{storage}$	2.52 C/cm²	2.23 C/cm²	2.74 C/cm²
methanol density $\hat{N}_{CH_3OH,\,storage}$	$4.4 \cdot 10^{-6}$ mol/cm²	$3.9 \cdot 10^{-6}$ mol/cm²	$4.7 \cdot 10^{-6}$ mol/cm²
equivalent methanol pore concentration $c_{CH_3OH}^{AD+AC+M}$	0.224 mol/dm³	0.199 mol/dm³	0.240 mol/dm³
equivalent CO coverage $\theta_{CO,eq}$	4.70	4.16	5.11

The possible implication of this storage phenomenon on future DMFC operation can be seen from the absolute numbers of the relative overshooting. For a 1 mol/dm^3 methanol feed concentration the maximum cell voltage increase is 4-5% with respect to the steady-state value, for 1.5 mol/dm^3 nearly 10% are reached. Even when this phenomenon was just discovered, the idea was born to check whether it is possible to sustain the maximum overshooting cell voltage by a pulsed methanol feeding, i.e. by regularly changing the feed between pure water and methanol solution or by pulsed injection of appropriate amounts of pure methanol into a pure water feed stream at the cell inlet. The obtained results from SUNDMACHER et al. [16] presented in Figure 5-5 indicate that it is in fact possible to achieve a sustained increase in the cell voltage by such a periodic operation, at least for low current densities.

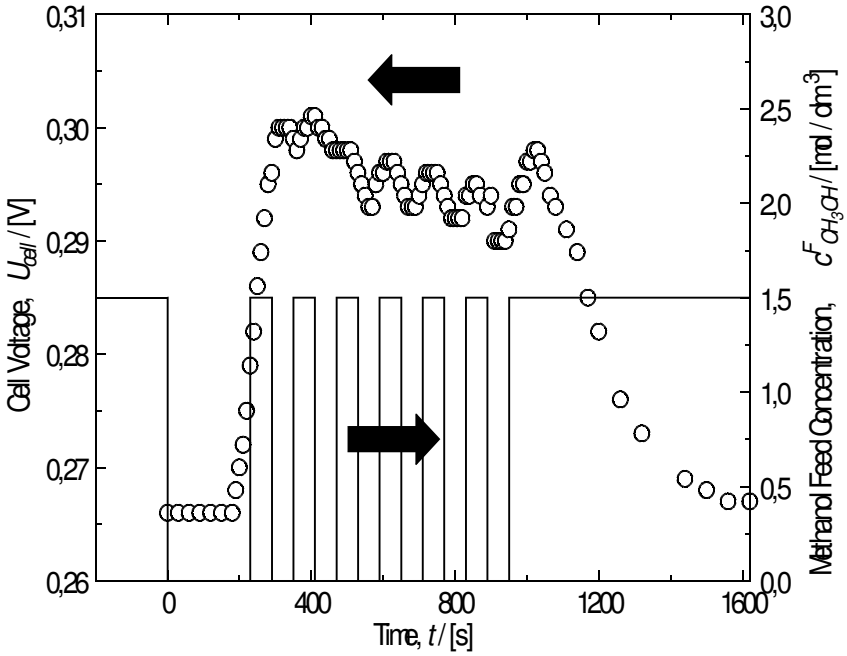

Figure 5-5 *Pulsed periodic feed operation, experimental data from* SUNDMACHER *et al. [16]*

5.2 Cell Current Step-Changes

A very typical dynamic change during practical operation of any type of fuel cell is the change in the electric load demand, simply the change in the cell current determined by the electrical load (switching the load on and off, changing from low power to high power mode like e.g. during acceleration of a car etc.). First results in this context have been published by ARGYROPOULOS et al. [92][93].

Experiments: Current steps between different operating regimes

A set of experiments was performed in which the cell current was changed stepwise from zero up to several higher values and back to zero, as illustrated schematically in the current voltage curves in Figure 5-6.

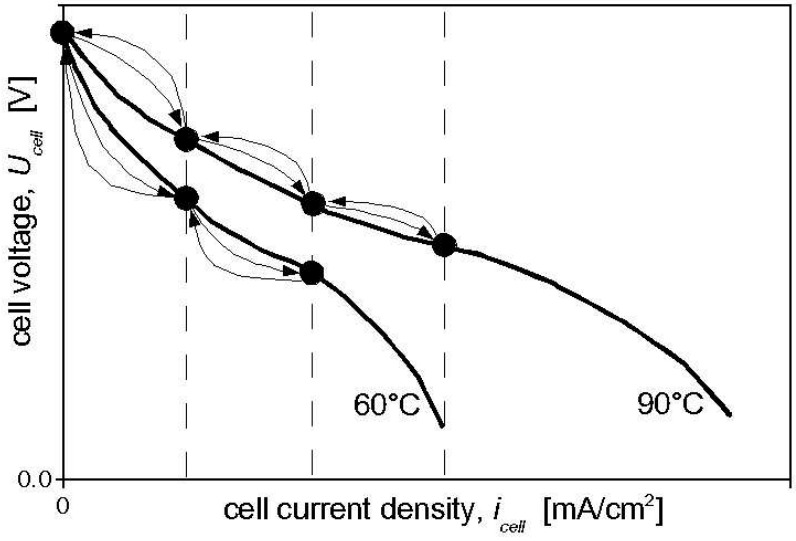

Figure 5-6 *Illustration of moderate current step experiments*

The currents were each maintained for five minutes. The standard operating conditions were the same as in the previous chapter. Experiments were carried out at cell temperatures of 60°C and 90°C. Each experiment was carried out at least twice in a sequential manner. It has to be noted that in most cases the potentiostat produces a sharp oscillation in the first two seconds after the cell is switched from open circuit to galvanostatic mode (see ellipse in Figure 5-7). This is therefore not a result of the DMFC operation.

The results for a cell temperature of 60°C are shown in Figure 5-7 (three identical sequential runs). The experimental results for 90°C are shown in Figure 5-8 (only first run plotted for better perceptibility, as the second run produced nearly identical results).

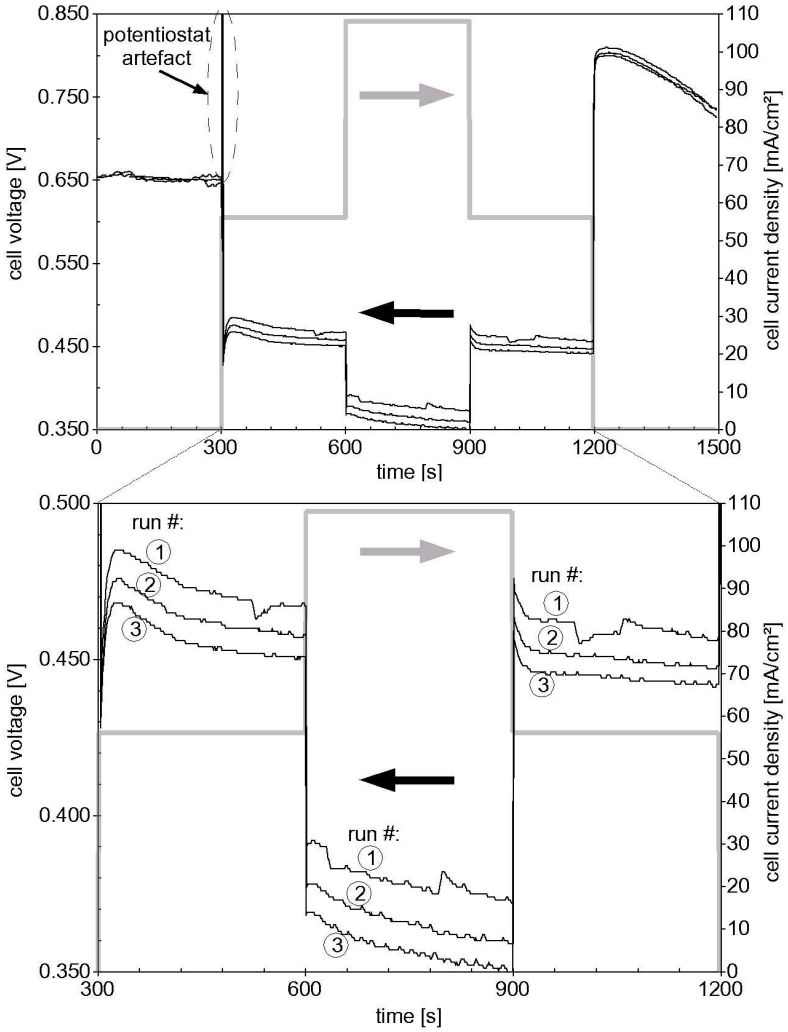

Figure 5-7 *Current-step experiments at 60°C: Three sequential runs, black (left axis) = cell voltages, grey (right axis) = cell current density.*

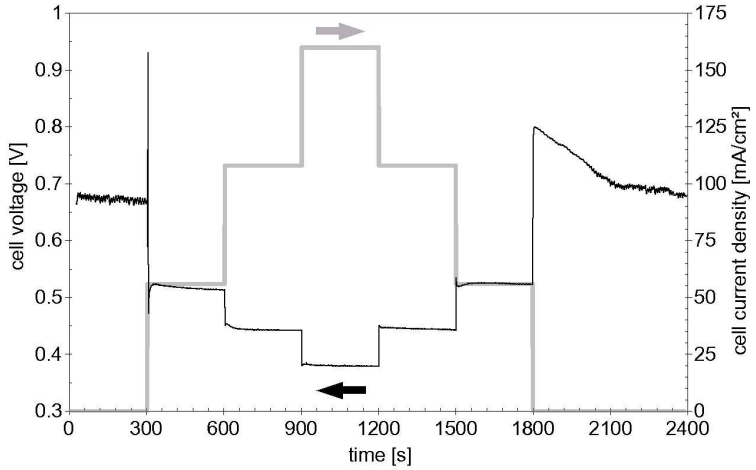

Figure 5-8 *Current-step experiment at 90°C, black (left axis) = cell voltage, grey (right axis) = current density*

In the following figures, the individual step responses at 90°C are magnified to show the differences in the cell voltage transients. The order is according to time, in the sequence given by Figure 5-8. First are the three current step-ups:

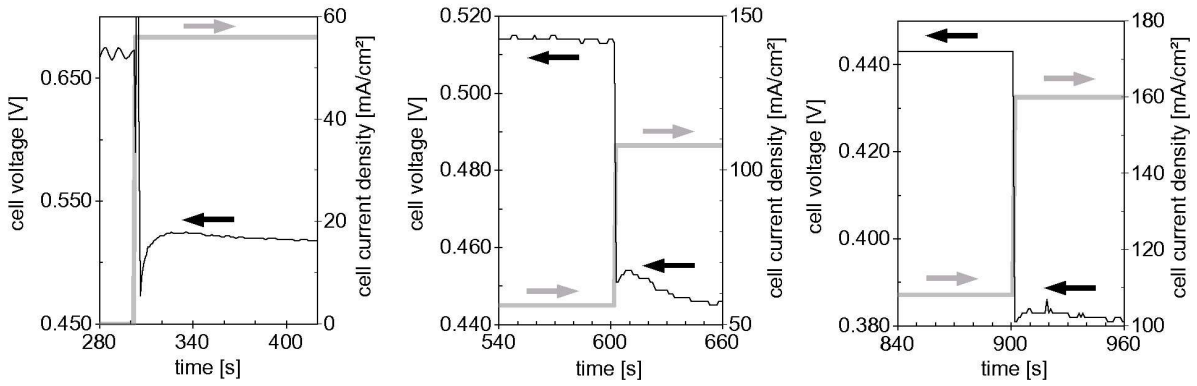

Figure 5-9 *Current step-up: Positions see Figure 5-8 from left to right, black (left axis) = cell voltage, grey (right axis) = current density*

One can clearly see that for low current densities a significant double overshooting of the cell voltage occurs, before a new steady state is reached (Figure 5-9, left). The higher the current densities, the less significant is this overshooting (Figure 5-9, middle). For high current densities, it is only a few millivolts, i.e. negligible (Figure 5-9, right). The cell reaches its new steady state within a few seconds, compared to a few minutes at low curent densities.
Next given are detailed views on the three current step-downs from Figure 5-8:

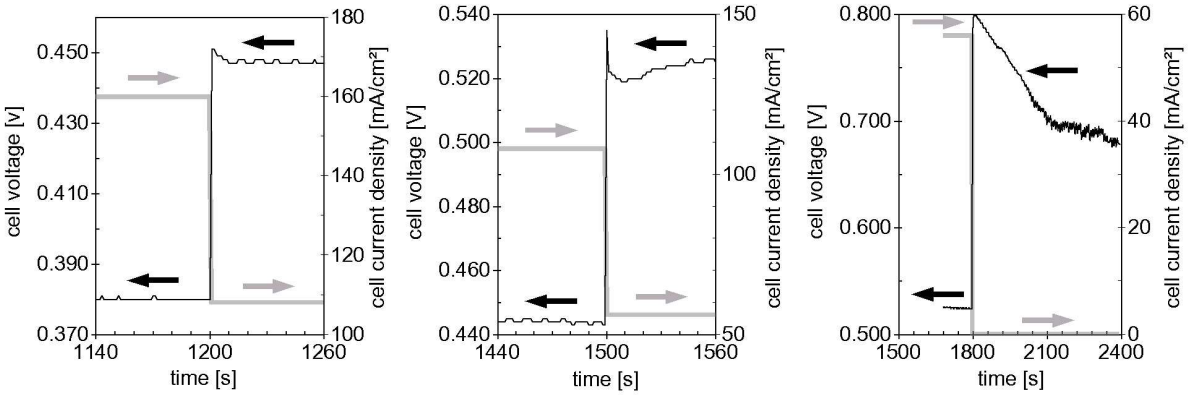

Figure 5-10 *Current step-down: Positions see Figure 5-8 from left to right, black (left axis) = cell voltage, grey (right axis) = current density*

In Figure 5-10 one can see the same tendencies as for the step-ups (Figure 5-9). The higher the current densities, the smaller the cell voltage overshoot, and the faster the system reaches a new steady state. For medium current densities (Figure 5-10, middle) the cell voltage even shows a double overshooting: A first very sharp positive one, followed by a much slower negative, until finally a new steady state is reached.

Discussion

It can be concluded, that in the low current density regime the DMFC response shows significant overshooting in the range up to 100 mV and slow relaxations in the time scale of a few minutes. In the medium current density regime the overshooting is also significant, but the maximum overshoots are in the range of only 10-20 mV and the time necessary to reach a new steady-state is in the range of one minute. In the high current density regime, finally, the overshooting is only marginal, a new steady state is reached within seconds. Except for the case of a step down to zero current, the cell voltage always exhibits a double oscillation: Immediately after switching the current, the cell voltage jumps in the direction of the new steady state, overshoots, oscillates back much smaller passing again the final steady state value and then shows a comparably slow relaxation into the final new steady state.

This behaviour can be explained by three phenomena which are assumed to take place in the DMFC (see schematig in Figure 5-11). The immediate response (Figure 5-11, A) is due to the sum of all ohmic losses within the DMFC (charge transport resistances and charge transfer resistances of the electrochemical reactions). The counterwise movement of the cell voltage following the cell voltage jump (Figure 5-11, B) might be due to the formation of a new methanol concentration gradient within the anode diffusion layer and the membrane, therefore here mass transport can be assumed to be governing the dynamic behaviour. The last (slowest) region in the dynamic responses (Figure 5-11, C) can finally be explained by adsorption phenomena on the anode catalyst.

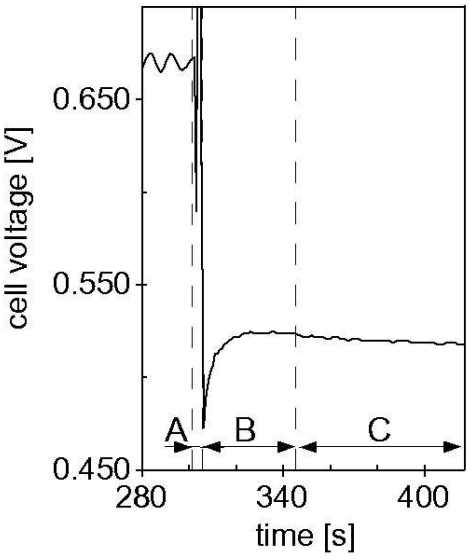

Figure 5-11 *Illustration of three regions of dynamic response of the DMFC to moderate cell current steps*

Experiments: Current steps between open circuit and maximum cell current densities

Finally similar experiments were performed, but in this case the cell current was switched from zero (open circuit) to a very high value close to the maximum sustainable cell current under the respective standard operating conditions (Figure 5-12). After five minutes, the cell was switched back to open circuit. The results are presented in Figure 5-13. In both cases three runs were performed, which produced nearly identical results. For better presentation, only the first runs are presented.

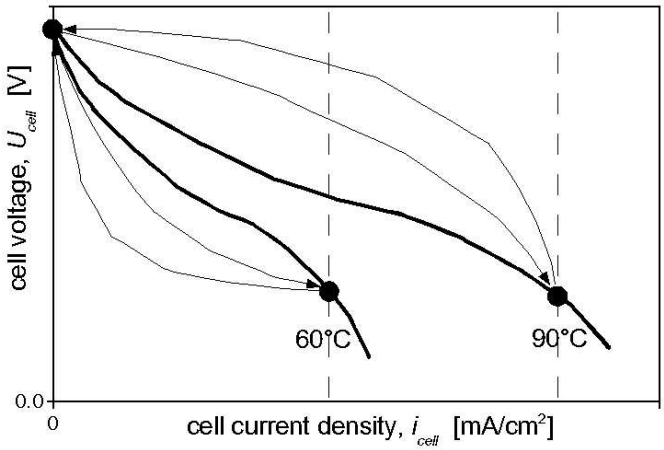

Figure 5-12 *Illustration of big current step experiments*

Except for the drastic oscillation at the current step-up at 90°C (Figure 5-13, bottom left), which is due to potenstiostat switch-on phenomena and not the DMFC (see above), the same qualitative behaviour can be observed as for the previously presented experiments. When the current is switched on, the cell voltage drops down within one to two seconds, but then rises again slightly before finally declining to the new steady state value in the form of an exponential decay. This is therefore a very slow single overshoot oscillation, which can be observed at low as well as high current steps (compare with Figure 5-9 and Figure 5-10).

Switching the cell back to open circuit, a similar long term behaviour is visible as in Figure 5-7 and Figure 5-8. The cell voltage rises fast to roughly 800 mV, shows a slight overshoot (double at 60°C, single at 90°C) and then decreases nearly linearly towards values below 700 mV. Another difference between 60°C and 90°C is that at 60°C the cell voltage curve has a negative curvature after the switch to open circuit, while at 90°C the curvature is positive. This difference in the curvature seems to be characteristic for the different temperatures, as it occurs independent of the value of the current density before the cell is switched back to open circuit. It is also obvious that at higher cell temperatures the cell reaches its open circuit voltage faster than at lower temperatures, but in any case this process takes between 10 minutes (at 90°C) up to 30 minutes (at 30°C, not shown here). Also approaching the open circuit steady state, the cell voltage starts to show noise-like fluctuations with increasing intensity. This behaviour also supports the supposition, that the cell reactions include very slow adsorption and reaction steps.

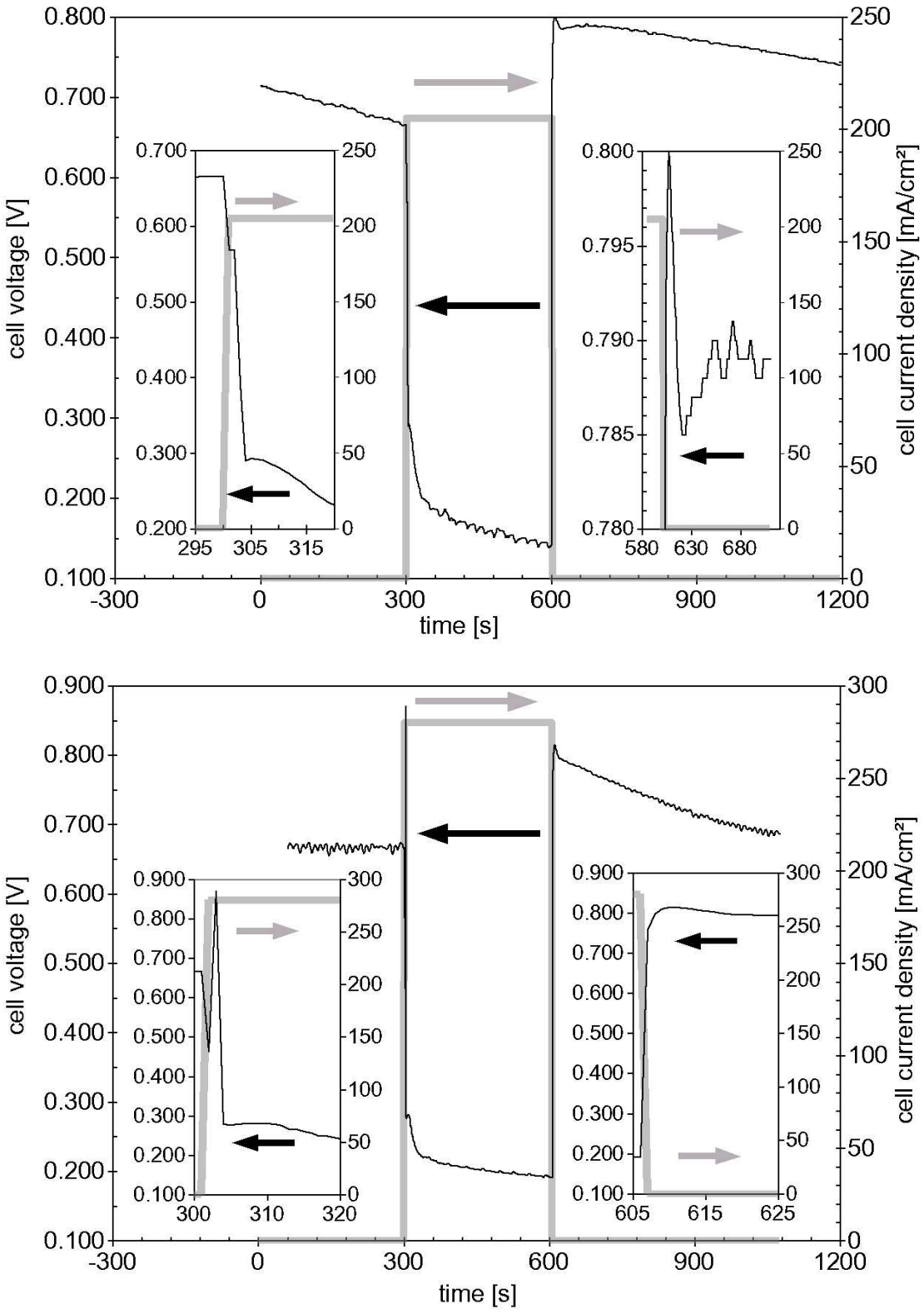

Figure 5-13 *Cell voltage transients for a current steps between open circuit and maximum current density (small plots illustrate transients), black (left axis) = cell voltage, grey (right axis) = current density, cell temperatures 60°C (top), 90°C (bottom).*

5.3 Concluding Remarks

First dynamic experiments have been carried out using the DMFC miniplant. In these experiments the DMFC response to step-changes of the methanol feed concentration and the cell current load were recorded and analysed.

It was found that switching the methanol feed concentration from a typical operating value down to zero while maintaining the cell current does not lead to an immediate decrease (breakdown) in the cell voltage. The cell voltage remains on a constant level for a certain dead time (resulting from dead volumes in the supply pipes, depending on the flow rate) followed by an intermediary increase before the inevitable final breakdown takes place. This overshooting phenomenon shows a significant dependence on the operating conditions. It can only be observed for low current densities (the lower the current density the more distinct the overshooting). Also higher cell temperatures and initial methanol feed concentrations lead to an increase of the overshooting. This phenomenon was related with carbon monoxide (as likely reaction intermediate of the methanol oxidation) adsorbed on the anode catalyst active platinum sites and unreacted methanol inside the pore space in the anode diffusion and catalyst layers as well as in the membrane. It turned out that even assuming maximum surface storage capacity of carbon monoxide does not explain the extent of the overshooting, which indicates that also unreacted methanol within the various porous layers of the DMFC plays a major role here. Possibly, also other adsorbed species on the anode catalyst exist, like e.g. unreacted but adsorbed methanol (on platinum sites), water (adsorbed on ruthenium sites) or other possible intermediates of the electrochemical methanol oxidation (see also chapter 1.2).

In a second set of experiments the electrical cell current was changed stepwise. A step change of the current leads to an immediate ohmic response of the cell voltage, followed by a single or double overshooting, which ends up with a slow relaxation period of up to a few minutes till a new steady-state is reached. The higher the final current the less distinct is this phenomenon. Obviously also here certain storages play a role, e.g. in the electrochemical double layer and due to adsorbed reactants. The slow approach to a new steady-state is a hint on slow overall reaction kinetics.

Concluding, the DMFC shows a very interesting dynamic response to step changes in the main operating parameters methanol feed concentration and cell current. Also the cell temperature plays a major role, as the observed overshoots are higher and faster for higher cell temperatures.

6 Model Formulation and Simulations

The necessity to formulate adequate mathematical models is based on (a) the need to reach a deeper understanding of internal processes (reactions, mass transport) which can not be observed directly in experiments, (b) the possibility to apply mathematical optimisation methods to obtain hints as to where further technical improvements may be required or beneficial, and (c) for the development of optimal control and operating strategies.

The foundation of the model formulation to be presented is the so-called potential flux vector concept introduced by GILLES [76] and MANGOLD et al. [77]. In this concept, the process is decomposed on several structural levels (process unit level, phase level, storage level) into finally only two types of elementary units: components and coupling elements. Components possess an accumulation capacity for physical quantities (e.g. energy, mass, momentum), coupling elements describe the fluxes between components. Figure 6-1 illustrates this principle. All elements are represented by boxes, where a box with a circle represents an element with storage function (denoted as components). The direction of the arrows only marks the direction of information flux. It does not imply the direction of the physical fluxes.

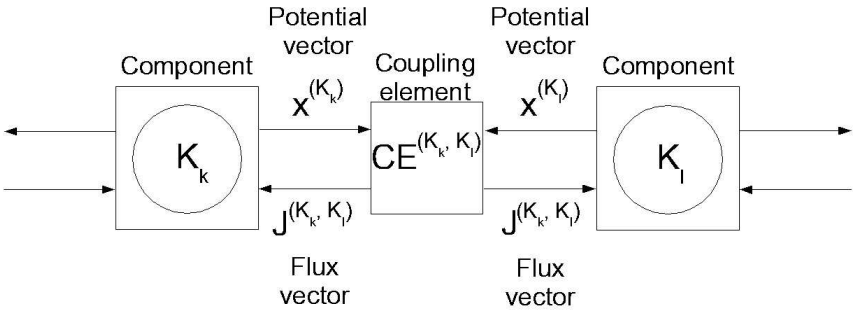

Figure 6-1 *Illustration of potential flux vector concept, adapted from [76]*

Of course, the number of coupling elements connected to one storage element is not limited, but was restricted to two in Figure 6-1 for better illustration. Also a coupling element can couple an unrestricted number of storage elements. For a very detailed and practical introduction to this network theoretic modeling concept the reader is referred to [77].

The presented model was implemented in and simulations were carried out using MatLab 6.1.0.450. The applied ODE-solver was ode15s.

6.1 General Model Structure

In the following, a model of a single cell DMFC will be presented. This model represents the cross-sectional structure of the DMFC, which is depicted in Figure 6-2. The model is one-dimensional, perpendicular to the cross-sectional area of the cell. All state variables are assumed to be constant in the other two space coordinates.

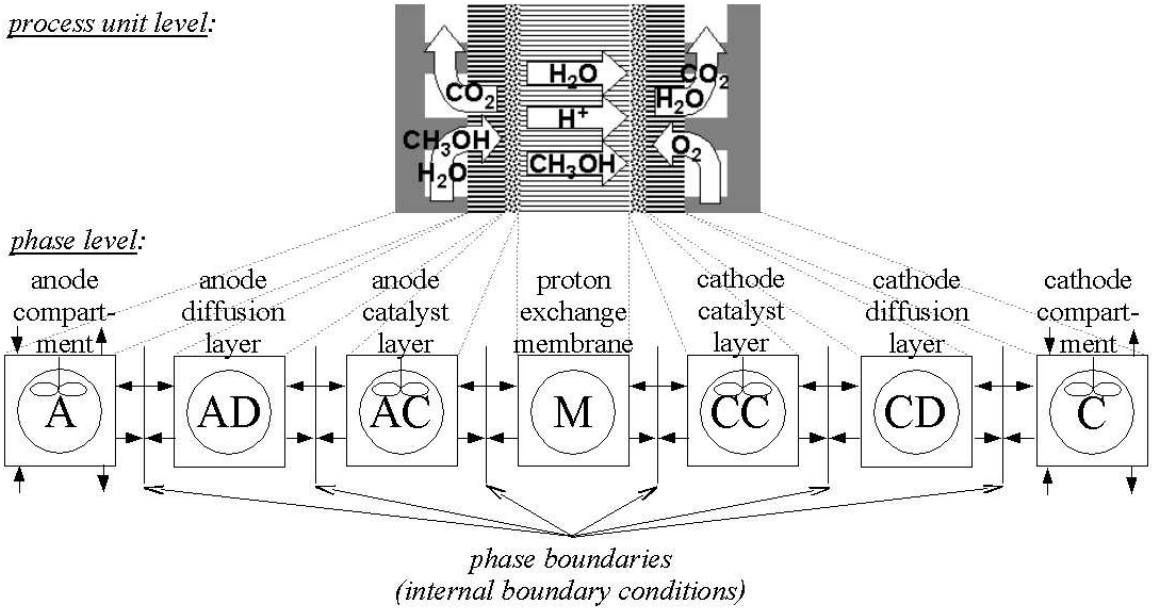

Figure 6-2 *One-dimensional decomposition of DMFC*

In the following chapters all model elements are described, both from the structural point of view as well as with all used equations, assumptions and parameters.

As can be seen in Figure 6-2, on this level of decomposition the cell consists of seven sequentially connected phases: anode and cathode compartments, both diffusion and catalyst layers and the PEM in the middle.

6.2 Basic Model Assumptions

The basic model assumptions, which apply to all elements, are:

- all gas phases obey the ideal gas law,
- all inert gases (components of air, like nitrogen, argon etc.) are merged to “nitrogen”,
- in liquid phases nonideal mixing behaviour is not accounted for, variations of activity coefficients are neglected due to the strong dilution of methanol in water,

- on the cathode side all species are assumed to be in the gas phase, condensation of water is not accounted for,
- the anode compartment (A) is isothermal (uniform temperature),
- the charge balances are quasi-stationary,
- electroneutrality is assumed in the polymer electrolyte membrane,
- and finally, ohmic losses other than in the PEM membrane are neglected.

These assumptions are justified over a wide range of operating conditions. The anode flowbed of the DMFC is nothing else than a heat exchanger, where a pre-heated liquid is pumped through a number of parallel channels. As in the here applied experimental setup the liquid flow rate is quite high (mean residence times in the anode compartment of less than one second), the temperature at the cell outlet is maximum one Kelvin lower than at the inlet. Therefore, a uniform temperature can be assumed at least in the anode compartment. But as the adjacent elements of the fuel cell (diffusion layers, catalyst layers, membrane) are very thin (together less than 0.5 mm) and especially the diffusion layers have a very good thermal conductivity (material: graphite), a very good overall thermal conductivity of this sandwich structure can be assumed. Therefore, the highest temperature gradient can be expected at the boundary between cathode diffusion layer and cathode compartment (cathode channels). The following table (Table 6-1) proves this, giving literature values for the thermal conductivities λ_j of the fuel cell layers and calculating the respective heat transfer coefficients α_j as

$$\alpha_j = \frac{\lambda_j}{d_j} \tag{6-1}$$

with the thicknesses d_j of the respective layers. The overall heat transfer coefficient is calculated as a series of thermal conductive layers:

$$\alpha_{overall} = \frac{1}{\sum_j \frac{1}{\alpha_j}} \quad . \tag{6-2}$$

One can see from Table 6-1 that the thermal conductivities of all layers are of a much higher order of magnitude as that at the outer side of the cathode diffusion layer (heat transfer from the cathode diffusion layer to the air flowing through the cathode supply channels). The overall heat transfer coefficient of the whole DMFC is of nearly the same value, meaning that nearly the total heat transfer resistance lies at this point. Therefore, as assumed, the major temperature gradient should appear between the outer side of the cathode diffusion layer and the air in the cathode channels, the temperature differences within the DMFC should be comparably small.

Table 6-1 *Estimation of heat transfer coefficients of DMFC layers*
(: For calculation see appendix chapter 9.6)*

	parameter		
DMFC layers	thickness *d* [µm]	thermal conductivity λ [W/(m K)]	heat transfer coefficient α [W/(m^2 K)]
A	-	-	2000 (water to wall)*
AD	190	1.7 (source: Toray Ind. Inc.)	8947
AC	35	1.7 (assumed equal to AD)	48571
M	100	0.43 (source: [64])	4300
CC	35	1.7 (assumed equal to CD)	48571
CD	190	1.7 (source: Toray Ind. Inc.)	8947
C	1700	0.03 (typical for a gas)	52*

To assume ideal gas behaviour seems justified, as the maximum system pressures do not exceed 5 bara ($5 \cdot 10^5$ Pa) and the temperature range does not exceed 10..120°C (283..393 K). Also all components (methanol, water, oxygen, carbon dioxide and nitrogen) have a low molecular weight.

The assumption of the nonexistence of liquid water on the cathode side is the major simplification on this level, as it is often observable that liquid water forms in the cathode compartment. The question whether liquid water can exist within the (strongly hydrophobic) cathode diffusion layer has to be discussed on a thermodynamic basis, but as a starting point this is neglected.

The final assumption that no ohmic drops are accounted for other than that in the PEM is based on the fact that all electron conducting parts of the DMFC (bipolar plates, diffusion layers, catalyst layers) are made from very good electron conducting materials (graphite, noble metals), and that especially the diffusion and catalyst layers are very thin, while having a large contact area.

6.3 Mass Transport and Balancing

For the description of mass transport the generalised Maxwell-Stefan approach is used. It is based on a mechanical equilibrium between driving forces acting on a species *j* and the friction between this species and all other species *i* around it.

For mass transport in porous structures, KRISHNA and WESSELINGH [94][95] formulated the following form of the generalised Maxwell-Stefan equations:

$$-\frac{c_j}{RT}\nabla_{T,p}\mu_j-\frac{c_j}{RT}\overline{V}_j\nabla p-\frac{\alpha_j'}{\mathcal{D}_{jM}}c_j\frac{B_0}{\eta^{vis}}\nabla p-c_j z_j^*\frac{F}{RT}\nabla\phi = \sum_{i\neq j}\frac{x_i n_j-x_j n_i}{\mathcal{D}_{ij}^{eff}}+\frac{n_j}{\mathcal{D}_{jM}^{eff}} \tag{6-3}$$

On the left hand side of eq.(6-3) are four terms describing the driving forces. Term one and two describe diffusive transport resulting from gradients in the chemical potentials μ_j (first term: at constant pressure, second term: pressure influence), term three is viscous flow due to a gradient in the total pressure p and the fourth term represents transport of charged species due to a gradient of the electric potential field ϕ (migration). On the right hand side are two terms describing friction: The sum accounts for the friction between species j and all other mobile species i (x_i are mole fractions, n_i are flux densities in [mol m^{-2} s^{-1}]), and the second term represents friction between species j and the (stationary) solid matrix (index "*M*").

The most important parameters in this equation are the binary Maxwell-Stefan diffusion coefficients $\mathcal{D}$. The lower indices denote the two respective species, an upper index "*eff*" means that this is an effective diffusion coefficient taking into account the porosity ε and the tortuosity τ of the solid matrix, while those without this index are valid for free space binary interactions. For a more detailed treatment of the diffusion coefficients refer to the appendix (chapter 9.1.8). The other parameters of the presented form of the generalised Maxwell-Stefan equations are explained in the respective sections and in the list of symbols.

As shown before, the modeling concept is based upon a finite volume discretisation along only one spatial coordinate *z*. For finite volume element simulations it is well known, that the simultaneous treatment of diffusive fluxes and convective flow can lead to numerical problems if the viscous flow contribution in relation to the overall mass transport is high. To prevent such problems, the viscous flow term (term three on the left hand side) of eq.(6-3) is skipped and the Maxwell-Stefan equation is formulated only for the individual driving forces acting on the species *j* (diffusion and migration):

$$-\frac{c_j}{RT}\left(\frac{\partial\mu_j}{\partial z}\right)_{T,p}-\frac{c_j}{RT}\overline{V}_j\frac{\partial p}{\partial z}-c_j z_j\frac{F}{RT}\frac{\partial\phi}{\partial z}=\sum_{i\neq j}\frac{x_i j_j-x_j j_i}{\mathcal{D}_{ij}^{eff}}+\frac{j_j}{\mathcal{D}_{jM}^{eff}} \tag{6-4}$$

In eq.(6-4) in the friction terms on the right hand side not the overall flux densities n_j appear but only the individual flux densities j_j.

The overall flux densities are then calculated from the individual flux densities and an additive term for the pressure-driven convective contribution:

$$n_j = j_j + \tilde{c}_j v_p \quad . \tag{6-5}$$

Here not the classical concentration c [mol m^{-3}] (with respect to the volume of mobile species) but a modified concentration $\tilde{c}$ [mol m^{-3}] (with respect to the total volume including the porous matrix) denoted by the tilde is used. v_p is the convective velocity [m s^{-1}], which is a function of the total pressure gradient according to Darcy' s law:

$$v_p = -\frac{B_0}{\eta^{vis}} \frac{\partial p}{\partial z} \quad . \tag{6-6}$$

The parameters are the dynamic viscosity η^{vis} [Pa s] of the mixture and the permeability coefficient B_0 [m^2]. The latter has to be determined experimentally, but for some simple geometries correlations are known. The simplest case is the flow through parallel straight tubular pores (Poiseuille flow):

$$B_0 = \frac{d_{pore}^2}{32} \quad . \tag{6-7}$$

In the following, this (simplifying) approach will be used. It can be shown that the combination of eq.(6-4) with the eqs.(6-5) and (6-6) is equivalent to eq.(6-3).

Using the overall flux densities, the general form of the component mass balances is

$$\frac{\partial c_j}{\partial t} = -\frac{\partial n_j}{\partial z} + \sum_k (r_k \cdot \nu_{j,k}) \tag{6-8}$$

with the reaction rates r_k of all occuring (electro-) chemical reactions [mol m^{-3} s^{-1}] and the stoichiometric coefficients $\nu_{i,k}$ of component i in reaction k.

Finally a total mass balance is formulated based on the continuity equation:

$$\frac{\partial \rho}{\partial t} = -\frac{\partial}{\partial z}(\rho v) \tag{6-9}$$

where ρ [kg m^{-3}] is the fluid mixture density and v [m s^{-1}] is the mean (superficial) mixture velocity (=convective velocity). For compressible fluids the relation between pressure and density at constant entropy (which is the case for moderate pressures as typical for DMFC operation) is given by

$$\left(\frac{\partial p}{\partial \rho}\right)_S = v_{sound}^2 \tag{6-10}$$

where v_{sound} [m s^{-1}] is the speed of sound in the fluid (see appendix chapter 9.1.9) and p [Pa] is the local pressure.

Finally, the product of mean mixture density and mean velocity is the total mass flux density m_{tot} [kg m^{-2} s^{-1}]:

$$m_{tot} = \rho\, v \tag{6-11}$$

Combining eqs.(6-9), (6-10) and (6-11) one can formulate the total mass balance in terms of the pressure as variable, and its time derivative as function of the total mass flux density:

$$\frac{\partial\, p}{\partial\, t} = -\, v_{sound}^{2} \frac{\partial\, m_{tot}}{\partial\, z} \quad , \tag{6-12}$$

The total mass flux density is the sum of the component mass flux densities, which in turn are the products of the molar flux densities and the molecular weights $\overline{M}_j$ [kg mol^{-1}]:

$$m_{tot} = \sum_j n_j \overline{M}_j \quad . \tag{6-13}$$

6.4 Energy Transport and Balancing

Within the DMFC, not only a variety of different mass transport phenomena occur simultaneously, but also energy transport and production. As the DMFC consists of porous layers in which mobile species are transported, energy transport can take place both due to transport bound to the moving species and due to thermal conduction. The latter takes place in the mobile phase as well as in the stationary solid matrices in the different layers. Additionally, chemical and electrochemical reactions take place in the catalyst layers (AC) and (CC), and finally within the membrane (M) a spatially distributed heat production occurs, due to the transport of charged species in an electric field within a conductor phase with an Ohmic resistance (Joule heating).

To get a most simple model description of all these phenomena, it makes sense to formulate two independent energy flux densities: Enthalpy flux densities e [J m^{-2} s^{-1}]

$$e = \sum_j e_j = \sum_j n_j\, h_j(T) \quad , \tag{6-14}$$

which are coupled to the flux densities n_j [mol m^{-2} s^{-1}] of the mobile species and their specific enthalpies h_j [J mol^{-1}], and heat flux densities q [J m^{-2} s^{-1}] due to thermal conduction (Fourier law)

$$q = -\,\lambda^{eff} \frac{\partial\, T}{\partial\, z} \quad . \tag{6-15}$$

In eq.(6-15) λ^{eff} [W m^{-1} K^{-1}] stands for the local effective thermal conductivity coefficient.

The specific enthalpies h_j of the mobile species are calculated from the specific enthalpies of formation, $\Delta_F H_j$ (data taken from [102b]), and the mean heat capacities $\overline{C}_{p,j}$ (values derived in the appendix, chapters 9.1.2 and 9.4):

$$h_j = \Delta_F H_j^\theta + \int_{T^\theta}^{T} \overline{C}_{p,j}(T)\,dT \approx \Delta_F H_j^\theta + (T - T^\theta)\cdot \overline{C}_{p,j} \qquad (6\text{-}16)$$

The upper index "*eff*" at the thermal conductivity coefficient λ denotes that it is dealt with a mixture of a fluid and a solid phase, which both contribute to the thermal conduction. The effective thermal conductivity has to be calculated from the thermal conductivities of both phases (appendix, chapter 9.1.3) taking into account their volume fractions. These calculations can be found in the appendix (chapter 9.3) for all DMFC layers.

By using enthalpy fluxes, all heats of reactions are accounted for automatically without the need of a heat production term in the energy balances of the respective DMFC layers (i.e. the catalyst layers).

Finally, Joule heating e_{Joule} [W m^{-3}] due to charge transport is described by the general equation

$$e_{Joule} = i\frac{\partial \phi}{\partial z} \quad . \qquad (6\text{-}17)$$

Heating due to transport of uncharged species is neglected here. Joule heating is always positive and independent of the direction of the charge flux.

Combining all three energy flux densities yields the general energy balance

$$\frac{\partial T}{\partial t} = \frac{1}{\widetilde{(\rho C_p)}}\left[-\frac{\partial e}{\partial z} - \frac{\partial q}{\partial z} + e_{Joule}\right] \quad , \qquad (6\text{-}18)$$

where $\widetilde{(\rho C_p)}$ [J m^{-3} K^{-1}] is the local mean volumetric heat capacity of the combination of the fluid phase and the solid phase (assuming same temperature of both phases).

6.5 Charge Transport and Balancing

Charge transport in the DMFC is bound to protons within the membrane material (proton conductor) and electrons in the electrical circuit (electron conductor). Therefore, the charge flux density i [A m^{-2}] within the proton conductor is coupled to the molar flux density of protons by Faradays law (z^* = number of single charges exchanged per molecule):

$$i = z^*_{H^+} F\, n_{H^+} = F\, n_{H^+} \quad . \qquad (6\text{-}19)$$

Charge production/consumption due to electrochemical reactions is similarly linked to the reaction rates with respect to the pore volume, r_k [mol m^{-3} s^{-1}], of the respective electrochemical reactions (as function of the respective overpotential η [V]):

$$i_k(\eta) = z_{H^+} F \nu_{H^+,k} r_k(\eta) \frac{V^{pores}}{A^S} \quad . \tag{6-20}$$

In both, the membrane and the catalyst layers, charge balances have to be formulated accounting for the outer electrical cell current (due to electron flux) i_{cell} [A m^{-2}] as well as for the above mentioned current densities resulting from proton flux in the membrane and the charge production in both catalyst layers. The general form of the charge balances is

$$\frac{\partial \widetilde{Q}}{\partial t} = -\frac{\partial i}{\partial z} + \Gamma(\eta) \tag{6-21}$$

where $\widetilde{Q}$ is the volumetric charge density [C m^{-3}] and Γ is the volumetric charge production [C m^{-3} s^{-1}] by electrochemical reactions:

$$\Gamma(\eta) = \sum_k i_k(\eta) \quad . \tag{6-22}$$

Simplifyingly it is assumed that the charge balances are fast compared to all other balances (material and energy) which leads to quasi-stationary formulations.

In the membrane no charge production occurs, therefore one ends up with the following quasi-stationary charge balance:

$$0 = -\frac{\partial i^M}{\partial z} \quad . \tag{6-23}$$

In the catalyst layers, when balancing the electrons, only the charge flux to or from the adjacent diffusion layer (electron conductor) occurs, which is the cell current density i_{cell}. Within the catalyst layers electrons are produced or consumed by the electrochemical reactions as described above. Therefore, the final quasi-stationary charge balances have the form:

$$0 = i_{cell} - \sum_k i_k(\eta) \quad . \tag{6-24}$$

6.6 Definition of Overpotentials

For the formulation of rate equations for the electrochemical electrode reactions, one needs a definition for the electrode overpotentials, which in this case is given by:

$$\eta = \Delta\phi - \Delta\phi^{\theta}_{i=0} \tag{6-25}$$

The overpotentials η [V] are defined as the difference between the real electrode potential $\Delta\Phi$ [V] (w.r.t. standard hydrogen electrode) and that at open circuit condition (i.e. no cell current, i = 0) and thermodynamic standard conditions (pressure 10^5 Pa, temperature 298 K, all reactants activities equal one, upper index θ). For the DMFC the following values can be found in the literature:

Anodic methanol oxidation: $\Delta\phi^{\theta}_{a,\,i=0} = 0.02$ V (6-26)

Cathodic oxygen reduction: $\Delta\phi^{\theta}_{c,\,i=0} = 1.23$ V (6-27)

Then the cell voltage can be calculated from the reversible open circuit cell voltage at the above mentioned standard conditions ($U^{\theta}_{cell,\,i=0} \approx 1.21$ V, exact calculation presented in chapter 2), the anode and cathode overpotentials, η_a and η_c [V], respectively, and the Ohmic losses within the membrane represented by the total difference in the polymer phase electrical potentials $\Delta\phi^M$ [V]:

$$U_{cell} = U^{\theta}_{cell,\,i=0} - \eta_a + \eta_c + \Delta\phi^M \quad . \tag{6-28}$$

6.7 Model Block 1: Anode Compartment (A) and Diffusion Layer (AD)

The anode compartment (A) represents the anode flowbed structure, which supplies the reactants to the anode diffusion layer (AD) and takes up the produced carbon dioxide. The anode diffusion layer connects the flowbed structure to the catalyst layer (AC).

6.7.1 Anode Compartment (A)

The anode compartment has one inlet (feed, index AF) and one outlet, and it is connected to the anode diffusion layer (AD). In the network theoretical modeling concept it is a component at the phase level, as illustrated schematically in Figure 6-3.

Fresh water methanol solution is fed at the inlet (feed, lower inlet in Figure 6-3), with a very low carbon dioxide content. Methanol and water are transported through the anode diffusion layer towards the anode catalyst, while produced carbon dioxide is transported in the opposite direction to leave the diffusion layer into (A), and on this way being removed through the anode outlet (upper side of element).

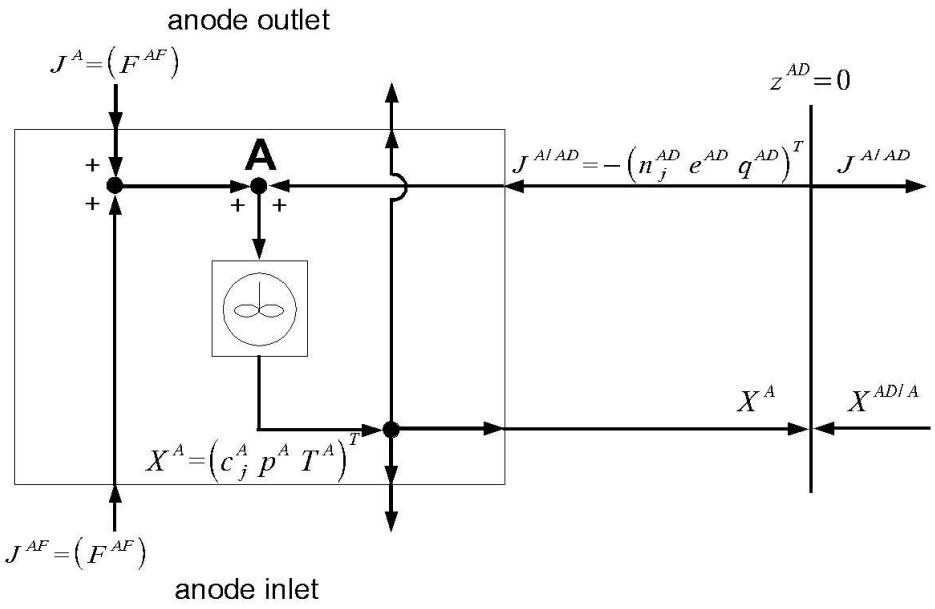

Figure 6-3 *Decomposition of anode compartment (A) on the level of storages (j = CH_3OH, H_2O, CO_2)*

The anode compartment is assumed to be a spatially concentrated phase element (ideally mixed phase, represented by the stirrer symbol inside the storage in Figure 6-3). The material balances are then given by:

$$\frac{dc_j^A}{dt}=\frac{1}{V^A}\left(F^{AF}\,c_j^{AF}-F^A\,c_j^A+A^S\,n_j^{AD}(z^{AD}=0)\right)\approx\frac{1}{V^A}\left(F^{AF}(c_j^{AF}-c_j^A)+A^S\,n_j^{AD}(z^{AD}=0)\right)$$

$$\text{with}\quad j=H_2O,CH_3OH,CO_2 \qquad (6\text{-}29)$$

In eq.(6-29) F^{AF} is the feed volume flow rate [$m^3\ s^{-1}$], V^A is the total volume of the channels [m^3], c_j^{AF} are the feed concentrations [mol m^{-3}] and F^A is the outlet volume flow rate [$m^3\ s^{-1}$]. The difference between the two flow rates F^{AF} and F^A can be assumed to be small, therefore it is neglected which results in the simplified formulation given in eq.(6-29).

The anode pressure p^A as well as the temperature T^A are given as input parameters which are known from the experiments. Therefore, no total mass and energy balances are formulated here.

6.7.2 Anode Diffusion Layer (AD)

The anode diffusion layer connects the anode compartment (A) and the anode catalyst layer (AC). It consists of a chemically inert carbon fibre material (in the here described case carbon paper type Toray TGP-H-060) coated with a certain amount of PTFE (23-25 wt-%). It has the function to supply educts (methanol and water) to the anode catalyst and remove the carbon

dioxide from there. It also has to collect the electrons from the anode reaction and ensure good electric contact with the bipolar plate (current collector). All fluxes are assumed to occur only perpendicular to the surface plane (i.e. in z direction). (AD) is represented by a 1-dimensional spatially distributed storage (see Figure 6-4). Data about porosity and other physical parameters are given in the appendix chapters 9.2, 9.3 and 9.4.

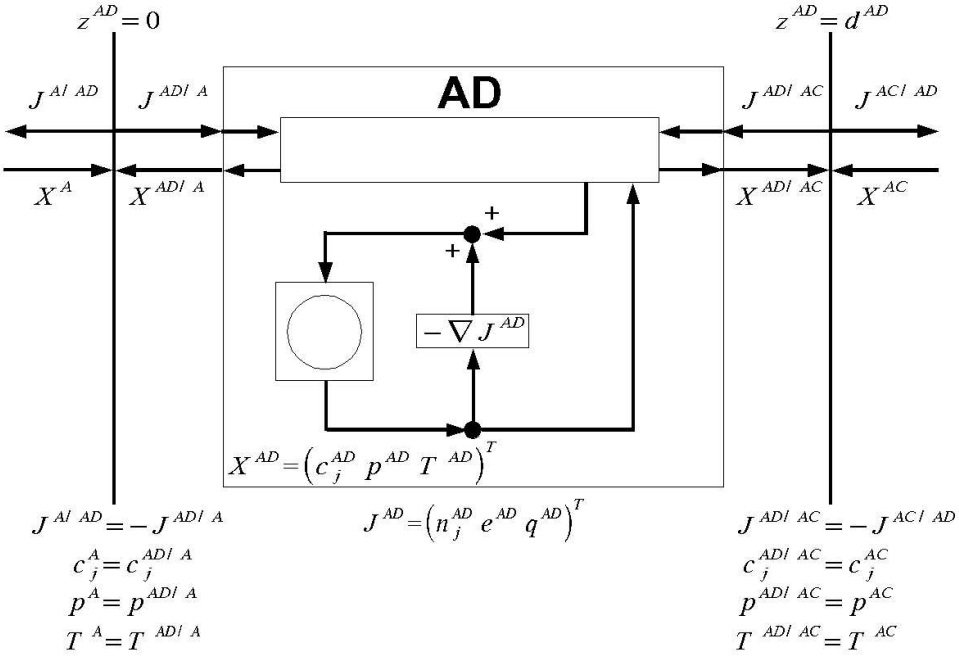

Figure 6-4 *Decomposition of anode diffusion layer (AD) on the level of storages, spatially distributed (j = CH_3OH, H_2O, CO_2)*

It is assumed that the complete pore space is filled with liquid methanol-water solution and soluted carbon dioxide. Formation of a gas phase from carbon dioxide is neglected for simplicity reasons, although carbon dioxide has a very low solubility and the surface tension between water and the PTFE-coated pore walls can be assumed to be high. In later stages it should be attempted to skip this simplification. Maybe also a model based on the assumption of complete evaporation within the pores might be of interest especially to describe high-temperature operation (above mixture boiling point, i.e. depending on pressure at roughly above 60-70°C). A final proof of the real phase state situation in the anode diffusion layer has not yet been found.

It is further assumed that also the pores in the adjacent anode catalyst layer (AC) are fully flooded with a liquid mixture of water, methanol and carbon dioxide, as it contains a noteable amount of hydrophilic polymer electrolyte material and is in direct contact with the liquid-filled membrane (M) (see following chapters).

The species accounted for are water and methanol as the reaction educts, and carbon dioxide as the reaction product of the anodic electrochemical methanol oxidation. For describing the mass transport within the diffusion layer, the generalised Maxwell-Stefan equations are applied. The finite-volume method is used to formulate this one dimensional model as a series of discrete elements.

6.7.2.1 Balances/Storage elements

For the three species water (H_2O), methanol (CH_3OH) and carbon dioxide (CO_2), the material balances using molar concentrations c_j are analogue to eq.(6-8):

$$\frac{\partial c_j^{AD}}{\partial t} = -\frac{1}{\varepsilon_{pores}^{AD}} \frac{\partial n_j^{AD}}{\partial z} \quad \text{with} \quad j = H_2O, CH_3OH, CO_2 \quad . \tag{6-30}$$

The total mass balance, analogue to eq.(6-12) , is given by

$$\frac{\partial p^{AD}}{\partial t} = -(v_{sound}^{AD})^2 \frac{\partial m_{tot}^{AD}}{\partial z} \quad . \tag{6-31}$$

Finally, the energy balance is

$$\frac{\partial T^{AD}}{\partial t} = -\frac{1}{\widetilde{(\rho c_p)}^{AD}} \left(\frac{\partial e^{AD}}{\partial z} + \frac{\partial q^{AD}}{\partial z} \right) \quad , \tag{6-32}$$

analogue to eq.(6-18), but Joule heating due to electron transport is neglected as the Ohmic resistance (and therefore the electric potential gradient) in the carbon paper can be neglected.

In eq.(6-32) the molar mixture heat capacity $\widetilde{(\rho c_p)}^{AD}$ is approximated by the value for pure water (see appendix chapter 9.1.2). e^{AD} represents the sum of the enthalpy flux densities connected with the material fluxes and q^{AD} is the heat flux density due to thermal conduction in the liquid mixture and the pore walls (carbon fibres).

As the model is formulated in a spatially discretised form for the implementation in MatLab, all differentials are approximated by finite differences. Thus the partial differential equation (PDE) system presented in eqs.(6-30), (6-31) and (6-32) is transformed into a set of ordinary differential equations (ODE system) which can be solved by the MalLab ODE solver ode15s.

6.7.2.2 Transport Equations

As given in chapter 6.2, for the description of multi-component mass transport through porous structures, the Maxwell-Stefan approach [95] is an appropriate choice. Diffusive one-dimensional transport in liquid mixtures can be described by the generalised Maxwell-Stefan equations, eq.(6-4).

For constant activity coefficients and pure liquid phase (i.e. gas phase formation by carbon dioxide bubbles neglected), eq.(6-4). simplifies to:

$$-c_{tot}^{AD}\frac{\partial x_j^{AD}}{\partial z}=\sum_{i\neq j}\frac{x_i^{AD}j_j^{AD}-x_j^{AD}j_i^{AD}}{\mathcal{D}_{ij}^{AD,eff}}+\frac{j_j^{AD}}{\mathcal{D}_{jM}^{AD,eff}} \qquad (6\text{-}33)$$

$$\text{with} \quad j=H_2O, CH_3OH, CO_2$$

where j_i^{AD} are the diffusive mass flux densities in [mol m^{-2} s^{-1}] and x_i^{AD} are the mole fractions.

The total concentration c_{tot}^{AD} [mol m^{-3}] is:

$$c_{tot}^{AD}=\sum_j c_j^{AD} \quad \text{with} \quad j=H_2O, CH_3OH, CO_2 \qquad (6\text{-}34)$$

As demonstrated by KRISHNA and WESSELINGH [95], this flux-implicit set of transport equations can be transformed to get explicit formulations for the flux densities:

$$(j^{AD})=-c_{tot}^{AD}[B^{AD}]^{-1}\nabla(x^{AD}) \qquad (6\text{-}35)$$

where the elements of the transport matrix [B^{AD}] are:

diagonal elements:
$$B_{ii}^{AD}=\frac{1}{\mathcal{D}_{iM}^{AD,eff}}+\sum_{k\neq i}\frac{x_k^{AD}}{\mathcal{D}_{ik}^{AD,eff}} \quad , \qquad (6\text{-}36)$$

all other elements
$$B_{ij\,(i\neq j)}^{AD}=-\frac{x_i^{AD}}{\mathcal{D}_{ij}^{AD,eff}} \quad . \qquad (6\text{-}37)$$

A convective transport contribution due to pressure gradients is not accounted for directly within this formulation, as already explained in chapter 6.3. Pressure-driven convective transport is described seperately by adding a term to the diffusion flux densities to get the overall molar flux densities n_j^{AD} [mol m^{-2} s^{-1}], analogue to eq.(6-5):

$$n_j^{AD}=j_j^{AD}+\tilde{c}_j^{AD}v_p^{AD} \quad \text{with} \quad j=H_2O, CH_3OH, CO_2 \quad . \qquad (6\text{-}38)$$

The convective contribution accounts for the local concentration of species j, $\tilde{c}_j^{AD}$, and the superficial pressure-driven convective velocity, v_p^{AD}. As this happens within a porous medium, the concentration is formulated with respect to the overall volume including the solid matrix (pseudo-concentration):

$$\tilde{c}_j^{AD}=c_j^{AD}\varepsilon_{pores}^{AD} \qquad (6\text{-}39)$$

The tilde at the symbol c is used to distinguish it from ordinary concentrations (which only refer to the volume of all fluid components).

The convective velocity v_p^{AD} [m s^{-1}] is calculated from the local pressure gradient following Darcy's law and assuming Poiseuille flow (as presented in chapter 6.3, eqs(6-6) and (6-7)):

$$v_p^{AD} = -\frac{(d_{pore}^{AD})^2}{32\,\eta^{vis}} \frac{\partial\, p^{AD}}{\partial\, z} \quad . \tag{6-40}$$

As the carbon dioxide and methanol concentrations in the liquid mixture in (AD) are small compared to the water concentration, for the dynamic viscosity as function of local temperature and pressure a correlation for pure water is used (see appendix chapter 9.1.5).

The binary diffusion coefficients related to species-species interaction were determined from literature correlations (see appendix chapter 9.1.8). The binary diffusion coefficients related to species-matrix interaction are unknown. But for liquid phase transport in large pores (in the diffusion layers the pore diameters are in the order of 10-100 µm, see appendix chapter 9.2.1) species-matrix interactions are small compared to the species-species interactions for diffusive transport. In the presented model the species-matrix friction is accounted for by Darcy's law in the pressure-driven convection, eq.(6-40). Unfortunately, it turned out that leaving out the terms with the species-matrix binary diffusion coefficients in eq.(6-36) leads to numerical problems. The resulting transport matrix B^{AD} can not be inverted by MatLab due to ill conditioning (too close to singular). Therefore it was decided to set the values for the binary species-matrix diffusion coefficients to values which are three orders of magnitude higher than those of the species-species interactions. Thus the numerical problems were solved while the influence of the wall friction on the individual flux densities j_j^{AD} is negligible.

The total mass flux densities, enthalpy flux densities and conductive heat flux densities are calculated as follows:

$$m_{tot}^{AD} = \sum_j (n_j^{AD}\, \overline{M}_j) \quad \text{with} \quad j = H_2O, CH_3OH, CO_2 \tag{6-41}$$

$$q^{AD} = -\lambda^{AD,\,eff} \frac{\partial\, T^{AD}}{\partial\, z} \tag{6-42}$$

$$e^{AD} = \sum_j \left(n_j^{AD}\, h_j(T^{AD}) \right) \quad \text{with} \quad j = H_2O, CH_3OH, CO_2 \tag{6-43}$$

The effective thermal conductivity $\lambda^{AD,eff}$ [W m^{-2} K^{-1}] and the specific enthalpies h_j [J mol^{-1}] are calculated in the appendix (chapters 9.3 and 9.1.4).

To use the here presented transport equations for a spatially discretised model, an upwind scheme is used which always uses the "upwind" concentrations, i.e. the concentrations in the left or the right neighbouring control volume depending on the direction of the convective flux, to calculate the convective contribution to the molar flux densities in eq.(6-38).

6.7.3 Submodel Evaluation

To evaluate the presented model of the anode compartment in combination with the anode diffusion layer, dynamic simulations are carried out to find steady-state solutions using some experimental data as boundary conditions.

From steady-state experiments water and methanol fluxes through the anode side of the cell are known. Additionally, assuming full conversion without by-products, the carbon dioxide flux density as function of the cell current density can be calculated. These fluxes can be used as boundary conditions in the simulations.

The methanol and water flux densities depend on the measured crossover flux densities through the membrane and the consumption in the anode electrochemical methanol oxidation (proportional to the cell current density):

$$n^{AD}_{CH_3OH}(z^{AD}=d^{AD}) = n^{cross}_{CH_3OH} + \frac{i_{cell}}{6F} \quad , \tag{6-44}$$

$$n^{AD}_{H_2O}(z^{AD}=d^{AD}) = n^{cross}_{H_2O} + \frac{i_{cell}}{6F} \quad . \tag{6-45}$$

The carbon dioxide flux away from the anode catalyst layer is proportional to the cell current density since the polymer electrolyte membrane is assumed to be impermeable for carbon dioxide and other gases:

$$n^{AD}_{CO_2,\,ncv^{AD}} = -\frac{i_{cell}}{6F} \quad . \tag{6-46}$$

On the side of the anode compartment, the feed state (feed flow rate F^{AF}, pressure p^A, liquid mixture temperature T^A and composition c_j^A) is used as boundary condition. Typical values for the membrane crossover fluxes are given in chapter 4.4. For the following simulations, the crossover fluxes and respective feed and operating conditions are presented in Table 6-2.

One further simulation parameter to be determined from the evaluation is the necessary number of control volumes to get a reasonable representation of the spatially distributed layer. Tested were 5 and 10 control volumes. In both cases, the simulation converges rapidly towards a steady-state, yielding nearly identical results. Therefore, to achieve a maximum simulation speed it seems justified to use only five control volumes as standard value in the full DMFC model. In Figure 6-5 simulation results are presented for 10 control volumes.

Table 6-2 *Simulation parameters for anode model evaluation*

parameter	***symbol***	***value***
Water crossover flux density	$n_{H_2O}^{cross}$	0.1 mol m^{-2} s^{-1}
Methanol crossover flux density	$n_{CH_3OH}^{cross}$	0.007 mol m^{-2} s^{-1}
Cell current density	i_{cell}	400 mA cm^{-2}
Temperature of anode catalyst layer (AC)	T^{AC}	90 °C
Temperature in anode compartment (A)	T^{A}	35 °C
Anode feed methanol concentration	$c_{CH_3OH}^{AF}$	3.2 wt.% = 1 mol dm^{-3}
Anode feed carbon dioxide concentration	$c_{CO_2}^{AF}$	0
Anode feed flow rate	F^{AF}	0.5 dm^3 min^{-1}
Anode pressure	p^{A}	$1.7 \cdot 10^5$ Pa

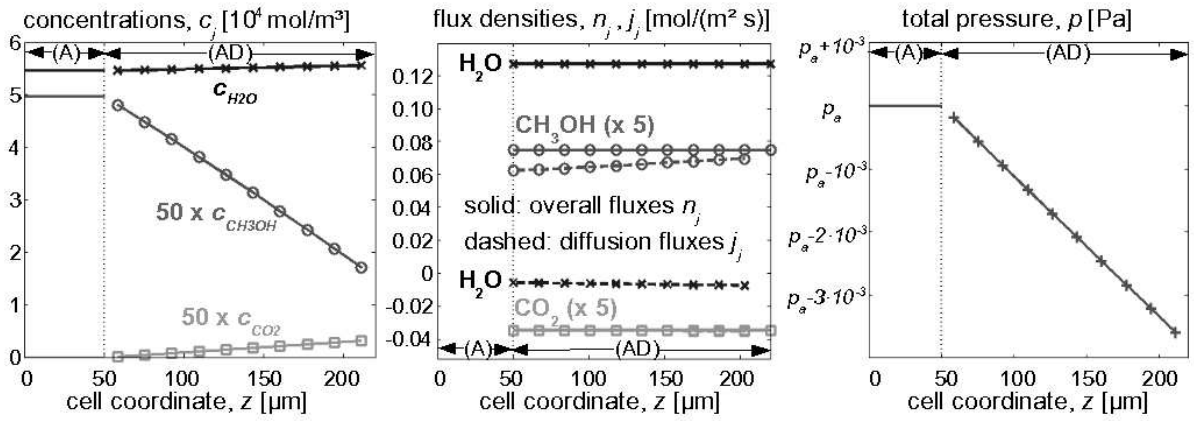

Figure 6-5 *Steady-state simulation results of anode model (model block 1)*

The most important results of the simulations shown in Figure 6-5 are:

- Even for these high membrane crossover fluxes and operating temperatures (at maximum cell performance) the concentration profiles are nearly linear.
- Water is mainly transported by pressure-driven convection (compare total flux density=solid and individual flux density=dashed lines for water and methanol in the middle plot of Figure 6-5). Nonetheless only a very small pressure gradient is built up (total pressure drop only a few Millipascal) due to the low flow velocity (v^{AD} in the order of a few micrometers per second)

Therefore the main transport resistance for water is the friction with the porous matrix, while the methanol transport is governed mainly by diffusion. The main transport resistance for methanol is the friction with water. For carbon dioxide, due to its low concentration, pressure-driven convection plays an insignificant role, also here diffusion is the main mode of transport.

This model approach assumes pure liquid phase and is not accounting for possible formation of a gas phase within the pores of the diffusion layer due to the low solubility of carbon dioxide. As experimental observations (e.g. flow visualisations carried out by SCOTT et al. [54] and ARGYROPOULOS et al. [55], Figure 1-10 on page 18) suggest that such phase splitting occurs for high current densities, it can be expected that for such conditions the model will predict too low transport resistances especially for methanol.

6.8 Model Block 2: Cathode Compartment (C) and Diffusion Layer (CD)

The cathode compartment (C) represents the cathode flowbed structure, which supplies air to the cathode diffusion layer (CD), and takes up the reaction products water and carbon dioxide. The cathode diffusion layer connects the flowbed structure to the catalyst layer (CC). The general structure is identical to that of the anode diffusion layer (AD) presented in model block 1 (chapter 6.7).

6.8.1 Cathode Compartment (C)

The cathode compartment has one inlet (feed) and one outlet, and it is connected to the cathode diffusion layer (CD) as depicted in Figure 6-6.

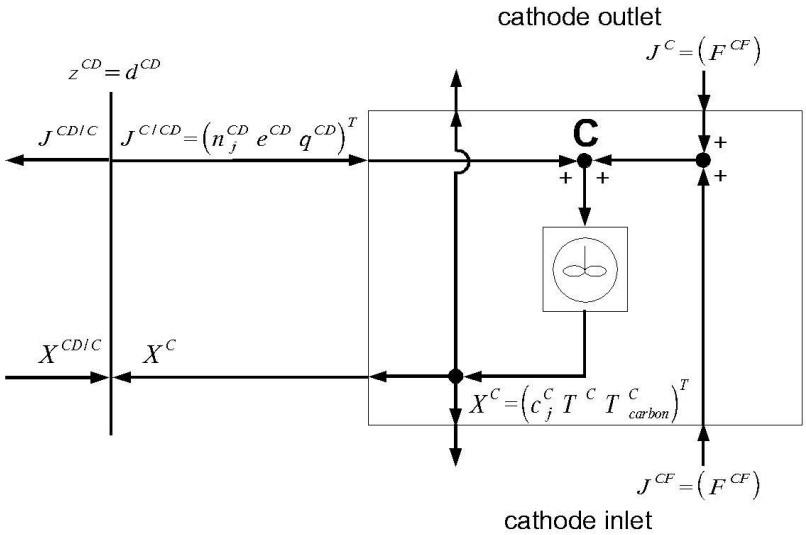

Figure 6-6 *Decomposition of cathode compartment (C) on level of storages (j = O_2, N_2, H_2O, CO_2)*

The inlet is fed with air with the components oxygen, nitrogen (including all other inert gases), water and carbon dioxide. The cathode compartment is modeled as an ideally mixed reactor (CSTR) which leads to the material balances

$$\frac{dc_j^C}{dt} = \frac{1}{V^C}\left(F^{CF}\, c_j^{CF} - F^C\, c_j^C + A^S\, n_j^{CD}\,(z^{CD} = d^{CD})\right) \qquad (6\text{-}47)$$

with $j = N_2, O_2, H_2O, CO_2$.

Here F^{CF} is the feed volume flow rate [m³ s⁻¹], V^C is the total volume of the channels [m³], c_j^{CF} are the feed concentrations [mol m⁻³] and F^C is the outlet volume flow rate [m³ s⁻¹]. The latter can be calculated from the inlet flow rate and the molar fluxes exchanged with the diffusion layer (CD) (quasi-stationary total material balance):

$$F^C = F^{CF} + \frac{R\,T^C}{p^C} A^S \sum_j n_j^{CD}\,(z^{CD} = d^{CD}) \quad . \qquad (6\text{-}48)$$

with $j = N_2, O_2, H_2O, CO_2$

The cathode pressure p^C as well as the gas and the bipolar plate temperatures, T^C and T^C_{carbon}, respectively (explanation for two temperatures in next chapter), are input parameters known from experiments. Therefore, no energy and no total mass balances are formulated.

6.8.2 Cathode Diffusion Layer (CD)

The cathode diffusion layer (CD) is described similar to (AD). Figure 6-7 shows the structure schematically, analogue to Figure 6-4.

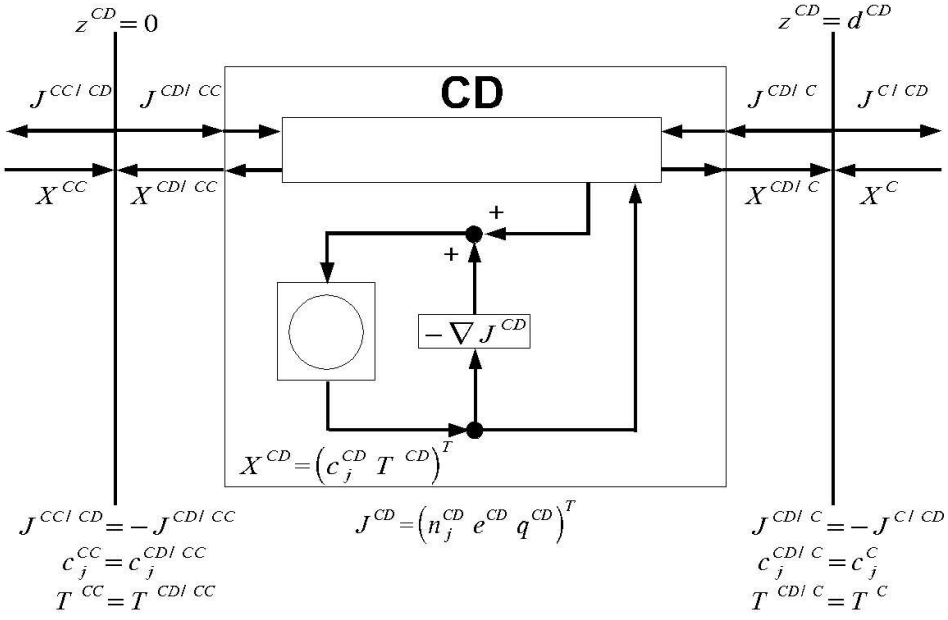

Figure 6-7 *Decomposition of cathode diffusion layer (CD) on the level of storages, spatially distributed (j = O_2, N_2, H_2O, CO_2)*

The mobile species are oxygen, nitrogen (summing up all inert gases), water vapour and carbon dioxide. Ideal gas behaviour is assumed.

6.8.2.1 Balances

Material and energy balances are formulated similar as in (AD). For the four species oxygen (O_2), nitrogen (N_2), water (H_2O) and carbon dioxide (CO_2), the material balances using molar concentrations c_j are:

$$\frac{\partial c_j^{CD}}{\partial t} = -\frac{1}{\varepsilon_{pores}^{CD}} \frac{\partial n_j^{CD}}{\partial z} \quad \text{with} \quad j = N_2, O_2, H_2O, CO_2 \quad . \tag{6-49}$$

The energy balance is given as

$$\frac{\partial T^{CD}}{\partial t} = \frac{1}{\widetilde{(\rho c_p)}^{CD}} \left[-\frac{\partial e^{CD}}{\partial z} - \frac{\partial q^{CD}}{\partial z} \right] \quad . \tag{6-50}$$

The major difference to (AD) results from the fact, that here the mixture is an ideal gas and not a liquid. Therefore, the total local pressure p^{CD} is given by the sum of the local partial pressures p_j^{CD}:

$$p^{CD} = \sum_j p_j^{CD} = RT^{CD} \sum_j c_j^{CD} \quad \text{with} \quad j = N_2, O_2, H_2O, CO_2 \quad . \tag{6-51}$$

6.8.2.2 Transport Equations

As in the anode diffusion layer, a mass transport approach based on the generalised Maxwell-Stefan equations is used, combined with a finite volume discretisation. For diffusive one-dimensional transport in a mixture of ideal gases, eq.(6-4) simplifies to:

$$-\frac{1}{RT^{CD}} \frac{\partial p_j^{CD}}{\partial z} = \sum_{i \neq j} \frac{y_i^{CD} j_j^{CD} - y_j^{CD} j_i^{CD}}{\mathcal{D}_{ij}^{CD,\,eff}} + \frac{j_j^{CD}}{\mathcal{D}_{j\,M}^{CD,\,eff}} \tag{6-52}$$

$$\text{with} \quad j = N_2, O_2, H_2O, CO_2$$

where j^{CD} are the diffusive mass flux densities in [mol m^{-2} s^{-1}], p_j^{CD} are the partial pressures in [Pa] and y_j^{CD} are the gas mole fractions.

The binary diffusion coefficients can be easily and quite reliably derived from several correlations (see appendix chapter 9.1.8) or alternatively from the kinetic gas theory. The species-matrix diffusion coefficients are calculated using the equation for Knudsen diffusion:

$$\mathcal{D}_{j\,M}^{CD,\,eff} = \frac{\varepsilon_{pores}^{CD}}{\tau^{CD}} \frac{d_{pore}^{CD}}{3} \sqrt{\frac{8RT^{CD}}{\pi \overline{M}_j}} \quad \text{with} \quad j = N_2, O_2, H_2O, CO_2 \quad . \tag{6-53}$$

In eq.(6-53) $\overline{M}_j$ are the molecular weights [kg mol^{-1}] and d^{CD}_{pore} [m] is the mean pore diameter in the matrix.

As presented for (AD), eq.(6-35), the Maxwell-Stefan equations, eq.(6-52), can be transformed from the flux-implicit to a flux-explicit formulation:

$$(j^{CD}) = -\frac{1}{RT^{CD}}[B^{CD}]^{-1}\nabla(p^{CD}) \tag{6-54}$$

where the elements of the transport matrix $[B^{CD}]$ are

$$B_{ii}^{CD} = \frac{1}{\mathcal{D}_{i\,M}^{CD,\,eff}} + \sum_{k\neq i}\frac{y_k^{CD}}{\mathcal{D}_{ik}^{CD,\,eff}} \quad \text{and} \tag{6-55}$$

$$B_{ij\,(i\neq j)}^{CD} = -\frac{y_i^{CD}}{\mathcal{D}_{ij}^{CD,\,eff}} \quad . \tag{6-56}$$

The convective transport contribution due to pressure gradients is accounted for to get the overall flux densities n_j^{CD} [mol m^{-2} s^{-1}]:

$$n_j^{CD} = j_j^{CD} + \tilde{c}_j^{CD} v_p^{CD} \quad \text{with} \quad j = N_{2,}O_{2,}H_2O, CO_2 \tag{6-57}$$

with the pseudo-concentration

$$\tilde{c}_j^{CD} = c^{CD}\varepsilon_{pores}^{CD} \tag{6-58}$$

and the convective velocity v_p^{CD} [m s^{-1}]

$$v_p^{CD} = -\frac{(d_{pore}^{CD})^2}{32\,\eta^{vis}}\frac{\partial\, p^{CD}}{\partial\, z} \quad . \tag{6-59}$$

For the dynamic viscosity η^{vis} as function of local temperature and pressure a correlation for air is used (see appendix chapter 9.1.5).

For the energy balance, transport equations are needed for thermal conduction and convective heat transport. Both are similar to the already described equations for (AD):

Conductive heat flux:

$$q^{CD} = -\lambda^{CD,\,eff}\frac{\partial\, T^{CD}}{\partial\, z} \tag{6-60}$$

Enthalpy flux (convective heat flux):

$$e^{CD} = \sum_j n_j^{CD} h_j(T^{CD}) \quad \text{with} \quad j = N_{2,}O_{2,}H_2O, CO_2 \tag{6-61}$$

The effective thermal conductivity $\lambda^{CD,eff}$ and the specific enthalpies h_j are calculated in appendix chapters 9.3 and 9.1.4, respectively.

To use these presented transport equations for a spatially discretised model, again an upwind scheme is used as described for the anode diffusion layer (AD).

In implementing this, one major difference to the anode side has to be accounted for. On the anode side, a liquid mixture (mainly water) is pumped through the channels of (A). Due to the high heat capacity of water and the relatively high heat transfer coefficients between the

liquid mixture and the channel walls, a uniform temperature T^A can be assumed. On the cathode side the situation is totally different in this respect, as the gas mixture has a heat capacity of only

$$(\rho\, c_p)_{air} \approx 1.3 \frac{\mathrm{kg}}{\mathrm{m}^3} \cdot 1010 \frac{\mathrm{J}}{\mathrm{kg} \cdot \mathrm{K}} \approx 1300 \frac{\mathrm{J}}{\mathrm{m}^3 \cdot \mathrm{K}} \tag{6-62}$$

which is negligible compared to that of the bipolar plate

$$(\rho\, c_p)_{graphite} \approx 2000 \frac{\mathrm{kg}}{\mathrm{m}^3} \cdot 711 \frac{\mathrm{J}}{\mathrm{kg} \cdot \mathrm{K}} \approx 1.422 \cdot 10^6 \frac{\mathrm{J}}{\mathrm{m}^3 \cdot \mathrm{K}} \quad . \tag{6-63}$$

For calculation of heat transfer coefficients refer to appendix chapter 9.6.

The effect of this situation, observed in the experiments, is that the air pumped through the cathode bipolar plate changes its temperature only marginally (around 1-2 degrees K maximum, see also model assumptions in chapter 6.1) and remains at 30-35°C, while the temperature of the bipolar plate is nearly the same as that on the anode side (up to 90°C in the presented experiments). Thermal energy is transported with low resistances through the planar contact areas at the outer gaskets and through the solid materials of the MEA.

Therefore, on the cathode side, two temperatures have to be accounted for as boundary/operating conditions: The gas temperature, which nearly equals the feed temperature T^C (simplifyingly assumed to be equal), and the solid temperature T^C_{carbon}. For the calculation of the enthalpy flux (convective heat flux) between (CD) and (C), the gas temperatures have to be accounted for, as the gases are the mobile species. For the calculation of the conductive heat flux, the temperatures of the solid matrices have to be used, as thermal conduction through the gas phase can be neglected in comparison to that through the solid materials.

But this distinction is only necessary for the energy fluxes between (CD) and (C). Within the diffusion layer (CD) still a uniform temperature valid for gas and solid matrix can be assumed, as here the flow velocity is some orders of magnitude lower as in the gas channels of (C) and due to the small pore diameters and high pore tortuosity an intense heat exchange between gas and solid can be expected. Therefore, the temperature can be expected to show only a slight slope within (CD), whereas at the interface between (CD) and the gas channels in (C) it can change dramatically, depending on the cathode and anode feed temperatures.

6.8.3 Submodel Evaluation

To evaluate the presented model block of cathode compartment (C) and diffusion layer (CD), dynamic simulations are carried out to get steady-state solutions using experimental data as boundary conditions.

From steady-state experiments water, oxygen and carbon dioxide fluxes through the cathode side of the cell are known. These fluxes are used as boundary conditions in the simulations. The water crossover flux through the membrane is measured directly:

$$n_{H_2O}^{CD}(z^{CD}=0)=n_{H_2O}^{cross} \quad . \tag{6-64}$$

The carbon dioxide flux is equivalent to the methanol crossover flux through the membrane, which is also determined experimentally (assuming full and immediate conversion of methanol to carbon dioxide at the cathode catalyst):

$$n_{CO_2}^{CD}(z^{CD}=0)=n_{CH_3OH}^{cross} \tag{6-65}$$

The oxygen flux through the cathode diffusion layer finally depends on the methanol crossover flux (oxygen consumption for direct methanol oxidation proportional to methanol crossover flux density through the membrane) and on the cell current density (electrochemical oxygen consumption, assuming that no side products are formed):

$$n_{O_2}^{CD}(z^{CD}=0)=-\frac{i_{cell}}{4\,F}+1.5\,n_{CH_3OH}^{cross} \quad . \tag{6-66}$$

At steady-state conditions, assuming the cell membrane to be impermeable for gases, the nitrogen flux has to be zero:

$$n_{N_2}^{CD}(z^{CD}=0)=0 \quad . \tag{6-67}$$

On the side of the cathode compartment the feed state (feed flow rate F^{CF}, pressure p^C, gas and solid temperatures, T^C and T^C_{carbon}, and feed air composition c_j^{CF}) is used as boundary conditions. For the calculation of the feed air composition from the measured humidity refer to appendix chapter 9.5.

Typical experimental values for the crossover fluxes have already been presented in chapter 4.4. For the following simulations, the maximum membrane crossover fluxes and respective feed and operating conditions are given in Table 6-3, some exemplary simulation results (profiles through (A) and (AD)) are presented in Figure 6-8.

Table 6-3 *Simulation parameters for cathode model evaluation*

parameter	***symbol***	***value***
Water crossover flux density	$n_{H_2O}^{cross}$	0.14 mol m^{-2} s^{-1}
Methanol crossover flux density	$n_{CH_3OH}^{cross}$	0.01 mol m^{-2} s^{-1}
Cell current density	i_{cell}	400 mA cm^{-2}
Temperature in (CC)	T^{CC}	90 °C
Temperature of cathode gas	T^{C}	35 °C
Temperature of cathode bipolar plate	T^{C}_{carbon}	87 °C
Dew point of cathode feed air	ϑ^{dew}	0 °C
Cathode feed flow rate	F^{CF}	0.5 scbm h^{-1}
Cathode pressure	p^{C}	$1.7 \cdot 10^5$ Pa

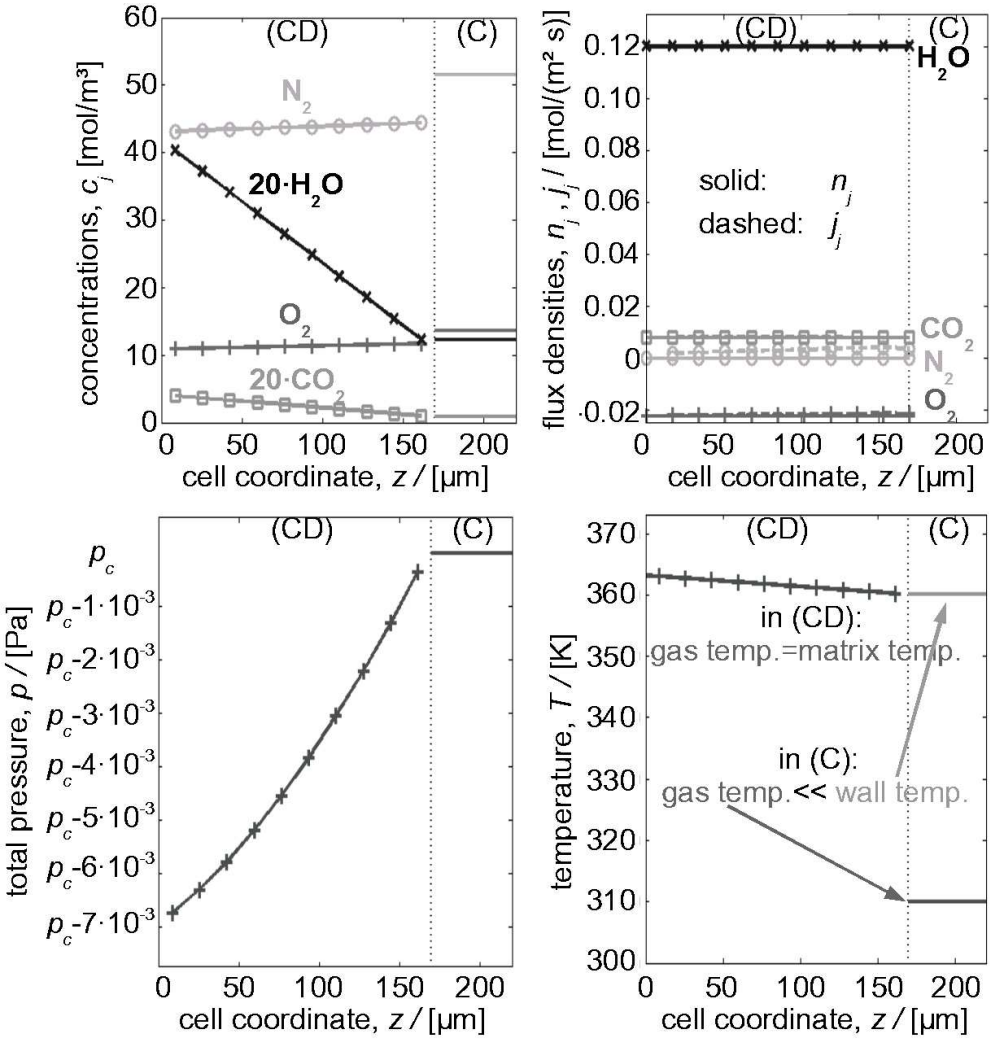

Figure 6-8 *Steady-state simulation results of cathode model (model block 2)*

The main results of the simulations shown in Figure 6-8 are:

- Even for the maximum membrane crossover fluxes and operating temperatures, the gas concentration profiles within (CD) are nearly linear and have only slight slopes.
- Water, oxygen and carbon dioxide are transported mainly by diffusion, along their partial pressure gradients.
- The partial pressure of nitrogen is lower in (CC) than in (C) due to dilution with the water and carbon dioxide produced in the catalyst layer. Therefore a diffusive flux density towards (CC) would be expected. But in the simulation a diffusive flux in the opposite direction is obtained due to drag exerted on the nitrogen molecules mainly by water being transported away from the catalyst layer. Note the large total water flux density compared to all other flux densities, shown in the upper right plot of Figure 6-8. The diffusive flux of nitrogen towards (C) is fully compensated by pressure-driven convection due to a pressure gradient towards (CC). This convective flow also shows some influence on oxygen, while water and carbon dioxide, due to their low concentrations, are only marginally influenced.
- The temperature profile shows the expected tendencies (see end of chapter 6.8.2.2): Within the porous diffusion layer the temperature gradient is very small, while in the cathode channels (C) a large difference is found between the (cool) gas and the (hot) channel walls.

It can be concluded, that in (CD) the main mode of transport for the active species (water, oxygen and carbon dioxide) is diffusion, while nitrogen is stagnant due to a balance between diffusive and convective driving forces. The overall mass transport resistances for oxygen, water and carbon dioxide are very small compared to those found on the anode side.

One further simulation parameter to be determined from the evaluation is the suitable number of control volumes. Tested values were 3, 5 and 10. With only three elements, the simulation converges rapidly to a steady state, while with 5 or more, convergence becomes somewhat slower, but still acceptable.

This model approach assumes pure gas phase and is not accounting for possible formation of a liquid phase within the pores of the diffusion layer due to condensation of water (cathode flooding, see chapter 1.5). The probability that such condensation takes place increases with increasing current density and decreasing cell temperature. The formation of a liquid water phase means a significantly increased transport resistance for oxygen. Therefore it has to be expected that the model will predict too low mass transport resistances for oxygen for high current densities and low cell temperatures.

6.9 Model Block 3: MEA = Membrane (M) and Catalyst Layers (AC,CC)

This block represents the polymer electrolyte membrane and the adjacent catalyst layers. These three layers form the membrane electrode assembly (MEA), which is the core element of the DMFC.

The catalyst layers are not only neighbouring the membrane, all three layers are highly interconnected by the proton-conducting membrane material content within the catalyst layers, as described in chapter 1. Electron microscopic investigations of the typical MEA structures show strains of polymer material running through the catalyst layers, connecting catalyst particles to the membrane on the ionic conductor level. Figure 6-9 (left) illustrates this situation schematically. These strains not only form an ionic connection for mobile protons to the membrane (M), but also with respect to all species which can enter the pores within these materials. In the case of NAFION^{TM} these species are water and methanol, whereas the membrane is assumed to be impermeable for all gases (carbon dioxide, oxygen, nitrogen). This assumption is justified by the fact that the maximum content of these gases in the pore fluid of the membrane is limited by their solubility in water (and methanol), which is very low, especially at high operating temperatures.

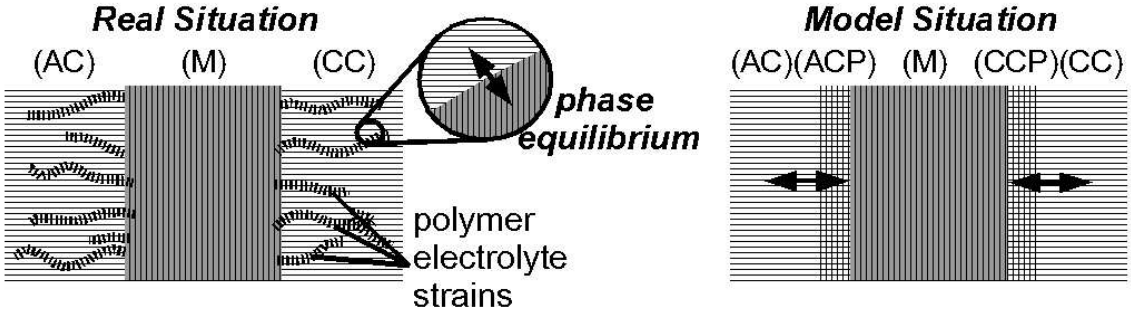

Figure 6-9 *Interfaces between membrane (M) and both catalyst layers (AC) (CC)*

As the pore volume of the polymer phase within the catalyst layers is small compared to its surface open to the free pores within the catalyst layers, it will be furthermore assumed that at this interface between the catalyst layers and the membrane phase equilibrium is always established (Figure 6-9 right). The phase equilibrium condition is expressed by the equality of the chemical potentials of all mobile species at the considered interface:

$$\mu_j^{AC} = \mu_j^{ACP} \quad . \qquad \text{and} \qquad \mu_j^{CC} = \mu_j^{CCP} \quad . \qquad \text{(6-68),(6-69)}$$

The indices ACP and CCP denote the polymer content within the two catalyst layers,(AC) and (CC), respectively. As the pore space within these polymer phases is small compared to that within the free pores in the catalyst layers, no balance equations are formulated.

To describe the phase equilibria in terms of the concentrations of the species water and methanol, models for the activities within the polymer material and within the free pores in the catalyst layers are necessary. In the anode catalyst layer (AC) it is assumed that only a liquid phase exists. The possible formation of gas bubbles within (AC) is not taken into account. As carbon dioxide is assumed not to be existing in the membrane material, this is a reasonable simplification. Therefore, in the free pores of (AC) the well-established UNIFAC method [86i], in its modified version [96], is used to calculate the water and methanol activities. In the polymer material itself, the Flory-Huggins activity model [94][97] is applied. In that model the activity of a species *j* is given as a function of the volume fractions ε_i of all mobile species and the polymer backbone, treating the polymer backbone and the mobile species as a "liquid" mixture (typical polymers are undercooled liquids):

$$a_j = \varepsilon_j \exp\left\{ \sum_{i \neq j} \left[\left(1 - \frac{\overline{V}_j}{\overline{V}_i} \right) \varepsilon_i + \chi_{j,i} \varepsilon_i^2 \right] + \frac{\overline{V}_j}{2 \cdot N_{M,cu} \cdot \overline{V}_{M,cu}} \varepsilon_M^{1/3} \right\} \quad . \qquad (6\text{-}70)$$

In eq.(6-70) for the polymer material the lower index "M" is used. For each pair of species, a non-ideality parameter $\chi_{j,i}$ is required. Crosslinking of the polymer material is accounted for in the last term on the right hand side. $N_{M,cu}$ is the number of sequential single polymer chain units (i.e. monomer units) within the main polymer chain between two cross-links, $\overline{V}_{M,cu}$ is the molar volume of such a single chain unit in [m^3 mol^{-1}]. As the molar volume of the polymer is some orders of magnitude higher than those of the mobile species, the term $\left(1 - \overline{V}_j / \overline{V}_i\right)$ is approximately 1.

In the following, three species are accounted for: The polymer backbone (index "M"), water and methanol. The protons, strictly speaking, are also a mobile species, but they are treated separately, as will be explained later in chapter 6.9.3. Then, for water and methanol the resulting activities are given by:

$$a_{H_2O} = \qquad (6\text{-}71)$$

$$\varepsilon_{H_2O} \cdot \exp\left\{ \varepsilon_M + \chi_{H_2O,M} \varepsilon_M^2 + \left(1 - \frac{\overline{V}_{H_2O}}{\overline{V}_{CH_3OH}} \right) \varepsilon_{CH_3OH} + \chi_{H_2O,CH_3OH} \varepsilon_{CH_3OH}^2 + \frac{\overline{V}_{H_2O} \varepsilon_M^{1/3}}{2 N_{M,cu} \overline{V}_{M,cu}} \right\}$$

$$a_{CH_3OH} = \qquad (6\text{-}72)$$

$$\varepsilon_{CH_3OH} \cdot \exp\left\{ \varepsilon_M + \chi_{CH_3OH,M} \varepsilon_M^2 + \left(1 - \frac{\overline{V}_{CH_3OH}}{\overline{V}_{H_2O}} \right) \varepsilon_{H_2O} + \chi_{H_2O,CH_3OH} \varepsilon_{H_2O}^2 + \frac{\overline{V}_{CH_3OH} \varepsilon_M^{1/3}}{2 N_{M,cu} \overline{V}_{M,cu}} \right\}$$

One can see that three non-ideality parameters are needed: Two for the interaction between the mobile species (water and methanol) with the polymer material, and a third which describes the interaction between water and methanol. A complete and detailed treatment of this approach, including determination of the non-ideality parameters, can be found in the appendix (chapter 9.7). Here only the results are given:

$$\chi_{H_2O,M} = 0.7177 \quad , \quad \chi_{CH_3OH,M} = 0.1348 \quad , \quad \chi_{H_2O,CH_3OH} = 1.3 \quad .$$

Finally, an activity model for the cathode catalyst layer (CC) pores has to be formulated. For this, first it has to be found out which phase state (gas or liquid) is predominant there. The experiments show high levels of water crossover fluxes, even in the absence of a pressure gradient over the membrane and/or the absence of an electric current flow. Therefore, only a diffusive flux can be the reason for the observed water transport. This in turn means there must be some activity gradient across the membrane, from (AC) to (CC).

Assumed hypothetically that also the cathode catalyst layer (CC) pores were filled with liquid water (methanol is always assumed to be fully consumed), all other species (nitrogen, oxygen and carbon dioxide) could only have very low concentrations due to their low solubility in water. In this scenario, the water activity in (CC) would be at least as high as in (AC), therefore the same were true for (CCP) and (ACP), respectively. In this case (Figure 6-10, left) an activity gradient directed from (CC) towards (AC) would result, leading to a diffusive water transport towards the anode side, which is the opposite direction from that observed in the experiments. Obviously, an activity gradient directed from anode towards the cathode is necessary to explain the experimental observation. This can only be the case if in (CC) the gas phase is predominant (Figure 6-10, right). In this case, a mixture of nitrogen, oxygen, carbon dioxide and water vapour is present in the pores of (CC).

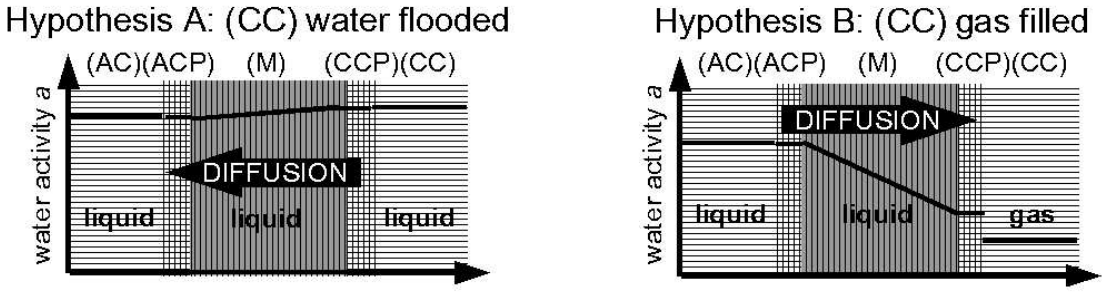

Figure 6-10 *Hypotheses for the phase state in (CC)*

Now that a realistic phase situation is identified, both phase equilibria have to be formulated for the implementation into the model. On the anode side, in both the pores within (AC) as well as in the polymer material (ACP) all mobile components are assumed to be liquid (see above), therefore equality of chemical potentials is simply given by equality of activities (same reference state):

$$a_j^{AC} = a_j^{ACP} \quad . \tag{6-73}$$

Using a UNIFAC model [96] for the free pore activity and the presented Flory-Huggins model for the polymer material leads to the equilibrium curves presented in Figure 6-11 (for detailed descriptions of the underlying calculations see appendix chapter 9.7.2). One can clearly see that the system is far from ideal behaviour, but especially in regions where a typical DMFC is not operated (i.e. methanol mole fractions above 0.03). Interestingly, for low methanol free solution concentrations methanol plays the role of a swelling promotor w.r.t. water uptake, i.e. the uptake of small amounts of methanol also leads to a further uptake of water leading to a significantly increased relative water content compared to PEMFC operation, as the final full DMFC model simulations will show. Only for higher methanol free solution concentrations, methanol successively displaces water from the membrane material.

The phase equilibria are calculated using a dynamic swelling model (see appendix chapter 9.7.2), which is rather time consuming w.r.t. simulation time. To speed up the DMFC model simulation itself, the simulated equilibria for methanol and water are approximated by third

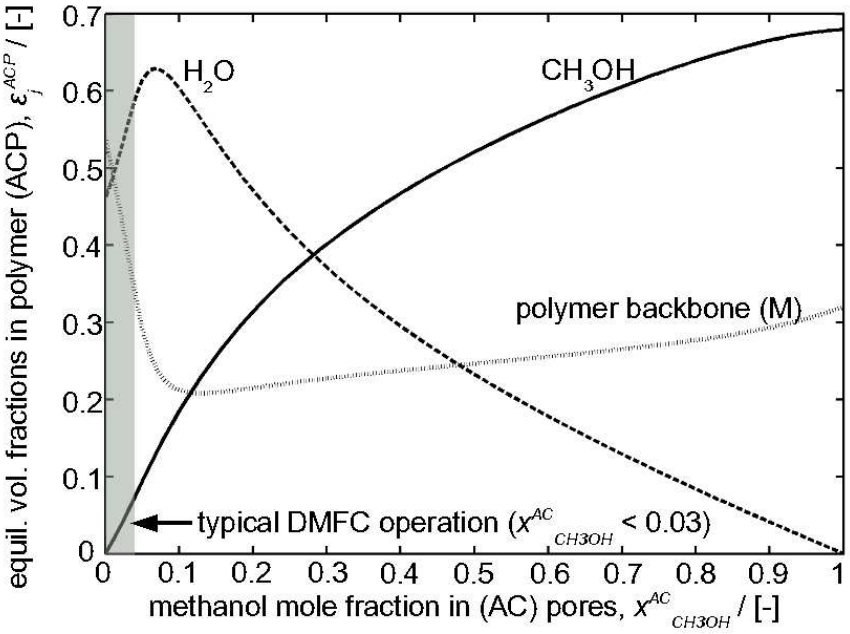

Figure 6-11 *Phase equilibrium volume fractions in NAFION™ material as function of free pore methanol mole fraction, according to Flory-Huggins/UNIFAC model (temp.: 60°C).*

order polynomials in the range of the methanol free pore mole fraction from zero to 0.03 (typical operation range of a DMFC, grey region in Figure 6-11):

$$\varepsilon^{ACP}_{CH_3OH} = 25.4831 \cdot (x^{AC}_{CH_3OH})^3 + 4.2821 \cdot (x^{AC}_{CH_3OH})^2 + 1.6354 \cdot x^{AC}_{CH_3OH} \qquad (6\text{-}74)$$

$$\varepsilon^{ACP}_{H_2O} = -104.9956 \cdot (x^{AC}_{CH_3OH})^3 + 20.9052 \cdot (x^{AC}_{CH_3OH})^2 + 2.6349 \cdot x^{AC}_{CH_3OH} + 0.4601 \qquad (6\text{-}75)$$

The temperature influence was found to be negligible. Activity coefficients predicted from the UNIFAC model for this system show only a weak temperature dependence, and in the Flory-Huggins model temperature influences only the molar volumes, which are nearly independent of temperature for liquids.

On the cathode side, the membrane is assumed to be in equilibrium with a pure gas phase (i.e. a mixture of oxygen, nitrogen, carbon dioxide and water vapour). From the literature (e.g.[98],[99]) experimental data are available for the equilibrium relative water content of NAFION™ (with respect to the number of fixed sulfonic acid groups $-SO_3^-$):

$$\Lambda^M = \frac{N^M_{H_2O}}{N_{R-SO_3^-}} \quad . \qquad (6\text{-}76)$$

as function of the "water vapour activity" (ideal gas, defined as in the references [98][99]):

$$a^*_{H_2O(g)} = \frac{p_{H_2O}}{p^{sat}_{H_2O}(T)} \quad . \qquad (6\text{-}77)$$

These data and related correlations are presented in Figure 6-12. The full square and diamond shaped dots represent the experimental values: Another known value (denoted as theoretical point) is that at the origin, because in a totally dry atmosphere also NAFION™ would be totally dry in equilibrium state. One can see that the experimental data sets differ quite significantly, especially for water vapour activities above 0.9 and between 0.4 and 0.8. The data by ZAWODZINSKI et al. [98] (square dots in Figure 6-12) show a curve with two inflection points and a maximum relative water content of about 14 for saturated water vapour atmosphere. This is somewhat astonishing from the thermodynamic point of view, as the relative water content in pure liquid water at the same conditions is about 21-23 [98]. Normally one would expect to find the same water content for immersion in liquid water and pure water vapour. This yet unexplained deviation is also found for many other ion exchange polymers. Doubts occur about these experimental data for high water vapour activities, based on the speculation that maybe in this region most experiments failed to provide true isothermal conditions (which is fundamental here). More recent results using modified experimental setups show a different behaviour [99] (Figure 6-12, diamond shaped data

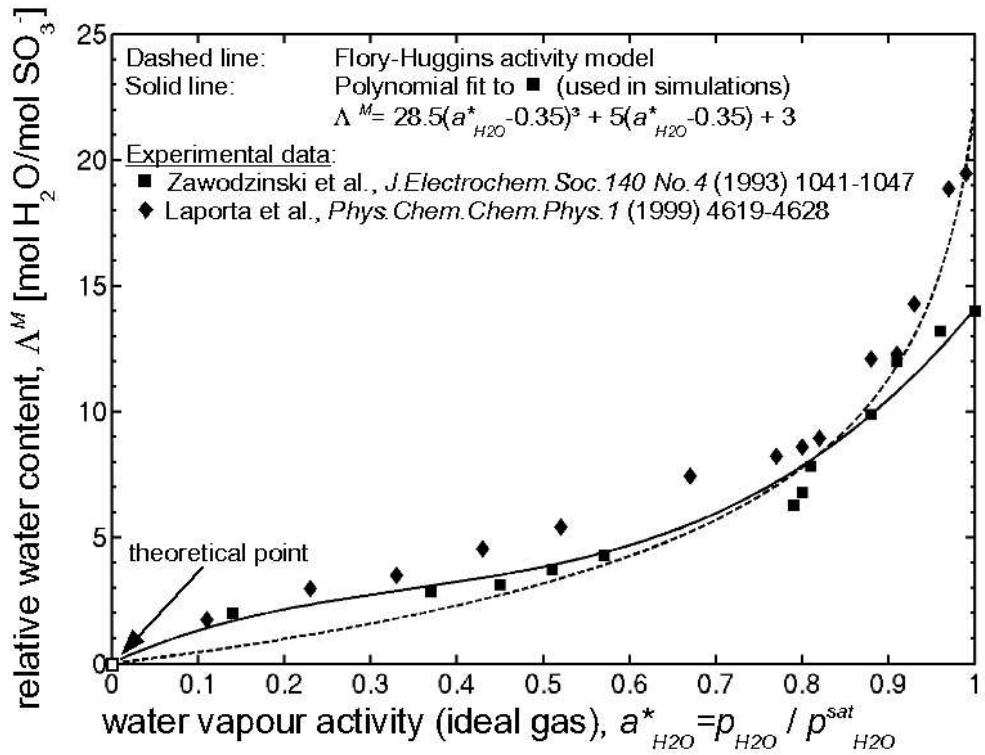

Figure 6-12 *Experimental data from equilibration of NAFION™ N-117 with water vapour and comparison with fitting curve and Flory-Higgins activity model (exp. data adopted from [98] Fig.4 and [99] Fig.1)*

points), where relative water contents around 20 are found for water vapour activities of 0.99. But as still most references report similar results to those of ZAWODZINSKI et al. [98], these data were used for fitting a third order polynomial to be used in the simulation model for cathode side phase equilibrium between the process air in the cathode catalyst layer pores (CC) and the adjacent polymer phase (upper index CCP):

$$\Lambda^{CCP} = 28.5 \cdot (a^{*,CC}_{H_2O(g)} - 0.35)^3 + 5 \cdot (a^{*,CC}_{H_2O(g)} - 0.35) + 3 \qquad (6\text{-}78)$$

with $$a^{*,CC}_{H_2O(g)} = \frac{p^{CC}_{H_2O}}{p^{sat}_{H_2O}(T^{CC})} \quad . \qquad (6\text{-}79)$$

Fortunately the possible systematic fault underlying the experimental data by ZAWODZINSKI et al. [98] only affects the equilibrium realtive water contents for very high water vapour activities of above 0.9. In the cathode of a fuel cell, one will always try to avoid such high water vapour activities to prevent condensation of water inside the cathode structures (cathode flooding). Ideally, the water vapour activity is kept below 0.9, where the experimental data are not in doubt. In this region also the data by LAPORTA et al. [99] are very similar to those from ZAWODZINSKI et al. [98] and are therefore nicely approximated by eq.(6-78).

Just for comparison, in Figure 6-12 also the curve obtained from the presented Flory-Huggins activity model (which is used on the liquid-fed anode side) is shown (dashed line). Here of course for a water activity of one, a relative water content of 23 is reached, thus giving a good approximation to the data from LAPORTA et al. [99] for activities above 0.8. For lower activities the Flory-Huggins model yields much too low relative water contents.

Finally some attention is paid to viscous flow in the membrane material. As the pores within NAFION™ are extremely small, i.e. in the range of a few nanometers (see Figure 1-7), the question arises whether small pressure differences over the DMFC (typically max. 2 bars) can lead to a significant viscous flow contribution. This question is addressed by some simple calculations:

In the presented model formulation, the velocity of pressure-driven flow is proportional to the pressure gradient over the membrane following Darcy's law (chapter 6.7, eq.(6-6)). Poiseuille's law is used to estimate the permeability (eq.(6-7)). As in reality we have twisted pores instead of tubular straight ones, the real permeability of NAFION™ is even somewhat lower. The question is now: Which minimum pressure difference over the membrane would be necessary to obtain the measured water crossover fluxes ? E.g. at 60°C from the experimentally determined crossover flux one can calculate a mean water velocity of roughly $v^{M}_{H_2O} \approx 2\,\mu\text{m/s}$. Assuming a fully hydrated membrane (i.e. maximum pore diameters = maximum permeability = minimum required pressure difference) with a minimum pore diameter of two nanometers (in fact one nanometer is more realistic) and a thickness of 140 micrometers one then ends up with a pressure difference of roughly $\Delta p^{M} \approx 25\,\text{bars}$. As all assumptions in this calculation have been made very cautiously leading to a much higher permeability than in reality, the real value of the required pressure difference should be even higher. As in real DMFC operation the maximum pressure differences do not exceed 1-2 bars, one can conclude that viscous flow can only contribute a few percent to the measured membrane crossover fluxes. Therefore, it is justified to neglect pressure-driven flow in the membrane model, leading to a simpler physical and mathematical description which in turn results in faster simulations.

After these preliminaries, the MEA submodel is formulated in the following chapters.

6.9.1 Anode Catalyst Layer (AC)

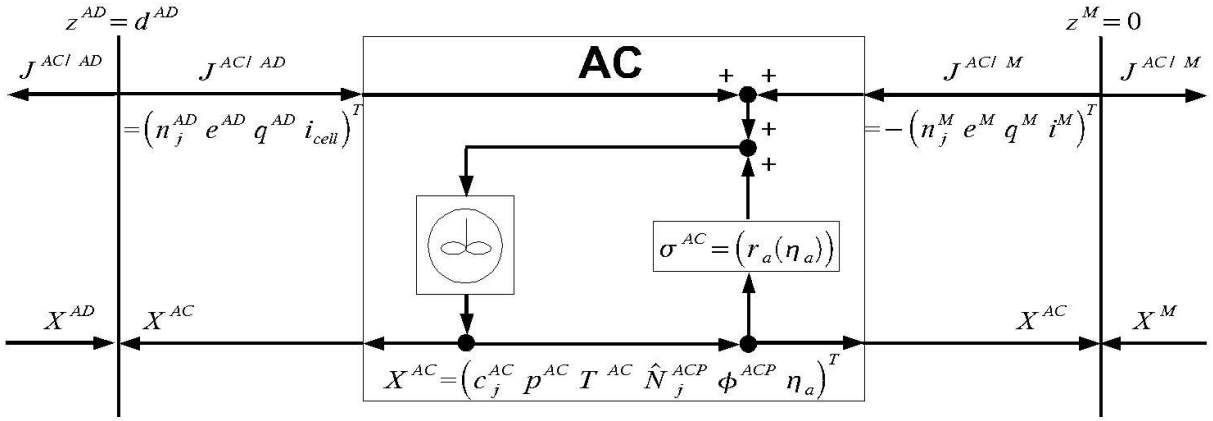

Figure 6-13 *Decomposition of anode catalyst layer (AC) on the level of storages*

As described above, in the anode catalyst layer we find several phases which are highly interconnected (free pores, polymer phase, electron conductor). In (AC) we have water, methanol and carbon dioxide as mobile species within the free pores. Figure 6-13 schematically shows the model structure according to the network theory. The catalyst layers are modelled as concentrated parameter systems. The species mass balances of (AC) are:

$$\frac{dc_j^{AC}}{dt} = \frac{n_j^{AD}(z^{AD} = d^{AD}) - n_j^{M}(z^{M} = 0)}{\varepsilon_{pores}^{AC}\, d^{AC}} + \nu_{a,j}\, r_a \qquad (6\text{-}80)$$

$$\text{with} \quad j = H_2O, CH_3OH, CO_2$$

with the stoichiometric coefficients of the anodic electrochemical methanol oxidation $\nu_{a,j}$:

$$\nu_{a,CH_3OH} = -1 \qquad \nu_{a,H_2O} = -1 \qquad \nu_{a,CO_2} = +1 \qquad \nu_{a,H^+} = +6 \qquad (6\text{-}81)$$

r_a is the rate expression (in the form of a Butler-Volmer equation as a first approach):

$$r_a = k_a \left[x_{CH_3OH}^{AC} \exp\left(\frac{\alpha_a 6F}{RT^{AC}} \eta_a \right) - x_{CO_2}^{AC} \exp\left(-\frac{(1-\alpha_a)6F}{RT^{AC}} \eta_a \right) \right] . \qquad (6\text{-}82)$$

In eq.(6-82) k_a is the rate constant [mol m^{-3} s^{-1}] (value for simulation: $k_a = 6 \cdot 10^{-3}$ mol m^{-3} s^{-1}), α_a is the charge transfer coefficient (set to $\alpha_a = 0.1$) and η_a is the anode overpotential [V]. The water mole fraction is not included due to the fact that it can be assumed to be close to unity and is not changing significantly. Therefore, the water concentration does not have an influence on the anode reaction kinetics.

Due to the very complex reaction mechanism (see chapter 1) the here applied Butler-Volmer rate equation, eq.(6-82), is of course a simplified kinetic description which should be exchanged by more detailed models in subsequent works. Such more detailed kinetic models

have to account for methanol oxidation reaction intermediates and adsorption and desorption phenomena on the binary anode catalyst. First approaches are proposed in [16][75], but the number of free model parameters to be determined is considerable.

The concentrations of water and methanol in (ACP) are calculated assuming phase equilibrium with the pores in (AC), as described above in the introduction of chapter 6.9.

The total mass balance is given by

$$\frac{dp^{AC}}{dt} = -\frac{v_{sound}^{2}}{d^{AC}}\left(m_{tot}^{M}(z^{M}=0) - m_{tot}(z^{AD}=d^{AD})\right) \quad . \tag{6-83}$$

As the cell is operated galvanostatically (i.e. the cell current density i_{cell} is a known operating parameter), the charge balance can be formulated quasi-stationary:

$$0 = i_{cell} - i^{M}(z^{M}=0) \quad .$$

Due to the quasi-stationarity of the charge balance, the mass and charge balances are not coupled. Therefore, the current density of the anodic reaction, i_a, expressed in terms of the anodic rate expression, eq.(6-82), is identical to the known cell current density:

$$i_a = d^{AC} \cdot \varepsilon_{pores}^{AC} \cdot 6 \cdot F \cdot r_a(\eta_a) = i_{cell} \quad . \tag{6-84}$$

From eq.(6-84) and the anodic rate expression, eq.(6-82), the anode overpotential can be calculated numerically.

Finally, the energy flux densities at the interfaces between (AC) and (AD) and (AC) and (M), respectively, are accounted for in the energy balance of (AC):

$$\frac{dT^{AC}}{dt} = -\frac{1}{\widetilde{(\rho c_p)}^{AC} d^{AC}}\left(\left(e^{M}(z^{M}=0) - e^{AD}(z^{AD}=d^{AD})\right) + \left(q^{M}(z^{M}=0) - q^{AD}(z^{AD}=d^{AD})\right)\right) \tag{6-85}$$

Joule heating is neglected within (AC).

6.9.2 Cathode Catalyst Layer (CC)

Very similar to (AC) also in (CC) spatially concentrated balances for mass, charge and energy are formulated (Figure 6-14). The mass balances for oxygen, nitrogen, water vapour and carbon dioxide are formulated in molar concentrations:

$$\frac{dc_j^{CC}}{dt} = \frac{n_j^{M}(z^{M}=d^{M}) - n_j^{CD}(z^{M}=0)}{\varepsilon_{pores}^{CC} d^{CC}} + \nu_{c,j} r_c + \nu_{cross,j} r_{cross} \tag{6-86}$$

with $j = N_2, O_2, H_2O, CO_2$

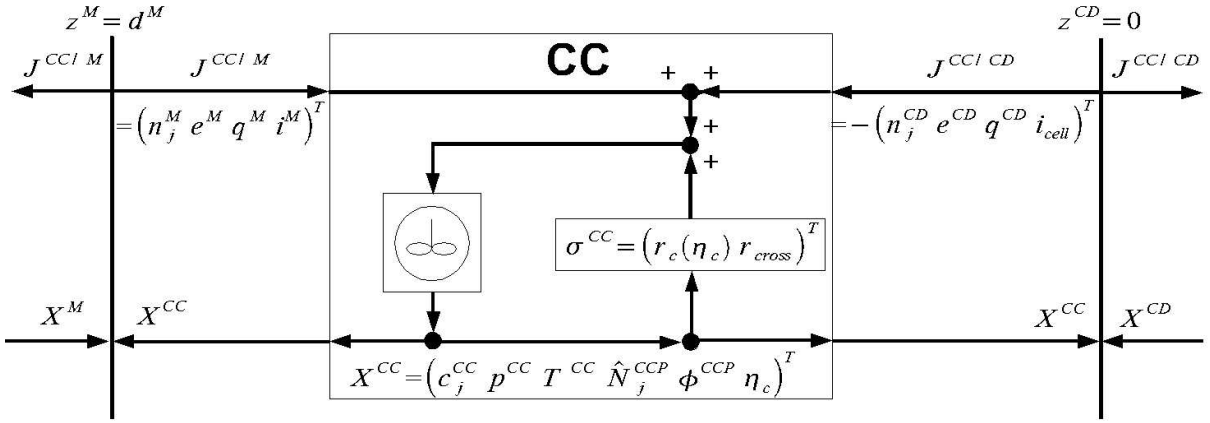

Figure 6-14 *Decomposition of cathode catalyst layer (CC) on the level of storages*

In eq.(6-86) not only the (desired) electrochemical oxygen reduction has to be accounted for, but also the (undesired) direct methanol oxidation:

a) Oxygen reduction (consumes H+ and e-): $1.5\ O_2 + 6\ H^+ + 6e^- \rightarrow 3\ H_2O$ (6-87)

b) Methanol oxidation (produces H+ and e-): $CH_3OH + 0.5\ O_2 \rightarrow CO_2 + 4\ H^+ + 4e^-$ (6-88)

The stoichiometric coefficients of these reactions are

$$\nu_{c,O_2} = -1.5 \qquad \nu_{c,N_2} = 0 \qquad \nu_{c,H_2O} = +3 \qquad \nu_{c,CO_2} = 0 \qquad \nu_{c,H^+} = -6$$

and

$$\nu_{cross,O_2} = -0.5 \qquad \nu_{cross,N_2} = 0 \qquad \nu_{cross,H_2O} = 0 \qquad \nu_{cross,CO_2} = +1 \qquad \nu_{cross,H^+} = +4 \ .$$

It is known that the reaction mechanism of the electrochemical oxygen reduction is complicated with several possible intermediates. However, as in (AC), in order to keep the number of unknown parameters small, again the Butler-Volmer equation is applied:

$$r_c = k_c \left[\left(\frac{p_{O_2}^{CC}}{10^5\ \text{Pa}} \right)^{1.5} \exp\left(-\frac{\alpha_c\, 6\, F}{R\, T^{CC}} \eta_c \right) - \exp\left(-\frac{(1-\alpha_c)\, 6\, F}{R\, T^{CC}} \eta_c \right) \right] \qquad (6\text{-}89)$$

In eq.(6-89) k_c is the rate constant [mol m^{-3} s^{-1}] (for simulation: $k_c = 1.27 \cdot 10^{21}$ mol m^{-3} s^{-1}), α_c is the charge transfer coefficient (set to $\alpha_c = 0.5$) and η_c is the cathode overpotential [V].

Methanol is assumed to be immediately consumed when coming into contact with the cathode. Therefore its concentration in (CCP) and (CC) drops to zero. Under these conditions the rate of the direct oxidation of methanol at the cathode, r_{cross}, is proportional to the methanol flux from (M) to (CC):

$$r_{cross} = \frac{n_{CH_3OH}^M (z^M = d^M)}{d^{CC}\, \varepsilon_{pores}^{CC}} \ . \qquad (6\text{-}90)$$

The concentration of water in (CCP) is calculated from an equilibrium condition (as described in the introduction of chapter 6.9).

The overall pressure p^{CC} is calculated from the concentrations of all four gas species $c_j^{CC,}$ according to the ideal gas law:

$$p^{CC} = R\,T^{CC} \sum_j c_j^{CC} \tag{6-91}$$

Following the same argumentation as for (AC) (chapter 6.9.1), the total charge balance is formulated quasi-stationary, and is decoupled from the mass balances as the cell is operated galvanostatically:

$$0 = i_{cell} - i^M\,(z^M = d^M) \tag{6-92}$$

As at the cathode two electrochemical reactions take place simultaneously (oxygen reduction with the charge production rate r_c, and methanol oxidation with the charge production rate r_{cross}), a charge balance has to be formulated either for the electron or the proton conductor phase. For the electron conductor phase this quasi-stationary charge balance is given by:

$$0 = i_{cell} + (i_{cross} + i_c) \quad . \tag{6-93}$$

In eq.(6-93) the current density of the cathode oxygen reduction reaction is given by

$$i_c = d^{CC}\,\varepsilon_{pores}^{CC}\,6\,F\,r_c \tag{6-94}$$

(6 exchanged electrons per net reaction) and the current density of the oxidation of crossover methanol analogous by

$$i_{cross} = d^{CC}\,\varepsilon_{pores}^{CC}\,4\,F\,r_{cross} \quad . \tag{6-95}$$

(4 exchanged electrons per net reaction).

From eqs.(6-93), (6-94) and (6-95) together with the cathode rate expresssion, eq.(6-89), the cathode overpotential η_c can be determined numerically.

Finally, analogue to (AC), the energy balance for (CC) is formulated as:

$$\frac{dT^{CC}}{dt} = -\frac{1}{\widetilde{(\rho\,c_p)}^{CC}\,d^{CC}}\left(\left(e^{CD}\,(z^{CD}=0) - e^M\,(z^M = d^M)\right) + \left(q^{CD}\,(z^{CD}=0) - q^M\,(z^M = d^M)\right)\right) \quad . \tag{6-96}$$

Like in (AC), Joule heating is neglected.

6.9.3 Polymer Electrolyte Membrane (M)

The membrane is connected to the polymer phases within both catalyst layers. In the polymer phase the only mobile species are protons, water and methanol, as the membrane material is assumed to be impermeable for all gases.

6.9.3.1 Balances

The membrane (M) is a one-dimensional transport element like the diffusion layers (AD) and (CD), as shown in Figure 6-15.

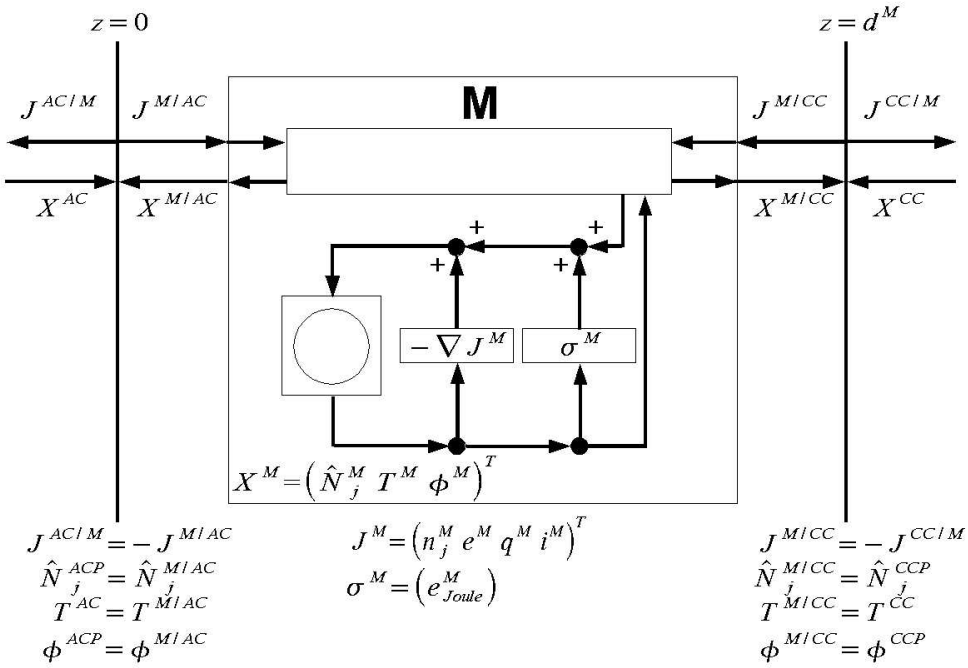

Figure 6-15 *Decomposition of membrane (M) on the level of storages, spatially distributed*

As described in chapter 1.2 and the introduction to chapter 6.9, the material structure and the occuring physical phenomena are much more complex than in the diffusion layers. The polymer electrolyte has not a constant porosity, but one that strongly depends on the local water and methanol content. The relative water content Λ, eq.(6-76), can have values between Λ=0 (totally dry membrane) and Λ≈30 (fully swollen with water and methanol at room temperature), depending on temperature and pre-treatment of the material. E.g. boiling in glycerol can increase the maximum relative water content up to values of 50-60 at high temperatures. Different water and methanol contents result in different degrees of swelling, and therefore different thicknesses and porosities. Therefore, it is not suitable to formulate mass balances in molar concentrations, as these refer to a constant overall volume. It is more convenient to use a concentration measure which refers to the constant cross-sectional area of the cell, A^S. This molar density $\hat{N}_j$ [mol m^{-2}] is defined as quotient of the total molar amount of species *j*, N_j [mol], and the cell cross-sectional area A^S [m^2]:

$$\hat{N}_j = \frac{N_j}{A^S} \quad . \tag{6-97}$$

For the mass transport equations (see next chapter) a variety of other concentration measures are needed. The necessary conversions are given in the appendix, chapter 9.8.

Using the introduced molar density, the mass balances for the control volumes (index *k*) in the discretised model have the form

$$\frac{d\,\hat{N}^{M}_{j,k}}{d\,t} = n^{M}_{j,k} - n^{M}_{j,k+1} \quad \text{with } j = \mathrm{H_2O},\ \mathrm{CH_3OH}. \tag{6-98}$$

In eq.(6-98), swelling of the membrane is assumed to be in the steady state. A total mass balance is not formulated, as pressures are not discussed within the membrane (see introduction to chapter 6.9).

The charge balance is considered in steady state (quasi-stationary):

$$0 = -\frac{\partial\, i^{M}}{\partial\, z} \quad . \tag{6-99}$$

Like the mass balances, the energy balance is quite similar to that in the diffusion layers. The only difference is that it has to account not only for convective and conductive heat fluxes, but also for Joule heating resulting from the (comparably high) electric resistance of the membrane caused by friction between mobile charged species and the immobilised counter charges at the pore walls. The heat production due to Joule heating, e^{M}_{Joule} [J m^{-3} s^{-1}], is proportional to the electric current i^M and the gradient of the electric potential Φ^M:

$$e^{M}_{Joule} = i^{M}\,\frac{\partial\,\phi^{M}}{\partial\, z} \quad . \tag{6-100}$$

Combining the general energy balance, eq.(6-18) on page 97, with eq.(6-100), one yields

$$\frac{\partial\, T^{M}}{\partial\, t} = \frac{1}{\widetilde{(\rho\, c_p)^{M}}}\left[-\frac{\partial\, e^{M}}{\partial\, z} - \frac{\partial\, q^{M}}{\partial\, z} + i^{M}\,\frac{\partial\,\phi^{M}}{\partial\, z} \right] \quad . \tag{6-101}$$

6.9.3.2 Transport Equations

In the following, transport equations for mass and energy are formulated for (M). The charge transport is expressed in terms of the proton flux. Mass transport is described using the Maxwell-Stefan approach, as has already been done for the diffusion layers. But in the membrane, as described in the previous chapters, a more complex formulation of the driving forces has to be chosen. First, the migration term has to be included, as one of the mobile species (protons) is charged and an electric field is present within the membrane. Second, the diffusive term has to account for the highly non-ideal behaviour of the mobile species within the membrane pores, i.e. the gradients of the chemical potentials have to be used as driving force, which are equal to the gradients in the species activities (calculated using the presented

Flory-Huggins approach). The pressure-dependency of the chemical potentials can be neglected as this is an incompressible (liquid) system. Also, as discussed in the introduction of chapter 6.9, viscous flow due to pressure differences over the membrane can be neglected. All this leaves the following form of the Maxwell-Stefan equations for the mobile species (j = H^+, H_2O, CH_3OH):

$$-c_j^M \frac{1}{a_j^M}\frac{\partial a_j^M}{\partial z} - z_j^* c_j^M \frac{F}{RT^M}\frac{\partial \phi^M}{\partial z} = \sum_{i \neq j} \frac{x_i^M n_j^M - x_j^M n_i^M}{\mathbb{D}_{ij}^{M,eff}} + \frac{n_j^M}{\mathbb{D}_{jM}^{M,eff}} \qquad (6\text{-}102)$$

In eq.(6-102), as superficial viscous flow due to pressure gradients is not accounted for, the total molar flux densities n_i appear in the friction terms on the right hand side of the equation. Three of the six binary diffusion coefficients $\mathbb{D}_{ij}^{M,eff}$ are taken from the literature [64], the others are estimated (see appendix chapter 9.1.8 for details).

As the flux density of protons $n_{H^+}^M$ is given by the electric current density i_{cell} using Faraday's law

$$n_{H^+}^M = \frac{i^M}{F} = \frac{i_{cell}}{F} \quad , \qquad (6\text{-}103)$$

only two unknown fluxes have to be determined (for water and methanol).

As presented for (AD) and (CD), the flux-implicit transport equations,eq.(6-102) , can be transformed into a flux-explicit form by formulating them as vector equations. But here, for only two mobile species, it is also possible to easily obtain an explicit formulation for the flux densities by simple rearranging.

The Maxwell-Stefan equations for water and methanol are:

$$\underbrace{-\frac{c_{H_2O}^M}{a_{H_2O}^M}\frac{\partial a_{H_2O}^M}{\partial z}}_{L_{H_2O}} = \frac{x_{H^+}^M n_{H_2O}^M - x_{H_2O}^M n_{H^+}^M}{\mathbb{D}_{H^+,H_2O}^{M,eff}} + \frac{x_{CH_3OH}^M n_{H_2O}^M - x_{H_2O}^M n_{CH_3OH}^M}{\mathbb{D}_{H_2O,CH_3OH}^{M,eff}} + \frac{n_{H_2O}^M}{\mathbb{D}_{H_2O,M}^{M,eff}} \qquad (6\text{-}104)$$

$$\underbrace{-\frac{c_{CH_3OH}^M}{a_{CH_3OH}^M}\frac{\partial a_{CH_3OH}^M}{\partial z}}_{L_{CH_3OH}} = \frac{x_{H^+}^M n_{CH_3OH}^M - x_{CH_3OH}^M n_{H^+}^M}{\mathbb{D}_{H^+,CH_3OH}^{M,eff}} + \frac{x_{H_2O}^M n_{CH_3OH}^M - x_{CH_3OH}^M n_{H_2O}^M}{\mathbb{D}_{H_2O,CH_3OH}^{M,eff}} + \frac{n_{CH_3OH}^M}{\mathbb{D}_{CH_3OH,M}^{M,eff}} \qquad (6\text{-}105)$$

One can see that the middle terms on the right hand sides are negative identical, so adding up both equations eliminates those terms, and by simple rearranging one obtains the methanol flux density:

$$n^M_{CH_3OH} = \frac{L_{H_2O} + L_{CH_3OH} - n_{H^+} L_1 - n_{H_2O} L_2}{L_3} \tag{6-106}$$

with

$$L_1 = -\frac{x_{H_2O}}{\mathcal{D}^{eff}_{H^+,H_2O}} - \frac{x_{CH_3OH}}{\mathcal{D}^{eff}_{H^+,CH_3OH}} \quad , \tag{6-107}$$

$$L_2 = \frac{x_{H^+}}{\mathcal{D}^{eff}_{H^+,H_2O}} + \frac{1}{\mathcal{D}^{eff}_{H_2O,M}} \quad \text{and} \tag{6-108}$$

$$L_3 = \frac{x_{H^+}}{\mathcal{D}^{eff}_{H^+,CH_3OH}} + \frac{1}{\mathcal{D}^{eff}_{CH_3OH,M}} \quad . \tag{6-109}$$

Inserting this into eq.(6-104), one obtains the water flux density:

$$n^M_{H_2O} = \frac{L_{H_2O} - n_{H^+}\left(L_4 - \frac{L_1 L_6}{L_3}\right) - (L_2 + L_3)\frac{L_6}{L_3}}{L_5 - \frac{L_2 L_6}{L_3}} \tag{6-110}$$

with

$$L_4 = -\frac{x_{H_2O}}{\mathcal{D}^{eff}_{H^+,H_2O}} \quad , \tag{6-111}$$

$$L_5 = \frac{x_{H^+}}{\mathcal{D}^{eff}_{H^+,H_2O}} + \frac{x_{CH_3OH}}{\mathcal{D}^{eff}_{H_2O,CH_3OH}} + \frac{1}{\mathcal{D}^{eff}_{H_2O,M}} \quad \text{and} \tag{6-112}$$

$$L_6 = -\frac{x_{H_2O}}{\mathcal{D}^{eff}_{H_2O,CH_3OH}} \quad . \tag{6-113}$$

With these equations, all necessary transport equations are available. What remains yet unknown is the electric potential gradient $\partial \phi^M / \partial z$ in the membrane material, due to the transport resistance to the proton flux ("Ohmic drop" over membrane). It is calculated from the Maxwell-Stefan transport equation for the protons:

$$\underbrace{-\frac{c^M_{H^+}}{a^M_{H^+}} \frac{\partial a^M_{H^+}}{\partial z}}_{L_{H^+}} - \frac{c^M_{H^+} F}{RT^M} \frac{\partial \phi^M}{\partial z} = \frac{x^M_{H_2O}\, n^M_{H^+} - x^M_{H^+} n^M_{H_2O}}{\mathcal{D}^{M,eff}_{H^+,H_2O}} + \frac{x^M_{CH_3OH}\, n^M_{H^+} - x^M_{H^+} n^M_{CH_3OH}}{\mathcal{D}^{M,eff}_{H^+,CH_3OH}} + \frac{n^M_{H^+}}{\mathcal{D}^{M,eff}_{H^+,M}} \quad . \tag{6-114}$$

Rearranging yields the electrical potential gradient in the membrane:

$$\frac{\partial \phi^M}{\partial z} = -\frac{RT^M}{c^M_{H^+} F}\left(L_{H^+} + n_{H^+} L_7 + n_{H_2O} L_8 + n_{CH_3OH} L_9\right) \tag{6-115}$$

with

$$L_7 = \frac{x_{H_2O}}{\mathcal{D}^{eff}_{H^+,H_2O}} + \frac{x_{CH_3OH}}{\mathcal{D}^{eff}_{H^+,CH_3OH}} + \frac{1}{\mathcal{D}^{eff}_{H^+,M}} \quad , \tag{6-116}$$

$$L_8 = -\frac{x_{H^+}}{\mathcal{D}^{eff}_{H^+,H_2O}} \quad \text{and} \tag{6-117}$$

$$L_9 = -\frac{x_{H^+}}{\mathcal{D}^{eff}_{H^+,CH_3OH}} \quad . \tag{6-118}$$

The problem with eq.(6-115) is, that for the protons no Flory-Huggins non-ideality parameters are known. Therefore, as a first approach, the activity of protons is approximated by the mole fraction of protons in the pore liquid, $x^M_{H^+}$.

As no superficial convective flow is calculated in the membrane, the question might arise whether electro-osmotic flow is correctly accounted for in the presented model. Basically electro-osmosis is transport of all mobile species in a mixture due to drag exerted on uncharged species by the charged species which move along an electric field. In the presented model, these phenomena are accounted for: Protons move along the electric field (migration) and exert friction on the uncharged species water and methanol (friction terms). One can show that the presented model, with respect to electro-osmotic flow, is equivalent to an often used approach first proposed by SCHLÖGL [100] for combined electro-osmotic and pressure-driven convective transport:

$$v = -\frac{k_\phi c^M_{H^+} F}{\mu^{vis}_{H^+/H_2O}} \frac{\partial \phi}{\partial z} - \frac{k_p}{\mu^{vis}_{H^+/H_2O}} \frac{\partial p}{\partial z} \quad . \tag{6-119}$$

In eq.(6-119) the superficial velocity v is the sum of an electro-osmotic term proportional to the gradient of the electric potential ϕ and one term for pressure-driven flow proportional to the gradient of the pressure p. Both terms feature a permeability parameter k (electrokinetic and hydraulic permeability, k_ϕ and k_p [m²], respectively) and the viscosity of the pore fluid $\mu^{vis}_{H^+/H_2O}$ [kg m^{-1} s^{-1}]. Other parameters are the proton concentration in the pores $c^M_{H^+}$ [mol m^{-3}] and Faraday's constant F (96485 A s mol^{-1}).

As here only electro-osmosis shall be discussed, the pressure-driven term is skipped:

$$v = -\frac{k_\phi c^M_{H^+} F}{\mu^{vis}_{H^+/H_2O}} \frac{\partial \phi}{\partial z} = -f_{Schlögl} \frac{\partial \phi}{\partial z} \tag{6-120}$$

For fully hydrated NAFION™ at 25°C the parameters can be found in the literature [101]:

$$k_\phi = 1.13 \cdot 10^{-19}\ \mathrm{m}^2 \quad ; \qquad c_{H^+} = 1200\ \mathrm{mol\ m^{-3}} \quad ;$$

$$\mu^{vis}_{H^+/H_2O} = 3.353 \cdot 10^{-4}\ \mathrm{kg\ m^{-1}\ s^{-1}} \quad .$$

With these values, the proportionality factor in SCHLÖGL's equation becomes

$$f_{Schlögl} = 3.9 \cdot 10^{-8}\ \mathrm{A\ s^2\ kg^{-1}} \quad . \tag{6-121}$$

Formulating the presented Maxwell-Stefan model (eq.(6-102)) for a fully hydrated membrane (i.e. no activity gradients) and only water and protons as mobile species (no methanol), one obtains the two transport equations:

H^+: $$-z^*_{H^+} c^M_{H^+} \frac{F}{RT^M} \frac{\partial \phi^M}{\partial z} = \frac{x^M_{H_2O} n^M_{H^+} - x^M_{H^+} n^M_{H_2O}}{\mathcal{D}^{eff}_{H^+/H_2O}} + \frac{n^M_{H^+}}{\mathcal{D}^{eff}_{H^+/M}} \quad \text{and} \tag{6-122}$$

H_2O: $$0 = \frac{x^M_{H^+} n^M_{H_2O} - x^M_{H_2O} n^M_{H^+}}{\mathcal{D}^{eff}_{H^+/H_2O}} + \frac{n^M_{H_2O}}{\mathcal{D}^{eff}_{H_2O/M}} \quad . \tag{6-123}$$

As only water and protons are assumed to be within the pores, their mole fractions sum up to unity:

$$x^M_{H^+} + x^M_{H_2O} = 1 \quad . \tag{6-124}$$

Combining these three equations and rearranging yields an expression for the molar proton flux density as function of the proton concentration and the electric potential gradient:

$$n^M_{H^+} = -\frac{1}{\beta_{H^+/H_2O}} \frac{c^M_{H^+} F}{RT^M} \frac{\partial \phi^M}{\partial z} \tag{6-125}$$

The binary diffusion coefficients and the proton mole fraction are combined in the parameter

$$\beta_{H^+/H_2O} = \frac{1 - x^M_{H^+}}{\mathcal{D}_{H^+/H_2O}} - \frac{x^M_{H^+}(1 - x_{H^+})}{\left(x^M_{H^+} + \frac{\mathcal{D}_{H^+/H_2O}}{\mathcal{D}_{H_2O/M}} \right) \mathcal{D}_{H^+/H_2O}} + \frac{1}{\mathcal{D}_{H^+/M}} \tag{6-126}$$

which has the dimension [s m^{-2}]. To transform this into a form which is comparable to SCHLÖGL's equation, the conversion between molar flux densities n_i and velocity v is performed needing the pore concentration $c^M_{H^+}$ and the pore volume fraction ε^M_{pores}:

$$n^M_{H^+} = \tilde{c}^M_{H^+} v = \varepsilon^M_{pores} c^M_{H^+} v \quad . \tag{6-127}$$

This yields an expression for the electro-osmotic velocity

$$v = \frac{n^M_{H^+}}{\varepsilon^M_{pores}\, c^M_{H^+}} = -\frac{F}{\varepsilon^M_{pores}\, \beta_{H^+/H_2O}\, R\, T}\frac{\partial \phi^M}{\partial z} = -f_{MS}\frac{\partial \phi^M}{\partial z} \qquad (6\text{-}128)$$

whose structure is equivalent to SCHLÖGL's equation for pure electro-osmotic flow, eq.(6-120). Using the literature values for the three binary diffusion coefficients [64] (appendix chapter 9.1.8) and the pore volume fraction of fully hydrated NAFION™ at 25°C, $\varepsilon^M_{pores} = 0.47$, one obtains a proportionality factor of

$$f_{MS} = 3.3 \cdot 10^{-8}\ \mathrm{A\,s^2\,kg^{-1}}$$

which is close to the SCHLÖGL proportionality factor $f_{Schlögl}$, given by eq.(6-121). Obviously the presented Maxwell-Stefan transport model accounts for electro-osmotic transport in a way which in the end yields the same results as the classical approach.

The advantage of the Maxwell-Stefan approach now lies in the following two facts. First, even in multi-component liquid mixtures it accounts for the individual electro-osmotic influence on each mobile species (represented by their binary diffusion coefficients with protons, the pore walls and water as main components). Second, the (strong) temperature and concentration dependence of the SCHLÖGL-parameter k_Φ is automatically accounted for in the Maxwell-Stefan model, as long as the diffusion coefficients are formulated as functions of temperature and water content. Especially the latter advantage is very important, as high gradients in the local relative water content can occur within the membrane.

For the energy balance in (M), transport equations are needed for thermal conduction and convective heat transport. Both are similar to the equations for (AD) and (CD):

Conductive heat flux: $$q^M = -\lambda^{M,eff}\frac{\partial T^M}{\partial z}\ , \qquad (6\text{-}129)$$

Enthalpy flux (convective heat flux): $$e^M = \sum_j n^M_j\, h_j(T^M)\ . \qquad (6\text{-}130)$$

The effective thermal conductivity $\lambda^{M,eff}$ (simplifyingly assumed fully hydrated NAFION™) and the specific enthalpies h_j are calculated in the appendix chapters 9.1.3 and 9.1.4, respectively.

6.10 Simulation of Full DMFC Model

Finally, all model blocks outlined above are combined to the full DMFC model containing all presented governing equations, i.e. balances, kinetics and thermodynamic relations. Figure 6-16 shows selected steady state simulation results and corresponding experimental data for

anode feed temperatures from 30°C up to 90°C. It has to be emphasised that all simulation results are obtained using the same set of parameters taken from the literature. All other operating conditions are given in the figures (See appendix chapter 9 for detailed derivation of all parameters). Only the parameters for the calculation of the binary diffusion coefficients have been slightly adjusted compared to the literature values in order to get a better fit of the experimental data (values given in Table 6-4):

Table 6-4 *Parameters for calculation of binary diffusion coefficients*

species pair i/j	***Original (* =[64]) parameters***		***Adjusted parameters***	
	$\mathcal{D}_{ij}^{\theta}$ ***[m² s⁻¹]***	E_{ij}^{A} ***[kJ mol⁻¹]***	$\mathcal{D}_{ij}^{\theta}$ ***[m² s⁻¹]***	E_{ij}^{A} ***[kJ mol⁻¹]***
H_2O / H^+	$0.85 \cdot 10^{-10}$ (*)	10.54 (*)	$0.15 \cdot 10^{-10}$	10.54
H_2O / M	$0.55 \cdot 10^{-11}$ (*)	20.25 (*)	$0.20 \cdot 10^{-11}$	50.25
H^+ / M	$0.22 \cdot 10^{-10}$ (*)	10.54 (*)	$0.22 \cdot 10^{-10}$	10.54
CH_3OH / H^+	$0.85 \cdot 10^{-10}$	10.54	$0.60 \cdot 10^{-10}$	8.43
CH_3OH / M	$0.55 \cdot 10^{-11}$	20.25	$5.00 \cdot 10^{-11}$	25.13
CH_3OH / H_2O	$1.25 \cdot 10^{-12}$	-	$5.00 \cdot 10^{-12}$	-

The activation energys used (right column in Table 6-4) are in the typical range for diffusive transport. Interesting is the high value for the pair water/membrane. Here possibly additional thermal effects are reflected, like those related with solvation.

As one can see from Figure 6-16, in general a reasonable approximation to the experimental steady state results has been achieved. The simulation results are in the orders of the experimental membrane crossover flux densities and the current-voltage curves, and also the trends are predicted correctly, i.e. water crossover fluxes increase with current density and methanol crossover fluxes decrease with current density. Especially for the methanol crossover, all simulation results are within or close to the error bars of the experimental data. As the methanol crossover plays a key role for the performance of the DMFC, its correct prediction is crucial for an adequate model.

Significant deviations from the experimental observations exist for the crossover water flux densities at very low and very high temperatures. The experimental crossover water fluxes through the membrane show an increasing gradient with increasing current density. Such a behaviour can not be explained by the Maxwell-Stefan model, as the model assumes a linear dependency between flux and current density. Also the binary diffusion coefficients within the membrane material are formulated such, that they are increasing linearly with the local

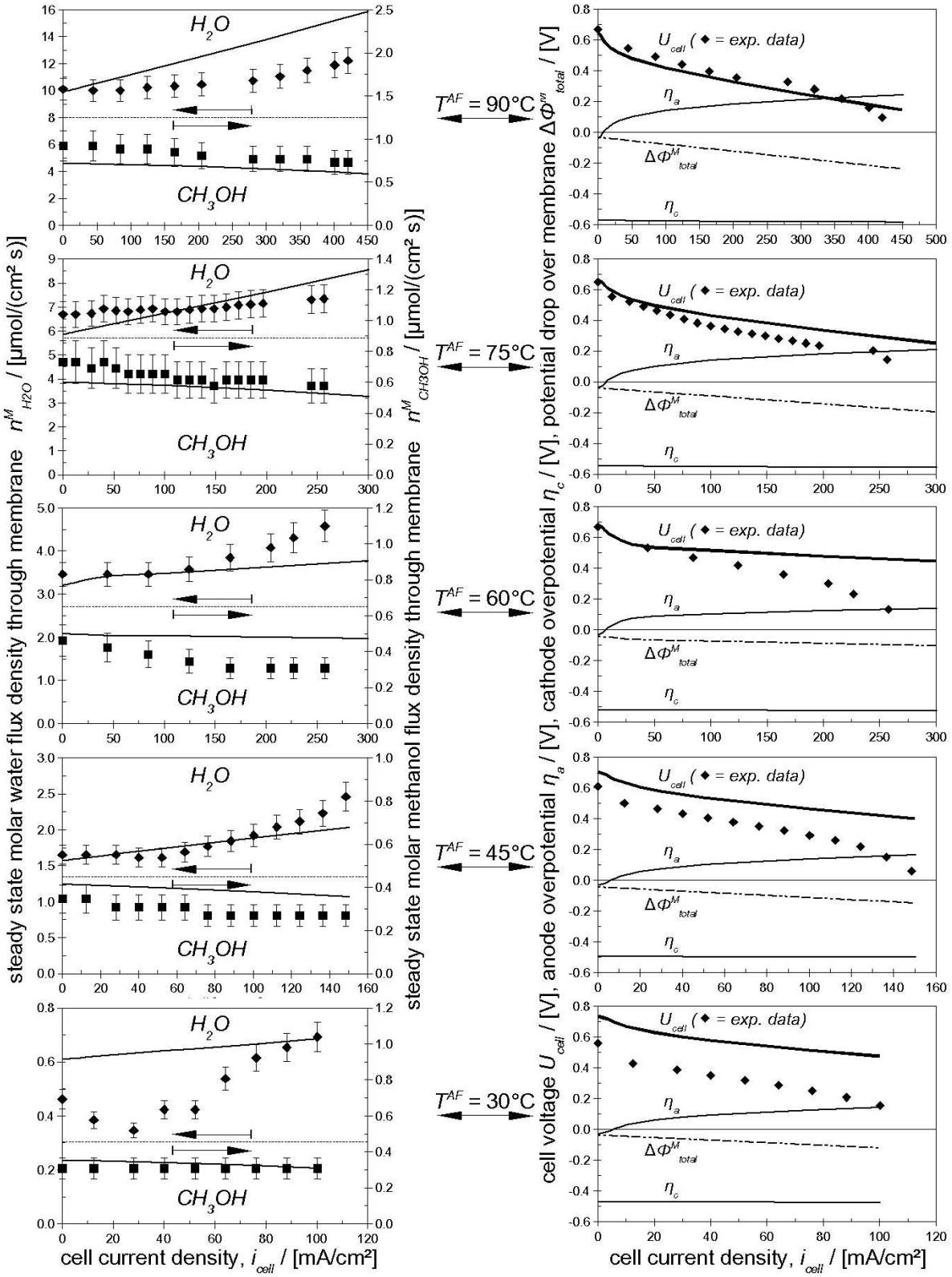

Figure 6-16 *Experimental (symbols) and simulated results (lines) for a single-cell DMFC*

Left: Crossover flux densities (left y-axis: H_2O, right y-axis: CH_3OH); Right: Current-voltage-curves (T^{AF}=30..90°C, $p^A=p^C$=1.7 bar, c^{AF}_{CH3OH}=1 mol/dm³, c^{AF}_{CO2} = 1 µmol/dm³, F^{AF}=0.5 dm³/min, F^{CF}=0.5 scbm/h, cathode feed: air with dew point 3°C @ 1 bar)

relative water content (chapter 9.1.8.1). The latter formulations for the diffusion coefficients have to be discussed. The influence of the relative water content should be taken out of the formulation for the binary diffusion coefficients, which should ideally only depend on the two respective species. Instead, the relative water content should be introduced in the transformation from the binary diffusion coefficients $\mathbf{D}_{ij}$ to the effective ones, $\mathbf{D}_{ij}^{eff}$, i.e. together with the geometric considerations (porosity and tortuosity). Also by further optimising the parameters for the calculation of the binary diffusion coefficients it can be expected to achieve a better approximation to the experimental crossover fluxes. For this purpose, numerical optimisation methods can be applied. But to do this, first the computational time of the model should be further reduced by either optimising the source code, or implementing the model in other, faster solver tools than MatLab. Finally, also the applied Flory-Huggins activity model influences the simulation results in terms of the membrane crossover fluxes. The Flory-Huggins model was originally formulated for mixtures of uncharged polymers and uncharged solvents, therefore its application for a polymer electrolyte has to be further discussed. This should be subject of subsequent works.

In the following, the current voltage curves, overpotentials and potential drops over the membrane are discussed, which are shown in Figure 6-16 (right hand side). Generally, it can be observed that the cathode overpotentials are very high, even for open circuit conditions. This is due to the oxidation of crossover methanol at the cathode, and the resulting mixed potential formation. The influence of the cell current density is only very small. In contrast to this, the anode overpotential shows a significant cell current dependency. At open circuit conditions, the anode overpotential is close to zero, for high current densities, values around 0.25 V are found. Finally, the total potential drop over the membrane shows a nearly linear increase of small extent. What is remarkable is the fact, that it is not zero at open circuit conditions. This can be explained with the diffusive flux of water through the membrane, which also takes place when no electrical current flows. The water molecules exert a drag on the protons in the membrane, but the protons are held in place by electrostatic forces between them and their counter-ions bound to the membrane material. An electric field is produced by this phenomenon, which is often referred to as streaming potential.

The next observation from Figure 6-16 is, that the experimental open circuit cell voltages increase with the cell temperature, while the model predicts a decrease. This is to a large extent due to the fact, that in the model the thermodynamic open circuit cell voltage is used as it was derived in chapter 2. There it was shown, that the open circuit cell voltage decreases

with increasing temperature. The difference between the thermodynamic and the real behaviour results from the fact, that in reality not a one-step total methanol oxidation takes place at the anode (as is assumed in the thermodynamic considerations), but a very complex, multi-step network of adsorption and desorption processes and reaction intermediates exists. A better prediction of the open circuit voltage, based on the real situation at both electrodes, would significantly enhance the prediction of the current voltage curves.

For moderate cell current densities, the model predicts slopes of the current voltage curves, which are close to the experimental results. In this regime, the cell behaviour is dominated by mass transfer phenomena within the membrane, which are reasonably represented by the model.

At high cell current densities, finally, the predicted cell voltages are much higher than the observed experimental values. Also in the respective range of the cell current density, the experimental results exhibit a typical limiting current behaviour (breakdown of the cell voltage), while the model shows such limiting current behaviour only for significantly higher cell current densities (not shown in the plots in Figure 6-16). Here it becomes evident that the model is not accounting for two-phase behaviour in both the anode and the cathode catalyst and diffusion layers. For higher current densities it is known that in the porous anode and cathode structures of the DMFC gas and liquid phases can coexist: On the anode, carbon dioxide is produced which has a very low solubility in water-methanol solutions. Therefore, especially at high current densities the formation of gas bubbles within the anode catalyst and diffusion layer pores can occur, as it was observed for the anode flow channels (see chapter 1.6). In the cathode pore structures, liquid water may be formed if the sum of water produced by the electrochemical reactions and of water reaching the cathode by crossover is higher than the water transport capacity of the cathode diffusion layer. Therefore, both phenomena lead to increased transport resistances for the fuel (methanol) and oxidant (oxygen) to the respective electrodes and they are both most important for high current densities, i.e. for the limiting current behaviour. Such two-phase transport behaviour is not accounted for in the presented model.

As the model is one-dimensional perpendicular to the cell plane, profiles through the DMFC are obtained for concentrations, temperature, pressure and all presented fluxes. Exemplarily selected profiles (in steady state) are shown in Figure 6-17 for an anode feed temperature of 60°C and a cell current density of 200 mA/cm². All other parameters are those used in the simulations presented in Figure 6-16.

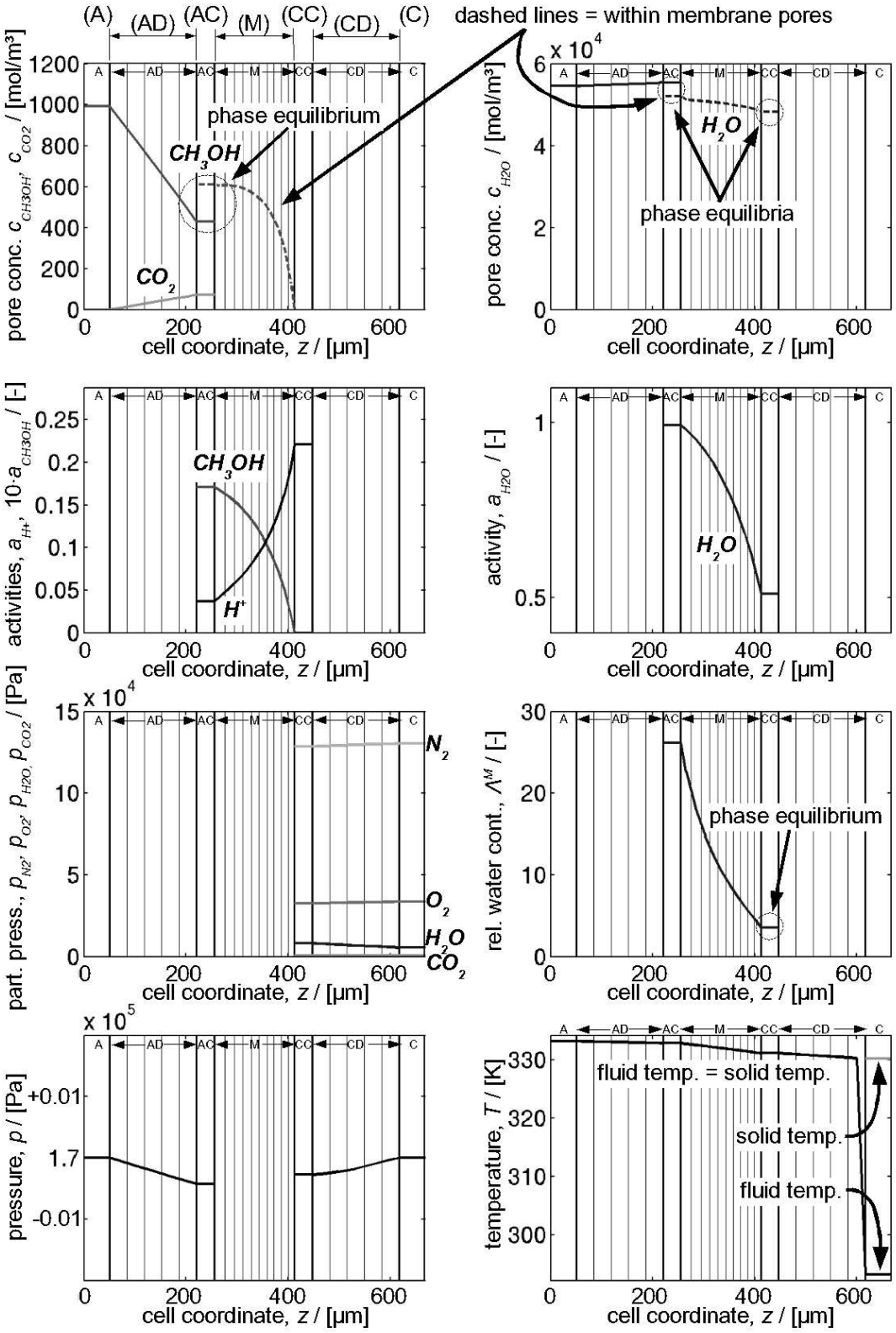

Figure 6-17 *Simulated steady state profiles (T^{AF} = 60°C, i_{cell} = 200 mA/cm², all other operating conditions as in Figure 6-16). Ordinate represents real cell geometry, vertical lines are limits of control volumes (abbreviations A, AD etc. used to denote the DMFC layers, see list of symbols)*

In Figure 6-17, the ordinates show the real cell geometry with respect to the thicknesses of the different layers of the DMFC. The vertical lines represent the limits of the control volumes, illustrating the spatial discretisation of both diffusion layers (AD,CD) and the membrane. One can see that both diffusion layers are represented by five control volumes each, and that the membrane is discretised into ten control volumes. It is also apparent, that the thicknesses (i.e. the volumes) of the diffusion layer control volumes are constant, as these layers consist of a rigid solid matrix. In contrast to this, the thicknesses (and therefore also the total volumes) of the membrane control volumes change due to different water and methanol contents, representing the swelling behaviour of the membrane material. Simplifyingly, in the model all volume changes due to swelling only influence the shown z-coordinate of the material (perpendicular to the cell plane). It has to be mentioned that the shown thicknesses of the anode and cathode channels, (A) and (C), respectively, are not plotted in the real scale.

Comparing Figure 6-17 with the profiles resulting from the submodel evaluations (anode and cathode diffusion layers, Figure 6-5, page 106, and Figure 6-8, page 113) one can see that also here for the diffusion layers nearly linear concentration and partial pressure profiles are obtained. Especially the partial pressure profiles in (CC) also exhibit only small slopes. Also similar to the submodel evaluations, for the total pressures only very small differences between the supply channels and the respective catalyst layers result (in the order of a few mPa). Obviously, according to the here applied model, mass transport in the diffusion layers is quite fast, especially on the cathode (i.e. gas) side.

Shown in the figure are also the phase equilibria for water and methanol within the catalyst layers between the free pore concentrations and the equilibrium concentrations within the membrane material (as described in chapter 6.9). One sees that on the anode side the methanol concentration in the membrane pores is higher than that in the free pores, while the water concentration in the membrane pores is lower than that in the free pores (see circles in the upper two plots of Figure 6-17). The phase equilibrium for water in the cathode catalyst layer (CC) is also highlighted by circles in the respective plots.

The most interesting concentration profiles develop within the membrane (dashed concentration profiles in the upper two diagrams of Figure 6-17). The methanol pore concentration shows a strongly bent profile in the direction of the overall flow, i.e. towards the cathode. This makes sense as methanol is dragged along with the water flow (diffusion and electro-osmosis). Also the water profile is slightly bent in the same manner due to electro-osmotic transport. Nonetheless, diffusion remains the major mode of transport for methanol and water. Most interesting is the big difference in the water content between anode and

cathode side of the membrane. While on the anode side a relative water content of around 26 is reached, on the cathode side only values around 4 are found. This is due to the operation of the cell with extremely dry air at high cathode flow rates. Water is transported away from the cathode catalyst layer (CC) very efficiently, drying out this side of the membrane according to the phase equilibrium relation (eq.(6-78)). This change in water content is also illustrated by the decreasing thickness of the membrane control volumes from anode to cathode.

The conductivity of the membrane is given by the friction exerted on the moving protons. This friction is represented by the binary diffusion coefficients, which in turn are functions of the local water content. Therefore, also the proton conductivity is a function of the local water content and thus varies locally. The same is true for the potential gradient in the membrane. In Figure 6-16 only the total potential drop over the membrane is plotted.

Finally, the temperature profile exhibits only very small gradients over the inner layers of the DMFC. The total temperature difference between anode channels and outer side of the cathode diffusion layer (CD) is less than 3 K. Only the air in the cathode channels has a much lower temperature close to its inlet temperature, due to the short residence time and the small heat exchange coefficients between channel walls and gas (see discussion in chapter 6.8.3 and Figure 6-8, page 113).

6.11 Concluding Remarks

Based on a systematic approach, a one-dimensional process model of a DMFC has been developed. In this model, mass transport within the different porous structures of the DMFC is described using the generalised Maxwell-Stefan equations. For the membrane an activity model based on the Flory-Huggins approach is used accounting for swelling phenomena, related non-idealities and phase equilibria at the boundary between membrane material and catalyst layer pores. The model yields good approximations to experimental data with respect to mass transport (crossover) and also reasonable results with respect to steady-state current voltage characteristics. It has to be pointed out, that all simulations were carried out with one single set of parameters.

The most significant deviations between simulation and experimental results occur for high current densities, in the limiting current regime. To get more realistic simulation results in this respect, two-phase flow in the anode (carbon dioxiode bubble formation) and cathode (condensation of water = cathode flooding) pore structures has to be accounted for in the model.

From the simulation results, it is possible to evaluate the importance of the different mass transport contributions (driving forces and friction) in the generalised Maxwell-Stefan framework, eq.(6-3). Table 6-5 presents the quintessence of this evaluation. In the top line, the complete eq.(6-3) is given. In the following rows the importance of the individual terms of the generalised Maxwell-Stefan equation is indicated for each of the three mass transport related layers of the DMFC and each mobile species by "++" (very important), "+" (moderately important) and blanks (not important/negligible).

Table 6-5 *Importance of mass transport contributions in eq.(6-3) (driving forces and friction terms): ++ = very important, + = important, blanks = not important/negligible*

		$-\frac{c_j}{RT}\nabla_{T,p}\mu_j$	$-\frac{c_j}{RT}\overline{V}_j\nabla p$	$-\frac{\alpha_j'}{Đ_{jM}}c_j\frac{B_0}{\eta}\nabla p$	$-c_j z_j^* \frac{F}{RT}\nabla\phi$	$=\sum_{i\neq j}\frac{x_i n$	
(AD)	H_2O	++		++		++	+
	CH_3OH	++		+		++	+
	CO_2	++		+		++	+
(M)	H^+	++			++	++	++
	H_2O	++				++	++
	CH_3OH	++				++	+
(CD)	N_2	++		++		++	+
	O_2	++		+		++	+
	H_2O	++		+		++	+
	CO_2	++		+		++	+

Obviously, multi-component diffusion represented by the gradient in the chemical potentials as driving force, left term, and both friction terms (species-species and species-matrix), right side of eq.(6-3), are the most important influencing factors for mass transport of all mobile species.

The pressure-dependence of the chemical potentials (second driving force term on the left hand side of eq.(6-3)) is negligible in all DMFC layers. This is generally justified for liquid phases if no large pressure gradients exist. This term is only relevant for applications with extremely high pressure differences as they can be found e.g. in reverse osmosis and pervaporation processes. On the gas side of the presented model, i.e. in the cathode diffusion layer (CD), it is also negligible due to the very low pressure gradient.

The third driving force is pressure-driven convection. This is accounted for in both diffusion layers and has shown to play an important role especially for the excess components in the respective fluid mixtures (water in (AD) and nitrogen in (CD)). Within the polymer electrolyte membrane this term is neglected due to the low permeability B_0 (pore diametres in the nanometer range, see chapter 6.9.3).

Finally, the electric field as driving force only plays a role for protons, which are the only mobile species carrying a charge.

7 Overall Conclusions and Outlook

The DMFC is a very promising power generation system with several possible applications especially as portable and mobile power supply, spanning the range from milliwatts up to a few kilowatts. Increasing research activities in the past ten years have resulted in considerably improved performance. Nonetheless the most important problems (methanol crossover through the membrane, slow anode kinetics, carbon dioxide evolution, cathode flooding) are yet unsolved. Some possible solutions in terms of improved membrane materials and electrocatalysts are under way, but still in the prototype state, especially stable long-term operation has still to be proven. A fairly new approach to improve performance is to establish forced dynamic operation of the DMFC [16]. While process improvements by dynamic operation are well known in other fields of chemical reaction engineering, its potential in the area of fuel cells has not yet been extensively evaluated. Also the implications of dynamic load and operating conditions on the performance of the DMFC have been as yet only sparsely addressed, although especially for portable and mobile power supply systems such operating conditions are often encountered.

In the presented work, DMFCs have been examined experimentally under steady state and dynamic operating conditions. For this purpose, a fully automated miniplant was designed, which allows the determination of water and methanol membrane crossover fluxes within the DMFC, and its dynamic operation under variation of all major operating parameters. Moreover, an own DMFC design was developed and a complete production line was established. By this, all materials and geometries of the cells to be modeled are known and can be influenced, thus knowing all material parameters of the model.

Some interesting experimental observations like cell voltage overshooting phenomena and slow drifts have been made, leading to the conclusion that the key to understanding the DMFC on the physical level are mass transport phenomena. Measured methanol and water crossover fluxes through the cell membrane indicate, that in the DMFC the main mode of transport for these two species is diffusion. The contribution of the electro-osmotic flow is significantly smaller in the DMFC as in the hydrogen-fed PEMFC.

In the development of a rigorous mathematical process model, as a first step the emphasis was put on an easily extendable (open) model structure and a detailed modeling of the transport phenomena. Concerning mass transport, good approximations to the experimental observations have been achieved using the generalised Maxwell-Stefan approach, combined with suitable activity models. The most complicated transport element in this model is the

membrane. It exhibits significant swelling behaviour which depends on the local water and methanol concentrations. To describe this highly non-ideal behaviour, the Flory-Huggins activity approach was utilised. The advantage of this combination of the Maxwell-Stefan mass transport equations and the Flory-Huggins activity model (UNIFAC activity model used in the other elements of the DMFC) is the independence of the basic transport parameters (i.e. the parameters used to calculate the binary diffusion coefficients) from the operating conditions (temperature, pressure, concentrations). These parameters can be fitted once from measured membrane crossover fluxes and remain unchanged in the further fitting of the parameters associated with the electrochemical reaction kinetics.

Further model refinement has to address the following points:

- Phase-splitting in the anode and the cathode diffusion layers,
- influence of pressure differences between anode and cathode on the water and methanol transport through the membrane (Can the respective term for pressure-driven convection in the Maxwell-Stefan equations really be neglected ?), and
- more realistic models for the anode and cathode reaction kinetics (accounting for reaction intermediates, adsorption/desorption phenomena etc.).

Parallel to the model refinement, now dynamic simulations will be started. Their results will be compared to the dynamic experimental results presented in chapter 5.

The model formulation revealed, that it is beneficial to choose a modular, systematic modeling approach. This allows the implementation of the model in a "virtual fuel cell lab", based on the modeling and simulation platform ProMoT/DIVA developed by the MPI Magdeburg and the University of Stuttgart [108]. In the last consequence, the model should be extended to a whole DMFC system consisting of a multi-cell stack, methanol water solution supply system, air supply, electrical DC/AC conversion units, electric loads (i.e. motors, electronic devices etc.), sensors, actuators and the attached process control system.

On the experimental side, further experiments will be carried out to fully examine the DMFC response to current and concentration pulses and steps, and to realistic operating scenarios. Also the differences between single cell and stack behaviour will be subject to analysis, as now a working stack concept is available. Tests using alternative catalysts and membrane materials are another step to further complete the understanding of the internal processes occuring inside the DMFC.

8 Appendix A: Error Tolerances of On-line Balancing

In the on-line balancing (sequential calculation of molar fluxes), many sensor signals are used as input information. These sensor values are afflicted with certain error tolerances (e.g. due to sensor drifts, sensor noise, fluctuations in other operational parameters inflicting the sensor etc.). To determine the overall influence on the calculated molar fluxes, the Gaussian error propagation law has to be used. All molar fluxes have to be formulated exclusively as functions of the sensor values. The final equation for the error tolerances is:

$$\Delta n_i = \sqrt{\sum_j \left(\frac{\partial n_i}{\partial v_j} \Delta v_j \right)^2} \tag{8-1}$$

with: Δn_i : error tolerance of molar flux

n_i : molar flux

v_j : sensor value

Δv_j : error tolerance of sensor (data from manufacturers)

The typical operational parameters and error tolerances based on manufacturers data are given in Table 8-1. For all temperatures, the composition of the atmospheric air and the electric current, the error tolerance was set to 0.0%. The temperatures only influence the densities of the liquids, which means negligible influence of slight temperature deviations on molar fluxes. The composition of air is extremely constant (tolerance below 0.1%). Finally, the potentiostat measuring the electric cell current also has a tolerance of less than 0.1%.

The resulting error tolerances of the molar fluxes are given in Tab.3-1. They are typically in the range of 5-20%, which corresponds to the observed fluctuations during operation of the miniplant.

Table 8-1 Sensor values and tolerances used for calculation of molar flux tolerances

Sensor value	***Meaning***	***Typical value***	***Unit***	***Tolerance [%]***	***Comment***
$\vartheta_{dew\ point}^{air\ in}$	dew point cathode inlet	3	°C	0.00	fixed/known value
$p_{dew\ point}^{air\ in}$	pressure of air supply	$8 \cdot 10^5$	Pa	0.00	fixed/known value
$y_{O_2}^{atmosphere}$	atmospheric O_2 content	20.95	vol%	0.00	fixed/known value
$y_{CO_2}^{atmosphere}$	atmospheric CO_2 content	0.035	vol%	0.00	fixed/known value
$p_D^{air\ in}$	vapour press. cath. inlet	758	Pa	0.01	from $\vartheta_{dew\ point}^{air\ in}$
$V_{CH_3OH}^{Z}$	CH_3OH dosing rate	2	cm^3/min	5.00	
$V_{H_2O}^{Z}$	H_2O dosing rate	2	cm^3/min	5.00	
ϑ^Z	ambient temperature	20	°C	0.00	minimal influence
V_{liquid}^{B}	liquid cycle flow rate	1	dm^3/min	5.00	
ϑ^B	liquid cycle temperature	80	°C	0.00	minimal influence
$w_{CH_3OH}^{B}$	methanol mass fraction	3.0	wt%	6.67	
V_{gas}^{K}	cathode air flow rate	1	m^3/h	6.50	
N_{cells}	number of single cells	1	-	0.00	fixed/known value
I_{cell}	electric cell current	5	A	0.00	highly precise
$Y_{H_2O}^{L}$	water loading cath. outl.	15	g/kg	1.50	
$y_{O_2}^{L}$	cathode outlet O_2 conc.	20.00	vol%	0.50	
$y_{CO_2}^{L}$	cathode outlet CO_2 conc.	0.10	vol%	10.00	
V_{gas}^{M}	separator air flow rate	1	m^3/h	4.00	
$w_{CH_3OH}^{D}$	methanol mass fraction	2.9	wt%	34.48	
$Y_{H_2O}^{N}$	water loading sep. outl.	60	g/kg	1.50	
y_{CO2}^{N}	sep. outlet CO_2 conc.	0.1	vol%	10.00	

9 Appendix B: Physical Properties and Parameters

In the following sections, all physical parameters used in the simulation model are presented. Where no values were available directly in the literature, the derivation procedure is given.

9.1 Physical Properties of Pure Components

9.1.1 Densities

The densities of all liquid and solid materials are assumed to be independent of temperature and pressure:

Table 9-1 *Densities (sources: [1] [102a], [2] [103], [3] [104], [4] [105])*

component j	***density ρ_j [kg m^{-3}]***
liquid water, H_2O (l)	997[1]
liquid methanol, CH_3OH (l)	791[1]
carbon/graphite (base material of TORAY™ carbon paper)	2000
Teflon™, PTFE	2190[2]
dry Nafion™	1970[4]
platinum, Pt	21400[3]
ruthenium, Ru	12400[3]

All gases are assumed to be ideal, therefore the density of dry air can be calculated using the ideal gas law:

$$\rho_{air}(p,T) = \frac{M_{air}}{V_{air}} = \frac{p}{R_{air}T} \qquad (9\text{-}1)$$

with the specific gas constant of air R_{air} = 287.22 J kg^{-1} K^{-1} [106a] , temperature T in [K] and pressure p in [Pa].

The density of the mixed anode catalyst can be calculated from the mass fractions w of both metals and their densities:

$$\rho_{PtRu} = w_{Pt}\rho_{Pt} + w_{Ru}\rho_{Ru} = 0.66 \cdot 21400 + 0.34 \cdot 12400 = 18300\,\mathrm{kg\,m^{-3}} \qquad (9\text{-}2)$$

9.1.2 Heat Capacities

For all materials the heat capacities are necessary for the energy balances. Literature data are given in the following table.

Table 9-2 *Heat capacities (sources: [1] [102b], [2] [103], [3] [104], [4] [85])*

component j	***heat capacity***	
	$\overline{C}_{p,j}$ ***[J mol^{-1} K^{-1}]***	$C_{p,j}$ ***[J kg^{-1} K^{-1}]***
liquid water, H_2O (l) [1]	75.29[1]	4183[1]
carbon/graphite (material of TORAY™ carbon paper)	8.23[4]	685[4]
Teflon™, PTFE	-	1010[2]
platinum, Pt	-	130[3]
ruthenium, Ru	-	238[3]
oxygen, O_2(g)	29.36[1]	-
nitrogen, N_2(g)	29.13[1]	-
water vapour, H_2O(g)	33.58[1]	-
carbon dioxide gas, CO_2(g)	37.11[1]	-

For air as a standard mixture of mainly nitrogen and oxygen, a mean heat capacity can be assumed:

$$\overline{C}_{p,air} = 0.79 \cdot \overline{C}_{p,N_2} + 0.21 \cdot \overline{C}_{p,O_2} = 29.18\ \mathrm{J\,mol^{-1}\,K^{-1}} \quad . \tag{9-3}$$

The mass-based value can be obtained by accounting for the molar masses of oxygen and nitrogen:

$$C_{p,air} = 0.79 \cdot \frac{\overline{C}_{p,N_2}}{\overline{M}_{N_2}} + 0.21 \cdot \frac{\overline{C}_{p,O_2}}{\overline{M}_{O_2}} = 1015\ \mathrm{J\,kg^{-1}\,K^{-1}} \tag{9-4}$$

9.1.3 Thermal Conductivities

For liquid water and air data for different temperatures are given in the literature (e.g. for water:[107a], for air:[107b]). The thermal conductivity is showing a nearly linear increase with temperature. Linear regressions yield the following simple expressions (with temperature T in [K] and λ_j in [W m^{-1} K^{-1}]):

$$\lambda_{H_2O\,(l)} = 0.341 + 9.26 \cdot 10^{-4} \cdot T \tag{9-5}$$

$$\lambda_{air} = 0.0034 + 7.6 \cdot 10^{-5} \cdot T \tag{9-6}$$

For wet Nafion™, in the literature a value of

$$\lambda_{wet\ Nafion} = 0.43\ \mathrm{W\,m^{-1}\,K^{-1}} \tag{9-7}$$

is reported [64].

9.1.4 Specific Enthalpies

The specific enthalpies h_j [J mol^{-1} K^{-1}] of the fluid components are calculated from the standard enthalpies of formation, $\Delta_F H^{\theta}_j$ [J mol^{-1} K^{-1}] at standard temperature T^{θ}=298.15 K, and the specific heat capacities $\overline{C}_{p,j}$ [J mol^{-1} K^{-1}]:

$$h_j = \Delta_F H^{\theta}_j + \overline{C}_{p,j}(T - T^{\theta}) \quad . \tag{9-8}$$

The values for the heat capacities are given in a chapter 9.1.2. The standard enthalpies of formation are:

Table 9-3 *Standard enthalpies of formation [102b]*

component j	***$\Delta_F H^{\theta}_j$ [kJ mol^{-1}]***
liquid water, H_2O (l)	-285.83
oxygen, O_2(g)	0
nitrogen, N_2(g)	0
water vapour, H_2O (g)	-241.82
carbon dioxide gas, CO_2 (g)	-393.51

For liquid methanol, no standard enthalpy of formation was found, but absolute values of the specific enthalpy for different temperatures [107c]. A linear regression and conversion from mass to molar basis yields the expression

$$h_{CH_3OH(l)} = -3726 + 48.8\,T \tag{9-9}$$

with $h_{CH3OH(l)}$ in [J mol^{-1}] and T in [K].

9.1.5 Viscosities

According to [86d] the viscosity of pure liquids in [Pa s] can be calculated from expressions of the type

$$\eta_j^{vis} = 10^{-3} \cdot \exp\left(A_j + \frac{B_j}{T} + C_j T + D_j T^2 \right) \tag{9-10}$$

with temperature T in [K]. Table 9-4 presents the values of the parameters for water, methanol and carbon dioxide as well as the temperature range, for which they are valid.

Table 9-4 *Parameters for calculation of liquid viscosities [86d]*

component j	***T [°C]***	A_j	B_j	C_j	D_j
water, H_2O(l)	0..+370	-24.700	4209.00	0.04527	$-3.376\cdot10^{-5}$
methanol, CH_3OH(l)	-40..+239	-39.350	4826.00	0.10910	$-1.127\cdot10^{-4}$
carbon dioxide, CO_2(l)	-56..+30	-3.097	48.86	0.02381	$-7.840\cdot10^{-5}$

At pressures well below 10 bara (10^6 Pa), the viscosity of most gases and gas mixtures is nearly independent of the pressure, but only a function of temperature. For air values for different temperatures (at a pressure of 1 bara = 10^5 Pa) are available in the literature:

Table 9-5 *Air viscosities at p=10^5 Pa [106a]*

T [°C]	0	10	20	30	40	60	80	100	120
η_{air}^{vis} ***[10^{-6} Pa s]***	17.24	17.74	18.24	18.72	19.20	20.14	21.05	21.94	22.80

These data show a nearly linear dependence between viscosity and temperature. A linear regression yields the expression

$$\eta_{air}^{vis} = (4.65 + 0.0464 \cdot T) \cdot 10^{-6} \qquad (9\text{-}11)$$

where the temperature T is in [K] and the viscosity results in [Pa s]. The relative error compared to the literature values is below 0.4%.

9.1.6 Vapour Pressures

The vapour pressures of water and methanol can be calculated using the Antoine equation

$$\log_{10}\left(\frac{p_{sat,j}}{[\text{bar}]}\right) = A_j - \frac{B_j}{\frac{T}{[\text{K}]} + C_j} \quad . \qquad (9\text{-}12)$$

The parameters A_j, B_j, C_j are:

Table 9-6 *Antoine equation parameters for calculation of vapour pressures [85]*

	temperature range	A_j	B_j	C_j
water, H_2O	304 - 333 K	5.20389	1733.926	-39.485
	334 - 363 K	5.07680	1659.793	-45.854
methanol, CH_3OH	288 - 356.83 K	5.20409	1581.341	-33.500
	353.4 - 512.63 K	5.15853	1569.613	-34.846

9.1.7 Liquid Molar Volumes

In some calculations, the liquid molar volumes of water. methanol, carbon dioxide and also solvated protons are necessary. For the first two, literature values are available [86e]:

$$\overline{V}_{H_2O} = 18.7 \cdot 10^{-6}\,\mathrm{m^3\,mol^{-1}} \tag{9-13}$$

$$\overline{V}_{CH_3OH} = 42.5 \cdot 10^{-6}\,\mathrm{m^3\,mol^{-1}} \quad . \tag{9-14}$$

The value for carbon dioxide can be calculated using the method of SCHROEDER [86f], which is a group contribution method. The result is

$$\overline{V}_{CO_2} = (3+2) \cdot 7\,\mathrm{cm^3\,mol^{-1}} = 35 \cdot 10^{-6}\,\mathrm{m^3\,mol^{-1}} \tag{9-15}$$

Following the same reasoning, a proton has a molar volume of

$$\overline{V}_{H^+} = 7 \cdot 10^{-6}\,\mathrm{m^3\,mol^{-1}} \quad . \tag{9-16}$$

9.1.8 Diffusion Coefficients

Two types of binary diffusion coefficients are necessary for the modeling of mass transfer using the Maxwell-Stefan approach: One for each pair of the mobile species and one for each mobile species' interaction with the wall of the porous structure. In general, all binary diffusion coefficients depend on the temperature and the overall composition.

9.1.8.1 Diffusion coefficients in the polymer electrolyte membrane (M)

For Nafion™, extensive studies have been made to determine those diffusion coefficients from experimental data. In [64] such expressions are presented. But as most research in polymer electrolyte membrane fuel cells is focused on hydrogen-consuming cells, these expressions are not accounting for methanol but just water within the ionomer pores. The expressions are of an Arrhenius type to account for the temperature influence. As only composition influence, the relative water content

$$\Lambda^M = \frac{N^M_{H_2O}}{N^M_{R-SO_3^-}} = \frac{x^M_{H_2O}}{x^M_{R-SO_3^-}} = \frac{x^M_{H_2O}}{x^M_{H^+}} \tag{9-17}$$

as ratio between water and sulfonic acid groups' mole fraction is accounted for. As the sulfonic acid groups at the pore walls are not balanced, it is more convenient to use the proton mole fraction instead. As no big deviations between the proton concentration and that of their counterions can build up (macroscopically electroneutrality is fulfilled at least in steady state), this is a justified simplification.

The general expression for the binary diffusion coefficients in [m²/s] according to [64] is:

$$\mathcal{D}_{ij}^{eff}(T, \Lambda^M) = \mathcal{D}_{ij}^{\theta} \Lambda^M \exp\left[-\frac{E_{ij}^{A}}{R}\left(\frac{1}{T}-\frac{1}{T^{\theta}}\right)\right] \tag{9-18}$$

with the reference temperature $T^{\theta} = 298$ K.

The values of the standard diffusion coefficients and the activation energies are given in the following table.

Table 9-7 *Literature parameters for calculation of binary diffusion coefficients in Nafion™ [64] (M represents solid matrix/pore wall)*

species pair i/j	$\mathcal{D}_{ij}^{\theta}$ ***[m² s⁻¹]***	E_{ij}^{A} ***[kJ mol⁻¹]***
H_2O / H^+	$0.85 \cdot 10^{-10}$	10.54
H_2O / M	$0.55 \cdot 10^{-11}$	20.25
H^+ / M	$0.22 \cdot 10^{-10}$	10.54

As in the case of the DMFC also methanol is present within the membrane pores, three more binary diffusion coefficients are necessary for the pairs (CH_3OH / H_2O), (CH_3OH / H^+) and (CH_3OH / M). As for the latter two no literature data are available, assumptions are necessary. As the methanol concentration is very low compared to that of water, an error in these two diffusion coefficients should have only a weak influence on the diffusion of water and protons. But the diffusion of methanol is of course severly depending on these three values. Nonetheless, as methanol is in many respects not so different from water (highly polar, small compact molecule) as a first approach it is assumed that methanol has the same diffusion properties as water, consequently the same parameters are used to calculate the diffusion coefficients according to eq.(9-18):

Table 9-8 *First parameter estimates for calculation of binary diffusion coefficients in Nafion™ (M represents the pore wall)*

species pair i/j	$\mathcal{D}_{ij}^{\theta}$ ***[m² s⁻¹]***	E_{ij}^{A} ***[kJ mol⁻¹]***
CH_3OH / H^+	$0.85 \cdot 10^{-10}$	10.54
CH_3OH / M	$0.55 \cdot 10^{-11}$	20.25

The remaining binary diffusion coefficient for the pair (H_2O / CH_3OH) is calculated assuming a free solution of methanol in water at infinite dilution (correlation of HAYDUK and MINHAS for solutes in aqueous solutions [86c], diffusion coefficient in [m²/s]):

$$\mathcal{D}_{CH_3OH,H_2O} \approx D^{\infty}_{CH_3OH,H_2O} = 1.25 \cdot 10^{-12} \left(\overline{V}^{-0.19}_{CH_3OH} - 0.292\right) T^{1.52} \left(\eta^{vis}_{H_2O}\right)^{\epsilon^*} \quad (9\text{-}19)$$

with the exponent $\epsilon^* = \frac{9.58}{\overline{V}_{CH_3OH}} - 1.12$, (9-20)

the molar volume of methanol $\overline{V}_{CH_3OH} = 42.5\,\mathrm{cm^3\,mol^{-1}}$

and the viscosity of pure water $\eta^{vis}_{H_2O}$ in [cP=10^3 Pa s] (see section 9.1.5).

9.1.8.2 Diffusion coefficients in the anode diffusion layer (AD)

The binary diffusion coefficients of the mobile species in the anode diffusion layer (AD) are calculated using the TYN-CALUS method [86g] for diffusion coefficients in liquid solutions at infinite dilution (in [m²/s]):

$$D^{\infty}_{ij} = 8.93 \cdot 10^{-12} \left(\frac{\overline{V}_i}{\overline{V}^2_j}\right)^{1/6} \left(\frac{P_j}{P_i}\right)^{0.6} \frac{T}{\eta^{vis}_j} \quad . \quad (9\text{-}21)$$

Here component *i* is the solute and *j* is the solvent. The molar volumes $\overline{V}_j$ are in [cm³/mol], the viscosities η^{vis}_j in [cP=10^3 Pa s] and the temperature *T* in [K]. P_i and P_j are so-called parachors, which are related to the liquid surface tension, but can also be estimated from a groups contribution method developed by QUAYLE [86g]. For water, methanol and carbon dioxide, this method leads to parachor values of

$$P_{H_2O} = 2 \cdot P_H + P_{-O-} = 2 \cdot 15.5 + 20 = 51\,\mathrm{cm^3\,g^{0.25}\,s^{-0.5}} \quad , \quad (9\text{-}22)$$

$$P_{CH_3OH} = P_{CH_3} + P_{-OH} = 55.5 + 29.8 = 85.3\,\mathrm{cm^3\,g^{0.25}\,s^{-0.5}} \quad , \quad (9\text{-}23)$$

$$P_{CO_2} = P_C + 2 \cdot P_O = 9 + 2 \cdot 20 = 49\,\mathrm{cm^3\,g^{0.25}\,s^{-0.5}} \quad . \quad (9\text{-}24)$$

According to the literature, if water is the solute, the parachor and molar volume values of water shall be doubled (water is treated as a dimer).

With the help of eq.(9-21), all six diffusion coefficients at infinite dilution for the three species (water, methanol, carbon dioxide) can be calculated. To get the necessary three binary diffusion coefficients, each pair of the former six values belonging to the same two species are combined using the method of VIGNES [86h]:

$$\mathcal{D}_{ij} \approx D_{ij} = \alpha_{Vignes} \left[\left(D^{\infty}_{ij}\right)^{x_j} \left(D^{\infty}_{ji}\right)^{x_i} \right] \quad . \quad (9\text{-}25)$$

Both mole fractions x_i and x_j are set to 0.5, the thermodynamic factor α_{Vignes} is assumed to be 1 (ideal mixing behaviour of the two species), leaving the expression

$$\mathcal{D}_{ij} = (D_{ij}^{\infty} D_{ji}^{\infty})^{0.5} \quad . \tag{9-26}$$

As the mass transport takes place within a porous matrix, effective diffusion coefficients are needed. To convert the gained values into effective coefficients, it has to be accounted for the morphology of the solid matrix represented by the tortuosity coefficient τ [95] (Note that there is a mistake in the mentioned reference: There both diffusion coefficient' sindices have been confused.):

$$\mathcal{D}_{ij}^{eff} = \frac{\varepsilon}{\tau} \mathcal{D}_{ij} \quad . \tag{9-27}$$

To describe the ratio between tortuosity coefficient τ and porosity ε, many approximations exist. According to [95],one of the most commonly used is based on the approximation that the tortuosity is only a function of the porosity (and not of the size of the mobile species):

$$\tau = \varepsilon^{-1.5} \quad . \tag{9-28}$$

The binary diffusion coefficients for the mobile species interactions with the walls of the porous structure (here: TORAY™ carbon paper) are estimated to be some orders of magnitude higher than the pair diffusion coefficients in order to account for the fact that on the one hand wall friction is negligible for diffusive transport in (AD) (following the argumentation given in chapter 6.7.2.2), on the other hand the numerical procedure to calculate the individual flux densities can run into numerical problems if the wall friction terms are omitted.

9.1.8.3 Diffusion coefficients in the cathode diffusion layer (CD)

In the cathode diffusion layer it is assumed that all mobile species (oxygen, nitrogen, water vapour and carbon dioxide) are ideal gases. The diffusion coefficients describing the influence of the pore wall are calculated using the Knudsen equation (according to [95]),

$$\mathcal{D}_{jM}^{eff} = \frac{\varepsilon}{\tau} \frac{d_{pore}}{3} \sqrt{\frac{8RT}{\pi \overline{M}_j}} \quad , \tag{9-29}$$

although here, strictly speaking, no Knudsen diffusion takes place due to the big mean pore diameter in the carbon paper which is some orders of magnitude bigger than the gas molecule diametres. It turns out that the coefficients calculated from eq.(9-29) are of such an order of magnitude, that in the end there is no significent influence of the wall friction on diffusion.

The pair diffusion coefficients of the mobile species are calculated according to the method of FULLER, SCHETTLER and GIDDINGS in free gas phase [107d] (in [m²/s]):

$$\mathcal{D}_{ij} \approx D_{ij} = \frac{10^{-7} T^{1.75} \sqrt{\frac{\overline{M}_i + \overline{M}_j}{\overline{M}_i \overline{M}_j}}}{p\left[\left(\sum \overline{V}^*\right)_i^{1/3} + \left(\sum \overline{V}^*\right)_j^{1/3} \right]^2} \quad . \tag{9-30}$$

Here the temperature T is in [K], M are the molecular weights in [g/mol], p is the pressure in [atm=10^5 Pa] and the sum terms are sums of atomic diffusion volumes, which are tabulated for many simple gases (Table 9-9). To get effective diffusion coefficients, also here eq.(9-27) is used.

Table 9-9 *Parameter values for eq.(9-30) (atomic diffusion volumes taken from [107d])*

	O_2	N_2	H_2O	CO_2
M_j [g/mol]	32	28	18	44
$\left(\sum \overline{V}^*\right)_j$ [cm³/mol]	16.6	17.9	12.7	26.9

In the simulations, the presented diffusion coefficients were used as starting values. In order to get a better fit to experimental data, some of these values have been slightly adjusted. The following table sums up the original/starting values (left), whose derivation has been shown in this chapter, and the adjusted values used in the simulation (identical to Table 6-4, p.133):

Table 9-10 *Parameters for calculation of binary diffusion coefficients*

species pair i/j	***Original (* =[64]) parameters***		***Adjusted parameters***	
	$\mathcal{D}_{ij}^0$ ***[m² s⁻¹]***	E_{ij}^A ***[kJ mol⁻¹]***	$\mathcal{D}_{ij}^0$ ***[m² s⁻¹]***	E_{ij}^A ***[kJ mol⁻¹]***
H_2O / H^+	$0.85 \cdot 10^{-10}$ (*)	10.54 (*)	$0.15 \cdot 10^{-10}$	10.54
H_2O / M	$0.55 \cdot 10^{-11}$ (*)	20.25 (*)	$0.20 \cdot 10^{-11}$	50.25
H^+ / M	$0.22 \cdot 10^{-10}$ (*)	10.54 (*)	$0.22 \cdot 10^{-10}$	10.54
CH_3OH / H^+	$0.85 \cdot 10^{-10}$	10.54	$0.60 \cdot 10^{-10}$	8.43
CH_3OH / M	$0.55 \cdot 10^{-11}$	20.25	$5.00 \cdot 10^{-11}$	25.13
CH_3OH / H_2O	$1.25 \cdot 10^{-12}$	-	$5.00 \cdot 10^{-12}$	-

9.1.9 Speed of Sound

For ideal gases the speed of sound is related to the ratio of the specific heat capacities $\kappa = C_p / C_v$, the temperature T in [K], the molar mass $\overline{M}_j$ in [kg/mol] and the universal gas constant R=8.314 J/(mol K) [107e]:

$$\kappa_{sound,\,j} = \sqrt{\frac{k_j R T}{\overline{M}_j}} \quad . \tag{9-31}$$

For air, the heat capacity ratio in the important temperature range (300..400K) and pressure range (1..5·10^5 Pa) is nearly constant at a value of 1.4 [107f].

The molar mass of air can be approximated assuming air consisting only of oxygen and nitrogen with the respective mole fractions y_{O2}=0.21 and y_{N2}=0.79:

$$\overline{M}_{air} \approx y_{O_2} \overline{M}_{O_2} + y_{N_2} \overline{M}_{N_2} = 28.84 \frac{\text{g}}{\text{mol}} \quad . \tag{9-32}$$

The speed of sound in water in the respective temperature and pressure range is nearly constant at a value of $v_{sound,H2O}$=1500 m/s.

9.2 Porosities and Volume Fractions of Fuel Cell Materials

For many purposes it is necessary to know the volume fractions of several combined materials, such as the PTFE-treated carbon papers used for the diffusion layers and the material mix forming the catalyst layers. As in the model all material balances are formulated for the free volume in the porous materials forming the respective fuel cell layers, the pore volume fractions (porosities) are vital parameters.

9.2.1 Diffusion Layers (AD/CD): PTFE-treated Carbon Paper

The major physical properties of TORAY™ paper TGP-H-060 (according to data sheet supplied by Toray Deutschland GmbH) are given in Table 9-11.

Table 9-11 *Physical properties of TGP-H-060 (from Toray Deutschland GmbH , * = own measurement used for further calculations)*

thickness [µm]	***electrical resistivity [mΩ cm]***		***thermal conductivity [W m^{-1} K^{-1}]***			***porosity [-]***	***bulk density [g/cm³]***
	through plane	in plane	through plane (20°C)	in plane (20°C)	in plane (100°C)		
190 (170*)	80	5.8	1.7	21	23	0.78	0.44

The pore size distribution is presented in Figure 9-1. The mean pore diameter is around $d^{AD}_{pore} = d^{CD}_{pore} = 40$ µm, 90% of the total pore volume is in pores between 10 and 100 µm.

As the carbon paper is PTFE treated prior to use in the DMFC, the real porosity has to be calculated as a function of the PTFE content.

The total volume of the carbon paper is the sum of the carbon, the PTFE and the free pore volume:

$$V_{tot} = V_{carbon} + V_{PTFE} + V_{pores} \quad . \tag{9-33}$$

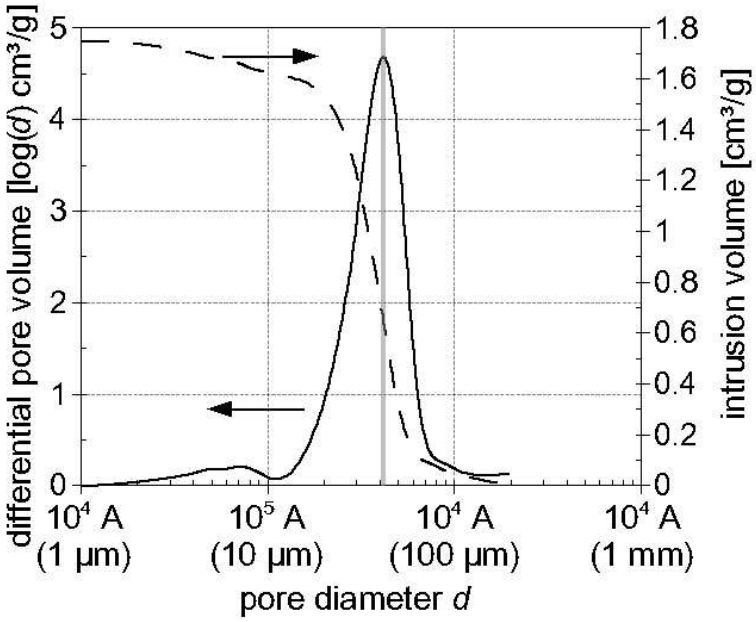

Figure 9-1 *Pore size distribution of TORAY™ carbon paper TGP-H-060 (data from Toray Deutschland GmbH)*

The carbon volume can be expressed by the porosity of the untreated carbon paper (see Table 9-11):

$$V_{carbon} = (1 - \varepsilon^{untreated\ Toray}_{pores}) V_{tot} \quad . \tag{9-34}$$

The carbon volume fraction is consequently

$$\varepsilon^{untreated\ Toray}_{carbon} = \varepsilon^{PTFE-treated\ Toray}_{carbon} = 1 - \varepsilon^{untreated\ Toray}_{pores} = 0.22 \quad . \tag{9-35}$$

The PTFE mass fraction

$$w_{PTFE} = \frac{m_{PTFE}}{m_{carbon} + m_{PTFE}} \tag{9-36}$$

can be rearranged to get the PTFE mass

$$m_{PTFE} = \frac{w_{PTFE}}{1 - w_{PTFE}} m_{carbon} \quad . \tag{9-37}$$

Substituting masses by bulk densities times volumes and rearranging we get the PTFE volume

$$V_{PTFE} = \frac{w_{PTFE}}{1 - w_{PTFE}} \frac{\rho_{carbon}}{\rho_{PTFE}} V_{carbon} \quad . \tag{9-38}$$

Substituting the carbon volume using eq. (9-34) one gets

$$V_{PTFE} = \frac{w_{PTFE}}{1 - w_{PTFE}} \frac{\rho_{carbon}}{\rho_{PTFE}} (1 - \varepsilon_{pores}^{untreated\ Toray}) V_{tot} \quad . \tag{9-39}$$

The resulting porosity (i.e. the pore volume fraction) of the PTFE-treated material is then

$$\varepsilon_{pores}^{PTFE-treated\ Toray} = \frac{V_{pores}}{V_{tot}} = \varepsilon_{pores}^{untreated\ Toray} - \frac{w_{PTFE}}{1 - w_{PTFE}} \frac{\rho_{carbon}}{\rho_{PTFE}} (1 - \varepsilon_{pores}^{untreated\ Toray}) \quad . \tag{9-40}$$

With the parameters given in Table 9-11, the typical PTFE mass content $w_{PTFE} = 0.25$ and the bulk densities of carbon and PTFE, $\rho_{PTFE} = 2.19$ g/cm³ and $\rho_{carbon} = 2.0$ g/cm³ the porosity of the PTFE-treated TORAY™ paper results as

$$\varepsilon_{pores}^{PTFE-treated\ Toray} = 0.71 \quad . \tag{9-41}$$

The PTFE volume fraction is then finally

$$\varepsilon_{PTFE}^{PTFE-treated\ Toray} = 1 - \varepsilon_{pores}^{PTFE-treated\ Toray} - \varepsilon_{carbon}^{PTFE-treated\ Toray} = 0.07 \quad . \tag{9-42}$$

9.2.2 Catalyst Layers (AC/CC)

An important physical parameter of the catalyst layer is the porosity. It can be calculated as the sum of the volumes of all dry materials within the catalyst layer (i.e. catalyst and NAFION™) divided by the total volume of the catalyst layer. The catalyst and NAFION™ volumes are calculated from the masses and the densities:

$$\varepsilon = \frac{\text{total volume - catalyst volume - NAFION volume}}{\text{total volume}} \tag{9-43}$$

One ends up with an equation using the catalyst and NAFION™ loadings w_{cat} and w_{NAFION}, and the catalyst layer thickness $d^{cat.layer}$:

$$\varepsilon = \frac{\frac{1}{A^S}\left(V_{tot}^{cat.layer} - \frac{m_{cat}}{\rho_{cat}} - \frac{m_{NAFION}}{\rho_{NAFION}}\right)}{\frac{1}{A^S}\left(V_{tot}^{cat.layer}\right)} = \frac{d^{cat.layer} - \frac{w_{cat}}{\rho_{cat}} - \frac{w_{NAFION}}{\rho_{NAFION}}}{d^{cat.layer}} \qquad (9\text{-}44)$$

For the applied MEAs the resulting calculations are shown in Table 9-12.

The porosities are very high, which is of course desired to a certain degree to achieve as many accessible catalyst sites as possible for the fluid phases. Nonetheless also an appropriate amount of ionomer phase is necessary to ensure good protonic contact of the catalyst particles.

Table 9-12 *Physical properties of catalyst layers and calculation of porosity*

	ANODE	***CATHODE***
thickness $d^{cat.layer}$ =	35 µm	35 µm
catalyst loading w_{cat}=	5 mg/cm²	5 mg/cm²
catalyst density ρ_{cat}=	0.66·21.4 + 0.34·12.4 = 18.3 g/cm³ (Pt:Ru mass ratio 66:34)	21.4 g/cm³ (Pt)
NAFION™ loading w_{NAFION}=	0.15 w_{cat} = 0.75 mg/cm²	0.10 w_{cat} = 0.5 mg/cm²
NAFION™ density ρ_{NAFION}=	1.97 g/cm³	1.97 g/cm³
	Calculation of volume fractions:	
catalyst	0.08	0.07
NAFION™	0.11	0.07
free pore space = **porosity ε**	**0.81**	**0.86**

9.3 Effective Thermal Conductivities in Diffusion Layers

As the diffusion layers are porous structures, their effective thermal conductivities have to be calculated accounting for the present materials and reactants as well as their volume fractions. From Toray Corporation a value for the through-plane thermal conductivity is available (see Table 9-12). But this value is only valid for the pores being filled with air, at 20°C. Therefore, this value is not applicable for the anode diffusion layer (AD) where the pores are filled with water (and traces of methanol and carbon dioxide). Also, as the thermal conductivity of air is

temperature dependent, using this value for the cathode diffusion layer seems problematic.

For these reasons first the thermal conductivity of the carbon fibres alone shall be calculated. Generally, assuming parallel thermal conduction through all present materials, the effective thermal conductivity can be calculated from

$$\lambda^{eff} = \sum_j \varepsilon_j \lambda_j \quad . \tag{9-45}$$

Using this expression for TORAY™ paper at 20°C we get the (assumed temperature-independent) thermal conductivity of TORAY™ paper in the vacuum (i.e. the contribution from the carbon material only):

$$\lambda_{Toray} = \frac{\lambda_{Toray+air}^{eff,\,20\,^\circ C} - \varepsilon_{pores}^{untreated\ Toray}\,\lambda_{air}^{20\,^\circ C}}{1-\varepsilon_{pores}^{untreated\ Toray}} = 7.63\ \mathrm{W\,m^{-1}\,K^{-1}} \tag{9-46}$$

The thermal conductivity of air at 20°C is calculated from eq.(9-6). The other values are taken from Table 9-12.

Using the value calculated in eq.(9-46) and the volume fractions of carbon fibres and PTFE as well as the porosity (see section 11.2), the effective thermal conductivity can be calculated accounting for the material filling the pores and for the temperature.

In the anode diffusion layer (AD) the pores are assumed to be filled with a liquid mixture, which mainly consists of water. For simplicity, the influence of methanol and carbon dioxide is neglected. The resulting expression is

$$\lambda^{eff,\,AD} = \varepsilon_{carbon}^{PTFE-treated\ Toray}\,\lambda_{Toray} + \varepsilon_{PTFE}^{PTFE-treated\ Toray}\,\lambda_{PTFE} + \varepsilon_{pores}^{PTFE-treated\ Toray}\,\lambda_{H_2O}(T) \quad . \tag{9-47}$$

For the thermal conductivity of water, the literature value eq.(9-5) is used.

In the cathode diffusion layer (CD) the pores are assumed to be filled with air. For simplicity, the changing composition due to the ongoing chemical and electrochemical reactions as well as mass transport phenomena is neglected. Eq.(9-6) is used for the thermal conductivity of air.

$$\lambda^{eff,\,CD} = \varepsilon_{carbon}^{PTFE-treated\ Toray}\,\lambda_{Toray} + \varepsilon_{PTFE}^{PTFE-treated\ Toray}\,\lambda_{PTFE} + \varepsilon_{pores}^{PTFE-treated\ Toray}\,\lambda_{air}(T) \quad . \tag{9-48}$$

9.4 Volumetric Heat Capacities

In the energy balances of the simulation model, the volumetric overall heat capacities in all control volumes are needed. These are calculated from the densities ρ_j [kg m^{-3}], the mass-based heat capacities $C_{p,j}$ [J kg^{-1} K^{-1}] and volume fractions ε_j [-] of all present materials and reactants:

$$\widetilde{(\rho C_p)} = \sum_j \varepsilon_j \rho_j C_{p,j} \quad . \tag{9-49}$$

The pores in the anode diffusion layer (AD) are assumed to be filled with liquid water and small amounts of methanol and carbon dioxide. As the mole fractions of the latter two are each well below 0.05, their influence on the overall heat capacity is neglected. It is only accounted for the carbon material and the PTFE forming the solid porous structure as well as the water filling the pores:

$$\begin{aligned}\widetilde{(\rho C_p)}^{AD} = {} & \varepsilon_{carbon}^{PTFE-treated\ Toray} \rho_{carbon} C_{p,carbon} \\ & + \varepsilon_{PTFE}^{PTFE-treated\ Toray} \rho_{PTFE} C_{p,PTFE} \\ & + \varepsilon_{pores}^{PTFE-treated\ Toray} \rho_{H_2O(l)} C_{p,H_2O(l)} \quad .\end{aligned} \tag{9-50}$$

As in the anode diffusion layer (AD), all pores in the anode catalyst layer (AC) are assumed to be filled with pure water. Methanol and carbon dioxide are neglected for the calculation of the mean heat capacity. Here the solid matrix is formed from the catalyst particles and ionomer (Nafion™):

$$\begin{aligned}\widetilde{(\rho C_p)}^{AC} = {} & \varepsilon_{PtRu}^{AC} \widetilde{(\rho C_p)}_{PtRu} + \varepsilon_{Nafion}^{AC} \widetilde{(\rho C_p)}_{Nafion} \\ & + \varepsilon_{pores}^{AC} \rho_{H_2O(l)} C_{p,H_2O(l)}\end{aligned} \tag{9-51}$$

with the heat capacity of the PtRu catalyst calculated from the mass fractions of both metals:

$$\widetilde{(\rho C_p)}_{PtRu} = 0.66\, \rho_{Pt} C_{p,Pt} + 0.34\, \rho_{Ru} C_{p,Ru} = 2.84 \cdot 10^6\ \mathrm{J\,m^{-3}\,K^{-1}} \tag{9-52}$$

In the literature [64] for wet NAFION™ a volumetric heat capacity of

$$\widetilde{(\rho C_p)}_{Nafion} = 2.4 \cdot 10^7\ \mathrm{J\,m^{-3}\,K^{-1}} \tag{9-53}$$

is given.

For the cathode catalyst layer (CC) the same reasoning is valid as for the anode catalyst layer (AC). The pores are filled with air, the porous matrix is formed from the catalyst (in this case pure platinum) and ionomer:

$$\begin{aligned}\widetilde{(\rho C_p)}^{CC} = {} & \varepsilon_{Pt}^{CC} \rho_{Pt} C_{p,Pt} + \varepsilon_{Nafion}^{CC} \widetilde{(\rho C_p)}_{Nafion} \\ & + \varepsilon_{pores}^{CC} \rho_{air} C_{p,air} \quad .\end{aligned} \tag{9-54}$$

In the cathode diffusion layer (CD) the same reasoning is valid as for the anode diffusion layer (AD). The only difference is that the pores are gas-filled.

$$\begin{aligned}\overline{(\rho C_p)}^{CD} = {} & \varepsilon_{carbon}^{PTFE-treated\ Toray} \rho_{carbon} C_{p,carbon} \\ & + \varepsilon_{PTFE}^{PTFE-treated\ Toray} \rho_{PTFE} C_{p,PTFE} \\ & + \varepsilon_{pores}^{PTFE-treated\ Toray} \rho_{air}(p,T) C_{p,air}\end{aligned} \tag{9-55}$$

For simplicity it is assumed that the gas mixture is standard air, for which the density and the heat capacity are available (see chapters 9.1.1 and 9.1.2). This simplification seems justified as the influence of the gas on the mean heat capacity is small anyway, due to the low heat capacities and densities of gases compared to solid materials.

9.5 Calculation of Feed Air Composition

The cathode of the DMFC is fed with relatively dry air, with the dew point ϑ^{dew} in [°C] as measure for the humidity being constantly measured by the miniplant. From the dew point, the water partial pressure in [Pa] can be calculated using the correlation

$$p_{H_2O} = 288.68 \left(\frac{\vartheta^{dew} + 109.8}{100} \right)^{8.02} . \tag{9-56}$$

The composition of absolutely dry air (mole fractions $y_j^{dry\ air}$) is well known:

Oxygen: $y_{O_2}^{dry\ air} = 0.20948$,

Nitrogen (including all inert gases): $y_{N_2}^{dry\ air} = 0.79017$,

Carbon dioxide: $y_{CO_2}^{dry\ air} = 0.00035$.

The mole fractions of the real, wet air can be calculated accounting for the water partial pressure p_{H_2O} as:

$j = O_2, N_2, CO_2$: $$y_j^{CF} = \frac{p^C - p_{H_2O}}{p^C} y_j^{dry\ air} , \tag{9-57}$$

$j = H_2O$: $$y_{H_2O}^{CF} = \frac{p_{H_2O}}{p^C} . \tag{9-58}$$

To get the molar concentrations, the ideal gas law is used:

$$c_j^{CF} = c_{tot}^{CF}\ y_j^{CF} = \frac{p^C}{R T^C} y_j^{CF} . \tag{9-59}$$

9.6 Heat Transfer Coefficients in the Anode and Cathode Channels

In the applied DMFCs, each of the 21 supply channels in each of the bipolar plates has a square area of $A^{channel}$=2x2 mm^2, a circumference of $L^{channel}$=2+2+2+2 mm, the typical maximum cathode air flow rate is F^{CF}_{max}=0.5 m^3 h^{-1} and the typical maximum anode liquid flow rate is F^{AF}_{max}=0.5 dm^3 min^{-1}. Therefore, the hydraulic diameter is

$$d_h = \frac{4 \cdot A^{channel}}{L^{channel}} = \frac{4 \cdot 4\ \mathrm{mm}^2}{8\ \mathrm{mm}} = 2\ \mathrm{mm} \quad , \tag{9-60}$$

the maximum mean air velocity is

$$v^{C}_{max} = \frac{F^{CF}_{max}}{A^{channel} \cdot N^{channels}} = \frac{0.5\ \mathrm{m^3\ h^{-1}} \dfrac{1}{3600\ \mathrm{s\ h^{-1}}}}{4 \cdot 10^{-6}\ \mathrm{m^2} \cdot 21} = 1.65\ \mathrm{m\ s^{-1}} \tag{9-61}$$

and the maximum mean liquid velocity is

$$v^{A}_{max} = \frac{F^{AF}_{max}}{A^{channel} \cdot N^{channels}} = \frac{0.5 \cdot 10^{-3}\ \mathrm{m^3\ min^{-1}} \dfrac{1}{60\ \mathrm{s\ min^{-1}}}}{4 \cdot 10^{-6}\ \mathrm{m^2} \cdot 21} = 0.1\ \mathrm{m\ s^{-1}} \quad . \tag{9-62}$$

This leads to maximum Reynolds numbers (at T=310 K) of

$$\mathrm{Re}^{C}_{max} = \frac{v^{C}_{max}\, d_h}{\mu^{vis}_{air}} = \frac{v^{C}_{max}\, d_h\, \rho_{air}}{\eta^{vis}_{air}} \approx 330 \quad \text{and} \tag{9-63}$$

$$\mathrm{Re}^{A}_{max} = \frac{v^{A}_{max}\, d_h}{\mu^{vis}_{methanol\ water\ solution}} = \frac{v^{A}_{max}\, d_h\, \rho_{methanol\ water\ solution}}{\eta^{vis}_{methanol\ water\ solution}} \approx 395 \quad , \tag{9-64}$$

which means laminar flow in both the anode and the cathode channels. For such flow conditions, the Nusselt number as representation of the heat transfer coefficient α, [W m^{-2} K^{-1}] defined as

$$\mathrm{Nu} \equiv \frac{\alpha\, d_h}{\lambda} \quad , \tag{9-65}$$

can be calculated from the correlation [106b]

$$\mathrm{Nu} = \left[\mathrm{Nu}_1{}^3 + 0.7^3 + (\mathrm{Nu}_2 - 0.7)^3 \right]^{\frac{1}{3}} \tag{9-66}$$

with:

$$\mathrm{Nu}_1 = 3.66$$

$$\mathrm{Nu}_2 = 1.615 \left(\mathrm{Re} \cdot \mathrm{Pr} \cdot \frac{d^{C}_{h}}{l^{channels}} \right)^{\frac{1}{3}} \tag{9-67}$$

and the length of the channels $l^{channels}$ = 40 mm.

The Prandtl numbers are

$$\mathrm{Pr}_{air} = \frac{C_{p,\,air}\,\eta^{vis}_{air}}{\lambda_{air}} \approx 0.7 \quad \text{and} \tag{9-68}$$

$$\mathrm{Pr}_{water\ methanol\ solution} = \frac{C_{p,\,water\ methanol\ solution}\,\eta^{vis}_{water\ methanol\ solution}}{\lambda_{water\ methanol\ solution}} \approx 3.3 \quad . \tag{9-69}$$

We end up with maximum Nusselt numbers of

$$\mathrm{Nu}^{C}_{max} = 4.2 \quad \text{and}$$

$$\mathrm{Nu}^{A}_{max} = 6.1 \quad .$$

The resulting heat transfer coefficients are then finally

$$\alpha^{C}_{max} \approx 59\ \mathrm{W\,m^{-2}\,K^{-1}} \quad \text{and}$$

$$\alpha^{A}_{max} \approx 1980\ \mathrm{W\,m^{-2}\,K^{-1}} \quad .$$

Not surprisingly, in the cathode channels the heat transfer resistances are much bigger than in the anode channels. Consequently, also taking into account that the absolute heat capacity of the anode liquid water methanol solution is some orders of magnitude bigger than that of the cathode air and that the liquid mixture is used to control the cell anode temperature, one can assume that at the anode the bipolar plate (= the channel walls !) will always have a temperature very similar to that of the water methanol solution. In the cathode channels, as the air is supplied with very low temperatures compared to the anode liquid solution and as the mean residence time is also much lower than on the anode side, no significant heat exchange between channel walls and air will take place. Therefore, on the cathode side there can be a significant difference between the air temperature in the channels and the channel walls.

9.7 Activities in Polymer Electrolyte Membrane (Flory-Huggins Model)

The Flory-Huggins model is a very simple model for activities of species within a polymer mixture. Its reasoning is based on pure geometric interactions of molecules of different lengths, levels of cross-linking and a few non-ideality parameters. As crystallisation and inhomogeny are not accounted for, this model can only be a very coarse description of the real situation, but it nonetheless is the best available on a tolerable level of complexity and regarding the number of available parameters.

The general form of the Flory-Huggins equation for the activity of a component (solvent) *j* within a mixture between a polymer *M* and some solvents is

$$a_j = \varepsilon_j \exp\left\{ \sum_{i \neq j} \left[\left(1 - \frac{\overline{V}_j}{\overline{V}_i} \right) \varepsilon_i + \chi_{j,i} \varepsilon_i^2 \right] + \frac{\overline{V}_j}{2 \cdot N_{M,cu} \cdot \overline{V}_{M,cu}} \varepsilon_M^{1/3} \right\} \quad . \qquad (9\text{-}70)$$

Here the overlined *V*s are the specific molar volumes in [m^3 mol^{-1}] of the solvent *j*, the polymer backbone *M* and a single chain unit of the polymer (lower index "cu", single chain unit of NAFION™: -CF_2-CF_2-, molar volume $\overline{V}_{M,cu} = 56 \cdot 10^{-6}\ m^3\ mol^{-1}$ according to SCHRÖDER method [86f]), respectively. The $\chi_{j,i}$ are non-ideality parameters, $N_{M,cu}$ is the average number of single chain units between two cross-links (approx. 5 for NAFION™).

In most polymer-solvent systems (as in the system water-methanol-NAFION™), the specific volume of the polymer is several orders of magnitude higher than that of the solvent(s). Therefore, the first round bracket degrades to a value of one. Formulating the above equation for water and methanol yields therefore

$$a_{H_2O} = \varepsilon_{H_2O} \cdot \exp\left\{ \varepsilon_M + \chi_{H_2O,M} \varepsilon_M^2 + \left(1 - \frac{\overline{V}_{H_2O}}{\overline{V}_{CH_3OH}} \right) \varepsilon_{CH_3OH} + \chi_{H_2O,CH_3OH} \varepsilon_{CH_3OH}^2 + \frac{\overline{V}_{H_2O} \varepsilon_M^{1/3}}{2 N_{M,cu} \overline{V}_{M,cu}} \right\} \qquad (9\text{-}71)$$

$$a_{CH_3OH} = \varepsilon_{CH_3OH} \cdot \exp\left\{ \varepsilon_M + \chi_{CH_3OH,M} \varepsilon_M^2 + \left(1 - \frac{\overline{V}_{CH_3OH}}{\overline{V}_{H_2O}} \right) \varepsilon_{H_2O} + \chi_{H_2O,CH_3OH} \varepsilon_{H_2O}^2 + \frac{\overline{V}_{CH_3OH} \varepsilon_M^{1/3}}{2 N_{M,cu} \overline{V}_{M,cu}} \right\} \qquad (9\text{-}72)$$

The only remaining parameters are the non-ideality parameters. If both the solvent and the polymer are chemically similar this parameter is zero, if both attract each other it has a negative value, and if both are repelling each other it has a positive value. For values of roughly one, demixing occurs which means that solvent and polymer are not completely miscible or even immiscible.

9.7.1 Estimation of Non-ideality Parameters

To evaluate the polymer interaction parameters for water and methanol, simple swelling experiments were performed. Data from literature could also have been used, but due to the special preparation procedure in which the membrane foil is fixed in a frame fully swollen and then dried, the materials swelling behaviour is slightly changed (it swells less than

original NAFION™). Therefore, experiments have been carried ot using a piece of membrane foil which had already been fixed to a frame and dried as if to be coated with the catalyst layers (see information on MEA preparation procedure in chapter 3.3.1).

The swelling was determined from measuring the dimensions of the foil. Length and width were measured with a ruler, the thickness with a micrometer gauge with an accuracy of one micrometer. The foil was measured in completely dry state after an one hour treatment in a drying oven (100°C) and after immersion in pure water and pure methanol, respectively, at room temperature. The results are:

total volume of dry material: $V_{dry,tot} = 563\ \text{mm}^3$

total volume of material swollen in water: $V_{H_2O,tot} = 1044\ \text{mm}^3$

total volume of material swollen in methanol: $V_{CH_3OH,tot} = 1785\ \text{mm}^3$

The volumes taken by water and methanol are then

$$V^M_{H_2O} = V_{H_2O,tot} - V_{dry,tot} = 481\ \text{mm}^3 \quad \text{and} \tag{9-73}$$

$$V^M_{CH_3OH} = V_{CH_3OH,tot} - V_{dry,tot} = 1222\ \text{mm}^3 \quad \text{respectively.} \tag{9-74}$$

Therefore, the maximum volume fractions of water and methanol are

$$\varepsilon^M_{H_2O,max} = \frac{V^M_{H_2O}}{V_{H_2O,tot}} = 0.46 \quad \text{and} \tag{9-75}$$

$$\varepsilon^M_{CH_3OH,max} = \frac{V^M_{CH_3OH}}{V_{CH_3OH,tot}} = 0.68 \quad . \tag{9-76}$$

The difference to one yields the volume fractions of the polymer backbone in the fully swollen states as

$$\varepsilon^M_{M,H_2O,max} = 1 - \varepsilon^M_{H_2O,max} = 0.54 \quad \text{and} \tag{9-77}$$

$$\varepsilon^M_{M,CH_3OH,max} = 1 - \varepsilon^M_{CH_3OH,max} = 0.32 \quad . \tag{9-78}$$

In case the membrane is fully swollen with either water or methanol, the chemical potentials of the solvent are the same within the pores and in the free solution outside the membrane. As we have liquid solvent within and outside the membrane, equality of chemical potrentials means equality of activities (same reference state), and the activity of the pure solvent outside the membrane is one (i = H_2O, CH_3OH):

$$1 = a_i^{free\ solution} = a^M_{i,max} = \varepsilon^M_{i,max} \exp\left[\varepsilon^M_{M,i,max} + \chi_{i,M} (\varepsilon^M_{M,i,max})^2 + \frac{\overline{V}_{H_2O} (\varepsilon^M_{M,i,max})^{1/3}}{2 N_{M,cu} \overline{V}_{M,cu}} \right] \quad . \tag{9-79}$$

These equations can be transformed to calculate the non-ideality parameters as functions of the crosslink-parameter $N_{M,cu}$ (all above experimental values already inserted):

$$\chi_{H_2O,M} = 0.811 - \frac{0.4664}{N_{M,cu}} \tag{9-80}$$

$$\chi_{CH_3OH,M} = 0.6416 - \frac{2.5342}{N_{M,cu}} \tag{9-81}$$

The third non-ideality parameter describes the interaction between water and methanol. It can be determined by applying the Flory-Huggins activity model for methanol, eq.(9-72), to a pure liquid mixture of water and methanol (i.e. without a polymer) and calculating the methanol activity using the UNIFAC model:

$$a_{CH_3OH,UNIFAC} = \varepsilon_{CH_3OH} \exp\left\{\left(1 - \frac{\overline{V}_{CH_3OH}}{\overline{V}_{H_2O}}\right)\varepsilon_{H_2O} + \chi_{H_2O,CH_3OH}\,\varepsilon_{H_2O}^2\right\} \tag{9-82}$$

$$\Rightarrow \quad \chi_{H_2O,CH_3OH} = -\frac{1}{\varepsilon_{H_2O}^2}\left[\ln(\varepsilon_{CH_3OH}) + \left(1 - \frac{\overline{V}_{CH_3OH}}{\overline{V}_{H_2O}}\right)\varepsilon_{H_2O} - \ln(a_{CH_3OH,UNIFAC})\right] \tag{9-83}$$

For methanol mole fractions between zero and 0.03 (typical DMFC operation) values between 1.28 and 1.31 are obtained for the non-ideality parameter, nearly independent of the temperature. Therefore in the simulations a fixed value of 1.3 is used.

9.7.2 Phase Equilibrium between (AC) and Membrane Phase (ACP)

Starting point is the assumption of phase equilibrium between the liquid phase in the pores of (AC) and the polymer (membrane) phase within the catalyst layer (denoted by upper index ACP):

$$a_j^{AC} = a_j^{ACP} \quad . \tag{6-73}$$

The Flory-Huggins activity equations (9-71) and (9-72) can not be simply rearranged to obtain the volume fractions of water and methanol, respectively, as functions of the liquid phase activities. Therefore a dynamic approach is used to get these relations. For this purpose a fictuous piece of membrane material is immersed in a methanol water solution of given composition (and therefore known UNIFAC activities). For the piece of membrane, volume balances are formulated for water and methanol within the material:

$$\frac{dV_j^M}{dt} = \overline{V}_j \cdot (A \cdot n_j) \quad \text{, with } j = H_2O,\ CH_3OH \tag{9-84}$$

Here $\overline{V}_j$ are the molar volumes of water and methanol in [m^3 mol^{-1}], respectively, and $(A \cdot n_j)$ in [mol s^{-1}] are the fluxes of water and methanol, respectively, entering or leaving the

membrane material across the outer surface A [m^2] to obtain the equilibrium swelling state. For the two fluxes simple kinetics are formulated based on the phase equilibrium condition from equation (6-73):

$$(A \cdot n_j) = k_j \cdot (a_j - a_j^M) \quad \text{, with } j = H_2O, CH_3OH \tag{9-85}$$

The activities in the free solution, a_j, are calculated using UNIFAC, those within the membrane material, a_j^M, are calculated using equations (9-71) and (9-72). The two kinetic constants were optimised to get a fast, reliable convergence:

$$k_{H_2O} = 5 \cdot 10^{-3} \quad \text{and} \quad k_{CH_3OH} = 10^{-2} \quad .$$

This simple model with its two differential equations is used to simulate the swelling of this fictuous piece of membrane, to finally obtain steady state volumes of methanol and water within the material. From these volumes the volume fractions can be calculated as the dry volume of the material (i.e. the volume of the polymer backbone) V_M^M is known:

$$\varepsilon_j = \frac{V_j^M}{V_{tot}^M} \quad \text{, with} \quad V_{tot}^M = V_{H_2O}^M + V_{CH_3OH}^M + V_M^M \;,\; j = H_2O, CH_3OH \tag{9-86}$$

In order to get a fast DMFC model simulation, it is not favourable to use the presented ODE swelling model within the full DMFC model. Therefore this swelling model was used to calculate equilibrium swelling curves for various temperatures over the full range of typical (AC) pore methanol concentrations. The temperature dependence was found to be insignificant, UNIFAC for this system shows only a weak temperature dependence, and in the Flory-Huggins model temperature influences only the molar volumes, which for liquids are nearly independent of temperature.. Therefore the obtained equilibrium curves were approximated by third order polynomials in the range of the methanol free pore mole fraction from zero to 0.03 (typical operation range of a DMFC):

$$\varepsilon_{CH_3OH}^{ACP} = 25.4831 \cdot (x_{CH_3OH}^{AC})^3 + 4.2821 \cdot (x_{CH_3OH}^{AC})^2 + 1.6354 \cdot x_{CH_3OH}^{AC} \tag{9-87}$$

$$\varepsilon_{H_2O}^{ACP} = -104.9956 \cdot (x_{CH_3OH}^{AC})^3 + 20.9052 \cdot (x_{CH_3OH}^{AC})^2 + 2.6349 \cdot x_{CH_3OH}^{AC} + 0.4601 \tag{9-88}$$

Figure 6-11 shows the complete simulation results, and the grey region to the very left shows the typical operating range of a DMFC where the above fitting equations are very good approximations to the simulation results.

9.7.3 Phase Equilibrium between (CC) and Membrane Phase (CCP)

As described briefly in the introduction of chapter 6.9, for the description of the cathode side phase equilibrium between membrane material and catalyst layer pores an empiric approach is used. Like for the anode side, phase equilibrium is assumed.

For this phase equilibrium experimental data and corresponding fitting functions for the relative water content exist (see also Figure 6-12):

$$\Lambda^{CCP} = 28.5 \cdot (a^{*,CC}_{H_2O(g)} - 0.35)^3 + 5 \cdot (a^{*,CC}_{H_2O(g)} - 0.35) + 3 \tag{6-78}$$

with $$a^{*,CC}_{H_2O(g)} = \frac{p^{CC}_{H_2O}}{p^{sat}_{H_2O}(T^{CC})} \quad . \tag{6-79}$$

Methanol is assumed to be immediately consumed at the cathode catalyst, $\tilde{c}^{CCP}_{CH_3OH} = 0$, therefore, only water and protons have to be accounted for in the membrane material in (CCP). To transform the obtained relative water content to the necessary pseudo-concentration of protons

$$\tilde{c}^{CCP}_{H^+} = \frac{\hat{N}^{CCP}_{H^+} \cdot A^S}{V^{CCP}} \quad , \tag{9-89}$$

the volume of the polymer phase within (CC) is necessary, which depends on the found relative water content:

$$V^{CCP} = A^S \left(\varepsilon^{CC}_M \cdot d^{CC} + \hat{N}^{CCP}_{H^+} (\overline{V}_{H^+} + \Lambda^{CCP} \cdot \overline{V}_{H_2O}) \right) \quad . \tag{9-90}$$

The pseudo-concentration of water can be calculated from that of the protons and the relative water content as

$$\tilde{c}^{CCP}_{H_2O} = \Lambda^{CCP} \cdot \tilde{c}^{CCP}_{H^+} \quad . \tag{9-91}$$

Using the relations given in appendix chapter 9.8, all necessary concentrations can now be calculated from the pseudo-concentrations, the water and methanol activities inside the polymer phase result from the Flory-Huggins equations (9-71) and (9-72).

9.8 Concentration Measures within the Polymer Electrolyte Membrane

To describe the physical phenomena within the membrane (M), several concentration measures are necessary, as none is convenient to describe all phenomena. Diffusive mass transfer needs activities $a_{i,}$ which in turn are calculated from volume fractions ε_i (using the Flory-Huggins equation). For calculation of the convective mass transport, the concentrations of the mobile cpecies within the pores c_i [mol m^{-3}] are needed. Finally, for the formulation of the mass balances within this system of shrinking and expanding pores, a concentration with respect to the (constant) cross-sectional area is more convenient than one with respect to volume. This mole density relative to cross-sectional area is denoted $\hat{N}_i$ [mol m^{-2}].

To convert these concentration measures, the concentration with respect to the total volume including the polymer backbone $\tilde{c}_i$ [mol m^{-3}] is useful:

$$\tilde{c}_j^M = \frac{\hat{N}_j^M}{dz^M} \quad \text{with } j = H_2O, CH_3OH, H^+ \tag{9-92}$$

This expression is applied in the (spatially discretised) model implementation in the form

$$\tilde{c}_{j,k}^M = \frac{\hat{N}_{j,k}^M}{\Delta z_k^M} \tag{9-93}$$

where the thickness Δz_k^M [m] of the respective control volume *k* is calculated from

$$\Delta z_k^M = \frac{d^{M,dry}}{ncv^M} + \sum_j \left(\hat{N}_{j,k}^M \overline{V}_j \right) \quad . \tag{9-94}$$

This thickness is also needed for the various flux calculations to calculate the distances between the centres of the control volumes.

From $\tilde{c}_j$, all other concentration measures can be easily calculated:

- volume fractions: $$\varepsilon_j^M = \tilde{c}_j^M \overline{V}_j \quad . \tag{9-95}$$
- concentrations within the pores: $$c_j^M = \frac{\tilde{c}_j^M}{\varepsilon_{pores}^M} \quad , \tag{9-96}$$

$$\varepsilon_{pores}^M = \sum_j \varepsilon_j^M = \varepsilon_{H^+}^M + \varepsilon_{H_2O}^M + \varepsilon_{CH_3OH}^M \quad . \tag{9-97}$$

- activities within the pores:

$$a_j^M = \varepsilon_j^M \exp\left\{ \sum_{i \neq j} \left[\varepsilon_i^M + \chi_{j,i} (\varepsilon_i^M)^2 \right] + \frac{\overline{V}_j}{2 \cdot N_{M,cu} \cdot \overline{V}_{M,cu}} (\varepsilon_M^M)^{1/3} \right\} \tag{9-98}$$

$$\text{with} \quad \varepsilon_M^M = 1 - \varepsilon_{pores}^M \quad . \tag{9-99}$$

10 References

[1] Höhlein, B.; v. Adrian, S.; Grube, T.; Menzer, R.: Critical assessment of power trains with fuel-cell systems and different fuels, *J. Power Sources 86* (2000), pp. 243-249.

[2] Thomas, C.E.; James, B.D.; Lomax, F.D.; Kuhn, I.F.: Fuel options for the fuel cell vehicle: hydrogen, methanol or gasoline ?, *Int. J. Hydrogen Energy 25* (2000), pp. 551-567.

[3] Hogarth, M.; Christensen, P.; Hamnett, A.; Shukla, A.: The design and construction of high-performance direct methanol fuel cells. 1. Liquid-feed systems, *J. Power Sources 69* (1997) pp. 113-124.

[4] Hogarth, M.; Christensen, P.; Hamnett, A.; Shukla, A.: The design and construction of high-performance direct methanol fuel cells. 2. Vapour-feed systems, *J. Power Sources 69* (1997) pp. 125-136.

[5] Scott, K.; Taama, W.M.; Cruickshank, J.: Performance and modelling of a direct methanol solid polymer electrolyte fuel cell, *J. Power Sources 65 (1997)* pp. 159-171.

[6] Ren, X.M.; Henderson, W.; Gottesfeld, S.: Electro-osmotic drag of water in ionomeric membranes - New measurements employing a direct methanol fuel cell, *J. Electrochem. Soc. 144 No.9* (1997) pp. L267-L270.

[7] Avery, W.H.: A role for ammonia in the hydrogen economy, *Int. J. Hydrogen Energy 13 No.12* (1988) pp. 761-773

[8] Deluchi, M.A.: Hydrogen vehicles - an evaluation of fuel storage, performance, safety, environmental impacts, and cost, *Int. J. Hydrogen Energy 14 No.2* (1989) pp. 81-130

[9] Hammer, A.; Hammer, K.: *Taschenbuch der Physik.* 6. Auflage, J. Lindauer Verlag, München (1983)

[10] Colsman, G.: Verfahrenstechnische Optimierung der Brenngaserzeugung für Brennstoffzellen in Kraftfahrzeugen, *Berichte des Forschungszentrums Jülich Nr. 3127*, Forschungszentrum Jülich (1995)

[11] Schultz, T.; Zhou, S.; Sundmacher, K.: Current status of and recent developments in the direct methanol fuel cell, Chem. Eng. Technol. 24 No.12 (2001) pp.1223-1233

[12] Wöhr, M.: Instationäres, thermodynamisches Verhalten der Polymermembran-Brennstoffzelle, *Fortschr.-Ber. VDI Reihe 3 Nr. 630.* Düsseldorf: VDI-Verlag (2000)

[13] Arico, A.S.; Srinivasan, S.; Antonucci, V.: DMFCs: From Fundamental Aspects to Technology Development, *Fuel Cells 1 No. 2* (2001) pp. 133-161

[14] Carrette, L.; Friedrich, K.A.; Stimming, U.: Fuel Cells - Fundamentals and Applications, *Fuel Cells 1 No. 1* (2001) pp. 5-39

[15] McNicol, B.D.: Electrocatalytic problems associated with the development of direct methanol-air fuel-cells, *J. Electroanal. Chem. 118* (1981), pp. 71-87

[16] Sundmacher, K.; Schultz, T.; Zhou, S.; Scott, K.; Ginkel, M.; Gilles, E.D.: Dynamics of the direct methanol fuel cell (DMFC): experiments and model-based analysis, *Chem. Eng. Sci. 56 No. 2* (2001), pp. 333-341

[17] Kennedy, B.J.; Hamnett, A.: Oxide formation and reactivity for methanol oxidation on platinized carbon anodes, *J. Electroanal. Chem. 283* (1990), pp.271-285

[18] Bönnemann, H.; Britz, P.; Vogel, W.: Structure and chemical composition of a surfactant-stabilized Pt3Sn alloy colloid, *Langmuir 14* (1998), pp. 6654-6657

[19] Götz, M.; Wendt, H.: Binary and ternary anode catalyst formulations including the elements W, Sn and Mo for PEMFCs operated on methanol or reformate gas, *Electrochimica Acta 43 No. 24* (1998), pp. 3637-3644

[20] Bagotzky, V.S.; Vassiliev, Y.B.; Khazova, O.A.: Generalized scheme of chemisorption, electrooxidation and electroreduction of simple organic-compounds on platinum group metals, *J. Electroanal. Chem. 81* (1977), pp. 229-238

[21] Xia, X.H.; Iwasita, T.; Ge, F.; Vielstich, W.: Structural effects and reactivity in methanol oxidation on polycrystalline and single crystal platinum, *Electrochimica Acta 41 No. 5* (1996), pp. 711-718

[22] Arico, A.S.; Modica, E.; Ferrara, I.; Antonucci, V.: CO and CO/H-2 electrooxidation on carbon supported Pt-Ru catalyst in phosphotungstic acid (H3PW12O40) electrolyte, *J. Appl. Electrochem. 28* (1998), pp. 881-887

[23] Ciureanu, M.; Wang, H.: Electrochemical impedance study of anode CO-poisoning in PEM fuel cells, *J. New Mat. Electrochem. Syst. 3* (2000), pp. 107-119

[24] Müller, J.T.; Urban, P.M.: Characterization of direct methanol fuel cells by AC impedance spectroscopy, *J. Power Sources 75* (1998), pp. 139-143

[25] Arico, A.S.; Creti, P.; Modica, E.; Monforte, G.; Baglio, V.; Antonucci, V.: Investigation of direct methanol fuel cells based on unsupported Pt-Ru anode catalysts with different chemical properties, *Electrochimica Acta 45* (2000), pp. 4319-4328

[26] Ren, X.; Zelenay, P.; Thomas, S.; Davey, J.; Gottesfeld, S.: Recent advances in direct methanol fuel cells at Los Alamos National Laboratory, *J. Power Sources 86* (2000), pp. 111-116

[27] Yagishita, T.; Sawayama, S.; Tsukahara, K.; Ogi, T.: Photosynthetic big-fuel cells using cyanobacteria, *Renewable Energy 9 No. 1-4* (1996) pp. 958-961

[28] Kim, H.J.; Park, H.S.; Hyun, M.S.; Chang, I.S.; Kim, M.; Kim, B.H.: A mediator-less microbial fuel cell using a metal reducing bacterium, Shewanella putrefaciense, *Enzyme Microbial Tech. 30* (2002) pp. 145-152

[29] Kim, N.; Choi, Y.; Jung, S.; Kim, S.: Development of microbial fuel cells using Proteus vulgaris, *Bull. Korean Chem. Soc. 21 No. 1* (1999) pp. 44-48.

[30] Divisek, J.; Oetjen, H.F.; Peinecke, V.; Schmidt, V.M.; Stimming, U.: Components for PEM fuel cell systems using hydrogen and CO containing fuels, *Electrochimica Acta 43 No.24* (1998) pp. 3811-3815

[31] U.S. Patent #5,525,436; Savinell, R.F.; Litt, M.H., June 11, 1996

[32] Wainright, J.S.; Wang, J.T.; Weng, D.; Savinell, R.F.; Litt, M.: Acid-doped polybenzimidazoles - a new polymer electrolyte, *J. Electrochem. Soc. 142 No. 7* (1995) pp. L121-L123.

[33] Weng, D.; Wainright, J.S.; Landau, U.; Savinell, R.F.: Electro-osmotic drag coefficient of water and methanol in polymer electrolytes at elevated temperatures, *J. Electrochem. Soc. 143 No. 4* (1996) pp. 1260-1263.

[34] Huslage, J.; Rager, T.; Schnyder, B.; Tsukada, A.: Radiation-grafted membrane/electrode assemblies with improved interface, *Electrochimica Acta 48 No. 3* (2002) pp. 247-254

[35] Heinzel, A.; Barragan, V.M.: A review of the state-of-the-art of the methanol crossover in direct methanol fuel cells, *J. Power Sources 84* (1999), pp. 70-74

[36] Cruickshank, J.; Scott, K.: The degree and effect of methanol crossover in the direct methanol fuel cell, *J. Power Sources 70* (1998), pp. 40-47

[37] Scott, K.; Taama, W.M.; Argyropoulos, P.; Sundmacher, K.: The impact of mass transport and methanol crossover on the direct methanol fuel cell, *J. Power Sources 83* (1999), pp. 204-216

[38] Kato, S.; Nagahama, K.; Noritomi, H.; Asai, H.: Permeation rates of aqueous alcohol-solutions in pervaporation through nafion membranes, *J. Membrane Sci.72 No. 1* (1992) pp. 31-41

[39] Carretta, N.; Tricoli, V.; Picchioni, F.: Ionomeric membranes based on partially sulfonated poly(styrene): synthesis, proton conduction and methanol permeation, *J. Membrane Sci. 166* (2000), pp. 189-197

[40] Jones, D.J.; Roziere, J.: Recent advances in the functionalisation of polybenzimidazole and polyetherketone for fuel cell applications, *J. Membrane Sci. 185* (2001) pp. 41-58.

[41] Kreuer, K.D.: On the development of proton conducting materials for technological applications, *Solid State Ionics 97* (1997), pp. 1-15

[42] Kreuer, K.D.: On the development of proton conducting polymer membranes for hydrogen and methanol fuel cells, *J. Membrane Sci. 185* (2001) pp. 29-39.

[43] Boysen, D.A.; Chisholm, C.R.I.; Haile, S.M.; Narayanan, S.R.: Polymer solid acid composite membranes for fuel-cell applications, *J. Electrochem. Soc. 147 No.10* (2000), pp. 3610-3613

[44] Kerres, J.; Ullrich, A.; Meier, F.; Häring, T.: Synthesis and characterization of novel acid-base polymer blends for application in membrane fuel cells, *Solid State Ionics 125* (1999), pp. 243-249

[45] Walker, M.; Baumgärtner, K.M.; Kaiser, M.; Kerres, J.; Ullrich, A.; Räuchle, E.: Proton-conducting polymers with reduced methanol permeation, *J. Appl. Polymer Sci. 74* (1999), pp. 67-73

[46] Finsterwalder, F.; Hambitzer, G.: Proton conductive thin films prepared by plasma polymerization, *J. Membrane Sci. 185* (2001) pp. 105-124.

[47] Libby, B.; Smyrl, W.H.; Cussler, E.L.: Polymer-zeolite composite membranes for direct methanol fuel cells, *AIChE J. 49 No.4* (2003) pp.991-1001

[48] Kjaer, J.; Yale-Andersen, J.; Knudsen, N.A.; Skou, E.: Solid-state electrolyte membranes for direct methanol fuel-cells, *Solid State Ionics 46* (1991) pp. 169-173

[49] Rao, N.; Andersen, T.P.; Ge, P.: Tin mordenite membranes for direct methanol fuel-cells, *Solid State Ionics 72* (1994) pp. 334-337

[50] Kerres, J.A.: Development of ionomer membranes for fuel cells, *J. Membrane Sci. 185* (2001) pp. 3-27.

[51] Eikerling, M.; Kornyshev, A.A.: Modelling the performance of the cathode catalyst layer of polymer electrolyte fuel cells, *J. Electroanal. Chem. 453* (1998), pp. 89-106

[52] Broka, K.; Ekdunge, P.: Modelling the PEM fuel cell cathode, *J. Appl. Electrochem. 27* (1997), pp. 281-289

[53] Baschuk, J.J.; Li, X.: Modelling of polymer electrolyte membrane fuel cells with variable degrees of water flooding, *J. Power Sources 86* (2000), pp. 181-196

[54] Scott, K.; Taama, W.M.; Argyropoulos, P.: Engineering aspects of the direct methanol fuel cell system, *J. Power Sources 79* (1999), pp. 43-59

[55] Argyropoulos, P.; Scott, K.; Taama, W.M.: Carbon dioxide evolution patterns in direct methanol fuel cells, *Electrochimica Acta 44 No.20* (1999) pp. 3575-3584.

[56] Eigeldinger, J.; Vogt, H.: The bubble coverage of gas-evolving electrodes in a flowing electrolyte, *Electrochimica Acta 45* (2000), pp. 4449-4456

[57] Springer, T.E.; Zawodzinski, T.A.; Gottesfeld, S.: Polymer electrolyte fuel-cell model, *J. Electrochem. Soc. 138 No. 8* (1991), pp. 2334-2342

[58] Kulikovsky, A.A.; Divisek, J.; Kornyshev, A.A.: Modeling the cathode compartment of polymer electrolyte fuel cells: Dead and active reaction zones, *J. Electrochem. Soc. 146 No. 11* (1999), pp. 3981-3991

[59] Costamagna, P.: Transport phenomena in polymeric membrane fuel cells, *Chem. Eng. Sci. 56 No. 2* (2001), pp. 323-332

[60] He, W.: Operating characteristics of a molten carbonate fuel-cell power-generation system, *Int. J. Energy Res. 23* (1999), pp. 1331-1344

[61] He, W.: An investigation on the dynamic performance of molten carbonate fuel-cell power-generation systems, *Int. J. Energy Res. 22* (1998), pp. 355-362

[62] He, W.; Chen, Q.: Three-dimensional simulation of a molten carbonate fuel cell stack under transient conditions, *J. Power Sources 73* (1998), pp. 182-192

[63] Neophytides, S.G.; Tripakis, A.: The transient operation of a solid oxide fuel cell monolith under forced periodic reversal of the flow, *Can. J. Chem. Eng. 74* (1996), pp.719-728

[64] Wöhr, M.; Bolwin, K.; Schnurnberger, W.; Fischer, M.; Neubrand, W.; Eigenberger, G.: Dynamic modelling and simulation of a polymer membrane fuel cell including mass transport limitation, *Int. J. Hydrogen Energy 23 No. 3* (1997), pp. 213-218

[65] Amphlett, J.C.; Mann, R.F.; Peppley, B.A.; Roberge, P.R.; Rodrigues, A.: A model predicting transient responses of proton exchange membrane fuel cells, *J. Power Sources 61* (1996), pp. 183-188

[66] Scott, K.; Taama, W.; Cruickshank, J.: Performance and modelling of a direct methanol solid polymer electrolyte fuel cell, *J. Power Sources 65* (1997), pp.159-171

[67] Scott, K.; Argyropoulos, P.; Sundmacher, K.: A model for the liquid feed direct methanol fuel cell, *J. Electroanal. Chem. 477* (1999), pp. 97-110

[68] Sundmacher, K.; Scott, K.: Direct methanol polymer electrolyte fuel cell: Analysis of charge and mass transfer in the vapour-liquid-solid system, *Chem. Eng. Sci. 54* (1999), pp. 2927-2936

[69] Siebke, A.; Schnurnberger, W.; Meier, F.; Eigenberger, G.: Investigation of the limiting processes of a DMFC by mathematical modeling, *Fuel Cells 3 No.1* (2003) pp.1-11

[70] Kulikovsky, A.A.; Divisek, J.; Kornyshev, A.A.: Two-dimensional simulation of direct methanol fuel cell - A new (embedded) type of current collector, *J. Electrochem. Soc. 147 No. 3* (2000), pp. 953-959

[71] Dohle, H.; Divisek, J.; Jung, R.: Process engineering of the direct methanol fuel cell, *J. Power Sources 86* (2000), pp. 469-477

[72] Meyers, J.P.; Newman, J.: Simulation of the direct methanol fuel cell: I. Thermodynamic framework for a multicomponent membrane, *J.Electrochem.Soc. 149 No.6* (2002), pp.A710-A717

[73] Meyers, J.P.; Newman, J.: Simulation of the direct methanol fuel cell: II. Modeling and data analysis of transport and kinetic phenomena, *J.Electrochem.Soc. 149 No.6* (2002), pp.A718-A728

[74] Meyers, J.P.; Newman, J.: Simulation of the direct methanol fuel cell: III. Design and optimization, *J.Electrochem.Soc. 149 No.6* (2002), pp.A729-A735

[75] Zhou, S.; Schultz, T.; Peglow, M.; Sundmacher, K.: Analysis of the nonlinear dynamics of a direct methanol fuel cell, *Phys. Chem. Chem. Phys. 3 No. 3* (2001), pp. 347-355

[76] Gilles, E.D.: Network theory for chemical processes, *Chem. Eng. Technol. 21 No. 2* (1998), pp. 121

[77] Mangold, M.; Motz, S.; Gilles, E.D.: A network theory for the structured modelling of chemical processes, *Chem. Eng. Sci. 57* (2002), pp.4099-4116

[78] Tränkle, F.; Zeitz, M.; Ginkel, M.; Gilles, E.D.: PROMOT: A modeling tool for chemical processes, *Math. Comp. Model. Dyn. Systems 6 No. 3* (2000), pp. 283-307

[79] Ganser, B.: Verfahrensanalyse: Wasserstoff aus Methanol und dessen Einsatz in Brennstoffzellen für Fahrzeugantriebe , *Berichte des Forschungszentrums Jülich 2748* (1993)

[80] Emonts, B.; Hansen, J.B.; Schmidt, H.; Grube, T.; Höhlein, B.; Peters, R.; Tschauder, A.: Fuel cell drive system with hydrogen generation in test, *J. Power Sources 86* (2000) pp. 228-236.

[81] Guzzella, L.; Amstutz, A.: CAE tools for quasi-static modeling and optimization of hybrid powertrains, *IEEE Transactions Vehicular Tech. 48* (1999) No.6, pp. 1762-1769.

[82] Hanke, R.; Mangold, M.; Sundmacher, K.: Modellierung und Dynamische Simulation von Brennstoffzellen - auf dem Weg zu einem virtuellen Brennstoffzellen-Labor, in: Hohmann, R. (Ed.), *Frontiers in Simulation-Proceedings 17. Symposium on Simulation Technique ASIM 2003*, Delft, SCS-Europe BVBA (2003), ISBN 3-936150-27-3, pp.19-26.

[83] Vidakovic, T.; Christov, M.; Sundmacher, K.: Investigation of electrochemical oxidation of methanol in cyclone flow cell, *Electrochimica Acta*, accepted 2003

[84] Christov, M.; Sundmacher, K.: Simulation of Methanol Adsorption on Pt/Ru Catalysts, *Surface Science*, **547** (2003), pp. 1-8.

[85] NIST webbook at www.webbook.nist.gov

[86a] Reid, R.C.; Prausnitz, J.M.; Poling, B.E.: *The properties of gases & liquids.* 4th ed., McGraw-Hill, New York (1987), p.656 (Appendix A)

[86b] pp.314-322

[86c] pp.602-603

[86d] pp.441 & Tab.9-8

[86e] p.54 Tab.3-9

[86f] p.52

[86g] pp.598-602

[86h] p.612

[86i] pp.314-332

[87] Novák, J.P.; Matous, J.; Pick, J.: *Liquid-Liquid Equilibria*, Academia, Prague (1987)

[88] Wilson, M.S.; Gottesfeld, S.: Thin-film catalyst layers for polymer electrolyte fuel-cell electrodes, *J. Appl. Electrochemistry 22 No.1* (1992) pp. 1-7

[89] Dinh, H.N.; Ren, X.; Garzon, F.H.; Zelenay, P.; Gottesfeld, S.: Electrocatalysis in direct methanol fuel cells: in-situ probing of PtRu anode catalyst surfaces, *J. Electroanal. Chem. 491* (2000) pp. 222-233

[90] Jörissen, L.; Gogel, V.; Kerres, J.; Garche, J.: New membranes for direct methanol fuel cells, *J. Power Sources 105* (2002) pp.267-273

[91] Steyer, F.: *Ermittlung und Analyse des Betriebsverhaltens von Direkt-Methanol-Brennstoffzellen (DMFC) mit flüssigem Brennstoff*, Studienarbeit, Deutsches Zentrum für Luft- und Raumfahrt e.V. (DLR), Stuttgart (1998)

[92] Argyropoulos, P.; Scott, K.; Taama, W.M.: Dynamic response of the direct methanol fuel cell under variable load conditions, *J. Power Sources 87* (2000) pp. 153-161.

[93] Argyropoulos, P.; Scott, K.; Taama, W.M.: The effect of operating conditions on the dynamic response of the direct methanol fuel cell, *Electrochimica Acta 45* (2000) pp. 1983-1998.

[94] Wesselingh, J.A.; Krishna, R.: *Mass Transfer in Multicomponent Mixtures.* Delft University Press, Delft (2000)

[95] Krishna, R.; Wesselingh, J.A.: The Maxwell-Stefan approach to mass transfer, *Chem. Eng. Sci. 52 No.6* (1997) pp. 861-911

[96] Gmehling, J.; Li, J., Schiller, M.: A modified UNIFAC model. 2. Present parameter matrix and results for different thermodynamic properties, *Ind. Eng. Chem. Res. 32 No.1* (1993) pp.178-193

[97] Wesselingh, J.A.; Vonk, P.; Kraaijeveld, G.: Exploring the Maxwell-Stefan description of ion exchange, *Chem. Eng. J. 57* (1995) pp.75-89, Fig. 18

[98] Zawodzinski, T.A.; Derouin, C.; Radzinski, S.; Sherman, R.J.; Smith, V.T.; Springer, T.E.; Gottesfeld, S.: Water Uptake by and Transport Through Nafion 117 Membranes, *J. Electrochem. Soc. 140 No. 4* (1993) pp.1041-1047

[99] Laporta, M.; Pegoraro, M.; Zanderighi, L.: Perfluorosulfonated membrane (Nafion): FT-IR study of the state of water with increasing humidity, *Phys. Chem. Chem. Phys. 1* (1999) pp.4619-4628

[100] Schlögl, R.: Membrane permeation in systems far from equilibrium, Berichte der Bunsengesellschaft für Physikalische Chemie 70 (1966) pp.400-414

[101] Bernardi, D.W.; Verbrugge, M.W.: Mathematical model of a gas diffusion electrode bonded to a polymer electrolyte, *AIChE 37* (1991) pp.1151-1163

[102a] Atkins, P.W.: *Physikalische Chemie.* VCH, Weinheim (1990), pp.857 Tab.0-1

[102b] pp.860 Tab.4-1

[103] data sheet for PTFE supplied by Bohlender GmbH, Grünsfeld (Germany)

[104] data sheets for platinum and ruthenium black catalysts, supplied by Alfa Aesar Johnson Matthey GmbH, Karlsruhe (Germany)

[105] data sheets for Nafion™, supplied by DuPont

[106a] *VDI-Wärmeatlas* 9.Auflage, VDI-Verlag, Frankfurt (2002), section Dbb1

[106b] section Ga

[107a] Perry, R.H.; Green, D.: *Perry's Chemical Engineers' Handbook*. 6th ed., McGraw-Hill, New York (1984), p.3-253

[107b] p.3-254

[107c] p.3-204

[107d] p.3-285

[107e] p.6-22

[107f] p.2-183 table 2-200

[108] Hanke, R.; Mangold, M.; Sundmacher, K.: Application of hierarchical process modelling strategies to fuel cell systems - towards a virtual fuel cell laboratory, *Fuel Cells*, submitted